Investigation of the Distribution Nucleation in a Fluidised Bed Using the Particle Coating Number

Layla Giuma Alhabeshi

A thesis submitted in partial fulfilment of the requirements for the degree of Doctor of Philosophy

The University of Sheffield

Faculty of Engineering

Department of Chemical and Biological Engineering

Supervised by:

Dr Rachel Smith

Dr Kate Pitt

Submission Date

September 2023

Declaration

To the best of my knowledge and belief, the work presented in this thesis is original, except as acknowledged in the text, and has not been submitted in whole or in part, for a degree at this or any other institution.

Layla Alhabeshi

May 2023

Acknowledgement

My first and foremost gratitude goes to my beloved parents, who tirelessly encouraged me to pursue my dreams, complete my studies, and endured my absence until their passing. May peace be upon them both. I can only imagine the joy you would feel if you were here today to celebrate my success. I miss you both immensely.

I would like to express my deepest appreciation to my supervisor, Dr Rachel Smith, for allowing me to embark on this PhD journey at the University of Sheffield and for her firm support. Thank you, Rachel, for your guidance, support, understanding, and motivation throughout my long PhD journey.

Additionally, I extend my heartfelt thanks to my second supervisor, Dr Kate Pitt, for the constant support she gave me. Her invaluable feedback on my work has been greatly helpful. Kate, your thoughtful comments and all your help is genuinely appreciated.

A special acknowledgement goes out to the exceptional technical staff of the Chemical & Biological Engineering Department, Andy Patrick and Mario Dorna, for their instrumental role in designing, creating, and modifying the fluidised bed throughout my study. I also wish to express my gratitude to Charles Walsh, Horace McFarlane, Julie Swales, and Millie Gillatt for their invaluable assistance in ensuring the safe operation of the laser. Your expertise and innovative ideas were invaluable.

I would like to thank all the Particle Technology Group members for their advice, technical assistance, and the wonderful times we've shared.

My deepest gratitude goes to my family, particularly my beloved husband and my dear children, who sacrificed their time with me during this demanding journey. Without your unwavering support, I would not have been able to complete my PhD.

I would also like to express my thanks to the Ministry of Higher Education in Libya for their generous financial support, which made this journey possible.

Above all, I am grateful to Allah for the blessings and opportunities that have enriched my life.

Abstract

In wet granulation, controlling binder distribution is critical to maintain control of subsequent growth. Distribution nucleation occurs when fine droplets wet larger powder particles before coalescing upon collision to form nuclei by forming liquid bridges. The dimensionless particle coating number Φp introduced by Kariuki is the first quantitative approach that aims to predict the fractional surface coverage of the solid material by liquid during nucleation. Φp is an equipment-independent number that uses simple parameters such as liquid-solid fraction, specific surface area and droplet diameter. This study was conducted in a lab-designed fluidised bed to examine the influence of various parameters on distribution nucleation and to validate and develop the PCN as a tool for predicting the behaviour of particle systems. A range of molecular weights of HPMC solutions were used as aqueous solutions. The solid system included model powder (glass beads) of different size ranges and pharmaceutical excipient lactose (capsulac 60). The PCN model proposed by Kariuki successfully predicted liquid coverage under varying conditions of liquid mass, viscosity, atomisation pressure, primary particle size, and material characteristics and unchanged when mixing time and fluidisation velocity were changed. Global PCN was designed to estimate liquid coverage across the entire bed system and successfully tracked changes in contact angle and footprint area. Additionally, local PCN was developed to approximate liquid coverage within the spray zone, incorporating additional key parameters like solid density, bubbling velocity, and ability to capture spray coverage area.

When changing the liquid mass introduced to the fluidised bed system, the agglomerated fraction increased, and the distributions broadened due to increased nuclei size. The PCN was able to predict the nucleation success outcome. Powders with similar particle size, glass beads and capsulac 60 showed increased PCN in response to more liquid mass introduced per surface area, capsulac 60 showed larger liquid coverage due to its smaller contact angle and larger droplet footprint. While capsulac 60 had more nucleation success, the glass beads formed larger nuclei due to the differences in their characteristics.

For glass beads, atomisation pressure significantly improved granulation quality by enhancing liquid dispersion. It increased the agglomerated fraction, reduced the mean nuclei size, and narrowed the size distribution. Global PCN was highly sensitive to small changes in droplet size and footprint and local PCN could also incorporate spray coverage area. This emphasises the crucial influence of PCN when altering atomisation pressure in fluidised bed granulation,

as small variations in PCN can have a substantial impact on the process. In a system with a constant PCN, i.e., stabilised liquid coverage per solid surface area, an increase in initial particle size dramatically reduced granulation and the mean nuclei size due to the dominant kinetic energy. A higher PCN is required to enhance granulation behaviour under these conditions. The physicochemical variable viscosity enhanced nucleation quality, the largest yield and narrowest distribution were achieved with the highest viscosity. The PCN was inversely proportional to viscosity and exhibited sensitivity to changes in contact angle and droplet size despite the complexities of viscoelastic binder behaviour. Mixing time exhibited a brief growth phase followed by a reduction phase in nuclei size, while rising air velocity which enhanced powder flux at the spray zone improved nucleation distribution to some extent. The highest velocity yielded the largest fraction of nuclei with a narrower distribution toward smaller sizes. These two parameters are unrelated to liquid distribution, and the PCN remains unchanged.

Alongside key contributors to nuclei formation, this study demonstrated the critical role of liquid dispersion in distribution nucleation. The PCN model has proven to be a highly effective and reliable method for quantifying particle coverage by liquids in fluidised bed granulation, showing clear superiority in predicting nucleation success compared to the liquid-solid ratio. As a result, it is expected to play a significant role in the future design and scale-up of fluidised bed granulators.

- Contents

List of Figures

List of Tables

Abbreviations

$\dot{a}_{d,T}$	total projected area covered by unit time
a_d	area covered by a single drop
A	cross-sectional area of a bed
a_d	footprint area of a single droplet
A_P	surface area of the particle.
A_P	Plate area (cm^2)
A_r	Archimedes number
d_d	average drop size
d_p	diameter of the particle
d_{Bv}	the equivalent volume diameter of the bubble mean bubble size
F	predicted fractional coating coverage
f	fraction of M panels coated by a droplet's footprint
g	acceleration due to gravity
H	height of the bed
h	thickness of the liquid layer on a particle surface
H_{mf}	bed height at U_{mf}
K	deformability of the particles
m_d	liquid mass delivered to the surface per unit time
M	number of panels
M_{Bed}	mass of the bed
$\dot{n}_d$	number of drops produced by a nozzle per unit of time
N	number of droplets
Q	actual gas flow rate to the fluid bed
Q_{mf}	volume flow rate of gas into bed at U_{mf}
r	harmonic mean particle radius
r	radius of the curvature of the liquid surface
R_{pore}	pore radius

Re_{mf}	Reynolds number at incipient fluidization.
A_{SA}	Specific surface area
St_v	viscous Stokes number
St_v^*	critical Stokes viscous number
t_c	circulation time
t_p	plate thickness
t_p	experimental drop penetration time
T_p	dimensionless penetration time
U_B	mean of a bubble rise velocity in a bed
U_C	velocity of the impact between two particles
U_{mb}	superficial gas velocity at a minimum bubbling
U_{mf}	minimum fluidisation velocity
$\dot{v}$	volumetric spray flow rate
x	half of the distance between two particles
X_{LS}	liquid–solid mass fraction
Δp_{cap}	capillary suction pressure
ΔA	area of a single panel
ΔP_{bed}	drop in the pressure across the bed
ΔP_{dis}	Pressure drop across distributor plate
ε_{eff}	effective porosity
ε_{tap}	tapped porosity
ε	loose-packed porosity or bed voidage
ε_{mf}	porosity of a bed at minimum fluidisation velocity
γ_{lv}	adhesive tension mN/m
γ_{sl}	liquid-solid interfacial energy
γ_{sv}	solid-vapour interfacial energy
θ	contact angle between the liquid drop and the solid surface
μ	gas viscosity
ρ_e	envelope density of the material
φ_d	spherical particle diameter

Φ_D	Permeability of plate material
Φ_p	particle coating number
Ψa	dimensionless spray flux
ψ^{geom}	geometrical success factor
ψ^{phys}	physical collision success factor
ρ	bed bulk density of the bed
ρ_f	fluid density
ρ_g	gas density
ρ_t	true density of a material
φ	sphericity of a particle
α	the ratio of liquid rate to solid renewal rate
ϑ_B	Constant for bed diameter

Chapter 1: Introduction

1.1 Background

Granulation is a size enlargement process in which particles are brought into contact with each other to form agglomerates called granules. This process is extensively applied in many industries, such as pharmaceuticals, detergents, food, and chemicals.

Granulation is a process used to produce granules with definite properties to meet end-product requirements (Seville et al., 2000, Litster and Ennis, 2004a). Therefore, controlling granulation and understanding the mechanisms underlying the process is crucial. For example, recent advances in pharmaceutical sciences and biotechnology create a trend in pharmacy of increasing drug potency in miscellaneous drug delivery systems. The potent novel drug is required in granulated form, containing only a low concentration of active ingredients well mixed with a high proportion of excipients. Granulation is used to eliminate the risk of an inadequate uniformity of the active component in the dosage form. Therefore, granulation has become a kind of particle design. According to Litster (2004), 'the technologist should have a prior proper knowledge about the desired granule product attributes.' These can be controlled by a combination of formulation properties and operating parameters and correct choice granulator equipment. As a result of the wrong choice for formulation properties or process parameters, poor granulation will lead to problems such as segregation, caking, and poor tableting, which impose significant economic losses (Iveson et al., 2001, Litster and Ennis, 2004a).

During wet granulation, a binder is used to agglomerate particles. Nucleation is first mechanism to occur when the powder comes into contact with the binder forming initial 'nuclei'. The ratio of droplet size / particle size is found to determine whether the mechanism of nucleation is distribution or immersion. When the droplet size is larger than the particle size, the nucleation is by an immersion mechanism. However, when the particle is larger than the droplet size, then nucleation occurs via a distribution mechanism. Due to the very short time for nucleation to occur, Hapgood (2009) indicated that researchers 'deliberately' focus

on the final stages of granulation. Therefore, the least understood mechanism is still the nucleation process. Understanding and controlling nucleation does not only control nuclei size distribution but also controls growth and the product granule size distribution. Although a method for predicting the nuclei size distribution based on the dimensionless spray flux has been developed, this is restricted to the drop controlled regime and, therefore, applicable only for immersion nucleation (Hapgood et al., 2009).

However, recent models have extended the nuclei size distribution prediction to a higher extent. Bellinghausen (2019) has developed a nuclei size distribution model using the dimensionless nucleation number Ψa. The empirical model was found able to precisely capture the Monte Carlo simulations (MCS) data and the predictions encompasses experimental results over a wide range of experimental conditions ($0 < \Psi a < 3$) (Bellinghausen et al., 2019)
For the distribution mechanism, Kariuki et al. (2013) used a Bernoulli model and developed a new dimensionless parameter, the particle coating number, Φ_p, to describe the fractional surface coating. This parameter estimates the amount of liquid available at the surfaces of the particles regardless of the thickness of the liquid layer, thus potentially could predict the granulation outcome. The authors experimentally validated the particle coating number by randomly adding different sizes of melted polyethene glycol PEG1000 drops over the surface of a model particle (standard ping pong ball). The fractional surface coating was measured using image analysis. However, this needs more investigation (Kariuki et al., 2013).

1.2 Motivations and novelty of the thesis

In wet granulation, nucleation plays a crucial role in determining the size and final attributes of granules. There is a lack of comprehensive information in the literature regarding the distribution nucleation mechanism despite its recognition by researchers. They indicated that the relative sizes of the primary particles and the binder droplets would influence the nucleation mechanism and described certain conditions under which the distribution mechanism controlled partial granulation outcome (Zhai et al., 2009, Schæfer and Mathiesen, 1996). Others have reported the granule attributes produced by the distribution mechanism by fluidised bed melt granulation (Abberger, 2001, Zhai et al., 2010, Tan et al., 2006). Kariuki (2013) introduced a quantitative approach to describe the distribution nucleation mechanism, a theoretically derived dimensionless quantity termed "the particle coating number”. This number aims to predict the fractional surface coverage of particles by the liquid during

distribution nucleation. This number was trialled by Kariuki and co-workers on stationary model particles using image analysis (Kariuki et al., 2013).

This thesis explicitly investigates the distribution nucleation mechanism inside a top spray lab scale fluidised bed. It focuses on studying the impact of formulation and operational parameters on the process. This work applied the concept of the particle coating number parameter to predict and control granule formation where small drops are distributed over larger particles. This research aims to improve the understanding of the distribution mechanism and aims to establish a practical application of the quantitative approach proposed by Kariuki and emphasises its use in controlling the fluidised bed system. Additionally, this thesis aims to contribute to the broader understanding of wet granulation processes and their applications in controlling the pharmaceutical, coating and food industries.

1.3 Aim of the thesis

Distribution nucleation is one of the key nucleation mechanisms involved in 'wet' agglomeration processes and controls granule product form and size, especially in fluidised bed systems. This study aims to understand the distribution nucleation mechanism and to develop a new conceptual theory that is able to describe and predict the effect of different variables on the distribution mechanism. This will have an impact on industrial fluid bed processing.

To achieve these goals, this thesis will focus on the following objectives:

1. To design a laboratory scale fluidised bed granulator.
2. To identify suitable model materials to study the distribution nucleation mechanism.
3. To study the effect of changing the material and the process variables on the granulation process inside the fluidised bed system.
4. To predict the effect of changing material variables on coating fraction using the novel dimensionless group, the particle coating number, developed by (Kariuki et al., 2013).
5. To develop the particle coating number further for use in fluidised bed granulation.

1.4 Structure of the thesis

A literature review is presented in Chapter 2. Firstly, granulation techniques and equipment are discussed, focusing on wet granulation techniques and equipment, followed by a detailed description of fluidised bed granulation as the technique used in this study. This includes the theory of fluidisation and a detailed description of the equipment. Furthermore, the effect of

formulation and operating variables is reviewed. The second part of the literature review focuses on granulation mechanisms occurring in a fluidised bed; in particular nucleation and liquid distribution, where immersion and distribution mechanisms are discussed in detail.

Chapter 3 gives a detailed account of the materials and methods used in this research and the equipment used for the characterisation of raw materials and final products.

Results: Chapter 4 describes the design and commissioning of the fluidised bed specifically developed for this work, finding the particle/binders required and optimising the operating conditions to conduct this research.

Chapter 5 presents the influence of material properties on distribution nucleation and particle coating number in fluidised bed granulator. The effect of binder viscosity and primary particle size using model particles (glass beads), and hydroxypropyl methylcellulose as the binder are investigated.

Chapter 6 presents the influence of operational parameters on both particle coating number and distribution nucleation outcome by investigating the effect of liquid flow rate, mixing time, atomisation pressure and fluidisation velocity.

Chapter 7 presents a particle coating number case study using a pharmaceutical excipient, lactose, to study how material properties affect the distribution mechanism.

Chapter 8 provides overall conclusions and recommendations for future work.

Chapter 2: Literature review

2.1 Introduction

Granulation is a process in which small particles are agglomerated to form larger granules. The original particles can still be distinguished in the agglomerates (Ennis, 2005). Manufacturing granules is more favourable than just using conventional powders for several reasons:

- Granulation increases the flowability of powder blends by enhancing both the flow rate and the flow consistency of the powder, which leads to a more controllable process.
- Granulation could improve the compaction properties of the powder mix by adding binders. This will enhance adherence under compression.
- Granulation reduces dust formation, which results in less exposure to toxic/potent materials.
- Uniform granules have less tendency to segregate. Granulated material will prevent constituents from segregation at the bottom of the container.
- Physical properties of some pharmaceutical products, such as porosity, wettability hardness, as well as dissolution rate, could be significantly improved by granulation.
- Granulation controls surface-to-volume ratio and produces dense granules which help with handling, shipping and storage of the bulk material.

2.2 Methods of granulation

Generally, in industry, the term granulation is referred to agglomeration by agitation. The material is introduced to a process container and is agglomerated, either in batches or in a continuous manner, to form a granulated product (Ennis, 2005). The granulation process is classified according to the method or technique used: dry granulation, wet granulation, melt granulation, and foam granulation. These will be discussed in the following sections.

2.2.1 Dry granulation

Dry granulation is a common method of processing in pharmaceutical manufacturing. In dry granulation, dry powders are compressed into compacts by pressure. Subsequent milling of these intermediates leads to the formation of granules (Am Ende, 2008). Here, blending is a

crucial step to achieve adequate uniformity before granulation. This type of granulation can be processed by either roller compaction or slugging using special tablet presses. The products are then sieved to give the desired granule size.

The main advantage of this method is that it eliminates the need for using a liquid binder. Therefore, this method is mainly applicable for solid oral dosage forms that are sensitive to heat and moisture. However, more dust is created by this process, and colour uniformity is difficult to achieve. Moreover, common defects in the tablets prepared by the dry granulation method might occur because of the dryness of the particles, such as capping, which is the cap of a tablet being sheared apart from the body, and lamination when the tablet body is fractured into horizontal layers.

2.2.2 Melt granulation.

Melt granulation can be achieved by using low-melting point binders. Heat is continuously applied during the process of granulation to melt the solid binder. Alternatively, the binder is heated, and the molten binder is attained before the process starts. Once the desired granules are obtained, the system is cooled in order to solidify the binder. The process is suitable for water-sensitive materials. However, thermolabile materials are not appropriate candidates. Usually, the process is referred to the type of equipment used; HSMG for high shear melting granulation and FBMG for fluidised bed melt granulation, which is more common (Mangwandi et al., 2015). Tan (2006) summarised the potential particle behaviour in a fluidised bed melt granulation, and the author identified five rate processes, starting from droplet particle collisions; binder solidification rate; particle-particle collisions rate; the liquid bridge formation rate; and the solid bridge rupture rate (Tan et al., 2006).

The mechanism in melt agglomeration resembles that in wet granulation. The only difference is that the growth process is not as complicated as in wet granulation, as there is no liquid evaporation. The growth is only dependent on the equilibrium between size enlargement and size reduction (Wong, 2005).

2.2.3 Foam granulation

Foam granulation is a relatively new process whereby liquid binders are added in the form of aqueous foam instead of liquid form. Keary & Sheskey (2004) indicated that less quantity of water is needed to be added to the powder than spray granulations and the foam to be incorporated later in the process and can be added in a single batch to the surface of the powder bed. This procedure eliminates the need for spray addition and avoids difficulties in considering

the nozzle features, such as the height of the nozzle, spray rate, and droplet size (Keary and Sheskey, 2004). Later, transformation maps were suggested by Tan and Hapgood (2012) relating variables like foam quality, powder size, binder concentration and mechanical agitation with the granule size distribution. Many formulations were effectively scaled up from the laboratory scale (Tan and Hapgood, 2012).

2.2.4 Wet granulation

The wet granulation process involves the use of liquid to act as a binder. This can be achieved by pouring or spraying a liquid binder on the wet powder particles while being mixed mechanically in appropriate equipment. The colliding particles are combined by capillary and viscous forces in the wet state. When drying the wet mass, permanent bonds are formed to give agglomerates (Saleh et al., 2015). Wet granulation is the most applied method in the pharmaceutical industry because it offers many advantages. It enhances the product sphericity and flow and improves the compressibility of the granules. It also reduces dust formation and, therefore, decreases the risk of cross contamination. Better dissolution rates for hydrophobic drugs also could be attained by wet granulation (Almaya, 2008).

Heat-sensitive or moisture-sensitive substances are not good candidates for wet granulation because of the drying process. However, alternative binders such as organic solvents can be used, but they are expensive. Additionally, wet granulation is multiple step process. Hence, many variables should be well controlled (Almaya, 2008).

2.3 Wet granulation equipment

Many types of equipment are used for wet granulation, including pans, rotating drums, mixers, fluidised beds, and compression granulators (Litster and Ennis, 2004a). They differ in size, methods, and typical applications and will be discussed in the following sections. As fluidised bed granulation is the focus of this research, it will be separately discussed in Section 2.4.

2.3.1 Mixer granulators

Mixer granulators are frequently used in the pharmaceutical, chemical and agricultural industries and are divided into two different types:

2.3.1.1 Low shear granulators

Compared with the high-shear granulators, low-shear granulators have lower speed and consume less energy. The powders are loaded into a container, and the blend is agitated by a

paddle after adding the binder. The product is then passed through a sieve screen using an oscillating container. The main disadvantages of low-shear granulators are that they are time consuming and a high material loss (Almaya, 2008).

2.3.1.2 High shear granulators

In high shear granulators, an impeller is usually located at the bottom of the bowl, with a chopper situated at or near the side of the bowl. However, the impeller can also be at the bottom or the top, and the chopper can be side or top-mounted (Briens and Logan, 2011). When the impeller and the chopper rotate at moderate to high speed, this generates high shear rates and impact velocities in some regions of the mixer. Both mixing and granulation can be achieved simultaneously and in a short interval of time (typically a few minutes). Trials were conducted by (Hoornaert et al., 1998) with the chopper off and with the chopper on at a speed of 3,000 rpm. Significant granulation was achieved when the chopper was on. The shear forces provided by the chopper were required for coalescence for granule growth. Before granulation starts, mixed or premixed powders can be loaded into high-shear mixers, and then the liquid binder can be pumped, poured, or atomized before or during the mixing. Further mixing with the impeller and the chopper will distribute the liquid binder across the wet mass while granule growth takes place. However, the procedure should be firmly controlled since over-growth may take place. Depending on the design of the mixer, high shear rates impact some regions of the blend more than others. Therefore, the design of the equipment used should be taken into consideration when assessing the experimental data (Almaya, 2008, Litster and Ennis, 2004a). According to Litster & Ennis (2004), mixers have advantages over other types of granulators. They can process both cohesive powders and viscous binders, producing the most robust and dense granules. Their main disadvantage is that they are challenging to scale and maintain product characteristics, as well as high operating costs.

2.3.2 Tumbling granulators

Tumbling granulators are widely used to process minerals and fertilizers because they are suitable for producing high density pellets, not highly porous granules (Litster and Ennis, 2004b). Powders are agitated by the tumbling action which is balanced between gravity and centrifugal forces (Ennis, 2010). There is a range of tumbling granulation equipment, such as discs, drums, and pans. They are able to produce large dense granules of 2-20 mm diameter, but they are not appropriate when small porous granules are desired (Litster and Ennis, 2004b).

The binder is added through a line of nozzles facing the bed. It should be noted that, due to the tumbling motion, segregation of the differently sized particles may occur in this process.

2.3.3 Twin screw granulators (TSG)

In the pharmaceutical industry, the TSG has recently become the equipment of choice for continuous wet granulation, compared to batch equipment such as high shear and fluidised bed granulators. TSGs have many advantages, such as continuous production, less space requirement and fewer scale up steps (Saleh et al., 2015). More importantly, a study by Steffens et al in (2020) found that granules produced by TSG achieved a narrower particle size distribution and a higher yield than the high shear (HSG) granules. Also, granulation parameters had only a minor impact on the particle size (Steffens et al., 2020).

2.4 Fluidised bed granulation

2.4.1 Introduction

Fluidised beds started to be operated commercially in Germany in a Winkler coal gasifier in the 1920s. Since then, fluidised beds have become extensively implemented in numerous chemical processes such as oil separations and nuclear fuel preparation (Cocco et al., 2014). In addition, fluidised beds have also been widely used for granulation, drying and coating processes in pharmaceutical industry. Fluidised bed granulators do not use mechanical agitation but utilize N_2 or air instead to move the particulate material. The air is passed through a gas distributor at the bottom of the container and collected by an air filter system (Litster and Ennis, 2004a). A diagram for a top-spray fluid bed granulator is demonstrated in Figure 2.1.

Fluidised bed granulators are appropriate for large scale production, possess excellent heat and mass transfer rates, and occupy only small areas. They provide smooth gentle flow of particles, and sampling could be performed during the process (Litster and Ennis, 2004a, Kunii, 1991). Unlike high shear granulators, fluidised beds produce porous granules that have better dissolution and compression properties. In addition, they show narrow size distributions without over-large granules. The fluid bed granulators are able to perform consistent mixing and continuous and concurrent wetting /drying, reduce the residual moisture and increase the stability of the granules (Burggraeve et al., 2013). Furthermore, they show great potential for continuous production (Loh et al., 2011).

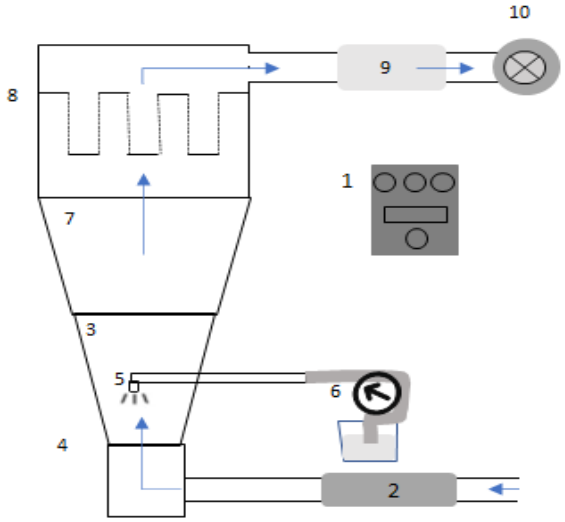

Figure 2.1: Schematic of a top-spray fluid bed granulator with basic components: (1) control panel, (2) air handling unit, (3) product container, (4) air distributor plate, (5) top-spray installed nozzle, (6) pump, (7) air expansion chamber, (8) filter bags, (9) air filter system, and (10) exhaust blower. Arrows indicate the direction of the airflow. Adapted from (Burggraeve et al., 2013).

The high costs for an air handling unit, and a dust recovery unit, as well as poor operation for fine cohesive powders, which are difficult to fluidise are main disadvantages. Also, uncontrolled variables may result in excessive growth and therefore defluidisation due to quenching (Litster and Ennis, 2004a).

2.4.2 Theory of fluidisation

In order to design a fluidised bed granulator, the theory of fluidisation should be understood. Improper design and operation could result in poor granulation and solids losses.

2.4.2.1 Voidage and pressure drop at incipient fluidisation

When a gas is passed upward through a bed of particles at low flow rate, there will be a drop in the pressure due to the frictional resistance, which increases gradually with the increasing velocity of the gas. When the flow rate increases, a few particles will visibly vibrate. The separation of the particles increases until the point at which the gas velocity is high enough that the drag force is equal to the weight of the bed, and the bed becomes fluidised, i.e., the pressure drop across the fluid bed is equal to the apparent weight of the particles per unit area of the bed. At this point, the bed can be lifted. The pressure drop across the fluid bed can be calculated as follows:

$$\Delta P_{bed} = \frac{HA\,(1-\varepsilon)(\,\rho_p - \,\rho_g)g}{A} \qquad (2.1)$$

Where**:** ρ_p is the particle density, and the bed is fluidised by a gas of density, ρ_g to form a bed of height, *H*, and voidage, ε, in a bed of cross-sectional area, *A*. The pressure drop across the fluidised bed becomes equal to net bed weight, which is then the product of bed volume, *HA*, net density, the fraction of the bed (1- ε) and the acceleration due to gravity, g (Rhodes, 2008). By rewriting Equation (2.1):

$$\Delta P_{bed} = H(1-\varepsilon)(\,\rho_p - \,\rho_g)g \qquad (2.2)$$

The gas velocity at this point is commonly referred to as the *minimum fluidisation velocity* U_{mf}, and it is the superficial fluid velocity at which the packed bed becomes a fluidised bed. Although the fluid velocity increases after minimum fluidisation velocity, U_{mf}, the drop in the pressure remains constant (Figure 2.2).

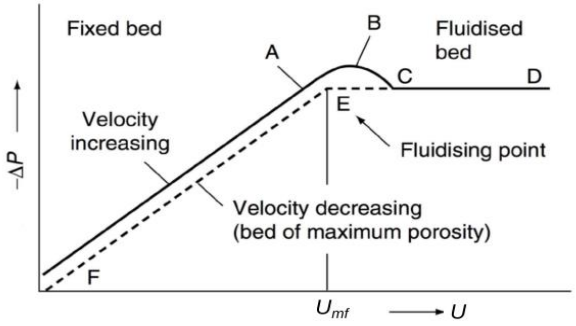

Figure 2.2: Diagram of the pressure drop ΔP as a function of the superficial velocity U. The point E is the Umf at which fluidisation occurs. At A & B, the particles are rearranged (Florida, 2015)

To mathematically estimate the minimum fluidisation velocity, suppose a single particle falling under gravity in a stationary gas; the particle will reach a terminal velocity when the forces of gravity, buoyancy and drag are balanced. If the gas is moving upwards at a speed equal to the particle's terminal velocity, the particle will be static. Suppose the gas is flowing upwards in a pipe at a velocity equal to the particle's terminal velocity. In that case, two main flow patterns will be observed: *laminar flow* and *turbulent flow*. The Archimedes number, *Ar*, is a dimensionless number used to define the motion of fluids due to density differences in viscous fluid dynamics. It is calculated as:

$$Ar = \frac{g{d_p}^3 \rho_f (\rho_{p-} \rho_f)}{\mu^2} \qquad (2.3)$$

Where g is the acceleration due to gravity, d_p diameter of the particle, ρ_f is fluid density, ρ_p is particle density and μ is the viscosity of the fluid. Different flow conditions can be defined in terms of the Reynolds number (Re_{mf}), which is a dimensionless number used to predict flow patterns in different fluids. The two main flow patterns are: (i) *Laminar flow*, which is characterized by smooth, constant fluid motion, dominated by viscous forces and the particle moves up or down depending on its radial position because of the parabolic velocity of the gas in the pipe, and (ii) *turbulent flow*, which is dominated by inertial forces, tends to be disordered, and velocity fluctuations make the actual particle movement less predictable. Laminar flow occurs with low Reynolds numbers. If the Reynolds number is less than 10, an absolute laminar condition occurs. However, if Re_{mf} is around 2000 this means the flow is fully turbulent (Rhodes, 2008).

Re_{mf} at incipient fluidisation is:

$$Re_{mf} = \frac{d_p U_{mf} \rho_g}{\mu} \qquad (2.4)$$

According to Rhodes (2008), Carman and Kozeny (1937) developed a model based on assuming the packed bed contains a number of capillaries. However, the Carman-Kozeny model is only applicable for laminar flow, i.e. the particle Reynolds number $R_{emf} < 20$ (Rhodes, 2008).

Ergun, in 1952, suggested a general equation for all ranges of flow (Cocco et al., 2014, Rhodes, 2008, Kunii, 1991, Parikh and Mogavero, 2005, Wong, 2005). As in the case of the drag force on a single particle, the pressure gradient $(-\Delta P)$ across a fixed bed packed with spherical particles of diameter, $\emptyset d$, can be calculated by the Ergun equation:

$$\frac{(-\Delta P)}{H} = 150 \ \frac{\mu U}{\emptyset d^2} \ \frac{(1-\varepsilon)^2}{\varepsilon^3} + 1.75 \ \frac{\rho_g U^2}{\emptyset d} \ \frac{(1-\varepsilon)}{\varepsilon^3} \qquad (2.5)$$

Where U is the superficial gas velocity, $\emptyset d$, is the diameter of spherical particles and ε is the bed porosity. The left side of the equation represents the pressure loss due to viscous drag (the Carman-Kozeny equation) whereas the right side represents kinetic energy losses, and it is valid for the range $1 < Re < 2000$.

Rewriting Ergun's equation for minimum fluidising conditions, Equation (2.5) by assuming the particles are spherical (∅= 1), and by substituting - ΔP by Equation (2.2) and Re_{mf} by Equation (2.4), the following equation is derived:

$$(1-\varepsilon)\left(\rho_{p}-\rho_{g}\right) g = 150\,\frac{(1-\varepsilon)^2}{\varepsilon^3}\,\frac{\mu U_{mf}}{d^2} + 1.75\,\frac{(1-\varepsilon)}{\varepsilon^3}\,\frac{\rho_g {U_{mf}}^2}{d} \qquad (2.6)$$

For simplification, the Archimedes number is substituted, and the equation is rearranged to give:

$$Ar = 150\,\frac{(1-\varepsilon)}{\varepsilon^3}\,Re_{mf} + 1.75\,\frac{1}{\varepsilon^3}\,Re_{mf}^2 \qquad (2.7)$$

2.4.2.2 Calculation of the minimum fluidisation velocity, U_{mf}

To estimate the U_{mf}, the bed voidage at incipient fluidisation, $\varepsilon_{mf,}$ should be found using Equation (2.6). As the bed voidage at incipient fluidisation becomes larger than that of the packed bed voidage, ε , a value of 0.4 is used. Wen & Yu (1966) developed an empirical correlation for predicting the U_{mf}. The Wen and Yu correlation is mainly applied to spheres > 100 µm, and for Re_{mf} in the range $0.01 < Re_{mf} < 1000$ (Rhodes, 2008):

$$\mathrm{Re_{mf}} = (33.7^2 + 0408Ar)^{1/2} - 33.7 \qquad (2.8)$$

For gases, the Archimedes number Equation (2.3) becomes:

$$A_r = \frac{{d_p}^3 \rho_g\left(\rho_p - \rho_g\right) g}{\mu^2} \qquad (2.9)$$

By substituting both the modified Archimedes number A_r (2.9) and Reynolds number Re_{mf} (2.4), into one equation, the following equation (2.10), is obtained:

$$\frac{d_p\, U_{mf}\, \rho_g}{\mu} = \left[(33.7^2 + 0.0408\,\frac{{d_p}^3 \rho_g\left(\rho_p - \rho_g\right) g}{\mu^2}\right]^{0.5} - 33.7 \qquad (2.10)$$

According to (Litster and Ennis, 2004a) this correlation is of accuracy of ± 30%, and applicable for a wide range of fluids and particles of wide size distribution, providing the $d_{3,2}$ particle size is used.

2.4.3 Types of fluidisation behaviour

Fluidisation behaviour depends on the velocities of gas, as well as the properties of the particles (Figure 2.3). At a very low flow rate of the gas through the bed, the gas only penetrates the stationary particle voids, which is a *packed bed*. When gas velocity through the bed is increased above the minimum fluidisation velocity, U_{mf} a variety of fluidisation behaviours could be observed. *Particulate smooth fluidisation* occurs immediately after fluidising. The bed may expand homogeneously.

When minimum fluidisation velocity is exceeded, the minimum bubbling velocity, U_{mb}, will be reached, and the bubbles are formed in the bed producing *bubbling fluidisation*. Notably, after this point, all additional gas will be introduced in the form of bubbles.

If the gas velocity is raised above the terminal settling velocity of the particles, *turbulent fluidisation* occurs where most particles are in the freeboard, and there is no definite bed surface noticeable. At this stage, there will be a high rate of elutriation, and particles should be recirculated to the bed (*fast fluidisation).* Finally, the lean phase *conveying regime* could be reached at very high gas velocities, and at this point all the particles are distributed at very low concentration throughout the vessel (Litster and Ennis, 2004a).

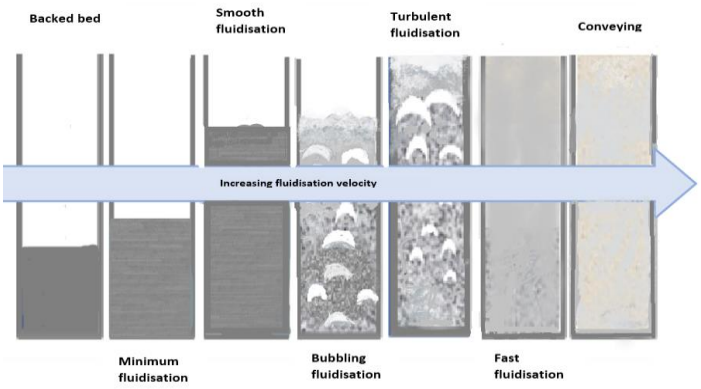

Figure 2.3: The types of fluidisation changes - Adapted from (Cocco, Karri and Knowlton, 2014).

2.4.3.1 Geldart classification of powders

As previously mentioned, fluidisation behaviour depends on the properties of the powders. Geldart (1973) classified powders into four groups according to their fluidisation properties. This classification is usually used by all sectors of powder technology and by which fluidisation behaviour for any powder in ambient conditions may be predicted (Figure 2.4).

Geldart Group A particles are the most frequently encountered in commercial gas fluidised systems. They are characterised by easy fluidisation and small particle size ranging from 30 µm to 125 µm, and densities of 1.500 kg/m^3 (Cocco, Karri and Knowlton, 2014). Group A powders show considerable particulate expansion without bubble formation when gas velocities are low. They could lose most of the bulk to downstream if they fluidised in wrongly designed vessels due to 100% expansion, i.e., $U_{mf} < U_{mb}$.

Geldart Group B particles are sand-like powders with particle sizes ranging from 150 -1000 µm (Cocco et al., 2014). They are also easy to fluidise but do not show any particulate expansion. Bubbles tend to form at the beginning of fluidisation. Above U_{mf}, all excess gas goes in the form of bubbles. Therefore, both the minimum fluidisation and the minimum bubbling velocities are similar, i.e., $U_{mf} = U_{mb}$.

Type C powders have small particle sizes (less than 30 µm) but are the most difficult to fluidize. They are cohesive and, therefore, they show significant channelling, i.e. the fast bubbles move in channels and bypass most of the bed. In fact, particles in this group tend to move in clusters rather than single particles. Sometimes, powders of group B are added to the bed to improve the fluidisation.

Type D particles (Spoutable): This group includes the largest particles, so they require high velocities of gas to be fluidised. The bubbles formed are extremely large, and slugging behaviour occurs even in beds of large diameter. Thus, these materials are processed in spouting beds. In this kind of bed, the gas primarily passes through the centre of the bed (Litster and Ennis, 2004a).

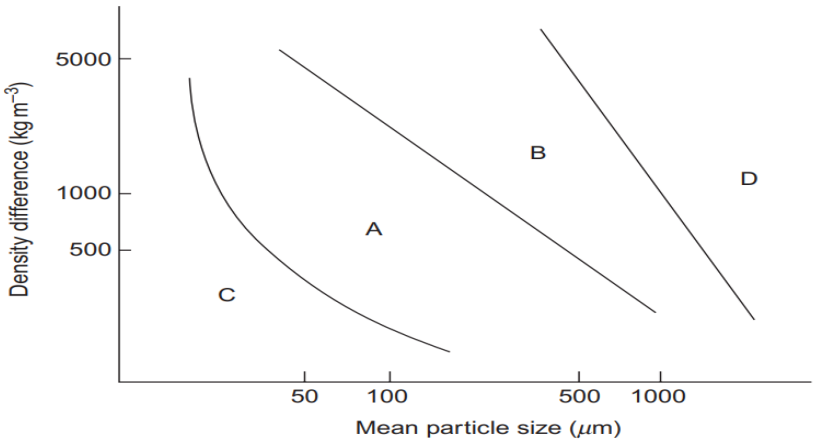

Figure 2.4: Geldart classification of powders (Smith, 2007).

2.4.3.2 The role of bubbles in a fluidised bed

Fluidised beds are typically operated at bubbling bed velocity, which is above the minimum fluidisation velocity and below the turbulent velocity (Zhai et al., 2009). Bubbles form when the gas velocities exceed the minimum fluidisation velocity and are responsible for the motion of particles in the fluidised bed. By means of rising bubbles, solids are thrown into the freeboard when the bubble bursts (Figure 2.5). Bubbling velocity depends on the size and density of the particles. Small and light particles tend to experience smooth fluidisation before bubbles form. Denser or larger particles tend to start bubbling at the point of minimum fluidisation. Bubbles are responsible for the expansion and mixing of the fluidised bed. As they grow as they rise through the bed, the small, formed bubbles at the distributor plate coalesce as they rise and burst at the surface. Solid particles are thrown and mixed by means of rising bubbles. This is because the pressure in the lower part of the bubble is less than in the surrounding emulsion. As a result, gas is dragged into the bubble, initiating instability and a slight and continuous interchange of solids between the emulsion and the region just below the bubble, thus turbulent mixing occurs (Kunii, 1991).

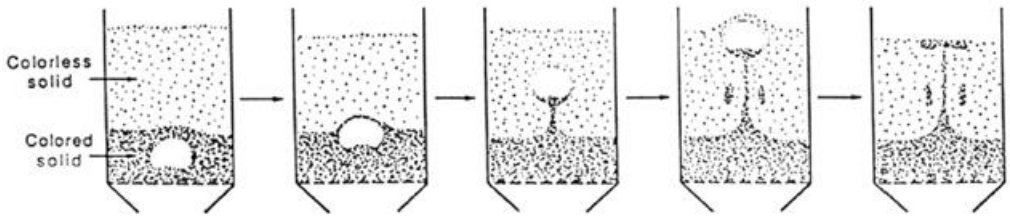

Figure 2.5: Sketches of images showing the entrainment of solids by a rising bubble by Rowe and Partridge (1965) (Kunii, 1991).

The formation of bubbles at a small aperture in a distributor plate was described by Zenz (1971) The fluidising gas passes through an orifice within the distributor plate at a velocity larger than Umf of the particles. When entering the dense phase inside the bed, it can lift the interface between gas and bed and then continue to rise as its velocity is greater than the minimum fluidisation velocity, while the interface remains intact, and the void will grow further. The relative velocity between particles in the bed is related to the size and the velocity of the bubbles. When the void is enlarged to its maximum size, the velocity through the interface decreases to become Umf. The pressure applied by particles is higher at the bottom of the void, therefore the interface collapses at the base of the void, shredding the introduced gas into a spherical bubble. The process then repeated when new interface between the inlet gas and particulate material formed (Smith, 2007).

2.4.3.3 Estimation of bubble size

There are some correlations to estimate the size of bubbles. Kunii (1991) mentioned that the amount of gas enters as defined bubbles until above 10 cm of the distributor is about a third of orifice gas, while the other two thirds of orifice gas enter the emulsion phase and increase its voidage. As these bubbles rise, they will coalesce and grow. Therefore, at 25 cm from the distributor, over two-thirds of the orifice gas becomes accounted as bubble flow. This estimation is then considered as general behaviour at orifice flows; however, it differs by powder type. Generally, bubble sizes are small in a group A bed, whereas bubbles grow to a large size with group B particles and can form slugs, especially in narrow beds (Kunii and Levenspiel, 1991). Rowe (1971) estimated the bubble size by 1–2 orders of magnitude of particle size, which implies a diameter of about 0.10 m in coarse particles and 0.005 m in fine particles (Kunii and Levenspiel, 1991, Collins et al., 1978, Davidson et al., 1977, Smith, 2007).

2.4.3.4 Estimation of minimum bubbling velocity, U_{mb}

The U_{mb} is defined as the gas velocity at which bubbles start to appear in an aggregative form of fluidisation (Smith, 2007). In order to describe the bubbling phase in a fluidised bed, in 1952, Toomey and Johnstone derived two-phase theory (Rhodes, 2008). It states that 'any excess gas beyond that required for incipient fluidisation will enter the bed as bubbles, while, in the dense phase (emulsion phase), both, gas velocity and voidage remain at minimum fluidisation conditions' (Figure 2.6) (Rhodes, 2008, Litster and Ennis, 2004a)

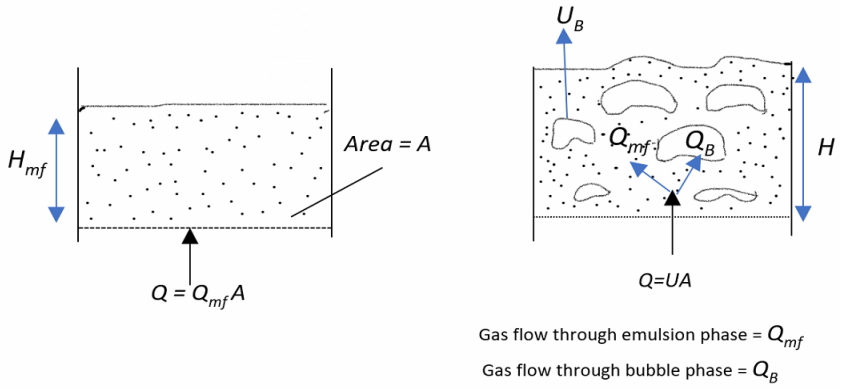

Figure 2.6: The gas flow pattern inside a fluidised bed according to the two-phase theory Adapted from (Rhodes, 2008).

In an expanding bed, Q is the actual gas flow rate to the fluid bed, and Q_{mf} *is* the gas flow rate at incipient fluidisation. If gas passes through an emulsion phase at U_{mf}*:*

$$Q_{mf} = U_{mf}\, A \tag{2.11}$$

, and the gas enters the bed in the form of bubbles:

$$Q - Q_{mf} = (U - U_{mf})A \tag{2.12}$$

Then the fraction of the bed occupied by bubbles is:

$$\varepsilon_B = \frac{H - H_{mf}}{H} = \frac{Q - Q_{mf}}{AU_B} = \frac{(U - U_{mf})}{U_B} \tag{2.13}$$

Here, H and H_{mf} are bed heights at $U_{mf,}$ and U respectively. U_B is the mean velocity of a bubble in the bed. Then the mean bed voidage is then given by:

$$(1 - \varepsilon) = (1 - \varepsilon_B)(1 - \varepsilon_{mf}) \tag{2.14}$$

However, practically, it has been found that the two -phase theory had overestimated the volume of gas passing the bed in form of bubbles, and bed expansion can be better estimated by replacing ($Q - Q_{mf}$) in Equation (2.14) with visible bubble flow rate, Q_B:

$$QB = YA = (U - U_{mf}) \tag{2.15}$$

Where 0.8 < Y < 1.0 for Group A powders, 0.6 < Y < 0.8 for Group B powders and 0.25 < Y < 0.6 for Group D powder (Rhodes, 2008).

2.4.4 Spray nozzle & droplet size

Nozzles are used to convert the liquid binders into fine droplets in the gas phase. This is called atomisation, and several variables control this process, such as *nozzle position, atomisation pressure, nozzle height, droplet size, orifice dimensions, and spray rate.* Some studies have investigated the impact of process variables or liquid properties on spray characteristics. Others have investigated the effect of these variables on the granulation process and granule attributes.

(Gao et al., 2002) found that the atomisation pressure and the liquid flow rate significantly affect granule size distribution in a fluidised bed. (Wan et al., 1995) found that increased atomisation pressure reduces the droplet size. Alternatively, an increase in binder flow rate increased the droplet size with a broader size range.

Hede et al. (2008) reviewed the position and types of spray nozzles and the prediction of mean droplet diameters produced. Hede and coworkers described two-fluid nozzle designs used in fluidsed bed granulation and their correlations for the prediction of mean droplet diameter. They found liquid characteristics such as surface tension, density, and viscosity can affect spray atomisation features. High viscosity liquids can result in larger droplet sizes for the same flow rate. Some studies found that liquid binder of high viscosity and low surface tension will prevent it from distributing uniformly (Dhenge et al., 2012). The nozzle dimensions have little influence on the mean droplet size for low viscosity liquids. Atomisation quality deteriorates with an increase in liquid viscosity and surface tension. For low viscous liquids, the mean droplet size is inversely proportional to the relative velocity between the air and the liquid at the nozzle outlet (Hede et al., 2008).

Nozzles normally produce a liquid sheet that breaks up into ligaments, breaking into very small droplets (Figure 2.7). The droplet size is affected by the viscosity and surface tension of the liquid. The droplet size increased as these both increased. Liquid density also has the same effect on the droplet size which has been explained by Hede that the higher liquid density is less exposed to the atomising action of the high velocity air. The same authors also pointed out that the nozzle type can affect the droplet size, as a full cone spray delivers the biggest droplet size followed by flat spray and hollow cone nozzles (Hede et al., 2008).

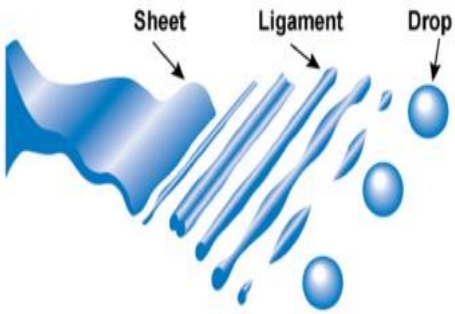

Figure 2.7: Nozzle produces a liquid sheet that breaks up into ligaments which break up further into very small droplets (Hede et al., 2008).

Increased liquid viscosity led to a decrease of the liquid flow rate, and a higher pressure was needed to maintain the same spray coverage. Similarly, the surface tension of the liquid influenced the liquid flow rate. The spray gun could be positioned at the top of the bed or submerged inside the bed. The bottom spray is also employed in the fluidised bed process, but defluidisation or wet quenching are risks associated with larger droplet sizes with this position (Smith, 2007).

The droplet size affects the final granule size. According to Schaafsma (2000), Scheafer and Worts in 1978, described the important mechanisms which control the granule growth process in a fluidised bed. They concluded that there is a relationship between droplet size and granule size, and the rupture of granules is of minor importance because the droplet size/granule size relation is preserved during the process (Schaafsma et al., 2000).

In a study carried out by (Ehlers et al., 2010), diode laser stroboscopy (DLS) and particle tracking velocimetry (PTV) were used for droplet detection inside the bed. The droplet size and speed were determined. The droplet speed increased as the pressure of atomisation increased. The technique also detected the coalescence of aqueous droplets after which only slight evaporation occurred (Ehlers et al., 2010). According to smith (2007), (Dewettinck and Huyghebaert, 1998) investigated the atomisation pressure and, thereby, the gas velocity at the nozzle outlet and found that it was a substantial variable where the high pressure created smaller droplets which were more susceptible to drying at the freeboard. In addition, the increased nozzle atomisation from top spray resulted in reduced bed temperature and influenced the interaction between bed particles and droplets (Smith, 2007).

Juslin (1995) concluded that by increasing pressure, 90% of the droplet size was reduced in a non-linear way. However, increasing the pressure to the highest level does not decrease the size any further. The concentration of the binder and the flow rate both affect the droplet size linearly as it increases as they increase (Juslin et al., 1995).

2.4.5 Gas distributors & the design criteria of a distributor plate

The ultimate purpose of using a gas distributer plate is to provide uniform distribution for the fluidising gas and, at the same time, to support the material inside the bed. The design of a good distributor plate is a key step for efficient operation of a fluidised bed. Geldart (1985) stated, ' The success of fluidised bed is primarily dependent upon distributor performance, which in turn depends on its design parameters'. Generally, a material with low bulk density requires a distributor plate with a minor open area to provide enough pressure drop and vice versa (Geldart and Baeyens, 1985, Parikh and Mogavero, 2005).

There is a wide range of distributors available for use, from simple fibre cloth (Zhai et al., 2009) or compacted wires (Kunii, 1991) to special purpose distributors (Saxena et al., 1979, Geldart and Baeyens, 1985). Most of the available plates are of 4–30% open area (Parikh and Mogavero, 2005).

Qureshi and Creasy (1979) indicated that several workers studied the flow through porous, bubble cap and simple orifice types. A good distributor plate should have the following characteristics (Qureshi and Creasy, 1979):

- Achieve an even gas distribution across the bed.
- Have sufficient mechanical integrity.
- Prevent excessive attrition.
- Elimination or reduction of dead zones in the fluidising area.
- Prevent the pack flow of the particles into the air chamber.

The most important factor considered for designing an efficient plate is to obtain sufficient pressure drop across the plate. If it is too low, this will result in poor fluidisation, which is characterised by temporary or persistent defluidisation of some parts of the bed or even blockage of the discharge zone.

The design of the gas distributor was originally based on 'rules of thumb', which assumes the criterion of the design is the pressure drop, ΔP, across the distributor, which should range between 0.01 to 1.0 times the pressure drop across the bed. However, many researchers found that this rule is not satisfactory. Leung (1972) argued that the same ΔP across distributors could be obtained from different distributors; for example, a distributor with a single hole or another with multiple holes. Researchers then adapted the rule and suggested different formulas to design the distributor. Leung (1972) recommended a formula for a large fluidising bed. Quereshi and Creasy (1979) reviewed the data on unsuccessful commercial fluid beds and concluded that aspect ratio has an influence. Geldart et al. (1985) reviewed the literature on different gas distributors and presented the main principles of design and equations for various gas distributors. Kunii and Levenspiel (1991) stated that for ideal gas distribution performance, the pressure drop across the plate should be about a third of the pressure drop across the bed (Leung, 1972; Qureshi and Creasy, 1979; Geldart et al., 1985; Kunii and Levenspiel, 1991).

2.4.6 Variables in a fluidised bed granulation

Control of the fluid bed agglomeration process is complicated as three processes are taking place simultaneously: wetting, drying and mixing. The quality attributes of the final granules obtained using a fluidised bed can be controlled by manipulating either the process or material variables (Table 2.1). Process variables are related to either the apparatus or the process parameters, while the material variables are related to the starting powders and the type and

concentration of binder. Most of these interrelated variables have been reviewed by (Faure et al., 2001, Hemati et al., 2003, Burggraeve et al., 2013, Mangwandi et al., 2015).

Table 2.1: Operating and material variables influencing granule attributs in top spray fluidised bed granulation (+ or -) refers to an increase or decrease in the granule size. The table was adapted from (Burggraeve et al., 2013).

Operating variables		**Material variables**	
Apparatus variable	Process variables	Starting material	Binder solution
Shape product container	Inlet air temperature (-)	Particle size distribution	Type of solvent
Design air distributor plate	Inlet air velocity (-)	Moisture content	Type of binder
Nozzle position	Inlet air volume	Particle shape	Binder concentration
Nozzle type	Inlet air humidity (+)	Cohesiveness	Droplet size (+)
	Fluid bed height	Binder viscosity (+)	Surfactant conc (+)
	atomization air pressure (-)	Wettability (+)	
	Binder liquid spray rate (+)		

Faure et al. (2001) stated that droplet size, spreading of the droplet on the powder bed and humidity in the bed are the main parameters which control most of the agglomeration. (Hemati et al. (2003) concluded that the capillary forces are the dominant forces, as they increase the adhesion forces of the binder on the particle surface Equation (2.17).

Faure et al. (2001) pointed out that wetting factors critically control the final granule size distribution due to low shear forces of the fluidised bed which restrict particle densification and liquid saturation, as it is more difficult for the liquid to be squeezed out of the agglomerate, so granule growth by coalescence is reduced. The wetting conditions, therefore, will dominate the agglomerate size distribution.

Schaafsma et al. (1999) have shown that relative humidity inside the bed should be more than 50% to increase the granule size due to liquid film formation and increase cohesiveness between the particles. Hence, enhanced mixing decreases the moisture less than a critical value doesn't affect the growth. This suggests that the relative humidity plays a role in the mixing behaviour by altering the cohesive forces between particles. When these forces are below the critical value, they are insufficient to affect the granulation process, leading to no significant change in the final granule size. Through their work on pulsed spray, they recognised two zones for mixing. Firstly, the wetting zone where the renewal of the powder is related to the spray

rate; slow renewal will result in over wetting and, in turn, to defluidisation of large granules. The other zone is the bulk zone, where the turnover of the granules is related to the drying rate, which will determine the later stage of growth (Schaafsma et al., 1999).

Schaefer and Wørts in (1977) found that the relationship between droplet size, and granule size is affected by the strength of liquid bridges in wet granules. Different binder solutions of same droplet size can give different granule characteristics. Raised inlet air temperature resulted in a reduction of granule size. However, it is a minor effect and could be attributed to a decrease in the viscosity of the binder, which weakens the liquid bridges. Faster evaporation of the binder at elevated inlet temperature is another reason for a decrease in the granule size (Schaefer and Worts, 1977, Faure et al., 2001, Parikh and Mogavero, 2005, Zhou and Lipp, 2009, Almaya, 2008).

Many other studies have looked at the parameters affecting fluidised bed granulation, and a summary of these is given in Table 2.2.

Table 2.2: Summary of studies that have investigated variables that affect granulation within a fluidised bed granulator.

Authors	**Material used**	**Effect of different variables on granulation**	
	Powder & Binders	**process variables**	**Material variables**
(Smith and Nienow, 1983)	Alumina Glass powder Solutions of PEG 4000 & benzoic acid in methanol	**Increased fluidisation velocity resulted in** Enhanced heat and mass transfer between moist particles and the fluidising gas. Improved binder distribution. More breakage due to increased kinetic energy due to collision of particles.	**Larger initial particle size resulted in** reduced granule size. Quenching of the bed and transition to size growth by layering. **Lower concentrations of PEG binder:** Weaker bonds and transition for coating. **Type of binder:** Benzoic acid-glass powder system favours size growth by layering.
(Hemati et al., 2003)	Nonporous: Sand, Glass beads Porous: Alumina, Silica	**Nozzle height:** higher atomiser location**.** Reduced granulation due to wall wetting and increased drying rate.	**Larger initial particle size:** Decreased the growth rate. **Interfacial tension:** Has a dominant effect over **viscosity** and granulation increased when

	NaCl aqueous solution CMC aqueous solutions 1%, 3%	**Nozzle position:** Atomiser submerged in powder bed led to cake formation. The ideal position is to situate the tip at the surface of the powder bed to become submerged when the bed is fluidised. **Increased liquid flow rate:** Relative humidity of the bed increased, and when it exceeded a critical value, the formation of liquid bridges increased and, consequently, the granule growth. **Increased atomised air pressure:** More uniform liquid distribution and more homogenous layering in sand-NaCl system. **Increased Fluidisation velocity:** Produced more fragile granules and increased rebound led to transition to coating mechanism.	wettability increased & contact angle decreased. **Particle shape:** After some time, the granulation rate decreases, and the granules are less resistant than those of primary spherical particles. **The porosity of the particles:** Porous particles have a characteristic non-growth period when the solute is deposited inside pores, then they follow the same growth pattern of non-porous particles.
(Pont et al., 2001)	Sand, Glass beads Carboxy Methyl Cellulose (CMC) 1% Interfacial tension lowered by adding anionic surfactant Triton X100		**Increased Interfacial tension:** 0.033 to 0.072N/m, and **Decreased Contact Angle**: 38° and 90° favoured agglomerates; thus, the capillary forces are dominating the forces **Viscosity of the solution:** Has less effect on granulation
(Abberger et al., 2002)	Lactose 164 µm PEG 3000 at different concentrations.	**Effect of droplet size**: (30-90 µm). Agglomerate formation depends on the size of the atomized binder droplets to the size of the solid particles.	

	Spray droplet sizes 30 µm Fluidised hot melt granulation (FHMG)		
(Walker et al., 2007)	Glass beads 100-150 µm Lutrol® F68 polyoxyethylene-polyoxypropylen	**Increased granulation time:** Un granulated fraction increased, large granules fraction decreased	**Increased binder content:** Has a dominant effect on granule growth mechanism from layering to coalescence; defluidisation occurred at 10% w/w binder content with irregular shaped granules.
(Zhai et al., 2009)	Glass beads 150–250 µm 300-400 µm Lutrol® F68		**Increased Primary particle size:** The mean granule mass increased, and it took longer to reach equilibrium granule size **Increased hydrophobicity by the coating of ballotini**: Lowered the extent of the granulation.
(Zhai et al., 2010**)**	Glass beads 150–250 µm Poloxamer 188 Poloxamer 407 (FHMG)		**Higher Viscosity of the binder:** increased time to achieve equilibrium, and granules more resistant to deformation and breakage. **Increased Binder particle size**: altered the granulation mechanism from distribution to immersion
(Mangwandi *et al.*, 2015)	Lactose monohydrate Polyethene glycol (PEG)1500 Methylene blue as a model active pharmaceutical ingredient API	**Increasing fluidising air temperature:** above the melting point of the binder the granulation improves; strong granules with improved API homogeneity **Increased fluidising air velocity:** More granule breakage, the growth rate reduced.	.

	(FHMG)	The homogeneity of the granules improved. **Granulation Time:** Has little influence on the API homogeneity. Shorter granulation time favours homogeneity	

In order to fully understand the effect of process and formulation variables on granulation, it is necessary to understand the mechanisms and the rate processes occurring during fluidised bed granulation. These will be reviewed in the following section.

2.5 Granulation mechanisms and rate processes inside a fluidised bed

In this section, the main granulation mechanisms and process rates in wet granulation will be discussed in general with reference to those which take place in fluidised bed granulators with a focus on the different types of inter-particle forces controlling the granule formation and the impact of operating parameters and material variables on this process.

It is generally understood that the production of granules involves key rate processes encompassing three main mechanisms: wetting and nucleation, coalescence and consolidation, and attrition and breakage. These mechanisms can occur simultaneously in all granulators. However, predicting and explaining some of these rate processes is still difficult. (Iveson et al., 2001).

Wetting and nucleation. This is the first step in the granulation process. The primary particles start to adhere to each other due to the distribution of the binder throughout the powder to form liquid films. These initial ‘nuclei' will grow further to form granules. As this rate process is the core of the research, it will be discussed in more detail in Section 2.5.3

Consolidation and growth. Coalescence means a successful combination between primary particles or initial granules due to the collision of two or more granules. Further collisions lead to granule compaction, i.e., they consolidate, and the density of the granule increases due to consolidation. The key factor which affects granule growth is liquid saturation formulation, and process variables determine the extent of consolidation (Rhodes, 2008). Granule growth is discussed in Section 2.5.1

Attrition and breakage. Here, the granules break up due to collisions with each other, the equipment walls, or by handling. Generally, attrition is undesirable since it affects product quality standards.

2.5.1 Granule growth in a fluidised bed granulator

(Smith and Nienow, 1983) primarily described the mechanisms of growth in a fluidised bed. They identified two types of granule mechanisms by changing the initial particle size in the experiment done in a fluidised bed. The first granule type consisted of two or usually more initial particles combined into an agglomerate. However, by increasing the fluidising gas velocity, layered granules were produced, consisting of primary particles with dried material adhering to the surface.

According to (Parikh and Mogavero, 2005), nucleation in a fluidised bed is normally starts by initial distribution of droplets in the spray zone. Atomized droplets spread over the particle surface. When they have enough liquid on the surface and on impact, they form nuclei held together by liquid bridges in a pendular state. Then the liquid bridges solidify to hold the particles together. This process is shown in Figure 2.8.

The strength of a solid bridge should exceed break up forces that arise from the collision of randomised moving particles which relate, in turn, to excess gas velocity and particle size. Evaporation in a fluidised bed is simultaneous, so it gives porous agglomerates. Densification of these granules is driven by capillary forces available in the liquid bridges. Fast drying before collisions occur between wet particles favours growth by a layering mechanism. The following section will describe interparticle forces that control granule formation.

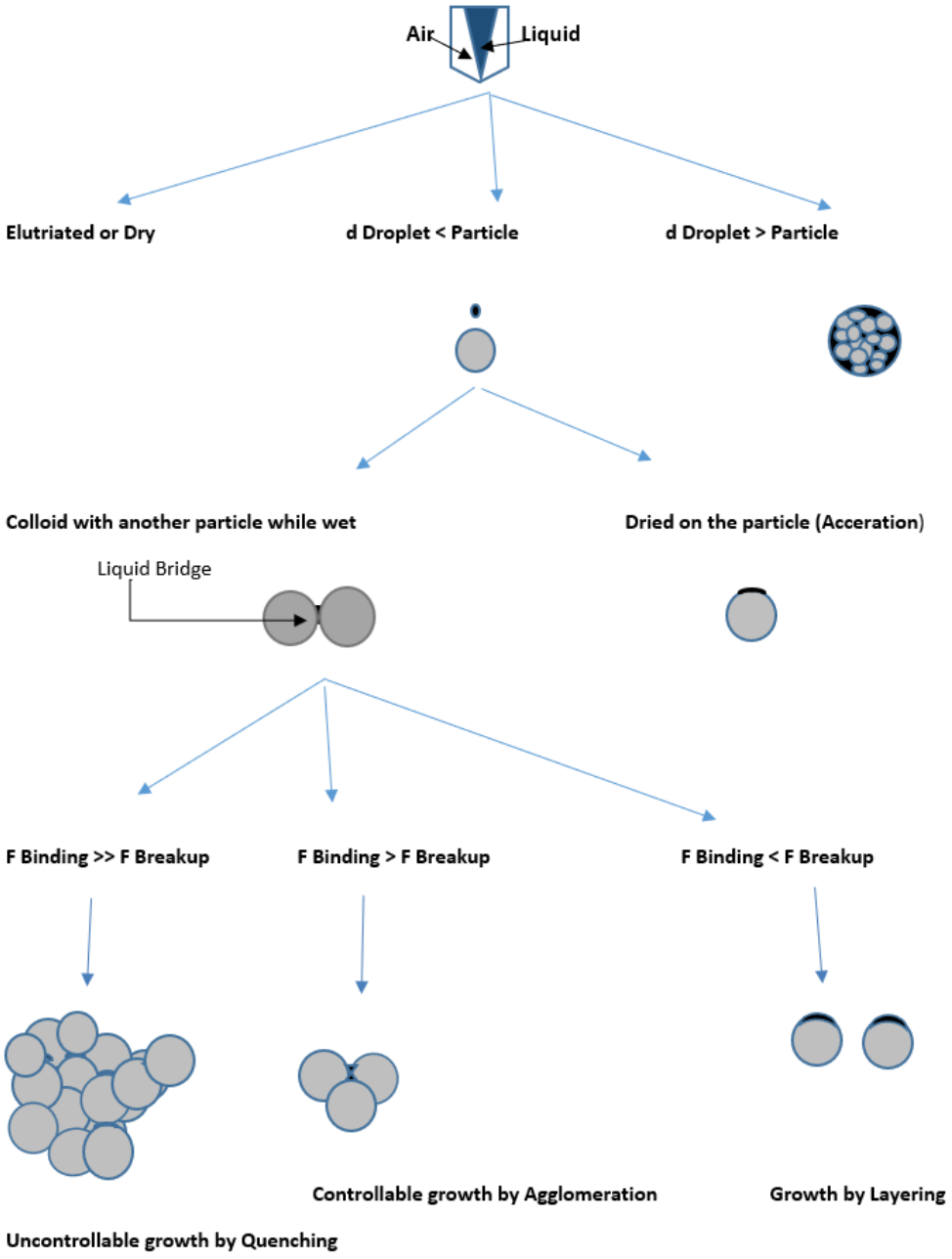

Figure 2.8: The addition of a liquid droplet and its consequences on the particle growth path inside a fluidised bed. Adapted from(Parikh and Mogavero, 2005).

2.5.2 Types of inter-particle forces controlling the granule formation

These forces act to form a net result of particle–particle bridges to form nuclei that could resist further attrition and grow to form a permanent agglomerate. The inter-particle forces differ in their strength and can strongly affect microscopic and macroscopic behaviour and determine the final granule size in a fluidised bed. These forces can be described as:

Electrostatic forces are usually created on the particle surface as a result of inter-particle and collisions with walls during processing. Electrostatic charges can be repulsive or attractive and are influenced by the particle's size, density, shape, temperature, and humidity. These forces also act over a relatively long distance (Zhou and Lipp, 2009, Rhodes, 2008). And Van der Waals forces are molecular-based attractive forces. They hold the energy of an order of 0.1 eV and decrease as the distance between molecules increases. They have a wide range compared with chemical bonds.

However, electrostatic and van der Waal forces become ineffective in wet systems containing particles larger than 10 μm (Iveson et al., 2001, Rhodes, 2008). Seville et al. (2000) indicated that the overall contribution of van der Waals and attractive electrostatic forces is to maintain particles in contact that allow other mechanisms to govern the agglomeration process, mainly the liquid bridges (Seville et al., 2000).

The most important is the interfacial tension attractive force which formed in response to any changes at the interface. They are usually generated between the liquid binder and the solid particles in order to wet the solid particle surface. If these forces are strong, the binder will enter the solid's pores and strengthen the liquid bridge (Rhodes, 2008). They are involved in the wetting process and liquid bridge formation.

Liquid bridges are forces that are responsible for the formation of permanent agglomerates. Seville et al. (2000) described the addition of thin layers of liquid in a fluidised bed, making the particles more cohesive. These liquid bridge forces are more complex than van der Waals as they exhibit static and dynamic forces (Seville et al., 2000). According to (Smith, 2007), Newitt and Conway-Jones (1958) described four types of *liquid states* depending on the liquid content within the granule: pendular, funicular, capillary and droplet (Figure 2.9). Particles are exposed to enough liquid to form liquid bridges in the *pendular state*. Particles are held together by a liquid neck at their contact points. These pendular bridges play an important role in granule growth and deformability (Ennis, 2005, Parikh and Mogavero, 2005).

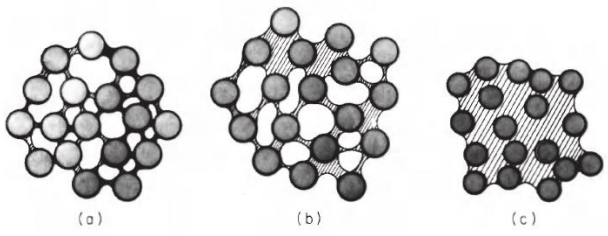

Figure 2.9: (a) pendular, (b) funicular, (c) capillary liquid states (Smith, 2007).

Simons & Fairbrother (2000), using a technique intended to study the adhesion forces between biological cells, observed and directly measured the adhesion forces created by different liquid binders applied to particles in a pendular state. This implies different contact angles and different wetting characteristics. Although the model was static, they applied very weak shear forces. In a system where binder was added to dry particles, they found that the effect of shear on bridge behaviour is dependent on the binder wetting characteristics. Binders with good wettability, i.e. having small contact angles, the movement of the liquid around the particle is energetically favourable and preserves the axisymmetric nature of the bridges. For binders of high contact angles, different behaviour was observed from that predicted in the literature. Theoretical toroidal equations were found to be overestimated due to inaccuracies in the predictions of the principal radii of curvature (Simons and Fairbrother, 2000).

In the static form of a pendular liquid bridge (i.e., U = 0), the curved liquid surface generates an attractive capillary suction pressure which is given by Laplace–Young equation, which gives the pressure difference across the liquid surface at any point in terms of the surface tension and the two principal radii of curvatures at that point:

$$\Delta p_{cap} = \gamma_{LV}\left(\frac{1}{r1} - \frac{1}{r2}\right) \qquad (2.16)$$

Where: γ_{LV} is the liquid surface tension, and *r1* & *r*2 are the radii of the curvature of the liquid surface, as in Figure 2.10.

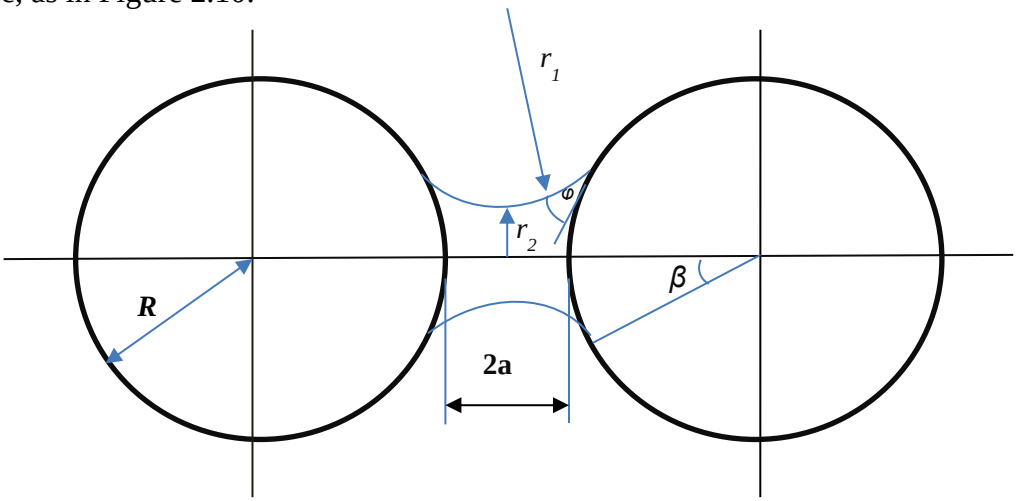

Figure 2.10: Liquid bridge between two equal spheres at half particle separation. Adapted from (Seville et al., 2000).

Also, there is a friction force which is normally activated by the inter-particle contact in the liquid bridge. According to (Zhai et al., 2009), (Kristensen et al., 1985) showed that the granule strength decreased as binder surface tension was lowered. Iveson et al. (2001) suggested that granule strength will decrease as the contact angle increases. However, there is no related data because of the difficulty of changing the contact angle and keeping other parameters the same (Iveson et al., 2001). However, Dongling (2020) developed a model to predict the capillary force between particles of different sizes and contact angles. They suggested that at small distances and low liquid volumes, capillary force decreases as distance and volume increase. The profile of a liquid bridge is influenced by factors like radius ratio, contact angle, and volume of liquid (Dongling et al., 2020).

Adding more liquid will fill the voids, and the capillary forces will draw the surface liquid back into the pores. In the *funicular state*, interstitial pores are partly filled with liquid, but most single bridges are still separate and independent of each other. The force between particles decreases due to fewer curved bridges to the surface tension to act on in the *capillary stat*, where almost the whole granule is filled with liquid. The addition of more liquid leads to complete coverage of the particles (*droplet form*) when the strength of the structure and voids are minimal. In granulation processing, the quantity of liquid should not exceed that available for the pendular state. However, an increase of liquid will increase the resistance of the bridges to rupture (Rhodes, 2008).

Finally, the solid bridge which is stronger and more permanent and can hold particles together within the granules. Generally, when two wet particles collide in a fluidised bed, a liquid bridge forms, and after subsequent drying, a solid bridge appears due to the solidification of the liquid (Schaafsma et al., 2000). Rhodes (2008) states that solid bridges can be formed via *crystalline*, *liquid*, and *solid* binder bridges. When the particle material is soluble in the liquid binder, evaporation of the liquid will result in high strength of the pendular state before a crystalline bridge is formed. A solid bridge could be formed from a liquid bridge due to a 'glue' effect of the binder itself, which starts working upon evaporation. In contrast, the solid binder bridge is based on ground solid reacting with the liquid to produce cement that holds the particles together.

2.5.3 Wetting and nucleation

In wet granulation three rate processes are taking place simultaneously wetting and nucleation, coalescence and consolidation, and breakage and attrition (Iveson et al., 2001) (Iveson et al.,

2001) Figure 2.11. *Wetting* is the first step when the liquid binder is added to the feed powder (Ennis, 2005). The rate and extent at which the liquid binder wets the powder are important. The extent of wetting is controlled by the thermodynamics of wetting represented by the adhesion tension, $\gamma_{lv}\, cos\theta$, which is the right-hand side of the Young-Dupré equation:

$$\gamma_{sv} - \gamma_{sl} = \gamma_{lv}\, cos\theta \qquad (2.17)$$

Where: γ_{sv} is the solid-vapour interfacial energy, γ_{sl} is the liquid-solid interfacial energy, γ_{lv} is the liquid-vapour interfacial energy, and θ is the contact angle between the liquid drop and the solid surface. It is a measure of the affinity of the liquid for the solid. The contact angle needs to be less than 90º to ensure liquid penetration. The liquid spreads completely on the solid surface when $\theta = 0$ (Litster and Ennis, 2004a).

In order to characterise the wetting mechanism, two key features control this process. One is the penetration, which refers to *the time* taken by a drop to penetrate through micro pores and macro voids of the loosely packed powder bed. The other is the actual spray rate or *spray flux*. Penetration time depends on the thermodynamics of wetting (represented by the adhesion tension) and wetting kinetics (represented by the viscosity of the liquid and size of powder bed pores). Time of penetration is inversely proportional to adhesion tension, i.e. penetration is driven by capillary action (Litster and Ennis, 2004a, Iveson et al., 2001, Ennis, 2005).

Nucleation is a term used to describe the formation of initial nuclei formed from primary particles and a binder where particles start to adhere to each other due to the distribution of the binder throughout the nucleation zone. The process is shown to be crucial to the final granule size distribution as controlling binder distribution is critical to maintaining control of subsequent growth. Several authors have found a marked correlation between the drop size and nuclei size distributions in fluidised bed granulators (Schaafsma et al., 2000, Waldie, 1991, Ehlers et al., 2010, Abberger et al., 2002). Uneven binder distribution results in a higher growth rate and forms large lumps (Hounslow et al., 2009, Kayrak-Talay and Litster, 2011, Hapgood et al., 2009, Litster et al., 2001).

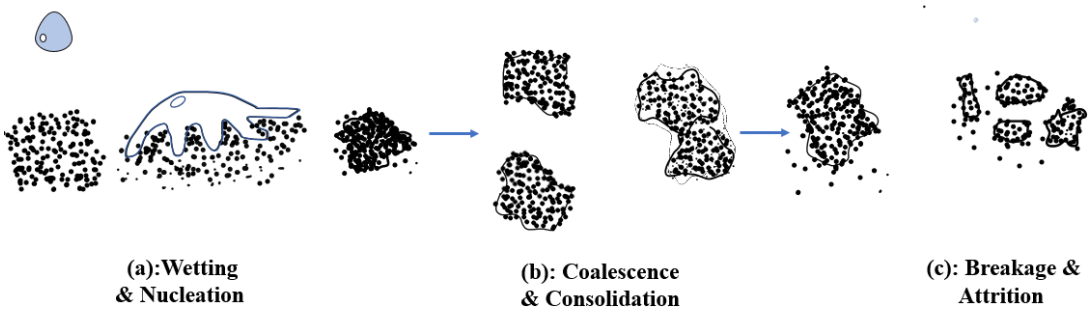

Figure 2.11: The rate processes of wet granulation rate, adapted from (Iveson et al., 2001).

Schæfer and Mathiesen (1996) presented two mechanisms of nucleation taking place in a high shear mixer. And concluded that the binder particle size was reflected in the granule size (Schæfer and Mathiesen, 1996). Furthermore, (Abberger et al., 2002) showed the same two mechanisms occurring in fluidised hot melt bed granulation experiments. In the case where liquid droplets are larger than the primary particles, the nucleation is termed *immersion* type, which refers to the immersion of the smaller particles into a larger drop. The nuclei produced possess saturated pores. Alternatively, if the liquid droplets are much smaller than the primary particles, in that case, the liquid droplets will individually spread over the particles, and on subsequent collisions, the primary particles will coalesce to form nuclei or small granules trapping air inside. This is called the *distribution* type mechanism and will be discussed in detail later in this review. Both mechanisms were previously proposed to describe melt granulation but have been extended to describe wet granulation (Scott et al., 2000).

2.5.4 Immersion nucleation

In research accomplished in a high shear mixer granulator, Litster and Hapgood (2001) proposed that immersion nucleation occurs in the spray zone (Figure 2.12). When a drop formed at the spray nozzle lands on the powder surface (1), it could break (2) or merge with an adjacent drop (3), then penetrate the powder bed by capillary action to form a loose granule or nucleus (4). Mechanical dispersion is required to go through further mechanisms (5). In a recent study, it has been found that the maximum spread of a droplet on a powder bed is a strong function of the moisture content in the bed. The total time from the impact to the complete penetration is longer for a dry powder, which indicates an optimum saturation that is necessary for faster penetration (Litster et al., 2001, Hapgood et al., 2002, Marston et al., 2013).

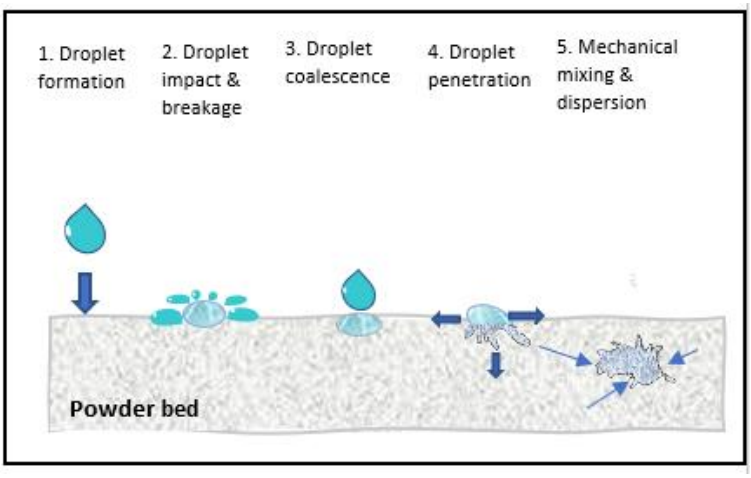

Figure 2.12: Immersion type nucleation. Adopted from (Hapgood et al., 2003).

2.5.4.1 Quantification of liquid distribution: The dimensionless spray flux

The quality of the granulation process is highly dependent on the quality of binder dispersion. It has been challenging to identify liquid dispersion because of the variance of the granulating equipment and the size, location, and shape of the spray zone. Previous studies pointed out a decreased granule size due to increased nozzle height, while others reported only a narrowing of the distribution with no change in the mean granule size, which reflects dependence on equipment type (Litster et al., 2001). Changing nozzle type, position or spray angle can alter the binder dispersion and nucleation. To standardise the spray zone, (Watano et al., 1997) suggested quantifying the liquid being delivered to the zone in terms of liquid rate (Iveson et al., 2001).

a) Deriving the spray flux

The dimensionless quantity which estimates the coverage of binder liquid and estimates the density of the drops on the powder bed is called the spray flux. The dimensionless group was derived by Hapgood (2000) by making two assumptions. The drops from the nozzle spray should not overlap on the powder bed surface. Furthermore, they should penetrate very quickly before coalescing with the adjacent drops on the powder surface (Hapgood, 2000).

If a spray nozzle with a volumetric spray flow rate, $\dot{V}$, delivers a number of drops, n_d, with an average drop size, d_d, the number of drops produced by nozzle per unit time are:

$$\dot{n}_d = \frac{\dot{v}}{\frac{1}{6}\pi\, \dot{d}_d^{\,3}} \qquad (2.18)$$

Assuming the drops are spherical in shape, the area covered by each drop when it lands can be calculated as a cross sectional area of a sphere*:*

$$a_d = \frac{\pi\, d_d^{\,2}}{4} \qquad (2.19)$$

So, the total projected area covered by unit time *T* is:

$$\dot{a}_{d,T} = \dot{a}_d \dot{n}_d = \frac{3\,\dot{V}}{2\,\dot{d}_d} \qquad (2.20)$$

The area will be distributed over a spray area, *A*. Therefore, Litster and co-workers defined the spray flux Ψ_a as the ratio of the wetted area is covered by droplets to the area flux of powder through the spray zone

$$\Psi_a = \frac{3\,\dot{V}}{2\,\dot{A}\,d_d} \qquad (2.21)$$

where the powder surface is traversing the spray zone with area flux $\dot{A}$ (m^2/s), $\dot{V}$ is the volumetric spray rate. To validate the new parameter, the authors used lactose, water, and hydroxypropyl cellulose HPC in a high shear granulator. They used a flat spray nozzle at varying impeller speeds and image analysis to quantify their findings. The study shows that the spray flux, Ψ_a, is the primary factor affecting nuclei formation and controls the size and shape of nuclei size distribution. The nuclei distribution is found dominated by the fluid coverage on the powder surface regardless of the small changes in the formulation (Figure 2.13), while low (Ψ_a <1) ($\Psi_a = 0.2$) in the same figure, showed drop-controlled regime, where one drop forms one nucleus and narrow nuclei size distribution obtained. Higher Ψ_a ($\Psi_a \approx 1$) led to wide nuclei size distribution. The highest Ψ_a ($\Psi_a = 1$) led to caking due to the high density of liquid droplets falling and overlapping on the powder (Litster et al., 2001).

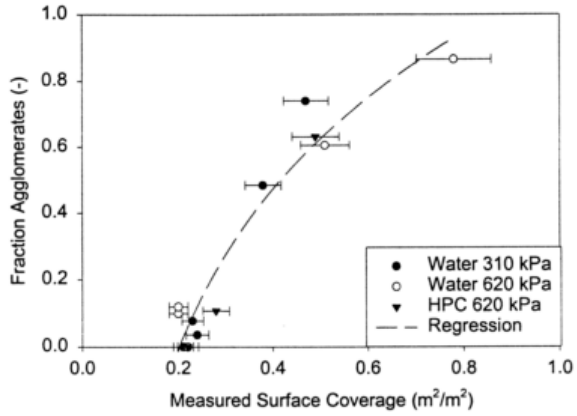

Figure 2.13: Fraction agglomerates as a function of measured surface coverage where curves of three different formulations collapse onto one line (Litster et al., 2001).

b) Nucleation kinetics

It is crucial to know nuclei formation kinetics and how they relate the nucleation process with time. Nuclei formation was presumed to be a fast process, and the aggregates are formed shortly after particle wetting occurs. However, in practice, this is only true with low viscosity binders similar to water. Higher viscosity binders take more time. Besides, mixing interference does not allow enough time for the nucleus to be formed (Hapgood et al., 2003). Schaafsma (1999) found that increased surface renewal rate i.e., mixing speed relative to the spraying rate, was sufficient to prevent over wetting and defluidisation. Schaafsma (2000) used a spray nozzle that delivered monosized drops into a fluidised bed in another experiment. It was found that the mixing with the spray rate in the spray zone gave different average granule sizes which verifies that the smallest nuclei were formed from the only single drop and the larger ones were produced from several coalesced drops inside the spray zone (Schaafsma et al., 1999, Schaafsma et al., 2000, Hapgood et al., 2003).

To quantify the nuclei formation kinetics, Hapgood (2002) studied single drop behaviour by video recording the penetration of drops of different binders through a loose porous powder bed. The kinetics were defined as the time required for a drop to penetrate into the powder surface. This penetration time is affected by both wetting thermodynamics represented by the surface tension of the liquid binder and the contact angle and the wetting kinetics, which are affected by viscosity and the size of the pores (Hapgood et al., 2002). Therefore, the kinetics of drop penetration is controlled mainly by formulation properties (Litster et al., 2001) the equation has been derived is related to the formulation properties:

$$t_p = 1.35 \frac{V^{\frac{2}{3}}}{\varepsilon^2 R_{pore}} \frac{\mu}{\gamma_{lv} cos\theta} \qquad (2.22)$$

where t_p is the penetration time, V is the total volume of the drop, R_{pore} is the pore radius γ_{lv}, is the surface tension of the liquid, ε is the powder bed porosity, μ is the liquid viscosity and θ is the dynamic contact angle. However, Hapgood (2002) found that the penetration time is actually longer than they calculated using the Kozeny Carmen approach to count pore radius, as it only considers the permeability of powder. But in reality, the experiments show that the binder takes a longer time to go through the heterogeneous powders containing macrovoids. These large voids were found not to participate in the flow, but they hinder the flow occurring by capillary action. Other possible reasons for this complex penetration kinetics suggested by the authors are the displacement of the air in the pores, dissolution of the substrate during penetration, and the effect of dynamic contact angle. Following this, they used another model and recalculated the penetration time using effective radius and effective porosity as follows:

$$t_p = 1.35 \frac{V^{\frac{2}{3}}}{{\varepsilon_{eff}}^2 R_{eff}} \frac{\mu}{\gamma_{lv} cos\theta} \qquad (2.23)$$

Where ε_{eff} related to both loose-packed porosity ε, and tapped porosity ε_{tap}, which can be calculated as:

$$\varepsilon_{eff} = \varepsilon_{tap} (1 - \varepsilon_{macrovoids}) = \varepsilon_{tap} (1 - \varepsilon + \varepsilon_{tap}) \qquad (2.24)$$

While R_{eff} is the effective radius of the pores, it can be calculated from:

$$R_{eff} = \frac{\emptyset \, d_{3,2}}{3} \frac{\varepsilon_{eff}}{(1 - \varepsilon_{eff})} \qquad (2.25)$$

Where $d_{3,2}$ is the specific surface particle diameter and $\emptyset$ is the sphericity of the particle, they found good agreement between the new estimated model and the experimental penetration results (Hapgood et al., 2002, Hapgood et al., 2003, Litster, 2003).

c) The Nucleation regime map

By relating the key factors impacting the nucleation process, the penetration time (encompasses formulation parameters), Hapgood et al. (2003) developed a nucleation regime map that clearly

shows the interaction between drop penetration time and spray flux. Hapgood et al. (2003) utilised the ‘‘transformation maps’’ developed by Mort and Tardos in 1999 to design the regime map. Those maps had presented the relation between material properties and operating parameters. In order to develop the regime map experimentally, the researchers used a range of liquid binders (which have different drop penetration times), different particulate sizes of lactose monohydrate powders, and different spray flux as they used different spray patterns (pouring /spray/different flow rate) in high shear mixer. The experiment was run for a specified interval time (10 sec). The produced nuclei size distributions as a function of changing the spray condition were plotted in each experiment; an example of one of the resulting data is shown in Figure 2.14. The regime map was constructed when the dimensionless spray flux was plotted against dimensionless penetration time T_p. T_p could be obtained by:

$$T_p = \frac{t_\mathrm{p}}{t_\mathrm{c}} \qquad (2.26)$$

where t_p is the experimental drop penetration time, t_c is the circulation time. Hapgood (2003) described the circulation time as the ‘time interval taken by a powder packet to leave and re-enter the spray zone. It is a function of powder flow patterns and the amount of material in the granulator’. T_p, the dimensionless penetration time, was defined as the quotient of the penetration time of spray drops in the powder bed and the circulation time of the powder to return to the spray zone (Hapgood et al., 2003, Wildeboer et al., 2005).

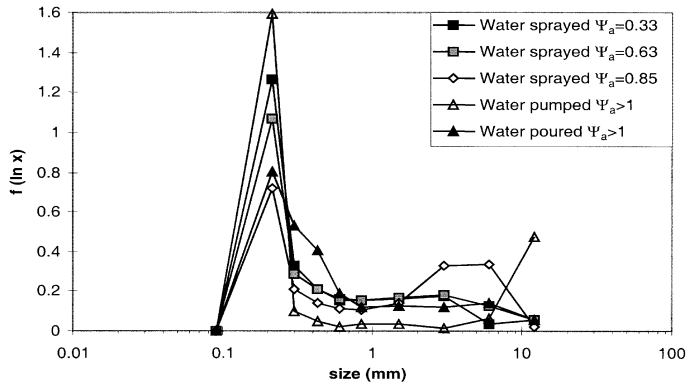

Figure 2.14: Narrow nuclei distribution as a function of changing spray conditions (water) after 10 s in a Hobart mixer (Hapgood et al., 2003).

The nucleation regime map characterises immersion nucleation (Hapgood et al., 2009). As in Figure 2.15, a drop controlled regime can be obtained only when spray flux Ψ_a, and penetration

time t_p are low, as in the case of water and lactose. There is intermediate regime, followed by the mechanical dispersion regime when one or both conditions are not met and the system requires good mixing to avoid caking. The regime map is useful tool in formulation design and scale up. However, it is still unable to predict granule attributes (Litster, 2003).

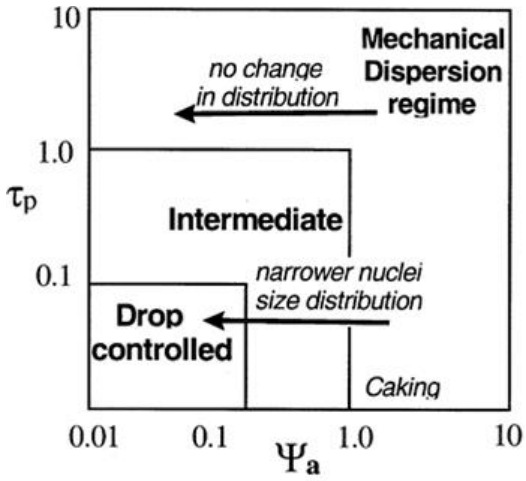

Figure 2.15: Nucleation regime map as proposed by (Hapgood et al., 2003).

2.5.4.2 Nucleation studies to improve wet granulation in the pharmaceutical industry

An attempt was made by Hapgood (2010), to improve wet granulation of a pharmaceutical product. The "balling formation problem" which means the formation of big size lumps during granulation was addressed (Figure 2.16). The nozzle spray was changed to reduce the spray flux, but the problem still existed. The drop size was measured, and a high-speed camera was placed in the granulator for different batches, and image analysis was used to process the information. The researchers found that the improvement of the liquid distribution will result in shorter induction time and higher growth rate. Eventually, this could be solved by reducing the quantity of fluid added (Hapgood et al., 2010).

Figure 2.16: Example of big lumps or balls encountered in a wet-granulated pharmaceutical product (2-2.5cm) (Hapgood et al., 2010).

To adopt a suitable analytical method for pharmaceutical granulation, Li et al (2007) explored the validity of the near infrared NIR method to characterize the granules during nucleation and growth. The traditional methods, HPLC or UV–VIS being used to assay the content uniformity and potency of tablets, according to Li, are not appropriate to describe other important process related properties as size distribution and moisture content. The NIR method has the capability to analyse changes in relative content of lactose and microcrystalline cellulose in addition to the active ingredient at different processing times (Li et al., 2007).

A priori study has been performed by Kayrak-Talay et al (2011) to examine the applicability of the nucleation regime map to a gabapentin Pfizer® formulation containing dry hydroxypropyl cellulose HPC binder, Hapgood's nucleation regime map was able to predict the effect of process parameters on the granulation which was measured by the width of size distribution and/or lump formation. The highest proportion of lumps with the widest granule size distributions occurred while moving from intermediate towards mechanical dispersion regime. The dripping binder method evidenced the worst case giving rise to fines besides lumps compared to spraying method. The dry binder increased the drop penetration time. This was unexpected from capillary flow perception and might be attributed to the liquid penetration into the related fine pores and consequent binder softening and dissolution. The authors measured the penetration time for dry binders directly to the blended formulation and then scaled to the drop size during spraying (Kayrak-Talay and Litster, 2011).

2.5.4.3 Modelling of nucleation in wet granulation

Modelling of granulation is becoming more accurate and sophisticated. However, the nucleation mechanism is still the least mechanism modelled. As have been mentioned, spray flux was introduced by Hapgood in 2001 to define the density of droplets landing on a powder surface. The nucleation regime map was developed in 2003 to describe the mechanisms that control the nuclei formation. This approach, however, was unable to predict entire nuclei size distributions, because it neglects the probability of nuclei being overlapped as they are larger than the drops. In addition, there is the assumption of uniform dispersion for the drops over the spray zone. Nevertheless, the spray pattern is similar to rain landing on soil, where raindrops are falling randomly and independent from previous or future raindrops (Hapgood et al., 2009, Wildeboer et al., 2005).

Hapgood (2004) used the Poisson distribution to model the fraction of nuclei formed from a single drop as spatial statistics could define the nearest-neighbour distances between a set of

random x and y events taking place in a specified area. To predict nuclei size distributions formed from multiple droplets, Wildeboer et al (2005) developed a Monte Carlo simulation for the nucleation. The authors used Hapgood's definition (2004) for the nucleation ratio K which limits the maximum size the granule could grow. It is expressed either in nucleation volume ratio K which is the ratio between the formed nucleus volume and the drop volume (mass/volume), or nucleation area ratio Ka which is the ratio between the projected areas of the nucleus and the spray drops (area/diameter) (Figure 2.17) The ratios of the nuclei diameter to drop diameter. The ratio has been found to increase as the particle size increases, then it slows down as the particle size increases further (Liu et al., 2013).

Figure 2.17: The ratios of the nuclei diameter to drop diameter. The ratio has been found to increase as the particle size increases, then it slows down as particle size increases further (Liu et al., 2013).

Both definitions were used as inputs in Wildeboer's Monte Carlo simulation model. The model showed agreement with the experimental nucleation data and was able to predict the nuclei size distributions in the case of non-uniform spray patterns and allows overlap of nuclei granules rather than spray drops. This represents Hapgood's nucleation regime map beyond the drop controlled nucleation regime (Wildeboer et al., 2005).

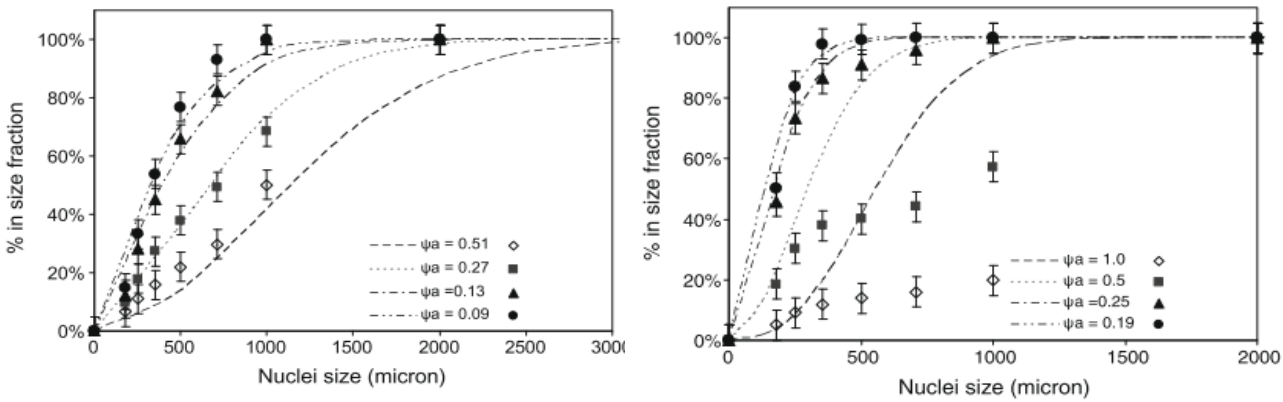

Figure 2.18: Experimental data and simulated nuclei size distribution for water 620 kPa (right) and HPC (left) 620 kPa, respectively (Hapgood et al., 2009).

Hapgood et al (2009) used the previously mentioned Poisson approach to simulate the entire nuclei distribution. The Poisson model showed weaknesses in representing multi-modal experimental data. The nuclei size distributions were predictable at low spray flux values (Ψ_a < 0.3) while at values higher than 0.5, the prediction wasn't successful for liquids with short penetration time. For long penetration time systems, the nuclei size distributions were predictable up to $\Psi_a = 0.51$ (Figure 2.18). The authors admitted that the Poisson model is only valid for simulation of a drop-controlled regime and should be used with caution when considering long penetration times with high spray fluxes. They also recommended using these predictions as a base for population balance modelling (Hapgood et al., 2009).

It is proposed that the nuclei formed will undergo an impaction before they grow further if they are strong enough to withstand the impaction. A nucleation model that includes breakage of the nuclei was proposed by Liu et al (2013) based on the nucleation model of Hapgood and the Stokes deformation number. The effect of material properties, as well as the operating parameters, were investigated. It was found that the model is usable, and the primary particle size plays a key role in deciding if the breakage of primary nuclei will occur or not (Liu et al., 2013).

More recently, using the dimensionless nucleation number Ψ_n, Bellinghausen (2019) has designed two novel nuclei size distribution models. The authors evaluated the semi-mechanistic and empirical models using data from Monte Carlo simulations (MCS). The empirical model, which assumes a lognormal distribution, was found able to capture the MCS results accurately, and the predictions agree well with the experimental results over a wide range of experimental conditions($0 < \Psi a < 3$) (Bellinghausen et al., 2019).

2.5.5 Distribution nucleation

Abberger (2001) proposed that the growth mechanism is dependent on the size droplet /particle ratio. Where a large droplet engulfs fine particles ($d_{drop} > d_{particle}$), the nucleation occurs by immersion (Abberger, 2001). However, distribution nucleation ($d_{drop} < d_{particle}$) occurs when a large powder particle is wetted by fine droplets while distributed over the particle surface. This nucleation is not instantaneous; it takes place when two particles collide at their wetted region. This collision forms liquid bridges between the particles and becomes stronger as they dry (Kariuki et al., 2013). Many researchers have identified both mechanisms in their work. Schaefer and Mathiesen, in 1996 indicated that the relative sizes of the primary binder particles would influence the nucleation mechanism (Zhai et al., 2009, Schæfer and Mathiesen, 1996).

Both mechanisms were further investigated via controlling temperature (Tan et al., 2006, Zhai et al., 2009, Zhai et al., 2010), using different concentrations of a meltable binder and different powder particle sizes. The distribution of agglomerates has been described as having an open structure with increased voidage due to trapped air in the nuclei (Waldie, 1991). The immersion mechanism results in a denser granule with saturated pores.

2.5.5.1 Liquid distribution mechanism & the particle coating number Φp

A schematic diagram of the distribution nucleation mechanism is given in Figure 2.19. After atomisation, when a droplet lands on the particle surface, it creates a solid-liquid interface until it reaches a pseudo-equilibrium on the surface. This is affected by factors such as the morphology of the particle, liquid viscosity, liquid surface tension, contact angle, drying rate, and the presence of other adjacent droplets. Gradually, the fraction surface area of the particle coated with droplets is increased. The droplets are randomly distributed over the surface, and the particle is not uniformly wetted. Nucleation could occur if two or more partially wetted particles collide at their wetted surfaces, resulting in liquid bridges being formed and becoming stronger as they dry (Štěpánek and Rajniak, 2006, Kariuki et al., 2013).

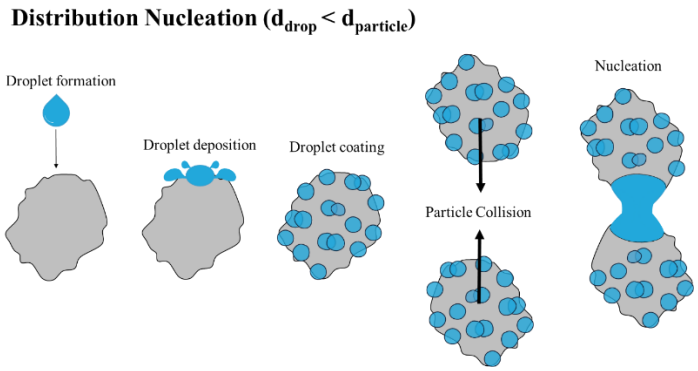

Figure 2.19: Distribution nucleation stages. Adapted from (Kariuki et al., 2013).

Liquid content has a major effect on the granule formation. Liu et al (2013) have analysed the coalescence criterion for deformable, wet surface granules during collision and suggested that the coalescence is successful if the kinetic energy of the collision is totally dissipated by viscous losses in the liquid layer and the plastic deformation in the granule matrix (Liu et al., 2013).

For the distribution nucleation, the droplets need to be deposited first on the particle surface then spread on the defined area of the surface before coalescence can take place by a collision between two primary particles, and a liquid bridge can be formed. Stepanek and Rajniak (2006) modelled an equilibrium configuration for a liquid droplet on the surface of non-spherical

(rough) particle using the volume of fluid (VOF) method. Neglecting deformation by gravity, they proposed that each binder droplet forms a spherical cap of volume on the particle and defined the *Surface Coverage Function* as the fraction of the total particle surface occupied by the liquid phase. It has been confirmed that relative droplet size and contact angle can affect the fractional surface coverage made by a certain volume of liquid more strongly than by particle shape itself, i.e. particle surface roughness (Štěpánek and Rajniak, 2006).

Later, Štěpánek and Rajniak (2009) attempted to find a relationship between primary particle morphology and granulation kinetics. They applied their model this time on wet agglomerates. They investigated the relationship between the amount of binder available on wet granule surfaces and the volumetric composition of wet granules and related it to real experimental results obtained for some pharmaceutical excipients. However, they pointed out the assumption of the binder's presence in a liquid state, whereas the binder solidifies by drying and cooling during the granulation process. They suggested that the number of successful collisions that resulted in agglomerate formation depends on physical and geometric success. The physical success factors can be obtained by the Stokes models, while the geometric success is attributed to the accessible binder fraction on the particle, i.e. whether a binder film is present on the collision point or not (Štěpánek et al., 2009).

2.5.5.2 Deriving the particle coating number Φ_p

Kariuki et al (2013) used the Bernoulli model to derive a new dimensionless group identifying the distribution nucleation, the particle coating number. When smaller droplets of liquid are covering a particle, the presence of liquid on the particle surface is counted, whatever the thickness of this liquid layer. By dividing the particle surface into many surface panels, the area of each panel will equal:

$$\Delta A = \frac{A_p}{M} \qquad (2.27)$$

where M is the number of panels, ΔA is the area of each panel, and A_p is the particle's surface area. After a liquid covers the surface, the droplet footprint will coat a fraction of these panels:

$$f = \frac{a_d}{A_p} \qquad (2.28)$$

where *f* is the fraction of *M* panels which will be coated by the droplets of a footprint, a_d is the footprint area of a single droplet. Using the Bernoulli model for coating coverage, *F* is given by:

$$F = 1 - (1 - f)^N \qquad (2.29)$$

where *N* is the number of droplets. Thus, a new dimensionless parameter, the particle coating number, Φ_p, which is the ratio of the theoretical area coated by the drops on a particle, to its total surface area, assuming no overlap is defined as follows:

$$\Phi_p = \frac{Na_d}{A_p} = Nf \qquad (2.30)$$

So, equation (2.29) can then be rewritten as*:*

$$F = 1 - (1 - f)^{\Phi_p/f} \qquad (2.31)$$

When *N* is large, *f* is vanishingly small, and the particle coating number is effectively held constant. The coating coverage fraction F then becomes:

$$F = 1 - \exp(-\Phi_p) \qquad (2.32)$$

The particle coating number Φ_p was validated experimentally by Kariuki et al (2013) using a standard ping pong ball and foam ball model. After dropping specific drop sizes of meltable coloured liquid, polyethylene glycol (PEG) 1000, the fractional surface coating for the assembly was measured by image analysis. They compared the droplet footprint area on the particle's surface, which was measured experimentally, with that calculated as a function of the size of the droplet, static contact angle, and the drops and particle size ratio using the simplest approximation developed by Litster et al. (2001) for the projected area of a spherical drop. The results of their work showed that the particle coating number Φ_p could be utilised to calculate the fractional surface coverage F using simple parameters without the need for a fitting coefficient (Figure 2.20). The deviations of their results from that calculated were attributed to the merging of the drops and also conduction of heat into the particle as it causes simultaneous drying and solidification of the drop's surface which wasn't considered in drop footprint estimates. Also, the contact angle between the drop and other solidified drops was

different to that between the drop and the particle surface. This difference generates a Laplace pressure and makes the drops displace towards lower contact angle surfaces (Hapgood et al., 2009, Kariuki et al., 2013).

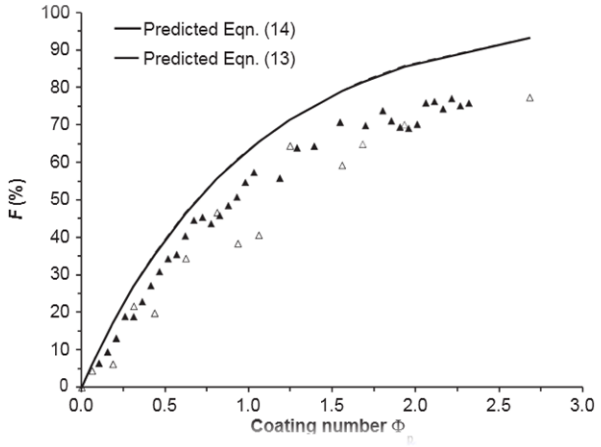

Figure 2.20: Coating coverage F (%) as a function of the particle coating number Φp for two 40 mm ping pong balls using a 21 ga needle. Theoretical predictions from Equations (2.31) and (2.32) respectively are shown overlapping (Kariuki et al., 2013).

2.5.5.3 Implications of particle coating number to control fluid bed granulation

Whilst the research work has been conducted on a stationary basis, it could have implications on granulation. For example, in a fluidised bed, the final granule size distribution depends on the coalescence rate, which is controlled by the amount of liquid available at the surfaces of the particles. Φp can be calculated for experimental fluid bed granulation process. By recalling the equation(2.30), and substitute the number of drops, liquid-solid mass fraction and particle surface area and rearranging:

$$N = \frac{X_{LS}\, d_p^3\, \rho_p}{d_d^3\, \rho_d} \qquad (2.33)$$

$$\mathrm{X}_{LS} = \frac{N d_d^3\, \rho_d}{N d_p^3\, \rho_p} \qquad (2.34)$$

$$A_p = \frac{\pi}{6}\, d_p^3\, \rho_p s_{SA} \qquad (2.35)$$

The result is a dimensionless group, and the particle coating number can be given by the equation

$$\Phi_p = \frac{6\, X_{LS}\, a_d}{\pi\, d_d^3\, \rho_d\, s_{SA}} \qquad (2.36)$$

Where X_{LS} is the liquid-solid mass fraction and is used to describe the amount of liquid added to a fluidised bed, *SSA* is the specific surface area of the particle, d_d is the droplet diameter and ρ_d is the liquid density of the droplet. Although Φ_p can help find the fractional coating of the particle, F, predicting the rate of granulation possible, using this method will include some errors because of the changes of some parameters. For example, the decrease in particle size will result in a larger specific surface area; consequently, Φ_p and F will be reduced. In addition, in reality, fluidised particles are in continuous movement. The droplet impacts the particle while it is moving with translational and rotational velocity, which will affect some variables such as drop spreading, dynamic contact angle, drop contraction, and the probability of droplet break-up due to the impact. The authors suggested using the particle coating number and developing it further to represent the coating coverage behaviour during real fluidisation experiments. This will help predict the effect of changing multiple factors such as liquid droplet size, particle size, and surface area on the coating fraction (Kariuki et al., 2013).

2.5.6 Coalescence of non-deformable primary particles or granules

Coalescence means a successful combination between primary particles or initial granules due to collisions. Deformability of the particles, K, is the capability of a surface to be stressed without breakdown or rupture and is related to both the yield strength of the material, σy, and depends on the shear intensity of the system (Figure 2.21). In systems of low agitation, as in drums or fluidised beds, the growth in size will depend on the surface deformability or the presence of liquid on the surface of the particles, which will dissipate the collisional kinetic energy. In this case, the deformability will be minimal, and the original particles will still be distinguished in the granule (Ennis, 2005).

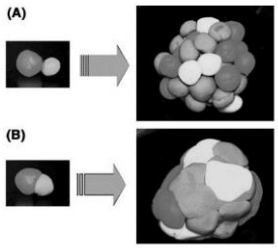

Figure 2.21: (A) low-deformability system and (B) high-deformability system. (A) is typical for fluid-beds (Ennis, 2005).

In order to study the coalescence of granules or primary particles, Ennis et al. (1991) modelled a situation where two rigid (non-deformable) spherical particles or the pair found under low shear condition as in a fluidised bed, i.e. have slow impact velocity (Figure 2.22), and if their impact will result in successful coalescence or not. It has been assumed that the successfulness of the coalescence will depend on the entire dissipation of the kinetic energy of the impact by viscous forces which dominate the situation, as capillary forces have been neglected, so the liquid bridge was assumed to be ruptured if they rebound after impact and at the same distance between two particles separated by a distance 2x (Iveson et al., 2001).

Therefore, the model entirely accounts for the viscous forces. The collision will be unsuccessful if the viscous Stokes number (St_v)for the particles is larger than the critical viscous Stokes number (Stv)*. The viscous Stokes number (St_v) is the ratio between the kinetic energy of the impact to the viscous dissipation force, equation (2.37) where d_g is the particle radius, ρ_g the density of the particle, U_C is the velocity of the impact, and μ is the viscosity of the liquid on the particles (Litster, 2016b):

$$St_v = \frac{4\rho_g U_c\, d_g}{9\mu} \qquad (2.37)$$

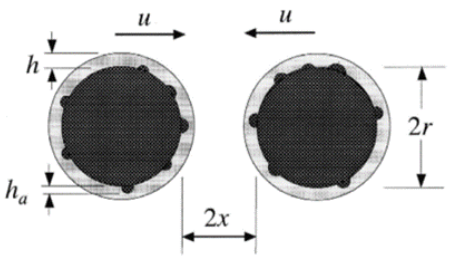

Figure 2.22: Schematic for coalescence of non-deformable particle model used by Ennis et al., 1991 (Iveson et al., 2001).

There are three stages for this model observed experimentally: *Non-inertial* regime where all collisions are successful while St_v <<Stv*. As the granules grow in size, r becomes larger and, consequently, St_v increases. The regime gradually goes into the *inertial phase* where $St_v = St_v^*$, and the possibility of coalescence is only between small granules or a small granule with a particle. Finally, when $St_v > St_v^*$, all collisions become unsuccessful, and the system enters the *coating regime*, where the growth is only by layering. This model has limitations as it is only valid for non-deformable particles when capillary forces are not counted.

2.6 Summary

Fluidised bed granulation is a technique successfully used to produce granules with a particle size distribution suitable for subsequent pharmaceutical processing (tablet pressing, capsule filling). Three simultaneous rate processes take place during granulation: wetting and nucleation; consolidation and growth; attrition and breakage. Granulation is being extensively investigated, and agglomeration models are becoming more accurate. The least understood mechanism is nucleation. Accurate modelling of nucleation enables estimating the liquid coverage and, consequently, predicting granule attributes. The type of nucleation mechanism occurring is dependent on the droplet to particle size ratio. For the immersion mechanism, the quality of the granulation process is highly dependent on the quality of binder dispersion at the nucleation stage. A dimensionless quantity, the spray flux Ψ_a, was found to quantify the coverage of binder liquid and estimate the density of the drops landing on a powder bed. This was mainly found to be related to the operating parameters. Another dimensionless quantity is the kinetic penetration time, T_p, which is related to formulation properties and considers the velocity of the spray zone. By relating the two dimensionless quantities, a nucleation a regime map was developed in 2003. The regime map can characterise immersion nucleation, and it is considered to be a useful tool to design and scale up the granulation. However, it is only able to predict granule attributes up to a certain extent. The regime map is still restricted to use in the drop-controlled regime where Ψ_a and T_p are low, but caution could be extended towards higher spray fluxes. Modelling nucleation needs to be more sophisticated to be able to predict the nucleation process attributes fully. The models closely match the experimental data for values of Ψ_a greater than 0.5.

On the other hand, a small droplet/particle size ratio leads to the distribution nucleation mechanism. A dimensionless parameter, the particle coating number, Φ_p, was derived by Kariuki et al. in 2013 to open up new options for real-time process control. The researchers validated the group on a stationary basis, but it still needs to be developed using actual granulation experiments. Doing so opens the door to predict the behaviour of particle systems and the rate of granulation. This will help to improve process control of both batch and continuous granulation in the pharmaceutical industry. For instance, to predict if the liquid-solid fraction is adequate for consistent wetting and coating processes. And to minimise agglomeration and maintain stable coating conditions in coating industry. Alternatively, if any adjustment in drop size, particle size is needed if fluctuations in produced granule size distribution occur.

This research particularly aims to explore changing the formulation and operational parameters on the distribution nucleation inside a fluidised bed. The data obtained will investigate how these variables can affect the particle coating number and, consequently, the coating fraction.

Chapter 3: Materials and Methods

This chapter describes the properties of materials used in this study, including the methods used to characterise them. The wettability of the powder-binder system is also investigated using contact angle measurements. The general granulation method will be presented, along with experimental details for studying the effect of different formulations and operating variables. The fluidised bed specifically built for granulation is described in Chapter 4. Finally, the methods for the analysis of the granular product will be presented. The methodology specific to an individual results chapter will be outlined in the relevant results chapter.

3.1 Materials

A range of particles and liquid binders have been explored for their suitability for studying the distribution nucleation mechanism in fluidised bed. Granulation systems of relatively large size particles can be fluidised and form granules that can undergo sieving analysis. Also, liquid binder solutions of a wide range of viscosities can be sprayed under pressure from a binary spray nozzle into fine droplets.

The choice of a simple model particle that allows for studying the surface distribution of the binder over the particle surface will make understanding and quantifying the impact of individual parameters less complex. The model system should have known variables, such as a smooth particle surface and narrow size distribution without the complexity of particle surface roughness or pores. Glass beads were chosen for the model system. Subsequently, a real powder, the lactose monohydrate, will be studied.

Hydroxypropylmethylcellulose (HPMC) solutions were selected as a liquid binder system to granulate the particulate material in this study. This polymer is available in different molecular weight powders and, when dissolved in water, gives solutions of different viscosities can be sprayed through a pneumatic spray nozzle. The particles used in this study are listed in Table 3.1, and the liquid binders are given in Table 3.2.

Table 3.1: Particles used in the study

Material	Supplier
Glass Beads 150-250 μm	Kuhmichel Abrasiv Limited
Glass Beads 250-425 μm	Kuhmichel Abrasiv Limited
Glass Beads 425 -600 μm	Kuhmichel Abrasiv Limited
Lactose monohydrate Capsulac60 150-250	MEGGLE

3.1.1 Glass Beads

The glass beads supplied by Kuhmichel abrasives were manufactured from soda lime glass and processed into spherical beads by means of a heat stream in a furnace. Their hardness is about 6 Mohs (Kuhmichel Abrasives, 2017). They were received in three different size ranges (Table 3.1). The images of the beads were taken using a Lumenera Infinity 3 Camera (Lumenera Corporation, Canada) fitted with a Navitar 12X zoom lens (Image Optics, UK) and a LGT.19.MF2D LED dome diffuser lamp (Honyu, China) are shown in Figure 3.1.

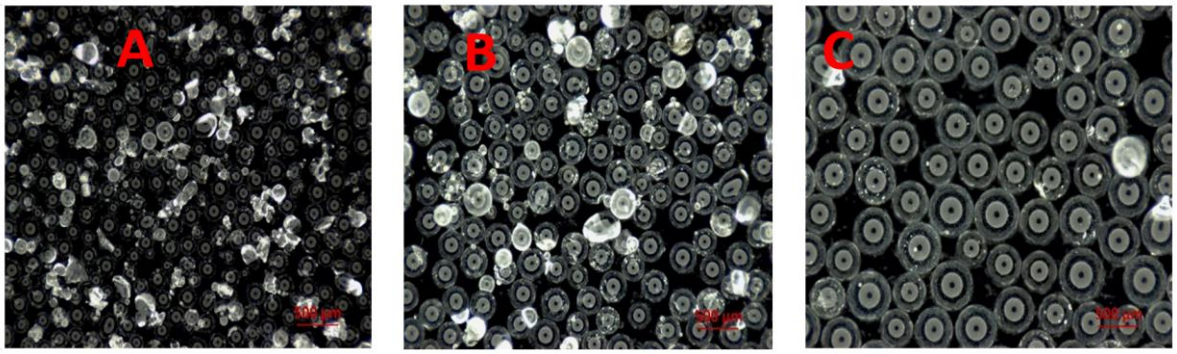

Figure 3.1: Images of the three sizes of glass beads powders from Kuhmichel Abrasive, size ranges of (A)150-250, (B) 250-425 and (C) 400-600 µm.

3.1.2 Lactose (Capsulac60)

The lactose crystals used in this research is capsulac 60; sieved alpha-lactose monohydrate grades from MEGGLE® Germany. It was received as a bulk powder and sieved further into the size range of 150-250 µm. The received raw capsulac 60 and the sieved size ranges 150-250 µm are shown in Figure 3.2

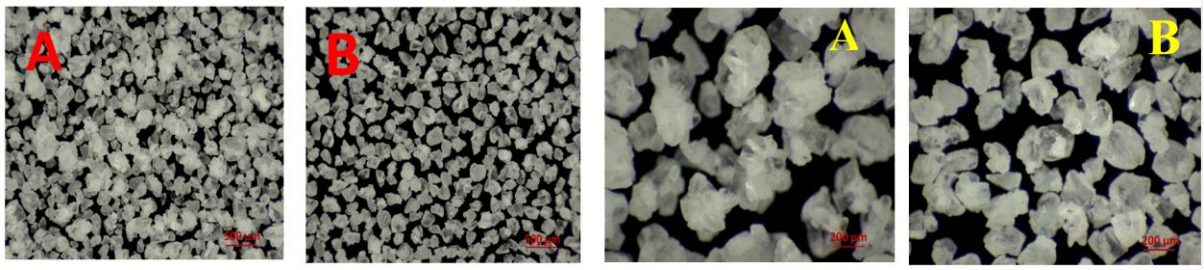

Figure 3.2: (A) Bulk Capsulac60 from MEGGLE®, (B) the sieved fraction 150-250 µm.

3.1.3 Hydroxypropylmethylcellulose (HPMC)

HPMC was used as the binder system Hypromellose TYLOPUR® from (shinEtsu® Japan.) was received in dry flake form, with a particle size ranging between 50-70 µm. The HPMC solutions

were chosen to represent a large range of viscosities. The viscosity was varied using different molecular weights of HPMC, which are of four different grades, and their molecular weights are given in Table 3.2. Solutions were prepared at a 10 % w/w concentration in distilled water, dyed with a 1 % w/w Acid red dye (Sigma Aldrich). The dye was used to aid the visualisation of the binder in the granular system. For preparation, the dry HPMC powder was weighed first and then added gradually to a freshly prepared 1 % w/w Acid red solution over a magnetic stirrer and left to dissolve at room temperature 21°C. It takes from 2 to 48 hours, according to the viscosity. The viscosity data for the different grades are given in section 3.2.5.

Table 3.2: HPMC grades & their molecular weights

TYLOPUR Grade	**603**	**645**	**606**	**615**
Mw (Da)	16,000	22,000	35,600	60,000

3.2 Raw material characterisation methods

A range of methods was used to characterise the materials involved in this research and to study their properties. The principle and the results of these methods will be described in the following sections.

3.2.1 Particle size distribution (PSD) by laser diffraction

Laser diffraction is based on a dispersed particulate sample subjected to a laser beam when the light is scattered at different angles, and the diffraction angle is inversely proportional to the size of the particle. The angular scattering intensity data is then analysed to calculate the size of the particles using Mie's theory for the interaction of light with matter. The particle size is displayed as a volume equivalent sphere diameter since the refractive indices of the particle material and suspending medium are known. This static light scattering technique consists of three main elements: an optical bench, sample dispersion units and instrument software. The range of particle sizing is between 0.1–2000 μm. Mean values are calculated from measured size distribution (Rhodes, 2008, Malvern, 2023a)

In order to determine the PSD of the powders, a sample was entered into a dry particle feeder of Malvern Mastersizer 3000 (Malvern Instruments Ltd., UK), and the measurements were monitored to ensure stable readings. A series of five laser diffraction measurements were performed. The diffraction of light is proportional to the volume of the particle. Therefore, this technique delivers volume-weighted results. The results of the powder size distribution are displayed as a volume frequency distribution graph, in addition to different particle size mean

diameters, depending on the applications in which the material's property is of interest. The Sauter mean $d_{3,2}$ (surface area mean diameter) represents the diameter of a sphere with the same volume ratio to the surface area. The Sauter mean is significant in fluid dynamics, catalysis and fuel combustion. As stated in Chapter 2, it is of particular relevance in fluidisation work, and this diameter is explicitly used to calculate U_{mf} of the particulate material.

The $d_{4,3}$ is the De Brouckere mean diameter and is the mean of a particle size distribution weighted by the volume, also called volume-weighted mean diameter (Webb, 2001). It is applied in mining, construction and mineral processing purposes (Folk and Ward, 1957). In addition, the most common d values, d_{10}, d_{50} and d_{90}, which relate to the cumulative distribution, are mainly used for quality control purposes. The d-values generally mean the diameter of which x percentage of the particles are smaller. Also, the width or broadness of any distribution is the span.

In order to analyse the particle size of the three-size glass beads and capsulac 150-250 µm powders, five different laser diffraction measurements were completed. Then the resulting PSDs were used to obtain the averages of mean values of $d_{3,2}$, $d_{4,3}$, d_{10}, d_{50} and d_{90}. They are illustrated in Table 3.3 and Table 3.4, respectively.

Table 3.3: Different glass beads used and their size properties. Standard errors are shown in brackets.

Glass beads size range (µm)	$d_{3,2}$(µm)	$d_{4,3}$ (µm)	d_{10} (µm)	d_{50} (µm)	d_{90} (µm)	Span
(150-250)	212	219	170 (0.98)	216 (0.76)	271 (0.25)	0.470
(250- 425)	324	330	275 (0.19)	327 (0.62)	392 (1.11)	0.359
(400-600)	511	518	441 (1.81)	514 (1.05)	598 (3.33)	0.305

The broadness of the glass beads fraction dispersions, the span, ranges from 0.305 for the largest size to 0.470 for the smallest size. In comparison, it is broader for the capsulac 60 (150-250 µm) than that of glass beads with the same size range, 0.788.

Table 3.4: Capsulac 60 (150-250 µm) size properties. Standard errors are shown in brackets.

Capsulac 60 (150-250 µm)	$d_{3,2}$(µm)	$d_{4,3}$ (µm)	d_{10} (µm)	d_{50} (µm)	d_{90} (µm)	Span
Particle size	190.9 (0.433)	207.5 (0.654)	134.6 (0.221)	201.4 (0.52)	294.5 (1.24)	0.788

The particle size distributions for the three-size powders glass beads 150-250, 250-425 and 400-600 µm are shown in Figure 3.3, Figure 3.4 and Figure 3.5, respectively.

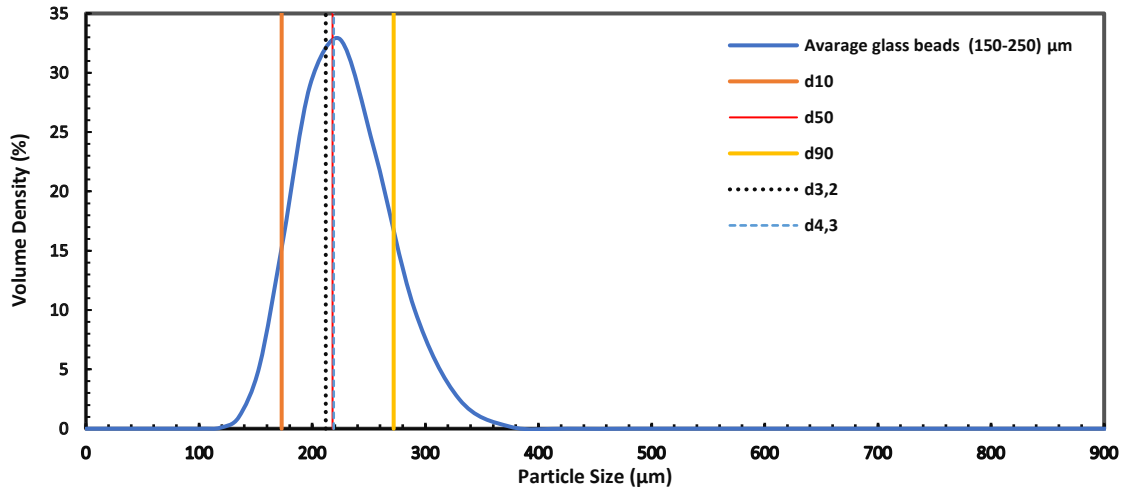

Figure 3.3: Average particle size distribution via laser diffraction of glass beads, 150-250 µm, showing the $d_{3,2}$, $d_{4,3}$, d_{10}, d_{50} and d_{90} values.

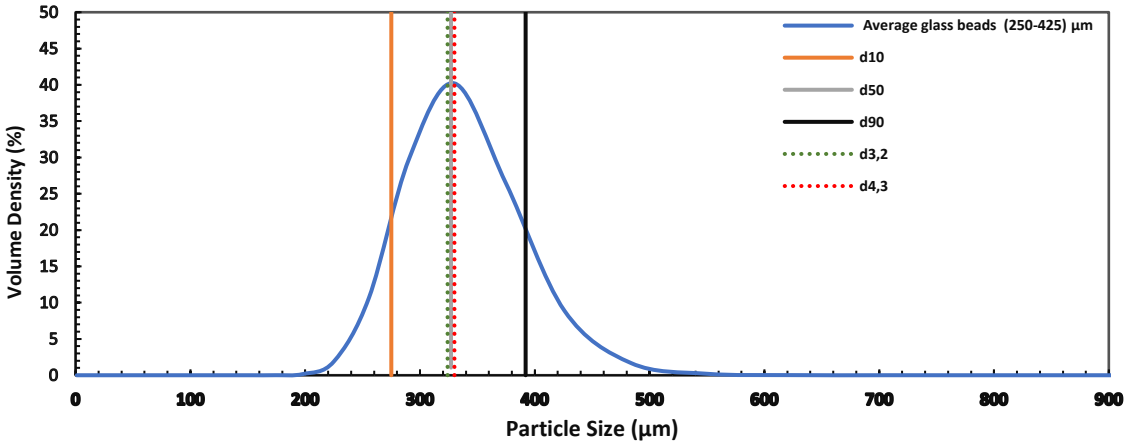

Figure 3.4: Average particle size distribution via laser diffraction of glass beads, 250-425 µm, showing the $d_{3,2}$, $d_{4,3}$, d_{10}, d_{50} and d_{90} values.

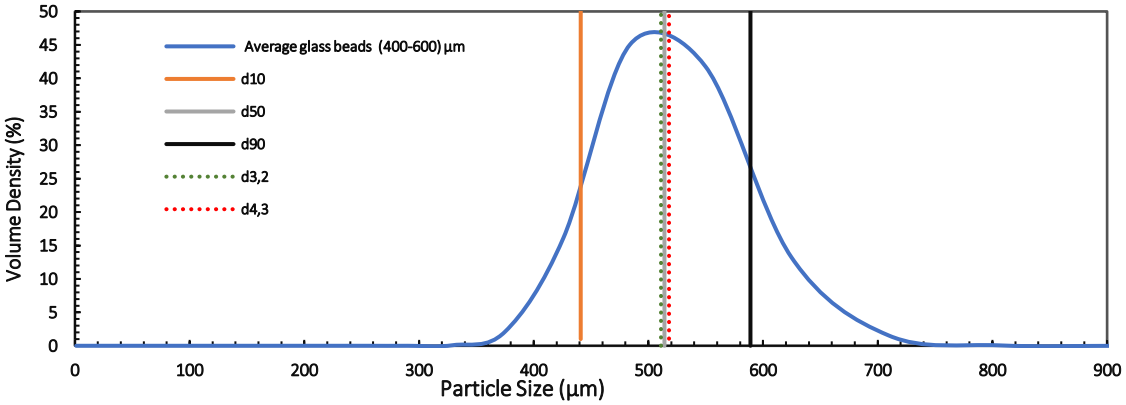

Figure 3.5: Average particle size distribution via laser diffraction of glass beads, 400-600 µm, showing the $d_{3,2}$, $d_{4,3}$, d_{10}, d_{50} and d_{90} values.

All the glass beads show narrow, monomodal dispersions with limited fines with standard error percentages ranging from 0.62 to 1.05 % for the d_{50}. Table 3.3 and Figures 3.3- 3.5 also show the median, surface, and volume diameters. As expected, the d_{50}, $d_{3,2}$, and $d_{4,3}$ values are close for a spherical material with narrow size dispersions.

For capsulac 60 (150-250 µm), as expected for pre-sieved powder, an unimodal PSD is obtained. The d_{50}, $d_{3,2}$ and $d_{4,3}$ are also close.

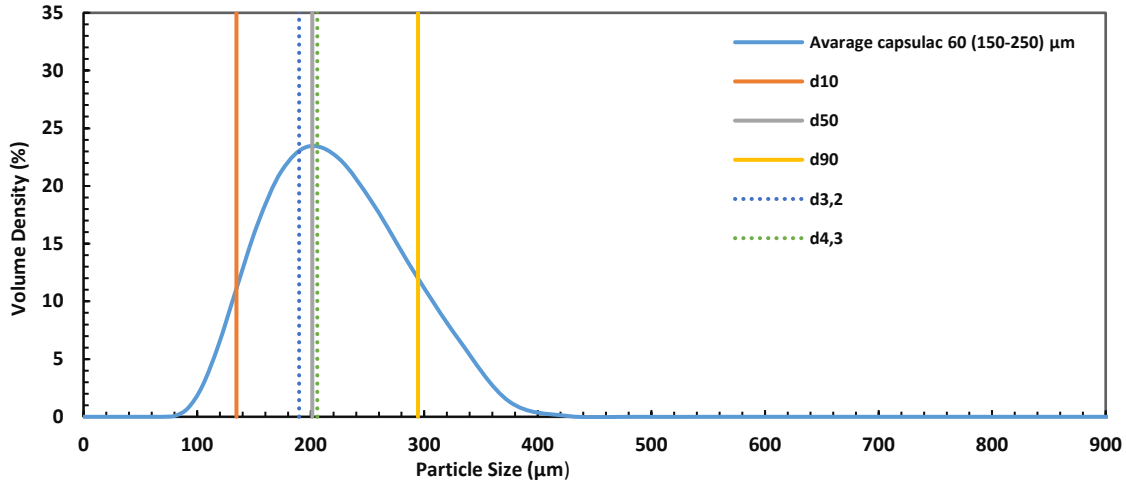

Figure 3.6: Average Particle size distribution via laser diffraction of capsulac 60 (150-250 µm), showing the $d_{3,2}$, $d_{4,3}$, d_{10}, d_{50} and d_{90} values.

For comparison, the capsulac 60 (150-250 µm) is selected to match the model glass beads (150-250 µm) as a real pharmaceutical excipient material. The glass beads have a narrower size distribution than capsulac 60 (150-250 µm), which shows a wider size distribution in favour of oversized particles.

As seen in Figure 3.5, glass beads (150-250) µm follow a very unimodal pattern and show the narrowest size distribution of all the materials studied, and the span is 0.47. All materials show narrow size distributions as indicated by the tight grouping of the d_{50}, $d_{3,2}$ and $d_{4,3}$.

Cumulative particle size distributions of the three glass beads size ranges are shown in Figure 3.7. In general, they all displayed a symmetric cumulative distribution. 150-250 µm size range has the narrowest size distribution. Median diameter, the d_{50}, from which half of the particles are smaller and the other half are larger, is so close to the d_{10} and d_{90} diameters.

The cumulative particle size distribution of capsulac 60 (150-250) µm is shown in Figure 3.8 and follows the same pattern. However, the d_{90} diameter has deviated to larger sizes.

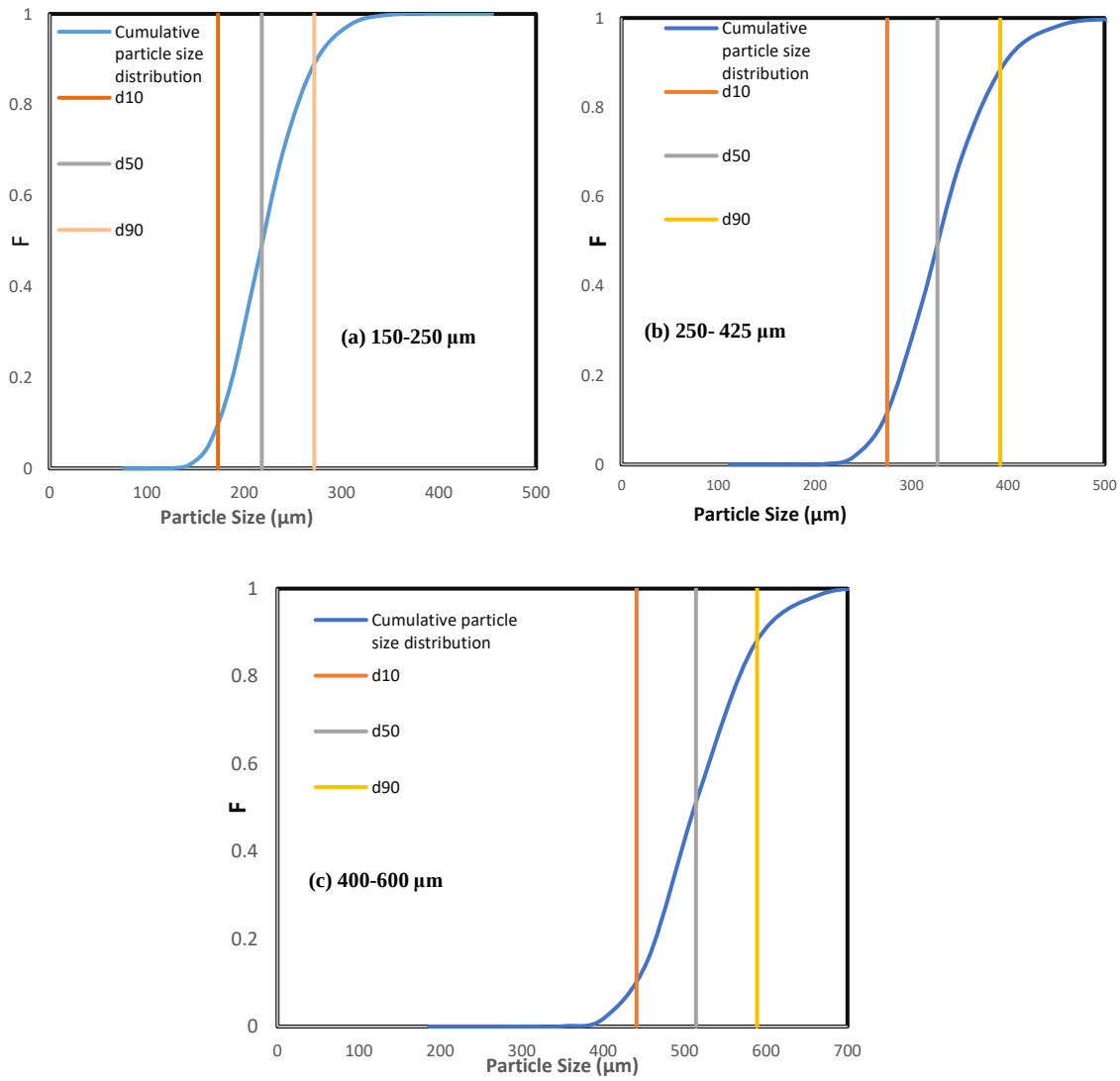

Figure 3.7: Cumulative particle size distributions of glass beads fractions obtained via laser diffraction with the d_{10}, d_{50} and d_{90} values; (a) 150-250 µm, (b) 250- 425 µm and (c) 400-600 µm.

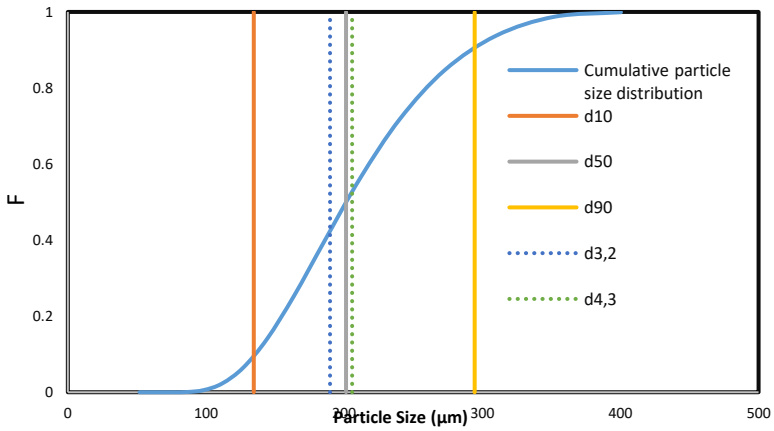

Figure 3.8: Cumulative particle size distribution of Capsulac 60 (150-250 µm) obtained via laser diffraction with the d_{10}, d_{50} and d_{90} values.

3.2.2 Specific surface area

Specific surface area (SSA) is a property of solids defined as the total surface area of a material per unit of mass (McNaught and Wilkinson, 1997). The (SSA) measurements were also obtained by laser diffraction (Malvern Mastersizer 3000) and by calculation. Malvern's concept is based on a mathematical analysis of the total area of the particles divided by the total weight, assuming the particles are spherical and non-porous (Malvern, 2023b). *SSA* is the total area of the particles divided by the total weight (Equation (3.1)

$$SSA = \frac{6\sum\frac{Vi}{di}}{\boldsymbol{\rho}\ \sum Vi} = \frac{6}{\boldsymbol{\rho}\ \mathrm{d}_{3,2}} \qquad (3.1)$$

Where V_i is the relative volume in class *i*, with a mean class diameter of *di* and ρ is the particle density, using $d_{3,2}$ as the particle diameter. This is based on the assumption the particles are spherical and non-porous.

Similarly, with the assumption that the particles are spherical and non-porous, the SSA of the spherical glass beads of all fractions can be calculated by finding the surface area of the whole bed per unit mass based on their Sauter mean $d_{3,2}$. For example, the specific surface area of glass beads of 150-250 fraction ($d_{3,2}$ = 212 µm = 2r), providing the surface area of a sphere, is:

$$A = 4\pi r^2 \qquad (3.2)$$

And its volume is:

$$V = \frac{4}{3}\pi r^3 \qquad (3.3)$$

Table 3.5 shows an example calculation of the SSA of the glass beads (150-250 µm) using the above equations.

Table 3.5: Calculation of the SSA of glass beads (150-250 µm)

The surface area of a single particle of glass bead $d_{3,2}$ = 212 µm (m^2)	The volume of the same particle (m^3)	Mass of a single sphere (Kg)	Number of particles in 0.930339 Kg of bed mass	The surface area of the total bed (m^2)	Specific surface area SSA of (150-250) glass beads ($m^2\ Kg^{-1}$)
1.41E-07	4.99E-12	1.21E-08	77058316	10.88	11.69

Table 3.6 displays measured and calculated SSA for glass beads and capsulac 60. As can be seen, the calculated values match the measured SSA for glass beads. However, for capsulac60, the predicted values are underestimated due to the irregular shape of the powder particles. Malvern SSA values were used in PCN calculations.

Table 3.6: Calculated and measured SSA for the materials used in the study.

Material	Glass beads			Capsulac 60
Size range (µm)	150-250	150-250	400-600	150-250
Surface mean $d_{3,2}$ (µm)	212	324	511	190.9
Calculated specific surface area (m^2/kg)	11.69	7.652	4.851	3.600
Malvern-specific surface area (m^2/kg)	11.55	7.557	4.793	20.51

3.2.3 Density measurements

Particulate material has three densities: true density, envelope density and bulk density. The true density of a particulate material is defined as the material mass over its volume that does not include the interparticle voids or internal pores inside the particles. The envelope density of particulate material is defined as it is mass per unit volume, including the pores within particles and excluding the interparticle voids. Bulk density is the weight of a loose particle bed per unit volume, including interparticle pores and intraparticle voids.

The true density was measured using helium pycnometry (AccuPyc II 1340, Micromeritics, Norcross, USA). The instrument measures the volume of the solid material in question, excluding the pores that the measuring helium gas cannot reach. A chamber of known volume was partially filled with pre weighed sample, and the helium gas was introduced at definite pressure to the sample chamber. Here it occupied the empty part of the chamber, penetrated the pores at the material's surface, and reached equilibrium pressure. The software estimated the true density using the volume occupied by the helium gas and the mass of the sample. The internal pores of porous material could be underestimated.

A Geopyc 1360 Envelope & T.A.P Density Analyzer (Micromeritics, Norcross, USA) was used to determine the envelope density. The instrument uses Dryflo powder for its good flowability due to its small particle size (d_{50} =130 µm) and spherical shape (Wade et al., 2015). This powder displaces the interparticle voids and attains close packing around the sample (Webb, 2001). Besides powders, it measures envelope density for granules. However, there will be an error in density measurement if the Dryflo powder is significantly larger than the

primary particle size of the powders (de Koster et al., 2019). This measurement is only applied to capsulac 60 powder.

A weighed sample was introduced into a cell containing Dryflo powder up to 25% of its volume. A plunger compressed the powder mixture as the cell vibrated with a force of 28 N. The displaced volume is then calculated by multiplying the difference in the distance that the piston travelled inside the Dryflo powder cylinder by a conversion factor, which refers to the volume per unit movement of the piston.

For the determination of the bulk density, a known mass of bulk powder was gently poured into a cylinder to occupy a particular volume, and the bulk density was calculated. Bulk density measurements were carried out in triplicate, and the average value was taken.

The true density of glass beads, averaged by 10 helium pycnometry measurements, was 2.504 g/cm^3, which is in reasonable agreement with the manufacturer's reported value of 2.5 g/cm^3. The true density of lactose monohydrate (capsulac 60) was found to be 1.543 g/cm^3, which also agrees with the supplier value of 1.54 g/cm^3.

The measured bulk, true for glass beads and lactose monohydrate (capsulac 60) size ranges, in addition to envelope density for capsulac 60 measurement are summarised in Table 3.7.

Table 3.7: Density measurements for glass beads size ranges and lactose monohydrate capsulac 60 (150-250 µm). Standard errors are also shown in brackets.

Material		**Glass beads**			**Capsulac 60**
Size range (µm)		**150-250**	**150-250**	**400-600**	**150-250**
Porosity (%)		**37.97**	**34.38**	**24.79**	**52.41**
Density ρ (g/cm^3)	Bulk	1.462	1.456	1.454	0.66 (0.0034)
	Envelope	-			0.73 (0.0046)
	True	2.504 (0.0005)			1.54 (0.0005)

The porosity of the bed was calculated using the true and envelope densities by the following equation (Wade et al., 2015).

$$\varepsilon = 1 - \left(\frac{\rho_e}{\rho_t}\right) x\ 100 \qquad (3.4)$$

As seen in Table 3.7, the bulk density of glass beads is consistent with the value of 1.4-1.6 g/cm3 provided by the supplier for the whole powder (Kuhmichel Abrasive, 2017). The bulk density for lactose monohydrate capsulac 60 (150-250 µm) is 0.66 g/cm3, which is in reasonable agreement with the manufacturer's reported value of 0.57 g/cm3 for the whole

powder. Calculated packed porosity shows there is a change in the porosity of the bed among different sizes of the glass powder. The porosity decreases as particle size increases, which is affected by how the particles are packed in the static bed. For capsulac 60, the powder bed is more porous than the glass bed of the same size, as the irregular shape and the density differences between the two materials. The porosity value will change during the fluidisation and granulation process.

3.2.4 Liquid binder (HPMC solutions) density measurements

A glass pycnometer (specific density flask of 50 cm^3 size) was used to carry out all the HPMC solutions density measurements. This glass vial is provided with a long thick stopper surrounding a capillary tube. It is intended to remove any excess liquid over the specific recorded volume at a certain temperature. Filling the pre-weighed empty flask with the liquid in question permits only the actual volume to be weighed again.

The pre-weighed empty flask was filled with the solution, and the total mass was reweighed to give only the 50 cm^3 solution mass. This process was repeated three times for each solution, with the vial being weighed before and after adding the liquid. All the measurements were carried out at 21 ◦C. The densities of all HPMC solutions used in this work are presented in Table 3.8.

Table 3.8: Liquid Densities of the different molecular weight HPMC 10%w/w solutions. Standard errors in brackets).

HPMC 10%w/w aqueous solution	603	645	606	615
Density (g/cm^3)	1.0296	1.030	1.030	1.030
Standard error	(± 0.0012)	(±0.0635)	(±0.0872)	(±0.0095)

As expected for 10 % polymers in water solutions, the density of water will dominate the mass, and the resulting liquids will have very similar densities.

3.2.5 Rheometric liquid viscosity measurements

A MCR502 Anton Paar Rheometer with CP50-2/TG (Graz, Austria) was used to measure the viscosities of the binder solutions. The rotameter was fitted with a conical plate of (2^o cone angle, 50 mm diameter). The sample was placed on a stationary bottom plate, and a moving cone attached to the rheometer's motor was lowered onto the sample and rotated at a definite speed. The torque as a result of the rotation of the cone was measured. The velocity that the upper plate rotated controls the shear rate applied to the sample. The shear stress was then

calculated as the force applied to the sample per unit area. The sample's viscosity was calculated as the shear stress divided by the applied shear rate (Paroline, 2016).

Three separately prepared solutions were analysed using rheometry to estimate the viscosity of the HPMC solution used for fluidised bed granulation. All measurements were taken at room temperature (20 ˚C). The applied shear rate was between 0.1 and 1000 s^{-1}, and the average of three measurements was calculated.

Figure 3.9, Figure 3.10, Figure 3.11, and Figure 3.12 show the viscosities of the 10%w/w aqueous solutions of HPMC 603, HPMC 645, HPMC 606 and HPMC 615, respectively. Table 3.9 shows the viscosity of solutions at a shear rate of 1000 s^{-1}.

Table 3.9: The viscosities of the 10%w/w aqueous solutions of HPMC 603, HPMC 645, HPMC606 and HPMC 615. Standard errors are shown in brackets.

HPMC10%w/w	603	645	606	615
Mw (Da)	16,000	22,000	35,600	60,000
Viscosity (mPa·s)	55.097±0.057	177.03 ± 1.0	352.36 ± 9.41	1138.5 ± 33.0
Standard Deviation (mPa·s)	0.1	1.73	16.3	57.77

The two lower viscosity solutions HPMC 603 and HPMC 645 in Figure 3.9 and Figure 3.10, behave as Newtonian fluids over the range of shear rates tested between $1s^{-1}$ and 1000 s^{-1} and appear constant at these shear rates. However, they undergo fluctuations at shear rates less than $1s^{-1}$ as the viscosity depends on the shear rate. These fluctuations at very low shear rates should be insignificant of because, during experimental conditions, spraying the liquid is likely to occur at high shear rates between 100 s^{-1} and 1000 s^{-1} (Paroline, 2016).

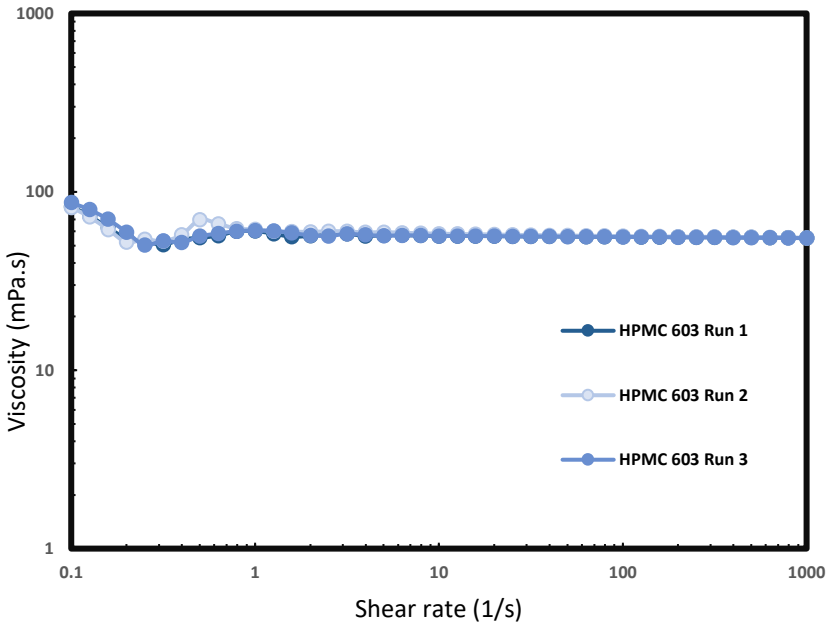

Figure 3.9: Viscosity of dyed HPMC 603 as a function of the shear rate, shown on logarithmic axes.

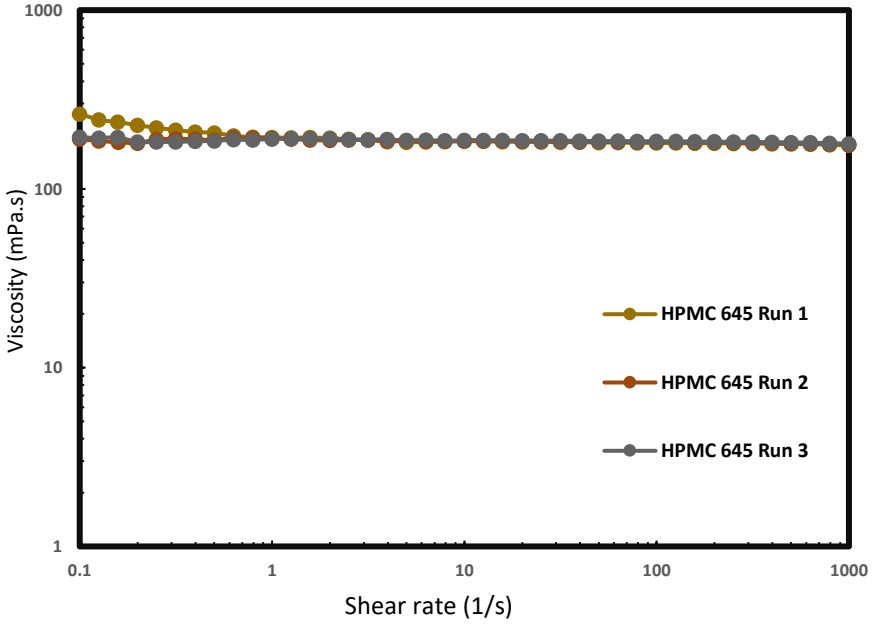

Figure 3.10: Viscosity of dyed HPMC 645 as a function of the shear rate.

The higher viscosities solutions HPMC 606 and HPMC 615 in Figure 3.11 and Figure 3.12 behave as visco-elastic liquids with constant viscosities at low shear, but they are shear thinning at shear rates, higher than 100 s^{-1} which is typical for polymer solutions.

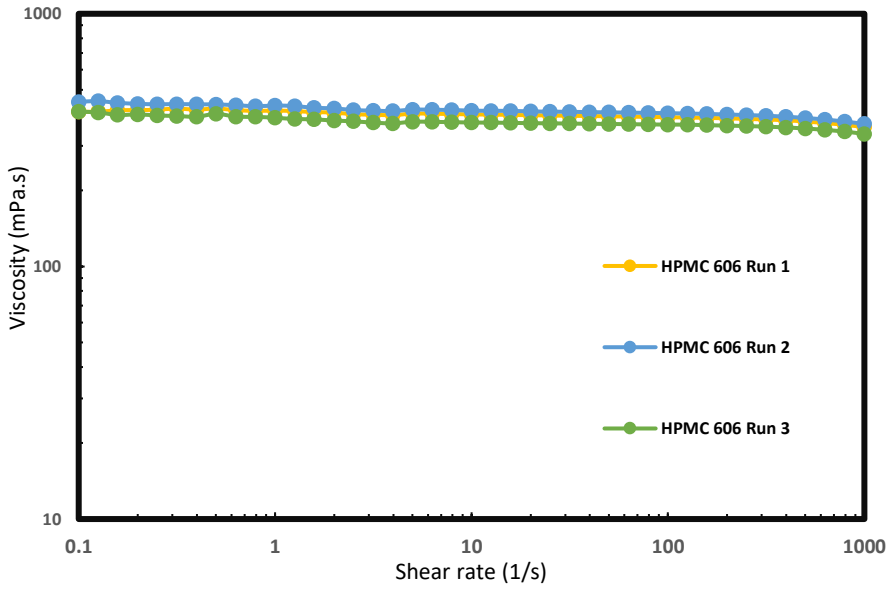

Figure 3.11: Viscosity of dyed HPMC 606 as a function of the shear rate.

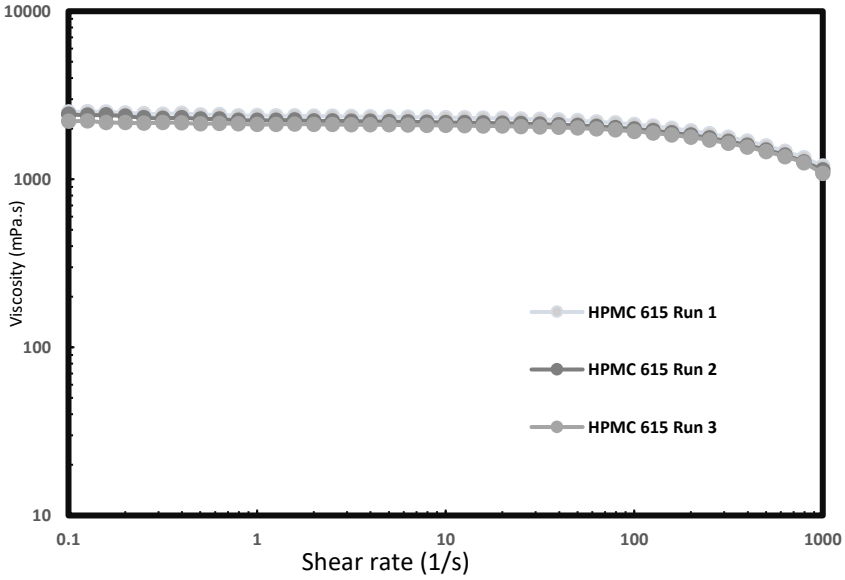

Figure 3.12: Viscosity of dyed HPMC 615 as a function of the shear rate.

A comparison of the four obtained curves is shown in Figure 3.13. HPMC solutions of high molecular weights show a noticeable decrease in viscosity at high shear rates.

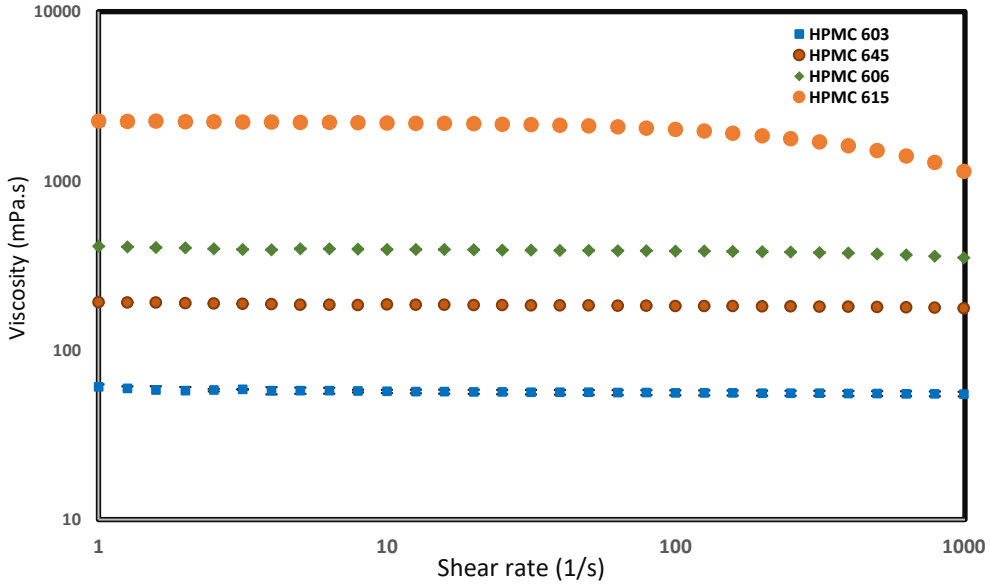

Figure 3.13: Average viscosities of all HPMC solutions as a function of shear rate.

3.2.6 Interfacial tension measurements

Surface or interfacial tension is a measure of the force necessary to pull adjacent parts of a liquid's surface together (intermolecular forces), thus decreasing the surface area of a liquid to the smallest possible size. It relates to cohesion forces which means more force is required to break the surface of a liquid. Surface energies can be used to predict the performance of binder solutions (Vu, 2021). The ability of a liquid to wet and spread over a solid surface is a function of its wetting tension. This characteristic also contributes to the formation of a liquid bridge. Surface energies of materials are important in the design of the wet granulation process, where good correlations were found between granule properties and granulating solvent drug spreading coefficients. For example, 20% ethanol solution with a larger spreading coefficient produced stronger and denser granules than water (Zhang, 2002).

The surface energy was measured by the pendant drop method in air. A First Ten Angstroms FTA1000 goniometer was used to quantify the interfacial tension of the liquid binders. The shape of the pendant drop formed by a 30 gauge (inner diameter 0.1524 mm, outer diameter = 0.3112 mm). The blunt needle is imaged by the Snapshot feature. The radii of curvature of the drop are measured. The accompanying software utilises Young-Laplace equation. The interfacial tension was then calculated using the liquid and the surrounding densities (air), and snapshots were captured. An example snapshot is shown in Figure 3.14.

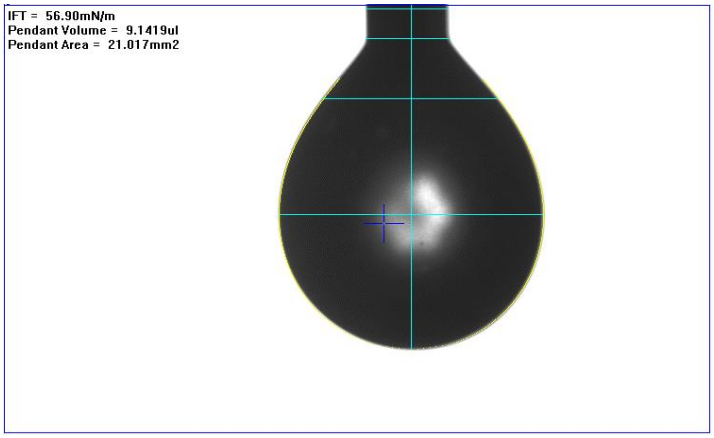

Figure 3.14: An image captured by an FTA1000 goniometer for the pendant droplet of HPMC 606 solution (352mPa·s viscosity) and interfacial tension measured by its software.

The average of ten measurements for each is shown in Table 3.10. All the tests were completed at room temperature (21 °C).

Table 3.10: Surface tension measurements of 10% HPMC aqueous solutions. Standard errors are shown in brackets.

HPMC 10%w/w aqueous solution	603	645	606	615
Viscosity (mPa·s)	55.9	177	352.36	1138.5
Interfacial tension (mN/m)	**58.86 (**±0.31**)**	**57.44 (**±0.09**)**	**56.25 (**±0.18**)**	**57.03 (**±0.15**)**
S.D. (m N/ m)	0.99	0.30	0.58	0.48

Table 3.10 shows the similarity in the interfacial tension, which is probably due to the high water constitution in all binder preparations (90%). This similarity will eliminate the impact of surface tension differences on the nucleation. Therefore, the effect of this parameter was not investigated in this thesis.

3.2.7 Contact angle measurements

The contact angle is a powder-liquid system character able to assess the affinity of the binder liquid to wet and spread over the particle surface or a powder bed. Contact angles of powder-binder systems used in this research were measured using a First Ten Ångstroms FTA1000 goniometer. This instrument is composed of a camera set up on a stage. The camera captures a video of up to 2000 frames for a pendant drop produced by a blunt needle of a 22 gauge needle (0.413 mm internal diameter). The contact angle is calculated by FTA software once the droplet lands on the material surface.

Although relatively large sized particles of the powders used in this research, dropping a sessile droplet on a single particle surface to measure the contact angle is unachievable. Therefore, the techniques used to prepare the material for contact angle measurement are by using either the material monolayer method, which requires crushing the powder first and then applying a layer of the crushed powder on an adhesive tap adhered to a glass slide. Alternatively, there is the compressed tablet method by pressing the powder into a tablet with a flat surface (Alghunaim et al., 2016). The limitation of these methods is that either the crushing or the compression force may alter the surface energy of the powders. In addition, the compressed tablet method couldn't be applied to the glass powder because the compressed glass tablet was fragile and easily fractured. Therefore, it was only limited to capsulac 60 powder. The monolayer method was applied to both glass and capsulac 60 powders.

3.2.7.1 Material monolayer method for contact angle measurements

Glass beads were crushed using a mortar and pestle, and then a layer of crushed powder was laid on adhesive tape adhered to a glass slide. A sessile droplet of solution of interest landed over the powder layer, and a video was recorded. Contact angle measurement also was carried out for monolayer of capsulac 60 (150-250 µm) powder with the same method, except the material was laid intact without grinding to not alter its surface energy.

Table 3.11 shows the averaged contact angle measured after 0.1 s and after 1.0 sec time for the four HPMC binder solutions. Earlier contact angle recorded by the software doesn't show clear differences among liquids because the pendant drops of high viscous binder take a longer time to detach from the needle tip. Therefore, in the very early time, lower viscosity liquids might show similar high contact angles to those of the highest viscosity.

After one second, when the droplet started to reach equilibrium, the different viscosities with both substances showed clear differences in the magnitude of contact angles. HPMC has an affinity for capsulac 60 more than the glass beads; hence, the contact angle was smaller than those with the glass beads powder at any time.

Table 3.11: The contact angle was measured by the monolayer method after 0.1 sec and after 1.0 sec. The standard deviation is shown in the table.

Time	Liquid binder viscosity (mPa·s)	Glass beads monolayer		Capsulac 60 150-250 µm monolayer	
		Contact angle (◦)	S.D (◦)	Contact angle (◦)	S.D (◦)
At 0.1 s	HPMC 55	83.85	5.88	56.41	0.72
	HPMC 177	97.93	16.3	83.09	3.13
	HPMC 352	99.25	9.47	85.01	2.88
	HPMC 1138.5	104.67	6.31	96.16	4.44
At 1.0 s	HPMC 55	**56.14**	3.42	**31.66**	0.567
	HPMC 177	**77**	8.59	**34.78**	3.37
	HPMC 352	**82.37**	7.78	**58.95**	7.62
	HPMC 1138.5	**90.79**	9.45	**84.43**	3.014

Figure 3.15 shows images of the deposited drop and the contact angle decreasing over time, captured for HPMC 177 mPa·s on the glass beads monolayer during the measurement. The baseline was increased in length as the drop spread over a larger area.

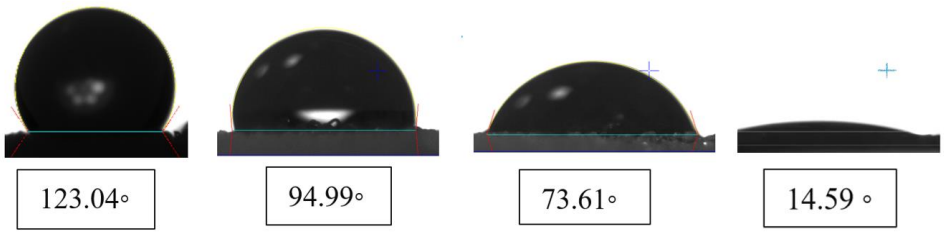

Figure 3.15: Images for HPMC 177 mPa·s on the glass beads monolayer contact angle by the software FTA1000 goniometer during measurements.

Figure 3.16 shows the contact angle for drops of the different HPMC systems deposited on the powdered glass bed and capsulac 60, averaged from three measurements. As can be seen, the HPMC systems wet the capsulac 60 better than the glass material. With capsulac 60 layer, the contact angle is lower than those with the glass, as all the liquids show a faster spreading rate. The lowest viscosity solution has the highest affinity and wetted the powder bed within short time. The contact angle decreased to less than 20◦ after 2.5 s. However, this took longer with the powdered glass monolayer, and the angle dropped to 20◦ after 11s. In contrast, solutions of higher viscosities have larger contact angles with the powder, and the contact angle magnitudes are slowly reduced over time before reaching their equilibrium values. The high affinity and better wettability for capsulac 60 could be referred to the polarity of the aqueous binder solutions and the hydrophilicity of the lactose compared with that of glass material.

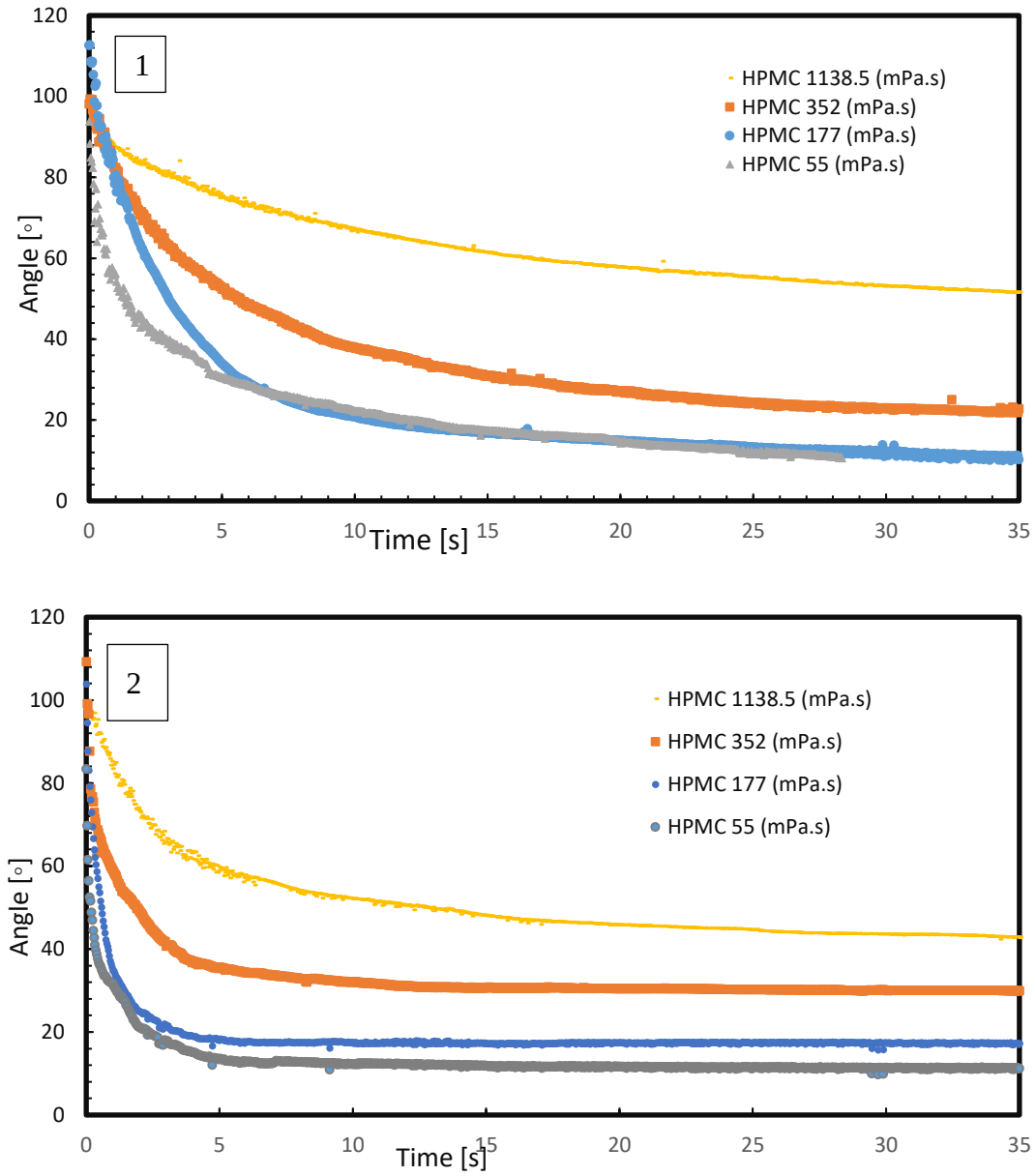

Figure 3.16: Contact angle as a function of time for four different viscosity binder solutions on (1) a powdered glass bed and (2) Capsulac 150-250 µm powder.

3.2.7.2 Compressed tablet method for contact angle measurements

This method was only applied to capsulac 60 powder. One g of capsulac 60 powder was compressed to form a tablet of 20 mm diameter and 2.64 mm height using a Specac hydraulic pellet press under a compression force of 3 ton; 3 ton was found to be the maximum applied force under which tablets with these dimensions can tolerate and can be removed intact safely. The binder HPMC solutions were filled into a 2 ml syringe (Gilmont Instruments) fitted with a 22 gauge needle (0.413 mm internal diameter), and the contact angle of the droplet deposited

on the lactose tablet was measured over time. All the measurements were performed in triplicate.

Figure 3.17 shows the contact angle as a function of time for four different viscosity binder solutions within a minute on the lactose tablets. The HPMC polymer aqueous solutions possess good wettability and high affinity for capsulac 60, especially the low viscosity binders, which tend to spread faster and penetrate microvoids available at the tablet surface. The HPMC 603 solution of 55 mPa·s has the lowest contact angle, which dropped to below 20°within the first 3 seconds. HPMC 645 of 177 mPa·s follows a similar trend and shows a slightly higher contact angle. By increasing binder viscosity, the HPMC 606 of 352 mPa·s droplets' contact angle was higher and decreased gradually to below 25 °after 40 seconds. The contact angle for HPMC 1138.5 mPa·s remained high at 40 °

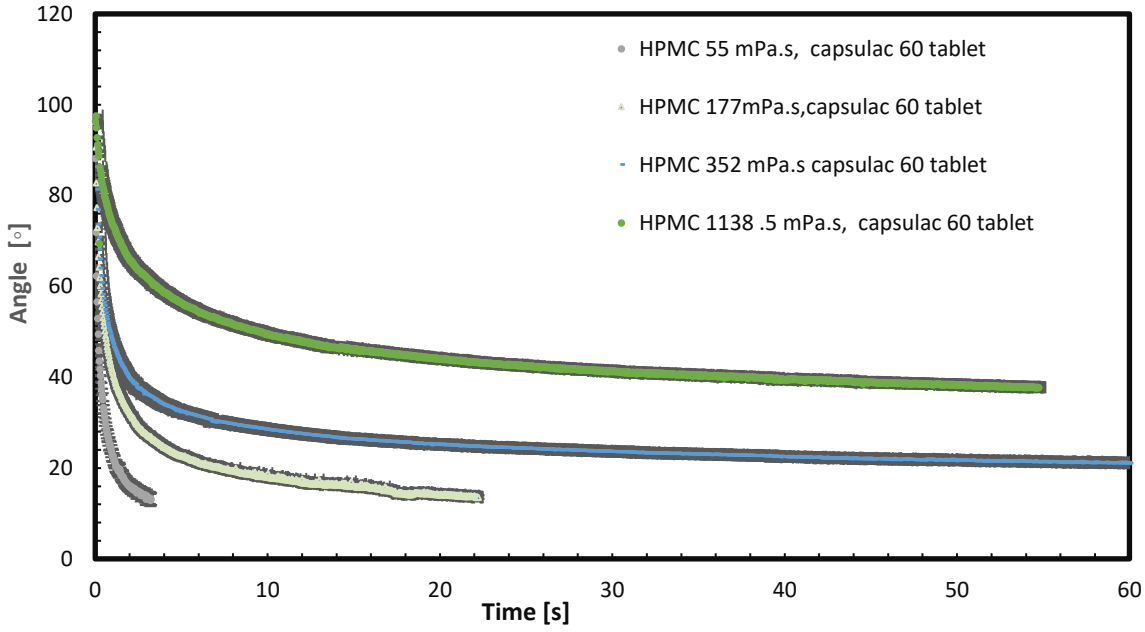

Figure 3.17: Contact angle as a function of time for four different viscosity binder solutions on 3 ton Capsulac 60 tablet.

Table 3.12 summarised the averaged contact angle measured after 0.1 s and after 1.0 sec for the four HPMC binder solutions on 3 ton capsulac 60 compressed tablets.

In conclusion, the contact angle is the angle which the liquid droplet forms with the solid surface once it reaches a stable state, where the spreading and evaporation processes have reached equilibrium. The contact angle measured by the sessile drop method is initially affected by surface tension, gravity, and capillary forces. As time passes, the angle undergoes some changes due to penetration and evaporation. The contact angle that is typically recorded in this

dynamic process is the "equilibrium contact angle" differences among liquids because the pendant drops of high viscous binder take a longer time to detach from the needle tip. Therefore, in the very early time, lower viscosity liquids might show similar high contact angles to those of the highest viscosity.

Table 3.12: The contact angle measured by the compressed tablet method after 0.1 sec and after 1.0 sec time. The contact angle measured by the monolayer method on the right side was copied from Table 3.11 for comparison.

Liquid binder viscosity (mPa·s)	**Capsulac 60 Compressed tablet**		**Capsulac 60 150-250 µm monolayer**	
	Contact angle (◦)	Standard deviation	Contact angle (◦)	Standard deviation
Time	**0.1 s time**			
HPMC 55	56.61	0.72	56.41	0.72
HPMC 177	76.39	3.13	83.09	6.92
HPMC 352	76.97	2.88	85.01	7.99
HPMC 1138.5	92.82	4.44	96.16	9.45
Time	**1.0 s time**			
HPMC 55	22.90	0.183	31.66	0.56
HPMC 177	41.28	7.07	34.78	3.37
HPMC 352	47.26	2.69	58.95	7.61
HPMC 1138.5	73.92	4.44	84.43	3.01

The results obtained by both methods with HPMC- Capsulac 60 system followed the same trend. More specifically, Table 3.12 displays similar contact angles obtained by the two methods. However, the contact angle measured by the Capsulac 60 monolayer method is slightly higher than that recorded over the compressed tablet. This is due to the particle-liquid interaction, and the compaction of the tablet provides a thicker layer and more surface for penetration than the material monolayer method, where the liquid may interact with the adhesive tape beneath the powder layer, resulting in an increased contact angle. However, although the spreading rate is different between the two methods, the contact angles are similar for the Capsulac 60 by the two methods. With the tablet method, the contact angle of 352 and 1138.5 mPa·s reached equilibrium values, while with 55 and 177 mPa·s binders, the contact angle dropped below 15◦ and eventually disappeared. . The contact angle magnitude selected in this research is the one recorded by the monolayer method after 1 second (differences among liquids because the pendant drops of high viscous binder take a longer time to detach from the needle tip. Therefore, in the very early time, lower viscosity liquids might show similar high contact angles to those of the highest viscosity. (Table 3.11). Because it was recorded after a

time, that can show differences in the droplet deposited on the surface at equilibrium or near equilibrium, moreover, this method applies to both materials in the study.

3.3 Calculation of particle coating number PCN Φp

The particle coating number (PCN) proposed by Kariuki et al. (2013) to predict fractional surface coating (F) using image analysis requires further development and validation in real granulation experiments, which constitutes the novelty of this work. In a fluidised bed with a top-spray nozzle, two distinct zones can be identified: the spray zone, where the nozzle delivers liquid at a specific volumetric rate, and the remaining fluidised bed.

Particles enter the spray zone at a certain surface renewal rate, which refers to the rate at which new surface particles are exposed to the sprayed liquid binder, while a fraction of particles are not being actively coated at that time. The *local PCN* inside the spray zone describes the actual coating rate process during the spray time. The *global PCN* represents the overall distribution of the liquid binder added to the system. In the results chapter, the global PCN will be presented.

3.3.1 The global PCN Φ_p

The global coating number accounts for the entire bed and describes the distribution of whole liquid mass over the whole bed mass and implies the X_{LS} fraction, droplet size, the liquid and particle surface interaction in terms of contact angle and the solid surface area available for coating. It was calculated for every solid-liquid system by recalling Kariuki's suggested equation (2.36).

$$\boldsymbol{\Phi_p} = \frac{\boldsymbol{6\, X_{LS}\, a_d}}{\boldsymbol{\pi\, {d_d}^3\, \rho_d\, A_{SA}}} \tag{3.5}$$

As has been previously mentioned, A_{SA} is the specific surface area of the particulate material, d_d is the spray nozzle droplet diameter, and ρ_d is the liquid density of the liquid binder. The droplet footprint area *ad* was calculated using the Clarke et al. (2002) assumption, which assumes the landing of a droplet on a particle with a flat surface:

$$\boldsymbol{ad} = \frac{V_d \sqrt{\pi}\ \ sin^3\theta}{2 - 3\cos\theta + cos^3\theta} \tag{3.6}$$

Where θ is the equilibrium contact angle between the droplet and the particle surface, this approximation is reasonably accurate when very small droplets land on very large particles and the particle's curvature is negligible compared with the droplet's (Kariuki et al., 2013).

3.3.2 The local particle coating number (inside the spray zone)

The local PCN at the bed surface predicts the liquid distribution at the spray zone using the ratio between the rate at which the liquid mass is added per spray coverage area and the rate at the solid surface being renewed and ready for coating in the spray zone.

To approximate this ratio (denoted as the local X_{LS}) for use in Equation (**3.5**), the following dimensionless quantity (α) is introduced. Here, α represents the ratio of the liquid mass delivered by the nozzle per unit time to the solid renewal rate in the spray zone:

$$\alpha = \frac{\dot{m}_d(\mathrm{kg}s^{-1})(m^{-2})(m^2)}{A\ (m^2)\ U_B(m\ s^{-1})\ (1-\varepsilon)\ \ \rho_P(kg\ m^{-3})} \qquad (3.7)$$

To find the local X_{LS} i.e. the liquid mass landing at the solid surface at the top of the fluidised bed per unit time per unit area (**$\dot{m}_d$**), the spray coverage area in the cylindrical column using a full cone nozzle can be approximated as the sectional area of the bed:

$$\dot{m}_d = \frac{liquid\ mass\ added\ per\ unit\ time(kg\ s^{-1})}{spray\ coverage\ area\ (m^2)} \qquad (3.8)$$

The total solid surface area is given by:

$$= \text{Solid mass (kg) x specific surface area of the solid } A_{SA}\ (\mathrm{m^2/kg}) \qquad (3.9)$$

Here U_B is the bubbling velocity, ρ_p is the density of the solid, ε is the bed porosity, and A is the bed cross sectional area. By applying α in Equation (**3.6**) instead of $X_{LS,}$ the local PCN can be estimated.

3.3.3 The coating coverage fraction F

This was also calculated according to Equation (2.32) (Kariuki et al., 2013).

$$\mathrm{F} = 1 - \exp(-\Phi \mathrm{p}) \qquad (3.10)$$

Table 3.13 shows an extract from an Excel file showing the calculation of Global and Local PCN and the coating coverage fraction F according to equations (3.5), (3.7), and (3.10).

Table 3.13: Excel extract showing Global and Local PCNs calculations taken from flow rate experiment when glass beads $d_{3,2}$ (212 µm) was granulated with 10% HPMC 352 mPa·s at 1 bar liquid pressure.

A - Global PCN Φp										
Glass beads 212µm mass (kg)	Liquid pressure (bar)	Liquid mass (kg)	Laser droplet Sauter mean (m)	X_{LS}	Drop volume (m^3)	*Drop footprint area (m^2)	Liquid density (kg/m^3)	A_{SA} (m^2/kg)	**Global PCN**	**F**
0.93033	1	0.00286	2.83E-05	0.0034	1.19E-14	1.14E-09	1030.83	11.5856	**0.0246**	0.024

B - Local PCN								
Solid mass (kg)	Cross-sectional area of the bed (m^2)	Liquid flow rate (kgs^{-1})	ε	ρ (kg/m^3)	Total surface area of the solid (m^2)	U_B	**(Local X_{ls})**** α	**Local PCN**
0.93033	0.006363	0.000286	0.4	2504	10.77	1.014	0.050	0.40

*Calculated using (Equation 3.6)

** α is the estimated local liquid solid fraction inside the spray zone and used in (Equation 3.7) instead of X_{LS}.

The Sauter mean of the droplets produced under the experimental conditions, the specific surface area for the solid material and the solid liquid fraction are needed to estimate the dimensionless PCN. Therefore, the following section will discuss the size of droplets produced by the pneumatic spray nozzle system and their velocity.

3.3.4 Droplet size measurements

The size and velocity distributions of droplets produced by the pneumatic spray nozzle system used in the research and required for the PCN calculation were measured using nano-particle imaging velocity (PIV) from Oxford Lasers Ltd/ UK. The system is composed of an LPU450 laser head with laser resonators producing infrared laser light at 1064 nm converted to visible 532nm. The LPU450 power supply unit has cooling requirements for the two laser oscillators and 532nm generation. It collects the images acquired by the camera and runs VisiSize software used to view the images and compile the relevant data within the images. Droplet image analysis was carried out by the set up shown in Figure 3.18, including the spray nozzle system, the pressure pot and the control panel to set the required pressures. The pressure pot was to control liquid pressure.

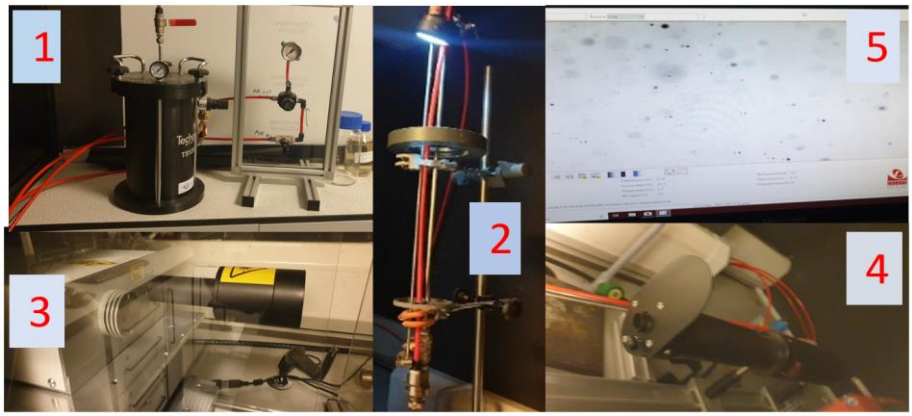

Figure 3.18: Laser set up for droplet image analysis: (1) pressure pot and control panel for liquid and air pressure regulation, (2) spray nozzle, (3) Nano PIV Laser head and the light source (4) digital camera enclosure and (5) screen showing droplets are distinguished from the background illumination byVisiSize software.

The light source and camera enclosures which are situated on a rail placed into the path of the event to be imaged. The PIV technique illuminates the region of interest with short flash of light from behind which acts as a bright background behind the subject spray and takes shadow images of the moving particle/ droplet with a digital camera. The short pulse of the laser freezes the motion of the drops so their sizes and shapes can be visualised. Images from the digital camera are transferred to the computer, and high-speed real-time particle sizing VisiSize software thresholds the images so the droplets are distinguished from the background illumination, their pixel area is measured, and the calibration gives the equivalent particle diameter.

The control panel was used to manage the atomisation pressure, and both used the pressurised lab air up to 5 bar. The spray nozzle was mounted at 15 cm above the camera. All measurements were performed in triplicate. Table 3.14 displays the droplet size as surface mean (d3,2).

Table 3.14: Droplet measurements obtained by PIV laser at all experimental conditions used in the research. Some conditions were shared in more than one experiment. Initial particle experiment A is carried out at fixed X_{LS} & Exp B is carried out at fixed liquid mass/surface area.

Exp	Liquid binder		Conditions			Results			
Title	HPMC Solution (10%)	Viscosity (mPa·s)	Liquid pressure (bar)	Liquid flow rate (g/s)	Atomisation pressure (bar)	Droplet size d3,2 (µm)	Average velocity (ms-1)	Estimated PCN	F
H_2O		1.001	3		4	44.03	6.368	-	-
Flow rate	606	352	1	0.286	4	28.33	7.364	0.024	0.024
	606		2	0.847	4	30.96	8.617	0.066	0.0645
	606		3	1.298	4	30.33	9.1353	0.104	0.099
	606		4	1.787	4	31.13	8.787666	0.14	0.13
	606		5	2.28	4	31.76	9.10966	0.175	0.16
Mixing time	606	352	3	1.29	4	30.33	9.135333	0.092	0.089
fluidisation velocity	606	352	3	1.29	4	38.6	5.0383	0.077	0.074
Atomisation pressure	606	352	3	1.31	3	34.23	8.071	0.093	0.089
	606		3	1.29	4	30.96	9.135	0.101	0.0968
	606		3	1.29	5	30.93	8.488	0.102	0.0969
Viscosity	603	55	1.76	1.3	4	32.83	3.558	0.1462	0.1360
	645	177	2.34	1.3	4	39.33	5.379	0.1037	0.0985
	606	352	3	1.3	4	30.33	9.135	0.0873	0.0836
	615	1139.5	4.85	1.3	4	39.46	5.032	0.071	0.0686
(Exp A) Initial particle size	615	1139.5	5	1.35	4	38.6	5.038	0.07	0.074
	615		5	1.35	4	38.6	5.038	0.118	0.111
	615		5	1.35	4	38.6	5.038	0.186	0.17
(Exp B) Initial particle size	615	1139.5	5	1.35	4	38.6	5.038	0.096	0.092
	615		3.7	0.907	4	37.8	5.852	0.083	0.0803
	615		2.7	0.566	4	35.83	5.648	0.077	0.074

3.3.5 Liquid solid fraction (X_{LS})

The liquid solid fraction, in the wet granulation process, is the liquid to solid ratio by mass. It describes how much liquid is sprayed and is available to granulate the solid material. It plays an important role in defining the binder liquid distribution process and granule attributes (Smirani-Khayati et al., 2009). This research used initial particles of a relatively large size in a fluidised bed, ranging from 150-600 µm. Therefore, rapid growth in size was attained in a short fluidisation time. Thus, liquid solid fractions in the experiments were minimal and ranged from 0.0031 to 0.024.

3.3.6 Stokes number calculation

In fluidised bed system, distribution nucleation and further growth in size will occur by coalescence when the coalescence/rebound criterion is met (Iveson et al., 2001), as was discussed in Section 2.5.6. in Iveson regime, the Stokes number St_v should be below a critical viscous Stokes number St_v*. Therefore, the Stokes number is calculated using Equation (2.37) for each data set. It is the ratio between the kinetic energy of the impact to the viscous dissipation force of the system:

$$St_v = \frac{4\rho_g U_c \, d_g}{9\mu} \qquad (3.11)$$

Uc is the average collision velocity of the impact and can be estimated as follows (Rhodes, 2008, Litster, 2016a) :

$$U_c = \frac{6U_B \, d_g}{d_b} \qquad (3.12)$$

Where U_B is the bubbling velocity and this can be calculated for B powders by Darton et al., 1977 equation (Rhodes, 2008).

$$U_B = \vartheta_B(\mathrm{g}d_{Bv})^{0.5} \qquad (3.13)$$

And, d_{Bv} is the equivalent volume diameter of the bubble mean bubble size by Werther's (1983) equation, g is acceleration to gravity and ϑ_B = 0.64 for bed diameter $\leq$ 0.1m (Rhodes, 2008).

$$d_{Bv} = \frac{0.54}{g^{0.2}} \, (U - U_{mf})^{0.4} \qquad (3.14)$$

for example, the Stokes numbers for four viscosity systems used in the viscosity Experiment in Section 5.1:

$$U_B = 1.014\ ms^{-1},\ d_g = 2.12x10^{-4}\ m,\ \rho_g = 2504\ kg/m^3,\ d_b = 0.1m$$

U_B was calculated using Equations (3.13) and (3.14). The average collision velocity of the impact should be calculated first (Equation (3.12), then Stoke's number could be found

$$\mathbf{U_c} = 6x1.014(ms^{-1}) \times 2.12x10^{-4}\ (m)/\ 0.1(m) = 1.29\ x10^{-2}\ ms^{-1}$$

$\mathbf{S_{tv}}$ for HPMC 0.055 Pa·s:

$$= 4 \times 2504\ (kgm^{-3}) \times 1.29\ x10^{-2}\ (ms^{-1}) \times 2.12x10^{-4}\ (m)/\ 9 \times 0.055\ (Pa{\cdot}s) = 5.5\ x10^{-2}$$

Similarly: $S_{tv} = 1.7x10^{-2}$ for HPMC 0.177 Pa·s

$S_{tv} = 8.63\ x10^{-3}$ for HPMC 0.352 Pa·s and

$S_{tv} = 2.67x10^{-3}$ for HPMC 1.1385 Pa·s.

The Stokes number decreases as the viscosity increases, which means the higher viscosity system is more capable of absorbing the kinetic energy of the impact and countering the rebound.

3.4 Granulation Methods

A flowchart showing an overview of the experimental procedure is presented in Figure 3.19.

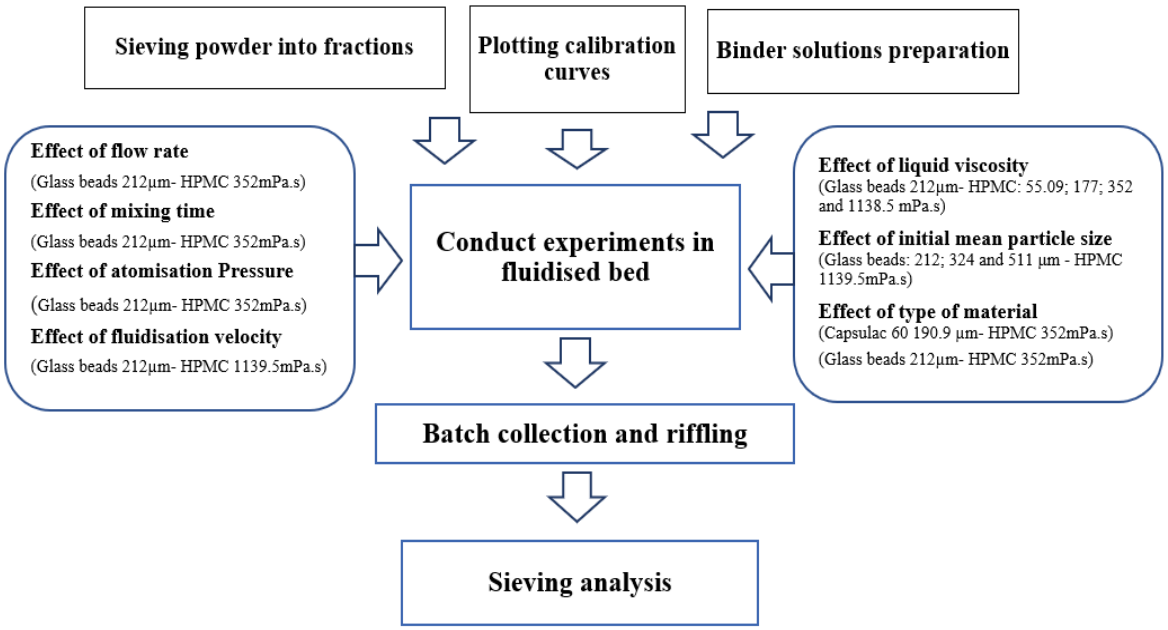

Figure 3.19: Flowchart showing an overview of the experimental procedure.

The general procedure was followed to perform experiments, plot the calibration curve and data analysis implementation method are explained in detail in the following sections. The calibration curve results are shown in Chapter 4, Section 4.4. Related results chapters provide more specific information about experimental conditions under the methods sections.

3.4.1 Liquid Pressure Calibration Curve

To identify the amount of liquid sprayed in each experiment, it was necessary to construct a calibration curve for every type of liquid binder to be used to set the precise liquid pressure for each experiment. This was important to ensure the same amount of liquid binder was delivered within 10 s spray period in each experiment under specific liquid and /or atomisation pressures used.

A range of liquid pressures was applied in an ascending order to avoid any loss or excessive pressure inside the tubes during the experiment. A table of liquid pressures used, and the corresponding mass of the liquid delivered in each condition within 10s was recorded. This was repeated three times, and the average of liquid masses was calculated. The calibration curves are given in Chapter 4, Section 4.7.1.

3.4.2 General Procedure for experimental work

A specially designed fluidised bed was used in this research and described in Chapter 4. Details of the methods for investigation of the effect of material and operational parameters are detailed in Section 3.5. However, a general fluidised bed experimental procedure was followed, and this is outlined as follows:

After the column was secured to its base, the required material quantity was placed in the column to achieve 100 mm depth. The material mass was calculated by Equations (3.15) and (3.16):

$$\text{Volume occupied } (m^3) = \text{Cross sectional area } (m^2) \times \text{column height h } (m) \qquad (3.15)$$

$$\text{Mass of material } (kg) = \text{volume occupied } (m^3) \times \text{bulk density } (kg/m^3) \qquad (3.16)$$

The liquid binder was placed inside a pressure pot, and the liquid pressure was set to the required pressure using the knob and the pressure dial on the top. The binder liquid was allowed to flow through the nozzle system in an external container to ensure it was ready to be sprayed at the same pressure. The nozzle system was inserted into the column, and the nozzle height was fixed at 15 cm from the top of the bed using a ruler fixed to the column wall. The pressure

gauge on the control panel was used to set the inlet air pressure at 3 bar, and a flowmeter was used to select the appropriate air volume to give the required fluidising velocity. The correspondent fluidising velocity was calculated as follows:

As the column's cross-sectional area is constant, changing the inlet air volume recorded by the flow meter as flow rate (L/min) will correspondingly change the superficial velocity (m/s). To find the volume of air per unit area, from that given by litre per minute for the whole bed surface, it was calculated by the Equation (3.17).

Where the fluidised bed column sectional surface area = 0.00636 m^2.

The experiment began by opening the inlet air to allow the bed of particles to be fluidised. Then the liquid and air tap on the spray system were opened simultaneously, allowing the nozzle to spray the liquid onto the fluidised bed. After 10 seconds, both valves were turned off, and the spray nozzle was immediately removed from the column to prevent any excess liquid from dripping. The particles continued to be fluidised for the desired mixing time, taking into

$$\text{Fluidisation Velocity}(m/s) = \left(\frac{\text{Air Flow Rate } (L/min)}{\text{Cross} - \text{Sectional Area } (m^2)}\right) = \left(\frac{0.001(m^3)}{60 * \text{pi}\, r^2(m^2)}\right) \qquad (3.17)$$

consideration the 10s of spray time. Then, the inlet air was turned off to stop fluidising the material. To collect the processed batch, the column was detached from the setup and the granulated material was poured gently into stainless trays and left to dry for two days at room temperature. The column and spray nozzle were cleaned and dried for the next experiment. The dried batches were subsequently riffled into two halves.

Sieve analysis was used to measure the size distribution of the granules. The Particle coating number φ_p was calculated for every system using the measured Sauter mean of the droplet size delivered under the specified liquid pressure. Primary particle and granule sizes were plotted against % frequency. The cumulative nuclei fraction was also plotted against nuclei size. Microscopy was used to examine the morphology of the granules.

3.5 Experimental variables.

In order to study the distribution nucleation in a fluidised bed, different interrelated factors need to be examined. They are categorised into material related parameters and process related parameters. Details about every experiment can be found in the method section in the results chapters, including the design of experiments and experimental conditions.

3.6 Data analysis

Sieve analysis was used to determine the size distribution of the granulated material in all experiments. Sieving is a simple, reliable method of size analysis. Particulate sample is subjected either to horizontal or vertical motions (horizontal circular sieving or throw-action sieving, respectively) on the sieve. According to the size of the individual particles, they either pass through the sieve mesh or are retained on the sieve surface. Dry sieving uses woven wire sieves of dimensions equal to the fourth root of two (e.g., 45, 53, 63, µm) (Rhodes, 2008). Sieve diameter is dependent on the particle dimensions, providing that its length does not detain it from the passage through the sieve apertures. Amplitude of the movement can be controlled digitally. Therefore, the quality of the sieved sample is dependent on the sieve movement parameters and the sieving time (Retsch, 2015).

The particle size distributions of the granulated material were analysed using a combinations of mana Retsch Sieve Shaker AS 200 Basic using throw-action sieving. A set of 23 different mesh size sieves were used in the analysis: from 150 µm to 8000 µm sieves. The material was sieved at 0.35mm or (mm/g) for 2 minutes duration.

The following sections explain the procedure to generate the results.

3.6.1 Sampling for sieving analysis

For the sampling of the dried material, the batch was split into two halves by a riffling method. This allowed only one half of the granulated material to be sieved.

Table 3.15: the sieve tray sizes used in the sieving.

Stack 1 (µm)	Stack 2 (µm)	Stack 3 (µm)	Stack 4 (µm)
8000	2800	850	300
6700	2360	710	250
5600	2000	600	212
4750	1700	500	180
4000	1180	425	150
3350	1000	355	0

To perform the sieving, a pre-weighed set of empty sieves is arranged in descending order, starting from 8000 µm mesh size at the top to 150 µm at the bottom. To keep the nuclei intact and avoid breakage, the series of sieve trays was divided into four stacks (Table 3.15), and the material was gently poured into the top sieve. It should be noted that in the 1000 µm sieve size and above, the material passed through the sieves without any mechanical agitation. The sample was passed through the sieve trays with slight manual movement until the 600 µm

sieve. The smaller sizes underwent mechanical sieving using a AS 200 basic Retch Sieve Shaker for two intervals of 1 minute each and at 0.35 mm amplitude. The sieves were removed from the shaker; each sieve was separately weighed again with the granules inside. The particulate mass held by each sieve was calculated by subtracting mass of empty sieves from those with material inside.

3.6.2 Size distribution analysis

3.6.2.1 Frequency of size distribution

The *Un-normalized* frequency distribution, *dx n(x),* is defined as the number of *particles n(x)* between size *x* and (*x* + *dx*). The *Normalised* frequency *fi.*Δ*x,* is the number of *fractions* per unit control volume in all size intervals (Litster, 2016b). To process the data and plot a normalised frequency distribution *fx.dx,* an Excel spreadsheet was used (Figure 3.20), and it represents most experiments where the material of fraction size (150-250 µm) and the sieves used for PSD analysis are from 0.15 to 8 mm aperture size. Except for the initial size experiment, the differences will be mentioned accordingly under the primary size experiment method described in Section 5.2.2

To process the data and plot the size distribution graph, Figure 3.20 shows a screenshot of the Excel spreadsheet for sieving analysis, and the following steps are followed.

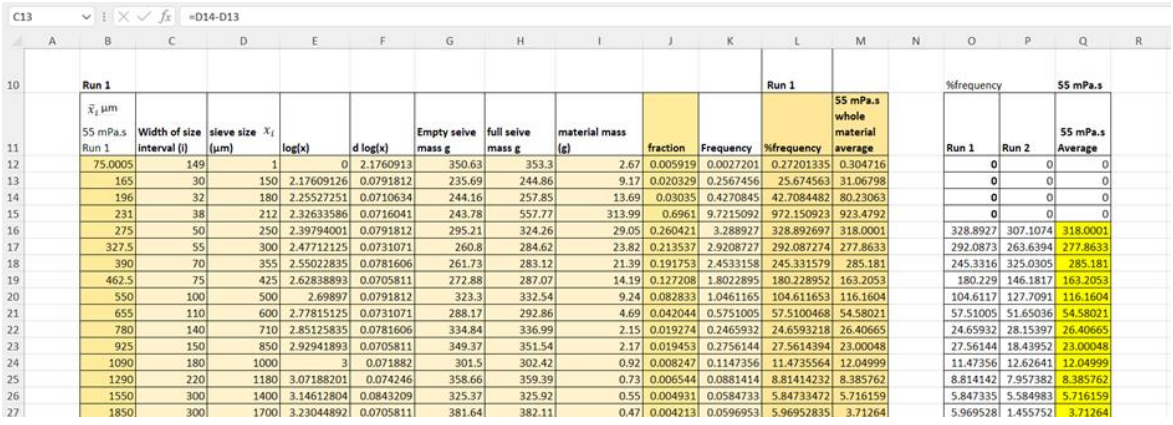

C13 =D14-D13

	B	C	D	E	F	G	H	I	J	K	L	M	O	P	Q
10	Run 1										Run 1		%frequency		55 mPa.s
11	$\bar{x}_i$ µm 55 mPa.s Run 1	Width of size interval (i)	sieve size x_i (µm)	log(x)	d log(x)	Empty seive mass g	full seive mass g	material mass (g)	fraction	Frequency	%frequency	55 mPa.s whole material average	Run 1	Run 2	55 mPa.s Average
12	75.0005	149	1	0	2.1760913	350.63	353.3	2.67	0.005919	0.0027201	0.27201335	0.304716	0	0	0
13	165	30	150	2.17609126	0.0791812	235.69	244.86	9.17	0.020329	0.2567456	25.674563	31.06798	0	0	0
14	196	32	180	2.25527251	0.0710634	244.16	257.85	13.69	0.03035	0.4270845	42.7084482	80.23063	0	0	0
15	231	38	212	2.32633586	0.0716041	243.78	557.77	313.99	0.6961	9.7215092	972.150923	923.4792	0	0	0
16	275	50	250	2.39794001	0.0791812	295.21	324.26	29.05	0.260421	3.288927	328.892697	318.0001	328.8927	307.1074	318.0001
17	327.5	55	300	2.47712125	0.0731071	260.8	284.62	23.82	0.213537	2.9208727	292.087274	277.8633	292.0873	263.6394	277.8633
18	390	70	355	2.55022835	0.0781606	261.73	283.12	21.39	0.191753	2.4533158	245.331579	285.181	245.3316	325.0305	285.181
19	462.5	75	425	2.62838893	0.0705811	272.88	287.07	14.19	0.127208	1.8022895	180.228952	163.2053	180.229	146.1817	163.2053
20	550	100	500	2.69897	0.0791812	323.3	332.54	9.24	0.082833	1.0461165	104.611653	116.1604	104.6117	127.7091	116.1604
21	655	110	600	2.77815125	0.0731071	288.17	292.86	4.69	0.042044	0.5751005	57.5100468	54.58021	57.51005	51.65036	54.58021
22	780	140	710	2.85125835	0.0781606	334.84	336.99	2.15	0.019274	0.2465932	24.6593218	26.40665	24.65932	28.15397	26.40665
23	925	150	850	2.92941893	0.0705811	349.37	351.54	2.17	0.019453	0.2756144	27.5614394	23.00048	27.56144	18.43952	23.00048
24	1090	180	1000	3	0.071882	301.5	302.42	0.92	0.008247	0.1147356	11.4735564	12.04999	11.47356	12.62641	12.04999
25	1290	220	1180	3.07188201	0.074246	358.66	359.39	0.73	0.006544	0.0881414	8.81414232	8.385762	8.814142	7.957382	8.385762
26	1550	300	1400	3.14612804	0.0843209	325.37	325.92	0.55	0.004931	0.0584733	5.84733472	5.716159	5.847335	5.584983	5.716159
27	1850	300	1700	3.23044892	0.0705811	381.64	382.11	0.47	0.004213	0.0596953	5.96952835	3.71264	5.969528	1.455752	3.71264

Figure 3.20: A screenshot of an Excel spreadsheet for the size distribution analysis.

In a column, the stacks' sieve sizes are outlined in ascending order (D column). This data is divided into sections (intervals). The width of each interval is obtained by subtracting the smaller sieve size from the upper sieve size (column C) $\Delta x_i = x_i - x_{i_{-1}}$.

1. The mean size of the interval $\bar{x}_i$ µm is obtained by finding the mean size of each two subsequent sieve sizes (column B), $\bar{x}_i = (x_i + x_{i+1})/2$. This would be the midpoint used on the particle size graph.

2. The weight of each sieve with the material retained is separately recorded. The granule mass retained by each sieve is then obtained by subtracting the empty sieve mass (column G) from the same full sieve mass (m*i*) (column H).

3. The total mass of the material retained by all sieve sizes is obtained by $\sum_{i=0}^{n} mi$ (summation of I column). The sieve sizes used for most experiments are from 0.15 to 8 mm. This material includes ungranulated and granulated materials.

4. The total mass of the ungranulated material, i.e. the primary particles, held by the sieve of sizes less than 212 µm. was obtained by = $\sum_{i=0}^{i=\bar{x}_{3,2}} mi$, (summation of cells 11-15 in I column).

5. The total mass of granulated material can be found by $\sum_{i=\bar{x}_{3,2+\Delta x}}^{n} mi$ (summation of granule mass retained by sieves larger than 212 µm size in column I).

6. The % granulated fraction is given by= $\frac{\sum_{i=\bar{x}_{3,2+\Delta x}}^{n} mi}{\sum_{i=0}^{n} mi}\ 100$.

7. The granulated fraction obtained by distribution nucleation is relatively low, $\leq 30\%$ in most experiments. Therefore, more explicit semi-logarithmic graphs of normalised frequency distribution were created that clarify minor changes within the small granulated fraction. The logarithm of the sieve size $\log x_i$ was used instead of the sieve size x_i for each interval (column E). Δx_i is substituted by $\Delta \log x$ (column F), which is the change in the logarithm among two adjacent sieve sizes (interval size) where: $\Delta \log x_i = log x_{i+1} - log x_i$.

8. The fractions of primary particle sizes i.e. of sizes within the ungranulated material $fi \leq \bar{x}_{3,2}$ is divided by the *total material* mass $\sum_{i=0}^{i=n} mi$ (column J until cell15).

9. The fraction of every granule size interval fi whereas $i > \bar{x}_{3,2}$, is obtained by dividing the mass of the granules retained in this interval, m_i, by the total granule mass = $\frac{i}{\sum_{i=\bar{x}_{3,2+\Delta x}}^{n} mi}$ (column J cell 16 and after). The only exception was in the primary

particle size Experiment where the fraction was obtained by dividing the mass of the granules retained in each interval by the total material mass.

10. The percentage frequency $f(x)$ (column J) is then taken by dividing the fraction fi, for every sieve size by the change in the logarithm of the size $\Delta \log x_i$ (column K), then multiplied by one hundred (column L).

11. For the *granule size distribution graph*, particles less than the specific surface mean size of the powder $\leq \bar{x}_{3,2}$ are omitted, the frequency starts from zero. The number repeats are outlined, and the average was taken.

12. From the data processed, a semi-logarithmic frequency distribution curve is plotted with the arithmetic X-axis being the percent *f*(x) μm^{-1}, against the midpoint of every size interval $\bar{x}_i$ µm, as a logarithmic scale i.e *f*(x) vs $\bar{x}_i$.

13. The number fractions of granules in all size intervals are integrated as the area under the curve.

14. All particle sizes are also included in Appendices 5 and 6 to show *the whole material frequency graph*, where two distinct regions are clearly shown in the diagram for both the ungranulated primary particles and the granules. In the result sections, only granulated fractions will be represented in the size distribution graphs.

3.6.2.2 Cumulative size Distribution

These distributions are useful for calculating the parameters d_{10}, d_{50}, and d_{90}. The cumulative distribution, N(x), is the number of particles per unit control volume less than size x (dimensions of L^{-3}) (Litster, 2016a). The normalised (continuous) cumulative distribution *Fi* is the number of fractions of granules in all size intervals less than and including particle size *i*.

10						Run 1	
11	Empty seive mass g	full seive mass g	material mass (g)	fraction	Frequency	%frequency	55 mPa.s whole material average
12	350.63	353.3	2.67	0.005919	0.0027201	0.27201335	0.304716
13	235.69	244.86	9.17	0.020329	0.2567456	25.674563	31.06798
14	244.16	257.85	13.69	0.03035	0.4270845	42.7084482	80.23063
15	243.78	557.77	313.99	0.6961	9.7215092	972.150923	923.4792
16	295.21	324.26	29.05	=I16/I38		328.892697	318.0001
17	260.8	284.62	23.82	0.213537	2.9208727	292.087274	277.8633
18	261.73	283.12	21.39	0.191753	2.4533158	245.331579	285.181

%frequency		55 mPa.s
Run 1	Run 2	55 mPa.s Average
0	0	0
0	0	0
0	0	0
0	0	0
328.8927	307.1074	318.0001
292.0873	263.6394	277.8633
245.3316	325.0305	285.181

sieve size um	e granules fraction	granules fraction	55 mPa.s
	Run 1	Run 2	55 mPa.s Average
0	0	0	
150	0	0	
180	0	0	0
212	0	0	0
250	0.260421	0.243171504	0.251796
300	0.473958	0.435910609	0.454934
355	0.66571	0.689956332	0.677833

Figure 3.21: A screenshot of an Excel spreadsheet for THE cumulative distribution graph analysis.

To process the data and plot the cumulative distribution graph in the Excel spreadsheet (Figure 3.21):

1. The fraction fi is obtained by dividing the mass held by each sieve mi by the total *granulated* mass $\sum_{i=\bar{x}_{3,2+\Delta x}}^{n} mi$.

2. This fraction is plotted against the maximum size of the size interval Fi vs xi. For example, if the sieve sizes interval is between 250 and 300 µm, the fraction is plotted against 300 µm in arithmetic scales.

3. In the cumulative distribution, three parameters were specified (d_{10}, d_{50} and d_{90}). Litster (2016) defined these parameters as $F(x_a) = \frac{a}{100}$, x_a is the passing size at which a% of the particles are smaller than this size.

4. So $d_{50,}$ which is the median, is the 50% passing size $F(x_{50}) = 0.5$, i.e., before which 50% of the granulated material is passed.

5. The parameters d_{10}, d_{50} and d_{90} were specified from the plotted cumulative distribution graphs.

3.6.2.3 Bias in the results

Agglomeration during tray drying can introduce bias in the results for granulated fraction, as well as the mean d50 and d90 nuclei sizes. This bias misrepresents the outcome, as it does not accurately reflect the true agglomeration process. In this study, aqueous polymer solutions were used as binders with short processing times (mostly one minute), and the model particles were nonporous glass beads. Excessive moisture can cause particles to adhere to one another, forming loose clusters that may be incorrectly counted as granules instead of individual particles. During drying, the material often became chunky, though it loosened easily during handling and sieving. However, when low-viscosity binders were used, small agglomerates were more difficult to sieve. This unwanted enlargement of particle size could have inflated the % granulated, thereby skewing the size distribution, with d50 and d90 values appearing larger than they actually are. This observation is referenced in the results section wherever relevant. Nevertheless, most experiments were conducted with moderate to high-viscosity binders, which accelerated drying and mitigated these issues.

3.7 Summary

In this chapter, the materials have been described and characterised. The method of granulation in a fluidised bed has been presented. Methods for product analysis, have been described. A lab scale fluidised bed was specifically designed and manufactured at the University of Sheffield to conduct this study. The details of the design and its implementation are presented in the following chapter.

Chapter 4: Fluidised bed design and commissioning

4.1 Introduction

The most widely used fluidised bed design in industry-fluidised granulation is that of a Glatt design, which employs a cone over the spray zone to increase particle circulation. In addition, most columns are topped by a conical freeboard. However, some researchers have used small cylindrical fluidised beds for lab scale studies. Their advantage is to minimise material consumption. They still provide a sufficient cross-sectional area to avoid overspray, as very narrow beds packed with certain materials could undergo slugging under very high velocities. Waldie (1991) used a 50 mm diameter glass-walled cylinder fitted with a sintered distributor. Smith (1983) used a 0.15 m diameter glass-walled cylinder equipped with a porous plate air distributor, and Patnaik (2010) used a 0.16 m glass-walled cylinder with a steel distributor plate punched in 29 holes (Waldie, 1991, Smith and Nienow, 1983, Patnaik et al., 2010).

The experimental investigations in this research have been performed using a small fluidised bed system. The fluidised bed was designed and manufactured in-house at the University of Sheffield. The design of this fluidised bed will be given in the following section.

4.2 The experimental setup:

The whole assembly used is shown in Figure 4.1. The fluidised bed was connected to a pressure pot to create enough pressure to deliver liquid through the spray nozzle.

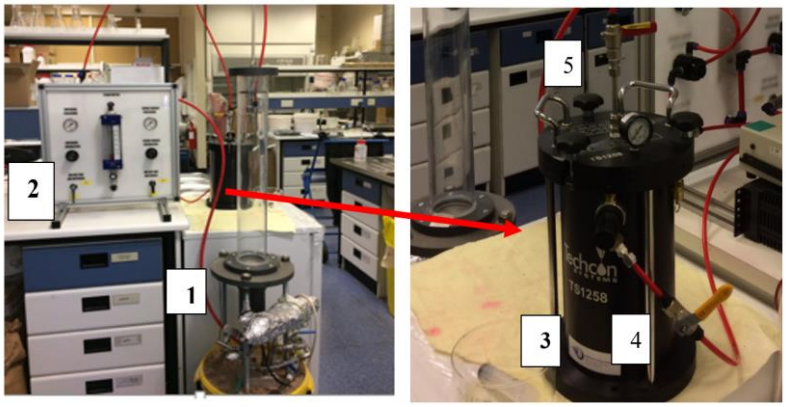

Figure 4.1: The experimental set up consisting of a small scale fluidised bed (1), A control panel (2) and a pressure pot (3) The air inlet to the pressure pot (4) pressurised liquid metallic tube (5).

A schematic diagram for the design of experimental set up components is presented in Figure 4.2. Further details of the design and experimental set up are provided in the following sections.

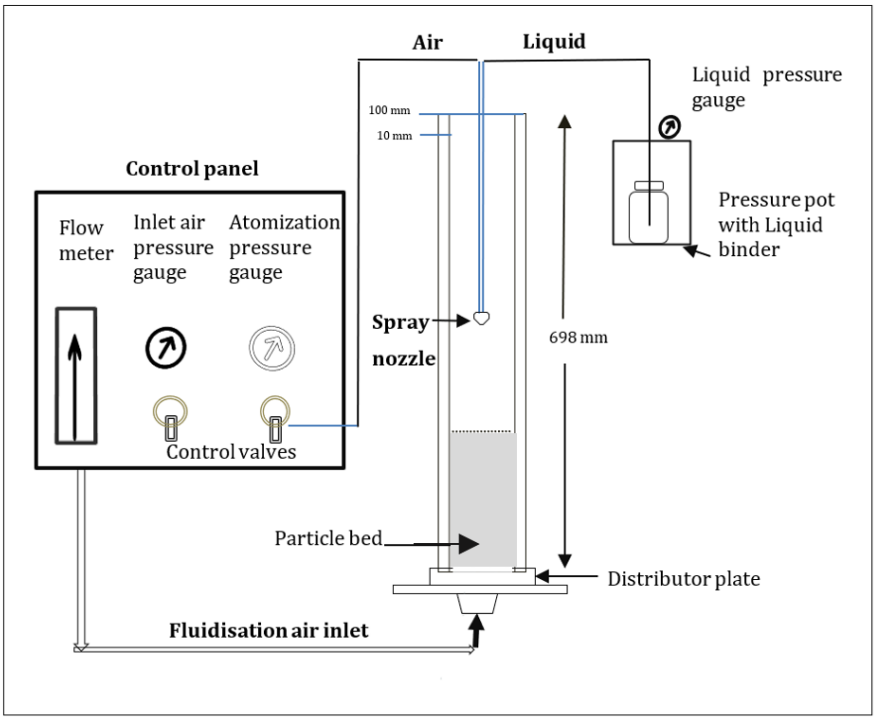

Figure 4.2: Schematic diagram for the experimental design set up.

Figure 4.3 shows the composition of the experimental set up. The fluidised bed tube (A) was an acrylic walled cylinder with an internal diameter of 0.09 m, external diameter of 0.1 m and 0.698 m in length, this had a 4.440 litre capacity.

The spray nozel was fitted to a mobile system so its height could be adjusted. This device was composed of a top plate cover with one central opening (B), along with an inner spacer with two openings; one holding a metallic tube for pressurised air and the other holding a plastic tube (Legris 8X6 Advanced Polyamide Calibre) with a 6.35 mm internal diameter, for liquid binder (C). The two tubes were joined together inside a binary nozzle spray, making the nozzle opening centralized (D). The liquid binder was placed inside the pot chamber. A feed stainless steel tube attached to the pressure pot lid was dipped into the liquid. This was fitted to the plastic tube attached to the nozzle in the mobile system.

The fluidised bed cylinder was placed over a conical steel chamber of the same diameter to supply the compressed air and to support the distributor plate at the base of the cylinder. A steel flange supports the whole structure (E). The set up was connected to a control panel that

controls the pressure of the supplied air and measures the volume of the air before the inlet by two rotameter systems: one of 1000 L/min and a smaller one of 100 L/min.

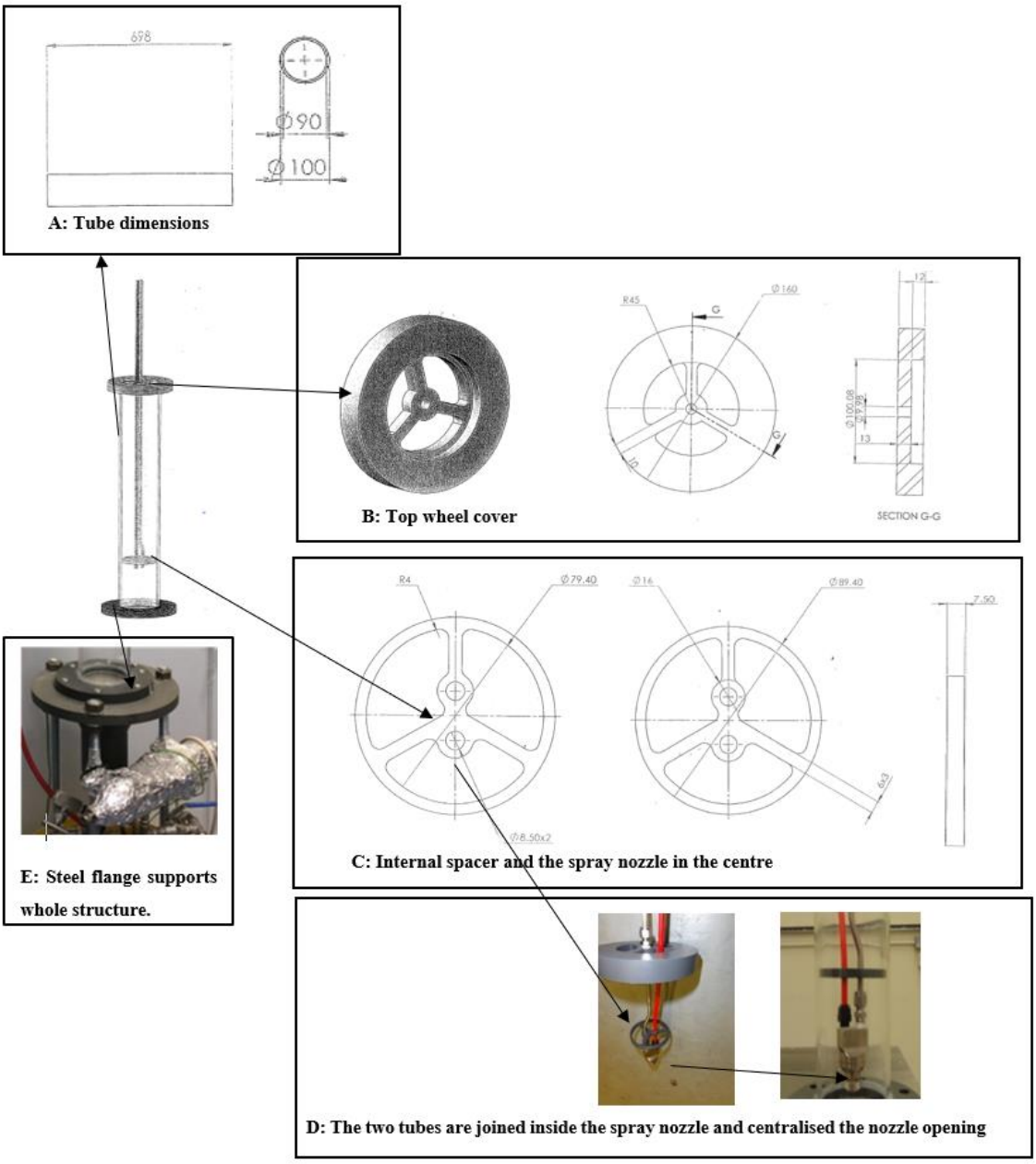

Figure 4.3: The fluidised bed set up and its components.

The pressure pot (TS1258, Adhesive Dispensing Ltd), with a capacity of up to 7 bar, is shown in Figure 4.1(4). To pressurise the liquid binder, the main air tap supplied the air via a tube (Legris 8X6 Advanced Polyamide Calibre) attached to the pot body-side and managed by a valve. The pressurised liquid leaves the pot through a metallic tube connected to another Polyamide Calibre tube and managed by a valve, as can be seen in Figure 4.1(5) before it is mixed with liquid inside the nozzle chamber (C).

4.3 Nozzle characteristics

A spray nozzle is a device that is used to atomize a liquid into fine droplets. In granulation, a spray nozzle is typically used to apply a binder solution to a powder mixture in order to form granules. The spray nozzle can be adjusted to control the size and distribution of the droplets, which can affect the properties of the final granules. Spray nozzles differ in their design, shapes and features according to the intended use. The main spray characteristics include spray pattern, orifice dimensions, spray angle and drop size. Nozzles range from standard nozzles to air atomising nozzles.

Finding a suitable nozzle is essential for a successful granulation process of particular objectives. In this research, very fine droplets are required. Therefore, the criterion for selecting a nozzle is a pneumatic nozzle with a small orifice and narrow angle. The air will help shred the liquid binder to the finest droplets possible. Also, it should be of a full cone spray pattern type with a small spray angle to cover the spray zone inside the bed without wetting the column wall. Air atomizing droplets are emitted as a fine mist which is formed by mixing liquid and air. Figure 4.4 shows a full cone spray pattern where the droplets are emitted in a cone shape.

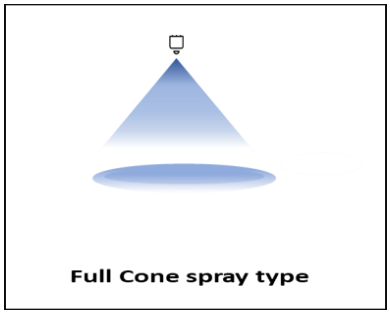

Figure 4.4: schematic diagram for full cone spray patterns.

The fluidised bed was equipped with a binary nozzle; a two fluid mixing nozzle (Spray System, PA64, PF1650), as shown in Figure 4.5. Air atomizing produced a full cone as a result of the atomisation of liquid by compressed air, and the internal mix impingement air atomisation produced very fine droplets. Figure 4.5 shows a schematic diagram for the spray nozzle system employed in this work; the fluid cap 1650 and an air cap 64 with an 0.064 orifice diameter.

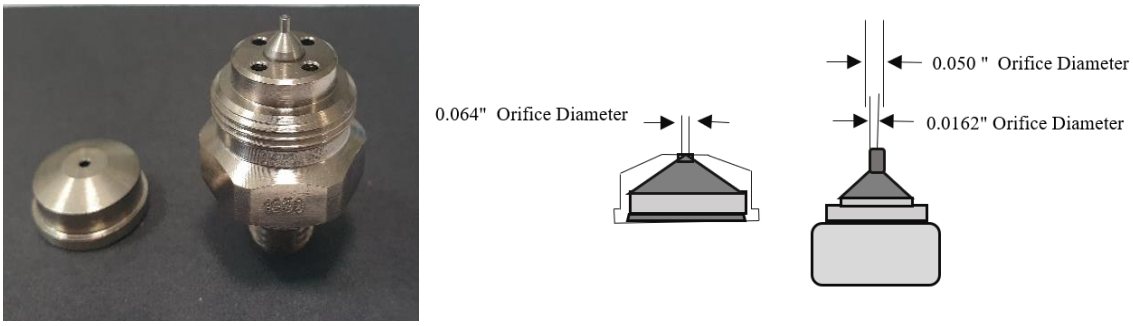

Figure 4.5: A photo and a schematic diagram for the binary spray nozzle from Spray system®.

Figure 4.6 shows the spray nozzle characteristics provided by the Spraying system®. The spray nozzle at 20 cm height gives a full cone siphon with a round coverage area with a spray angle of 18◦ (A). This spray pattern is maintained throughout a distance of 28-36 cm (B). Beyond this distance, it becomes turbulent (C). The gravity head at 15 cm with 3 and 4 bars pressure delivered 1.7 and 1.8 litters /hour, respectively (Spraying system.,2017). The nozzle height applied in this study is within the established limit at 15 cm from the bed's surface and 25 cm from the air distributor.

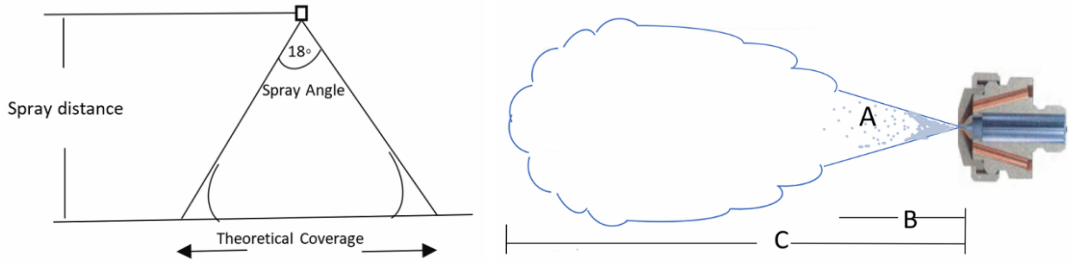

Figure 4.6: The main spray nozzle characteristics: orifice diameter 0.064◦, gives round spray angle 18◦ (A) maintained to 28-36 cm (B), then the spray pattern becomes turbulent (C).

4.4 Gas distributor plate

The ultimate purpose of using a gas distributor plate is to provide uniform distribution for the fluidising gas and to support the material inside the bed. A wide range of distributors is available for use, from simple fibre cloth (Zhai et al., 2009) or compacted wires (Kunii and Levenspiel, 1991) to particular purpose distributors (Saxena et al., 1979, Geldart and Baeyens, 1985). Most available plates are of 4 –30% open area (Parikh and Mogavero, 2005). The most important factor for designing an efficient plate is obtaining a sufficient pressure drop across the plate. The distributor plate used in this study is shown in Figure 4.6, and it was composed of a circular perforated metallic plate of 0.9 m diameter and of (1.0 mm) orifice diameter beside a fibre cloth underneath.

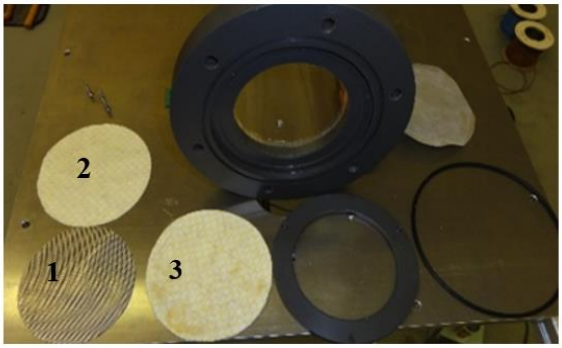

Figure 4.6: The disassembled distributor plate used in the study consisted of a perforated metallic plate (1) and a fibre cloth underneath (2, 3).

4.5 Gas supply and piping

The gas used was dry compressed air supplied to the laboratory via a bench tap. A gauge was used to control the air pressure. The compressed air was controlled by a 1000 L/min rotameter and conveyed to the instrument via flexed plastic tubing.

4.6 Spray pattern

The spray pattern refers to the shape and distribution of the droplets that are emitted from a spray nozzle. It is determined by the design of the nozzle and the operating conditions. The spray pattern, which is the spray's area distribution, can be adjusted by nozzle parameters such as the nozzle design, height, or atomisation pressure. The liquid properties, such as viscosity or the pressure of the liquid, can also affect the spray area distribution. The desired spray pattern depends on the specific application and the desired outcome. In granulation, a spray pattern that is consistent and uniform can help ensure that the binder solution is evenly distributed and that the granules formed have the desired properties. (Börner et al., 2014) investigated the spray zone boundaries for a two-fluid nozzle in top-spray mode as a function of the nozzle position and atomisation pressure. Also (Tafreshi et al., 2002) studied the air to liquid mass ratio (ALR) and used it to optimise the dispersion of the spray.

To ensure uniform liquid dispersion during the granulation process, the spray nozzle should distribute the liquid evenly throughout the particle bed within the spray zone. Thus, prior to experimental work, the spray system pattern characterisation was needed.

The experiment was performed using the pneumatic nozzle spray system 1650, 64 to assess the liquid binder mass that was sprayed during the spray time throughout the spray zone. Due to the cylindrical shape of the set up column, the best way to determine the liquid mass per unit

area distributed across the sectional area of the spray zone is to investigate the liquid binder mass by unit area in a square with a diagonal of the same column diameter. However, as Figure 4.7 shows, the circle area couldn't be totally covered by the liquid. The liquid was collected across the spray centre line, and it was assumed to be an axisymmetric spray pattern.

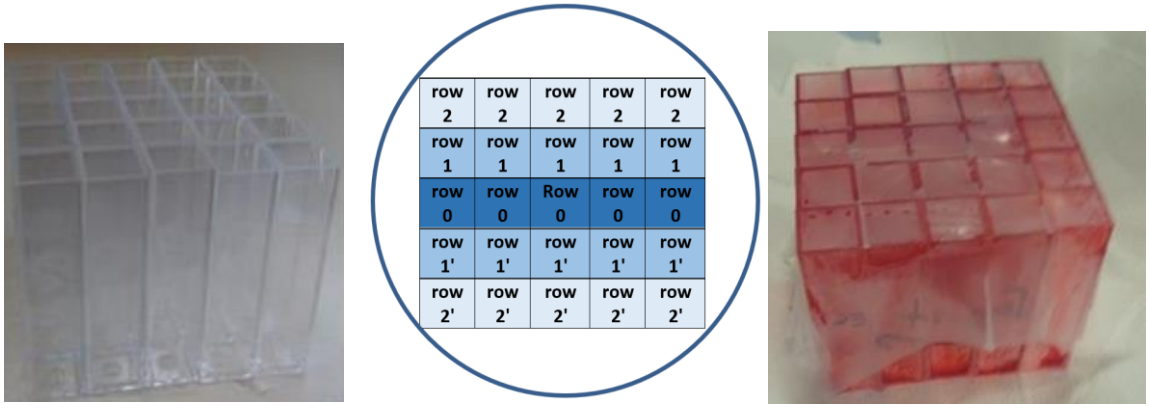

Figure 4.7: An array of 5 x 5 cuvettes was used to collect the 352 mPa·s HPMC liquid from the sprayed nozzle across the spray centre line.

Pre-weighed individual plastic cuvettes of 1 cm length, 1 cm width, and 4.5 cm height with 0.01 cm wall thickness (4.5 ml volume) were tied together by means of plastic adhesive tap to form 5*5 rows matrix of 7.07 cm diagonal (Figure 4.7) and were placed at the bottom of the fluidised bed. The spray nozzle was mounted at 25 cm height from the distributor plate, which is the height used in the experiments. The liquid binder, 10% HPMC 606 solution of 352 mPa·s viscosity, was sprayed for ten seconds, the same spray time used in the experiments. When the spray stopped, the cuvettes were taken out immediately and covered with parafilm to prevent liquid evaporation until they were weighed. The mass transversal volumetric distributions collected within 10 seconds were determined by using a precision balance. Every experiment was repeated three times, and the average mass was taken.

The factors investigated were pneumatic pressure, liquid pressure and liquid viscosity. Graphs were plotted using the distance from the centre for each row against the liquid mass.

4.6.1 The effect of atomisation pressure on the spray pattern:

In this study, HPMC 352 mPa·s was used at a spray rate of 1.31 g/s and 3, 4 and 5 bar atomisation pressure. The liquid mass collected was plotted against the distance and is presented in Figure 4.8.

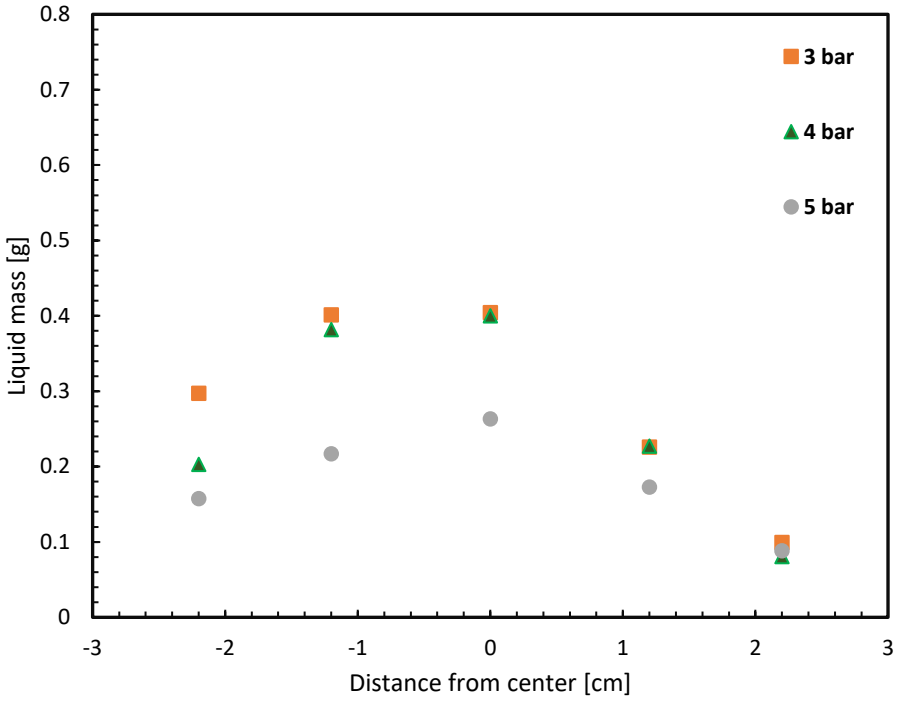

Figure 4.8: HPMC 352 mPa·s liquid mass collected at the centre line (Row 0) for the spray rate 1.31 gs^{-1} at 3, 4 and 5 bar atomisation pressures.

Figure 4.9 shows the different spray distributions for HPMC 352 mPa·s at a constant spray rate. Increasing the atomisation pressure decreased the liquid mass reaching the middle line (Figure 4.8) because it widened the total spray area covered with the liquid (Figure 4.9).

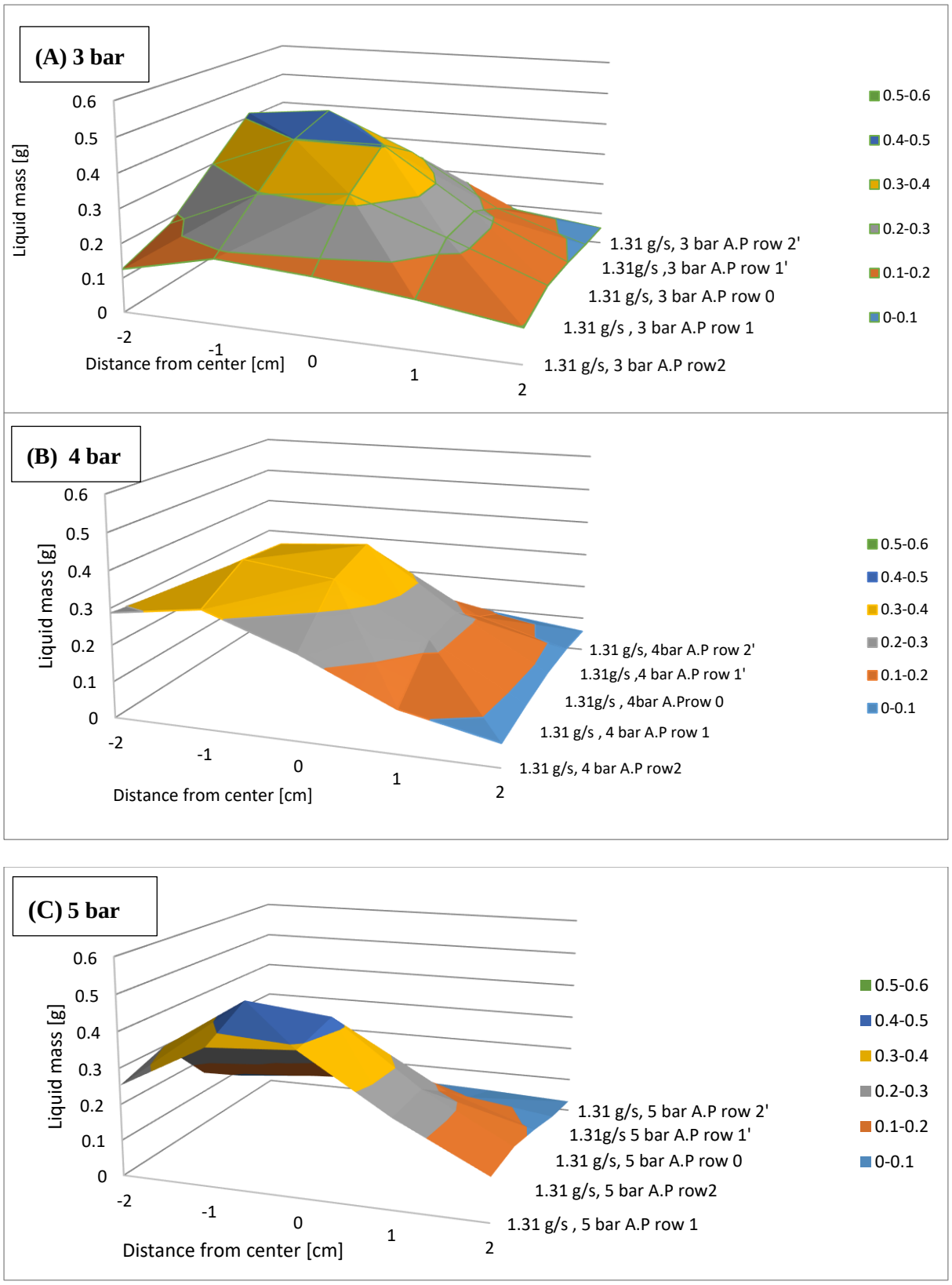

Figure 4.9: The effect of atomisation pressure on the spray pattern. Different spray distributions for 1.31 gs-1 of HPMC 352 mPa·s delivered by the two-phase nozzle spray system at different atomisation pressures A, B and C for 3, 4 and 5 atomisation pressure, respectively.

4.6.2 The effect of liquid pressure on the spray pattern

HPMC 352 mPa·s solution was sprayed at three liquid pressures: 1, 2 and 3 bar to have flow rates of 0.28, 1.31 and 2.31 gs-1, respectively. The liquid mass collected by the cuvettes was plotted against the distance and shown in Figure 4.10 and Figure 4.11.

Figure 4.10 also reveals a significant increase in HPMC 352 mPa·s liquid mass collected at the centre line of the array as the spray rate increased from 0.28 to 1.31 and 2.31gs^{-1}. However, the HPMC liquid spray pattern revealed wider dispersion towards the left side of the spray zone.

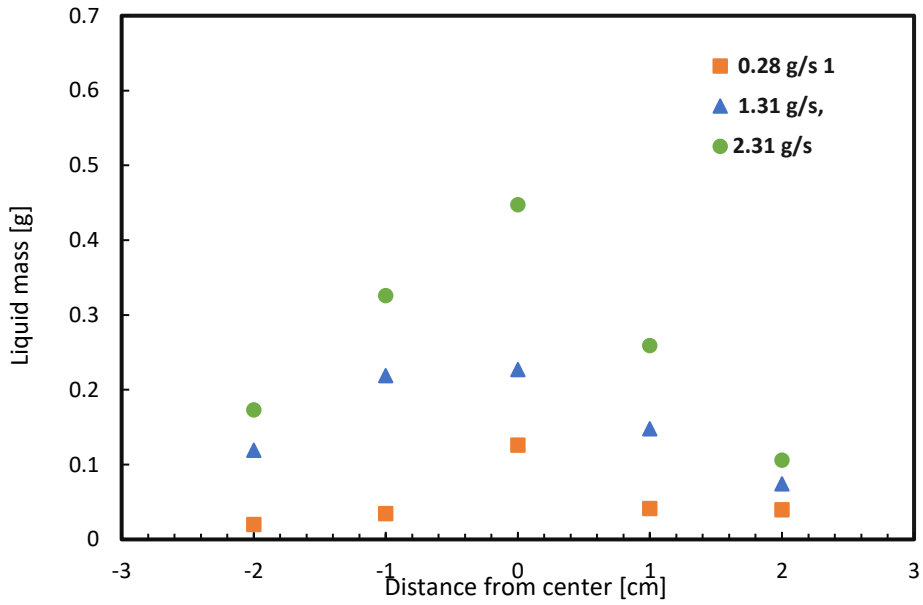

Figure 4.10: The effect of liquid flow rate on the spray pattern. Liquid mass collected from the centre line of cuvettes array for HPMC 352 mPa·s solution sprayed at flow rates of 0.28 1.31 and 2.31 gs^{-1}.

Figure 4.11 shows that altering the liquid binder spray rate with the same atomisation pressure gave better spray dispersion and increased coverage area.

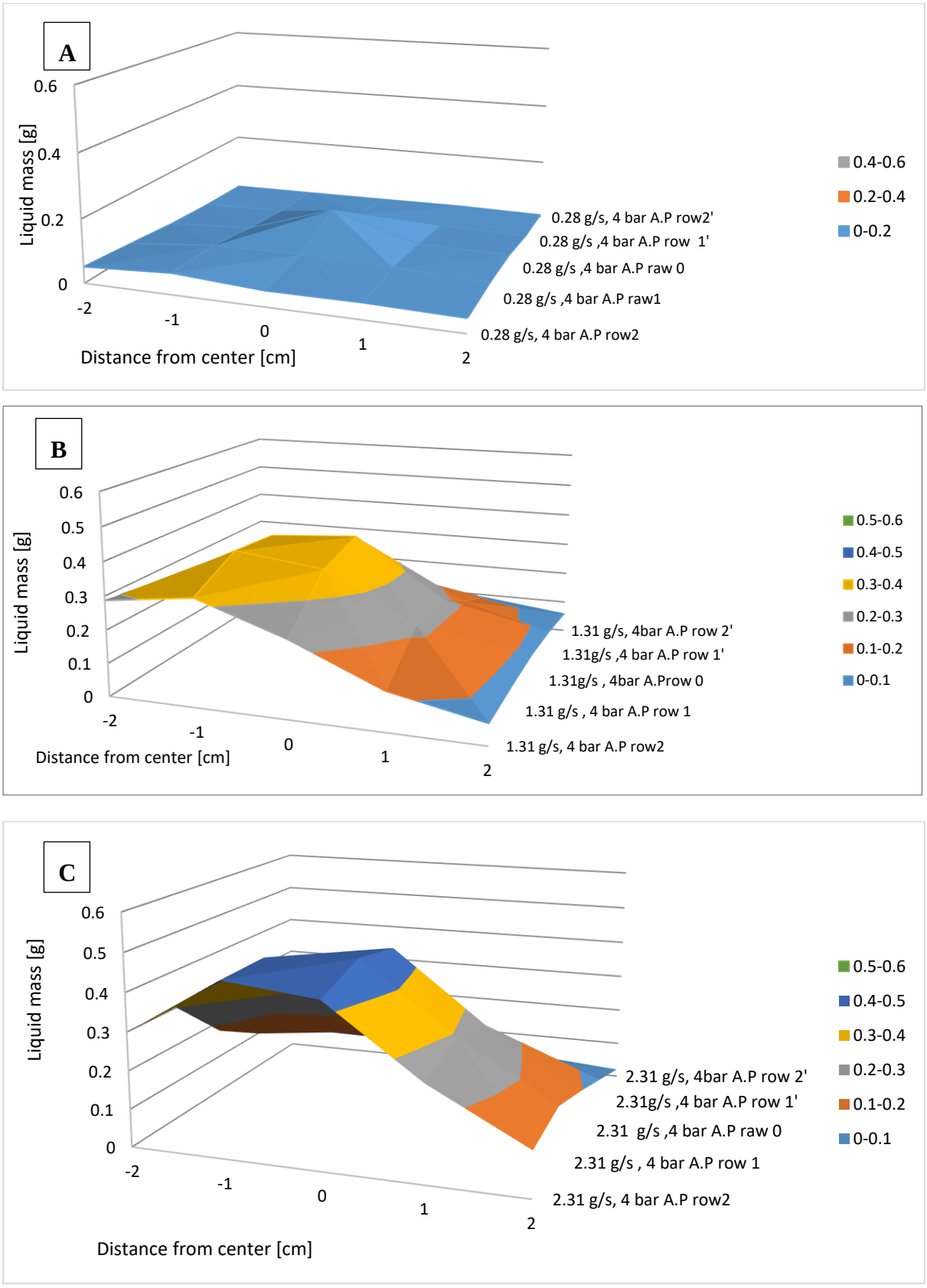

Figure 4.11: The effect of liquid pressure (flow rate) on the spray pattern. Coverage area and spray dispersion were obtained at 0.28 gs^{1} (A), 1.31 gs^{1} (B) and 2.31 gs^{1} (C) HPMC 352 mPa·s spray rate.

4.6.3 The effect of viscosity on the spray pattern

To investigate the effect of liquid viscosity, two molecular weights of polyethene glycol, PEG 4000 and PEG 10,000, were used in a 40 wt % aqueous solution. These solutions were used in the research trials, fluid bed commissioning and characterisation of the nozzle behaviour used in the study. This experiment, which shows the effect of viscosity on the spray pattern, couldn't be repeated using the HPMC systems. The solutions for PEG 4000 and PEG 10,000 gave viscosities of 53.7 mPa·s and 251.47 mPa ·s, respectively. Spray pattern analysis is shown in Figure 4.12.

0.5 g/s of 40 wt % PEG 4000 and 40 wt % PEG10,000 solutions were sprayed at 1, 2 and 3 bar atomisation pressure and the equivalent liquid pressures. The viscosity of the PEGs and the conditions used in the characterisation are shown in Table 4.1.

Table 4.1: PEG polymer solution concentrations and viscosities with atomisation and equivalent liquid pressure.

0.5 g/s of 40 % PEG 4000		**0.5 g/s of 40 % PEG 10,000**	
Viscosity 53.75 mPa·s		Viscosity 251.47 mPa·s	
Atomisation pressure (bar)	Liquid pressure (bar)	Atomisation pressure (bar)	Liquid pressure (bar)
1	0.42	1	2.6
2	0.31	2	2.44
3	0.52	3	2.38

The graphs in Figure 4.12 show that the spray cone of 0.5 g/s sprayed of the two solutions was affected by viscosity. The PEG 53.7 mPa·s solution was affected by the atomisation pressure, and the cone widened as the atomisation pressure increased. Higher viscosity PEG 251.47 mPa·s showed the same behaviour. However, the spray cone was wide at the lower atomisation pressure of 1 bar. This is because the higher liquid pressure applied to the higher viscosity PEG 251.47mPa·s to obtain the same liquid rate can also affect its spray dispersion and increase its coverage area.

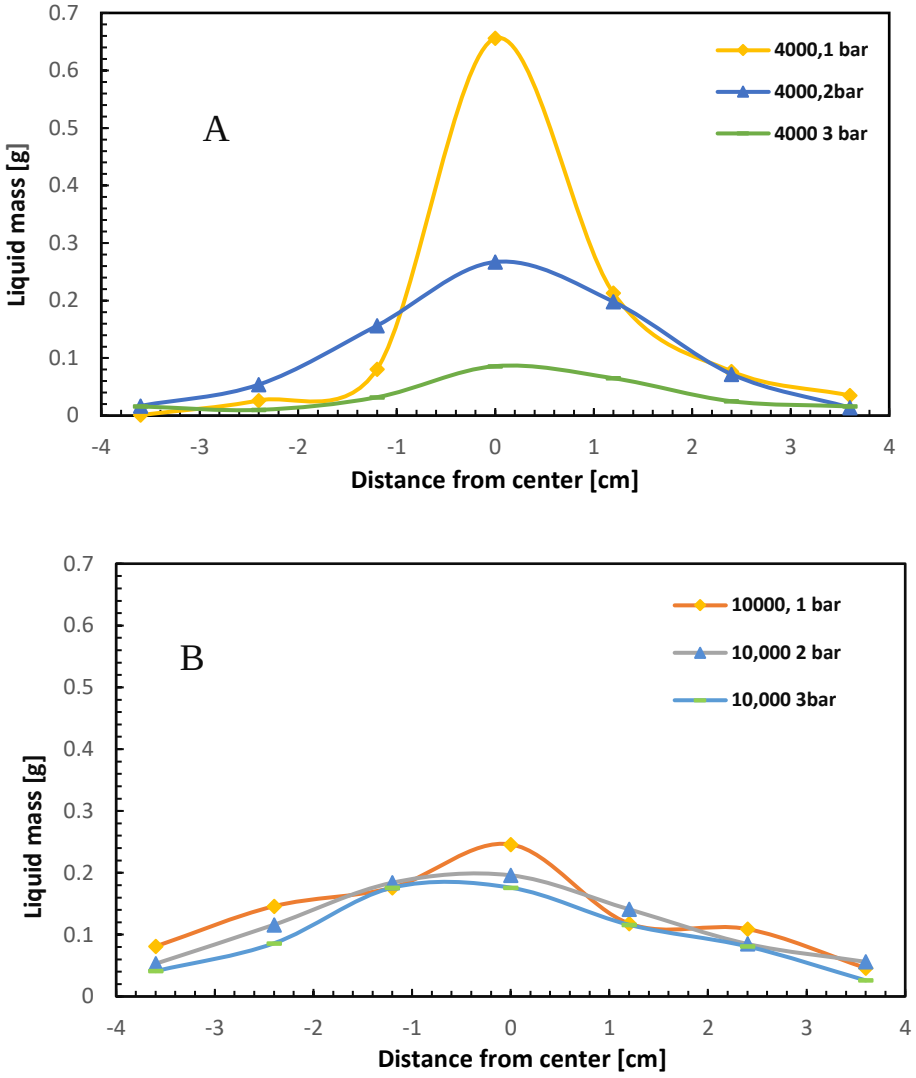

Figure 4.12: The effect of liquid viscosity on the spray pattern. Liquid mass collected from the X axis for 0.5 gs^{-1} of PEG 4000 53.7 mPa·s solution and 0.5 gs^{-1} of PEG10,000 251.47mPa·s collected at equivalent liquid pressures and 1, 2 and 3 bar atomisation pressure.

4.7 Calibration of liquid mass delivered by the spray nozzle system

As mentioned in Chapter 3, a calibration curve was needed to identify the liquid mass to be delivered by the top spraying system built in-house as a function of liquid pressure. This amount could be affected by the type of liquid and the atomisation pressure used. Therefore, three calibration curves were constructed. The first one was to relate the liquid pressure with liquid mass delivered by unit time for the main liquid binder used in the study, HPMC 352 mPa·s. The second curve was to relate the viscosity of the liquid binders used in the effect of the viscosity experiment with the obtained flow rate by changing the liquid pressure. The third

one was to show the effect of atomisation pressure on the liquid flow rate of the same liquid binder prior to the atomisation pressure experiment.

4.7.1 Liquid pressure calibration curve

As was mentioned in Chapter 3. Section 3.4.1, at constant 4 bar atomisation pressure, to calculate the liquid masses of HPMC 352 mPa·s that the spray nozzle delivers by applying different liquid pressures, the liquid pressure was gradually increased using the pressure gauge on the pressure pot to avoid any loss or excessive build-up of the pressure inside the tubes. The corresponding mass of the liquid delivered within 10 s by the spray nozzle in each condition was recorded. This was repeated three times, and the average of liquid masses was taken. Figure 4.13 shows the calibration curve, and a linear relationship between the liquid flow rate in g/s and the liquid pressure in bars was obtained. Thus, the liquid flow rate at any liquid pressure within the graph can be estimated.

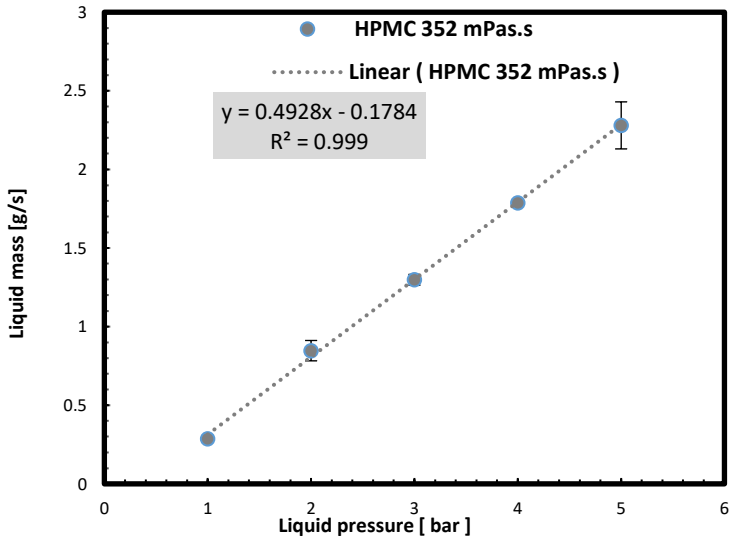

Figure 4.13: Liquid flow rate of HPMC 352 mPa·s at 4 bar atomisation pressures. A linear relationship between the liquid pressure and the liquid mass delivered by the binary spray nozzle. The correlation was 0.999.

4.7.2 Liquid viscosity calibration curve

The viscosity of the hydroxypropyl methylcellulose (HPMC) solutions was varied by using different grades at the same concentration (10 % w/w): HPMC 603 (55.097 mPa·s), HPMC 645 (177.03 mPa·s), HPMC 606 (352.36 mPa·s) and HPMC 615 (1138.5 mPa·s). To construct a calibration curve as a function of liquid binder viscosity, the liquid pressure for every system was changed at a constant atomisation pressure (4 bar), and the spray rate for each of the HPMC

solutions was determined. Calibration curves were plotted to calculate the liquid mass of each system used in this research (Figure 4.14)

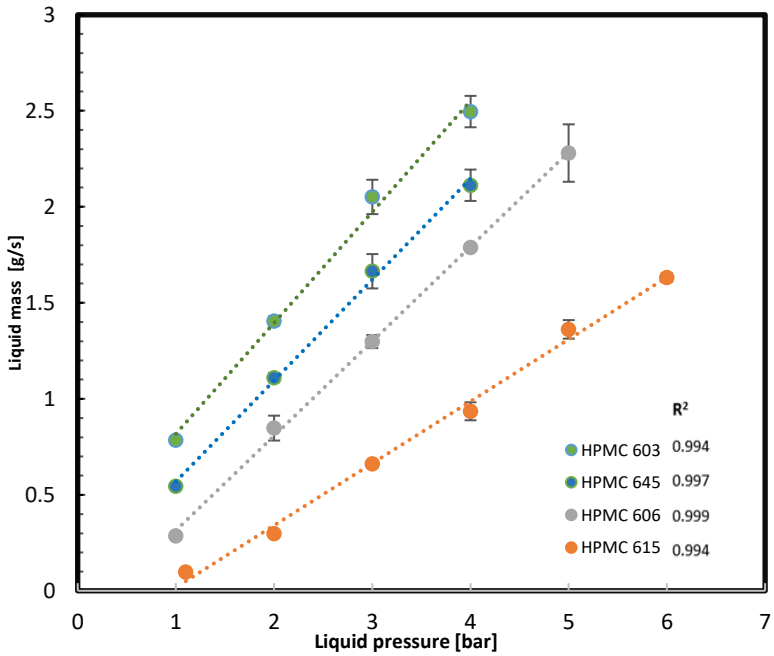

Figure 4.14: Calibration curve showing liquid flow rates delivered by the spray nozzle as a function of liquid binder viscosity. R^2 values are also shown for each system.

As the graph shows, increasing the liquid pressure increased the liquid mass delivered by the spray nozzle for all systems. In addition, the higher the viscosity of the liquid, the less liquid was delivered by the spray nozzle.

4.7.3 Atomisation pressure calibration curve

Figure 4.15 shows a calibration curve was plotted to relate the liquid mass delivered by 1-5 bar liquid pressures at three different atomisation pressures (3 , 4 and 5 bar) in triplicate. The graph clearly shows that the atomisation pressure does not affect the liquid mass delivered and only depends on the liquid pressure.

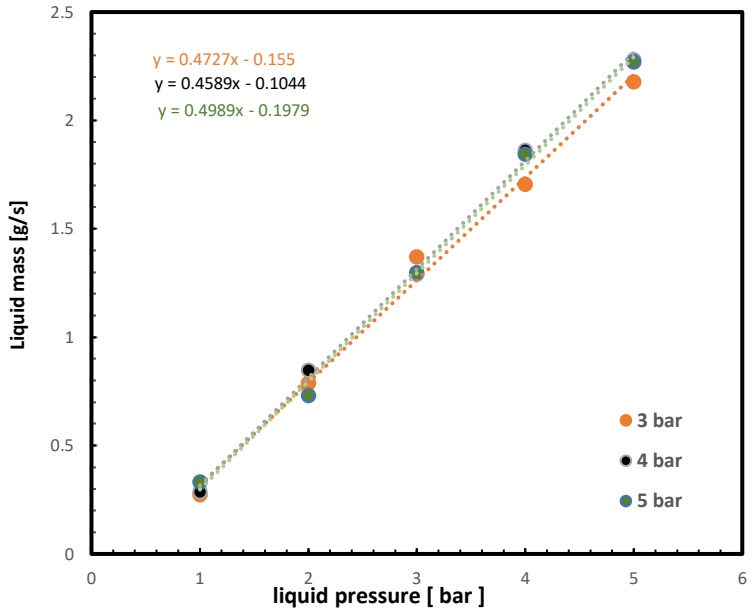

Figure 4.15: Liquid mass of HPMC 352 mPa·s plotted against liquid pressure at 3, 4 and 5 bar atomisation pressures. A linear relationship exists between the liquid pressure and the liquid mass delivered by the binary spray nozzle at the three atomisation pressures.

4.8 Theoretical calculation of the minimum fluidisation velocity (U_{mf})

As discussed in Chapter 2, the theoretical approach to calculate the minimum fluidisation velocity, U_{mf} is by using the Wen and Yu correlation:

$$Re_{mf} = (33.7^2 + 0408Ar)^{1/2} - 33.7 \qquad (4.1)$$

By recalling the equations written in Chapter 2, for Archimedes' number A_r (3.4) and the modified Reynolds number Re_{mf} (3.9) and substituted in Wen and Yu equation, the minimum fluidisation velocity U_{mf} can be calculated:

$$\frac{d_p\, U_{mf}\, \rho_g}{\mu} = \left[(33.7^2 + 0.0408\, \frac{{d_p}^3 \rho_g (\rho_p - \rho_g) g}{\mu^2}\right]^{0.5} - 33.7 \qquad (4.2)$$

The Sauter mean $d_{3,2}$, measured by laser diffraction, was used in the U_{mf} calculation (Litster and Ennis, 2004a). The air density ρ_g is 1.2 kg/m^3 at 20 °C and air viscosity μ is 1.98E-05 kg/(m*s) (Engineeringtoolbox, 2009). The estimated and measured minimum fluidisation velocities for the materials used in the research are shown in Table 4.2.

4.9 Experimental measurement of the minimum fluidisation velocity

The experimental approach to measure the minimum fluidisation velocity, U_{mf}, is by fluidising the bed vigorously and gradually reducing gas velocity. A known mass of glass beads was introduced into the bed column. The height of the bed was recorded by using an adhesive ruler. Air was then allowed into the system, increasing the flow gradually until the particles were vigorously fluidised. Then, the air flow rate was progressively decreased in 20 L /min increments, and the flow rate was recorded against bed height until the minimum flow rate, Q_{mf}, was reached. This is the air flow rate below which the bed height became constant. The Umf was obtained by dividing the flow rate by the cross-sectional area of the bed (see Section 3.4.2. For example, the experimental minimum flow rate Q_{mf} for glass beads $d_{3,2}$ (212 µm) was found by the flow meter to be 15 L /min. i.e. the air that enters the bed of volume (15 * 0.001) m3 across the (0.00636255 m^2) column cross-sectional area per 60 s. This equals the air passing through the bed per unit distance (m) per unit time (s). Accordingly, the minimum fluidisation velocity U_{mf} is 0.0392 ms^{-1}. Table 4.2 shows the measured and estimated for materials used in the thesis. It should be noted that the experimentally measured U_{mf} was used in the U calculations.

Table 4.2: Estimated and actual U_{mf} s for glass beads and lactose monohydrate powders. Material properties used in the calculations are outlined.

Material	Glass beads			Capsulac 60
Size range (µm)	150-250	250-425	425- 600	150-250
Malvern $d_{3,2}$ (m)	0.000212	0.000324	0.000511	0.000191
Bed mass (kg)	0.9303	0.9262	0.9249	0.4208
Minimum air volume Q_{mf} (L/min)	15	35	77	13
Theoretical U_{mf} (m/s)	0.0334	0.0768	0.1804	0.0272
Experimental U_{mf} (m/s)	0.0393	0.0916	0.2017	0.034

4.10 Calculation of actual superficial velocity

The actual superficial velocity means the fluidising velocity at which the bed operates during the experiment. However, the particulate material velocity will change because of size growth or reduction. A superficial velocity that shows noticeable differences during the nucleation process was required to run the experiment. For example, in this research, a turbulent velocity of 0.524 m/s was practically chosen to run most experiments for a time of 60 seconds without defluidisation. This velocity could be achieved by setting the corresponding air volume

entering the bed per min, using the calculation mentioned in the Section 4.9, which was 200 L/min, and the required velocity was reached.

4.11 Calculation of the bubbling velocity

Bubbling velocity U_B is the velocity of the bubbling regime where bubbles rise through the bed, causing mixing and turbulence. it is useful for estimating powder renewal rate at the spray zone and Stokes number calculation. Therefore, it was discussed in Section 3.3.2 and Section 3.3.6.

U_B can be calculated for B powders by Darton et al., 's 1977 equation.

$$U_B = \vartheta_B(\mathrm{g}d_{Bv})^{0.5} \qquad (3.13)$$

Where, d_{Bv} is equivalent volume diameter of the bubble mean bubble size by Werther's (1983) equation (Rhodes, 2008), g is acceleration to gravity and ϑ_B = 0.64 for bed diameter $\leq$ 0.1m (Rhodes, 2008, Litster, 2016a).

$$d_{Bv} = \frac{0.54}{g^{0.2}}\ (U - U_{mf})^{0.4} \qquad (3.14)$$

4.12 Calculation of excess velocities for different primary particle sizes

For the effect of primary size experiments, it was necessary to use comparable air velocities for the three sizes used in the study. These velocities were found by adding fixed excess ($U-U_{mf}$) for each size (Smith and Nienow, 1983). Accordingly, the fluidisation velocities selected were 0.65, 0.70, and 0.81 m/s for the glass beads particle sizes 212, 324, and 511 µm with an excess ($U-U_{mf}$) of 0.615 m/s. As their minimum fluidisation velocities, U_{mf}, were 0.0392, 0.091 and 0.201 m/s, respectively. Hence, the correspondent inlet air volume used was calculated as described in Section 4.9.

4.13 Conclusion

Many aspects were considered when planning to study the distribution nucleation mechanism in the lab design fluidised bed: A spray nozzle that delivers fine droplets of different viscosity systems. Relatively large particles could be fluidised and granulated within a short operation time. A successful granulation process inside the fluidised bed with considerable yield is produced via the distribution nucleation mechanism. A reliable analysis method for the nuclei

size distribution keeps the large sized particles within the granules intact without breakage. Thereby, various materials of different sizes/concentrations were characterised and explored in many trials to find the most suitable material for the study, for example, granulated recycled glass particles, different lactose powders and polyethylene glycol solutions. The experimental conditions were also optimised to find the best operating conditions to run the experiments. In conclusion, a description of the lab scale fluidised bed design was presented in this Chapter. Characterisation of the pneumatic nozzle was implemented to identify and quantify its performance. The solid material fluidising characteristics were also specified. The objectives have been met in designing, constructing and commissioning of the in-house equipment and ready for conducting the research.

Chapter 5: Effect of Material Parameters on Distribution Nucleation in a Fluidised Bed

5.1 Introduction

This chapter investigates the effect of formulation properties on distribution nucleation in a small-scale fluidised bed. The analysis is based on the nuclei size distribution. The aim is to relate the findings with the calculated particle coating number to see if it is possible to predict the process outcome.

A fluidised bed was designed and operated as mentioned in Chapte 4 to carry out these experiments. Also, preliminary trials were carried out to choose appropriate materials and identify optimal operating parameters to ensure that throughout this study, size enlargement is taking place by the distribution mechanism and the granulation outcome could be measured. This chapter investigates the effect of changing variables related to the material being used. Liquid binder viscosity and the initial particle size of the powder are selected to study their impact on the particle coating number, and this will be related to the granulation outcome. In the following sections, the aim of each experiment will be briefly outlined.

The effect of liquid viscosity

When the viscosity of the liquid binder is altered, the droplet size will change accordingly, and the calculated particle coating number value will also change. To limit the findings only to viscosity change, different molecular weights of hydroxypropyl methylcellulose HPMC were used to make 10 %w/w aqueous solutions. As they have similar surface tension, this will show the effect of the Stokes number on the success of nuclei formation because of the viscosity dissipation for particle impact energy (Iveson et al.,2001)**.**

The effect of primary particle size

This study was carried out to investigate the effect of initial particle size on distribution nucleation and to relate the findings with the calculated particle coating number and the predicted liquid binder surface coverage. Also, to investigate if the liquid distribution on the

surface is better described as the commonly used by liquid mass to the solid mass, or by liquid mass per the solid surface area was studied.

5.2 Materials and Methods

The experiments were conducted in the small lab design fluidised bed (as described in Chapters 3 and 4).

5.2.1 Materials

The model particulate material chosen to perform this study was non-porous glass powder from Kuhmichel Abrasive Limited®, of three size ranges. The liquid binder selected was hydroxypropyl methylcellulose (HPMC). Different molecular weight HPMC were used to give solutions of various viscosities.

In this research, as was explained in Chapter 3, the primary particle size distributions (PSDs) of the glass beads were measured by laser diffraction and will be referred to by their Sauter means $d_{3,2}$. The size distributions of the resulting granules were measured by dry sieving analysis. True density measurements were conducted using helium pycnometry. The specific surface area (SSA) measurement was obtained by laser diffraction. Bed porosity was calculated. The main characteristics of the glass beads size ranges are listed in Table 3.3, Table 3.6,

Table 3.7 and Table 4.2.

Hydroxypropyl methylcellulose (HPMC) of different grades, Tylopur 603, 645, 606 and 615 were used which have molecular weights of 16,000, 22,000, 35,600, and 60,000 Da, respectively. They were supplied by Shin-Etsu Chemical Co. Ltd. and received as white powder/ flakes. The liquid binder solutions were prepared at 10% w/w using an aqueous acid red 1% w/w solution. The dye was added to facilitate the identification of the binder within the product. The preparation procedure is explained in Section 3.1.3 in Chapter 3. The properties of the liquid binder solutions used in the viscosity experiment are given in Table 3.8, Table 3.9,Table 3.10 and Table 3.11.

The different HPMC solutions will be referred to by their viscosity values in this chapter. The droplet size of liquid binder at the given flow rate and pneumatic pressure was measured using a Nano PIV laser sizer, VisiSize N60 series by Oxford Lasers Ltd. The PCN Φ_p values were calculated using equation (3.5). The Sauter mean of droplet under given conditions was used

in the calculation. The predicted fractional coverage, F, was also calculated using equation (3.10) (Kariuki et al., 2013). Further details can also be found in Chapter 3, Section 3.3.

5.2.2 Methods

5.2.2.1 Effect of Liquid Viscosity

In this experiment, the glass beads in size range of 150-250 μm ($d_{3,2}$ = 212 μm) were granulated using 10 % w/w an aqueous binder solution: HPMC 603 (55.097 mPa·s), HPMC 645 (177.03 mPa·s), HPMC 606 (352.36 mPa·s) and HPMC 615 (1138.5 mPa·s). A flow rate of 1.29 g/s for all systems was selected to deliver 12.9 g of all systems in 10 s spray time. From the calibration curve shown in Figure 4.14 (Chapter 4 Section 4.7.2), this rate is obtainable at 1.76, 2.34, 3, and 4.85 bar liquid pressure for HPMC: 55.097; 177.03; 352.36, and 1138.5 mPa·s respectively. All the experiments were carried out at room temperature (21˚C), bed height was 10 cm, nozzle height was 25 cm and spray time was 10 s. All the experimental conditions are given in Table 5.1. Further details are given in the general procedure in Chapter 3. Section 3.4.2.

Table 5.1: Effect of viscosity experimental conditions.

Binder HPMC (10% w/w)	603	645	606	615
Liquid binder viscosity (mPa·s)	55.09	177.03	352.36	1138.5
Liquid pressure (bar)	1.76	2.34	3	4.85
Liquid binder flow rate (g/s)	1.29			
Glass beads range size (μm)	150-250			
Powder mass (g)	930.33			
The volume of air (L/min)	200			
Fluidisation velocity U (m/s)	0.524			
U/U_{mf}	13.33			
$U-U_{mf}$	0.48			
Atomisation pressure (bar)	4			
Mixing time (s)	60			

5.2.2.2 Effect of initial mean particle size

In this experiment, three size ranges of glass beads of 1.46 g/cm^3 density (150-250 μm, 250-425 μm and 400-600 μm) were granulated using HPMC 1139 mPa·s. The Sauter mean ($d_{3,2}$) were 212, 324 and 511 μm, respectively. The particulate surface areas of every powder bed mass were calculated using the specific surface area obtained by Malvern, which is very close to the calculated SSA shown in (Section 3.2.2, Chapter 3, Table 3.6). The particulate bed

surface area was 10.74 m^2, 6.99 m^2 and 4.43 m^2, respectively. The bed masses of each size were 630.33 g, 926.26 g and 924.99 g.

The study was conducted using two approaches; the first (Experiment A) was to maintain a constant ratio of liquid mass to powder mass, i.e. XLS was held constant for three primary particle sizes.

The second approach (Experiment B) was to maintain a constant liquid mass added to the surface area of the material (kg/m^2), irrespective of the primary particle size.

Table 5.2 demonstrates the experimental conditions for both experiments, A and B. As the table shows, the liquid pressure was set at 5 bar in experiment A. The three sizes of the glass beads were granulated with the same liquid mass, 13.5 g of HPMC 1139 mPa·s. The highest viscosity liquid was selected to achieve a considerable agglomerated fraction even with large size glass beads. The X_{LS} was 0.0145 with a standard deviation of 4.37E-05 due to the slight differences between the three bed masses. The velocities chosen were able to keep the bed fluidised throughout the experiment. However, the largest size range did undergo slugging after agglomeration because of the size growth. The inlet air volume required to be introduced was calculated in accordance with Neinow & Smith,1983, to give the same excess air velocity (U-Umf = 0.615 m/s) for the three sizes of 212 µm, 324 µm and 511 µm as their U_{mf}, were 0.039, 0.091 and 0.201 m/s respectively. Therefore, the velocities used were 0.65, 0.70 and 0.81 m/s.

Table 5.2: Experimental conditions for both initial mean particle size A and B experiments.

Experiment	**A. Constant X_{Ls}**			**B. Constant binder mass / bed surface area**		
Glass beads size (µm)	150-250	250-425	400-600	150-250	250-425	400-600
Liquid pressure (bar)	5			5	3.7	2.7
Liquid mass added (g)	13.5			13.5	9.075	5.66
Powder mass (g)	930.33	926.26	924.99	930.33	926.26	924.99
Volume of air (L/min)	250	270	312	250	270	312
Fluidisation velocity U (m/s)	0.65	0.70	0.81	0.65	0.70	0.81
U/Umf	16.66	7.71	4.05	16.66	7.71	4.05
U-Umf	0.615			0.615		
HPMC 615 viscosity (mPa·s)	1138.5			1138.5		
Atomisation pressure (bar)	4			4		
Mixing time (s)	60			60		

In experiment B, the liquid mass per total solid bed surface area was kept constant for the three sizes of glass beads and was 0.0011 kg/m^2. Thus, the three sizes were granulated with 13.5 g, 8.92 g and 5.66 g of liquid binder HPMC 1138 mPa·s with X_{LS} of 0.01459, 0.00964 and

0.00611, respectively. Liquid pressure was varied 5, 3.7 and 2.7 bar to deliver the required mass.

The air was pressurised at 3 bar, and the inlet air volume was varied (250, 270, 312 L/min) to give corresponding fluidisation velocities of 0.65, 0.70 and 0.81 m/s for each size. Other operational variables didn't change for both experiments. The nozzle height was 25 cm, the spray time was 10 s, the atomisation pressure was 4 bar, and the bed was fluidised for 60 s.

5.3 Results and discussion

5.3.1 The effect of liquid viscosity

This section shows the results after 60s granulation using four different HPMC systems: 55.097, 177.03, and 1138.5 mPa·s. The experiments were performed in duplicate. The nuclei size distribution for the granulated material of the two repeats is shown in Appendix 5A.1(1A - 4A). The particle size distribution for the whole material of the two repeats is shown in Appendix 5A.1(1B - 5B). Table 5.3 shows the PCN for all systems.

As mentioned in the data analysis section, the nuclei in this research are defined as any granulated material held by 275 μm sieve size and above (Chapter 3, Section 3.6.2.1).

Table 5.3: Liquid binder viscosities used, the Stokes numbers, the correspondent measured droplet size, their velocities with standard error in brackets, and the calculated global PCN and F%.

Liquid binder	HPMC 603	HPMC 645	HPMC606	HPMC615
liquid mass/ total material surface area (kg/m^2)	0.0010			
Liquid mass added (g)	12.9			
X_{LS}	0.0139			
Liquid binder viscosity (mPa·s)	55.09	177.03	352.36	1138.5
Liquid pressure (bar)	1.76	2.34	3	4.85
Stokes number	0.055	0.017	0.0086	0.0026
Contact angle (°)	56.14	77	82.37	90.79
Droplet Sauter mean ($d_{3,2}$) (μm)	32.83 (± 0.589)	39.33 (± 0.676)	30.33 (± 0.26)	39.46 (± 0.12)
Average velocity of the droplets (m/s)	3.56 (± 0.54)	5.38 (± 0.10)	9.14 (± 0.27)	5.03 (± 1.96)
Global PCN	0.1462	0.0873	0.1037	0.071
Local PCN	2.382	1.422	1.689	1.1575
F%	0.1361	0.0836	0.0985	0.0686

Figure 5.1 shows the average granulated mass fractions plotted against liquid binder viscosity. As was explained in Chapter 3, Section 3.6.1, after rifling and sieving half of the processed batch. The percentage granulated fraction by mass is calculated by dividing the mass of the nuclei obtained from the sieved fraction by its total mass. As can be seen in Figure 5.1, apart

from the lowest viscosity, the agglomerated fraction increased as the viscosity increased. The highest viscosity HPMC, 1139 mPa·s, resulted in the highest agglomerated mass fraction, which is 30.9 %. Surprisingly, the lowest binder viscosity of 55 mPa·s gave a higher agglomerated fraction than the 177 mPa·s solution.

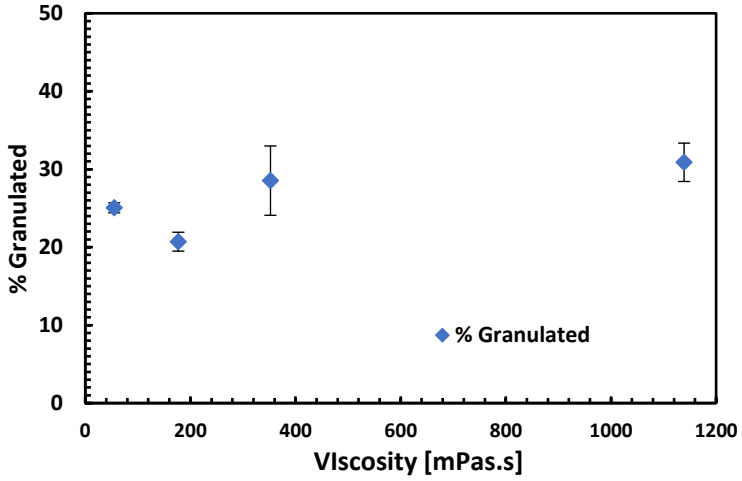

Figure 5.1: The agglomerated fraction obtained by each viscosity system in 60 s granulation time.

The relatively high granulated fraction of 25% obtained by the lowest viscosity could be because of the longer time needed for the solution to dry. As a result, it produced more nuclei on a static basis. i.e., after processing time. This was noticed while performing the sieving analysis. The bed consisted of big chunks that were difficult to sieve. Figure 5.2 compares the batches of granules obtained by the lowest viscous liquid binder (HPMC 55 mPa·s) and the highest viscous liquid binder used (HPMC 1138.5 mPa·s).

Figure 5.2: Batch of two repeats with the highest viscosity HPMC 1138.5 mPa·s system and another batch produced by the lowest viscosity HPMC 55 mPa·s system. The low viscosity showed agglomeration in the tray, which could bias d_{50} and d_{90} sizes.

Visual inspection shows the product of the lowest viscosity HPMC consisted of chunks that were difficult to sieve. The pan contains a mixture of high and low-intensity coloured granules besides the primary particles. This low intensity coloured granules were reflected in the size distribution graph Figure 5.3. The highest viscosity was easy to sieve (Figure 5.2).

Figure 5.3 shows the average nuclei size distribution of the granulated glass beads as a function of liquid binder viscosity. The graph indicates that the binder of the lowest viscosity, 55 mPa·s, produced granules with the narrowest nuclei size distribution.

As the viscosity increases, the nuclei size distribution broadens. However, HPMC 352 mPa·s produced the broadest nuclei size distribution, favouring the nuclei size >1 mm. In contrast, the highest viscosity, 1139 mPa·s, has a narrower size distribution favouring smaller nuclei size.

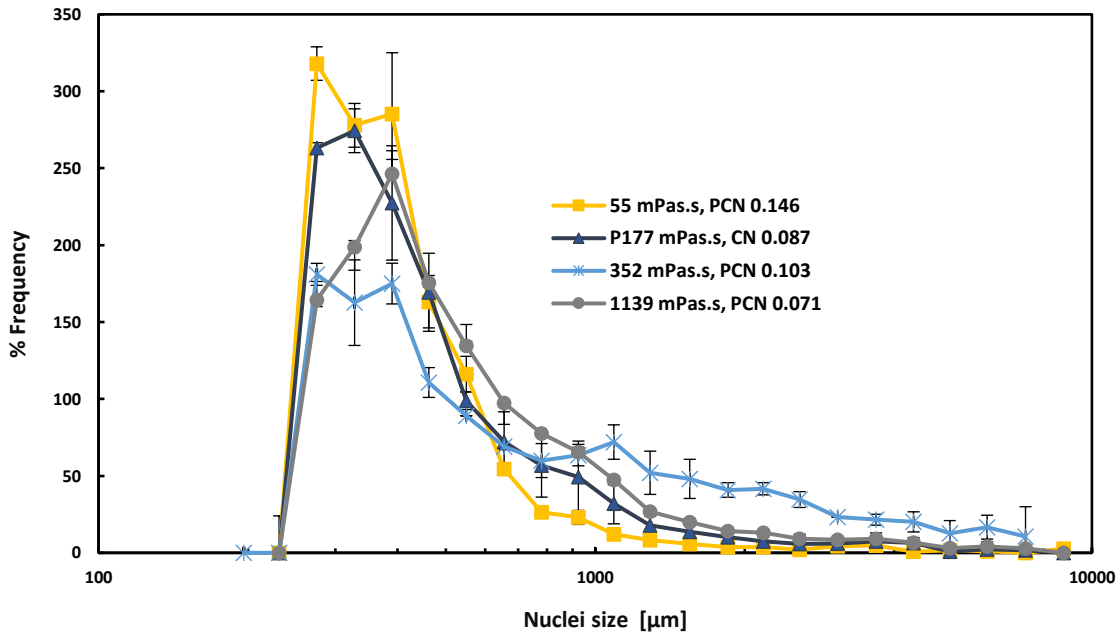

Figure 5.3: Nuclei size distribution as a function of binder viscosity. The glass beads (d3,2 = 212 µm) were granulated with HPMC of different molecular weights and viscosities. PCN magnitudes are also shown.

Figure 5.4 shows the mean nuclei size d_{50} produced by the four systems as a function of contact angle. The d_{50} is directly affected by viscosity and the contact angle; as the viscosity increased, the mean size increased up to 352 mPa·s. The highest viscosity of 1139 mPa·s produced a slightly smaller d_{50} than the lower viscosity of 352 mPa·s.

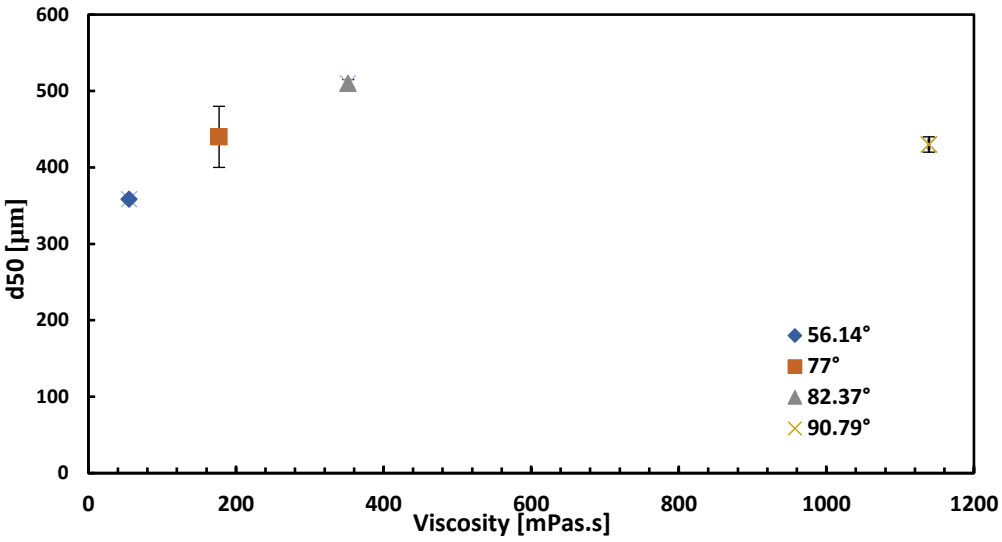

Figure 5.4: d_{50} of nuclei as a function of contact angle for each system used in the 60 s experiment.

Figure 5.5 shows the mean nuclei size d_{50} as a function of the calculated PCN. The change in PCN magnitude calculated in this experiment is limited to the change in droplet size (Table 5.3).

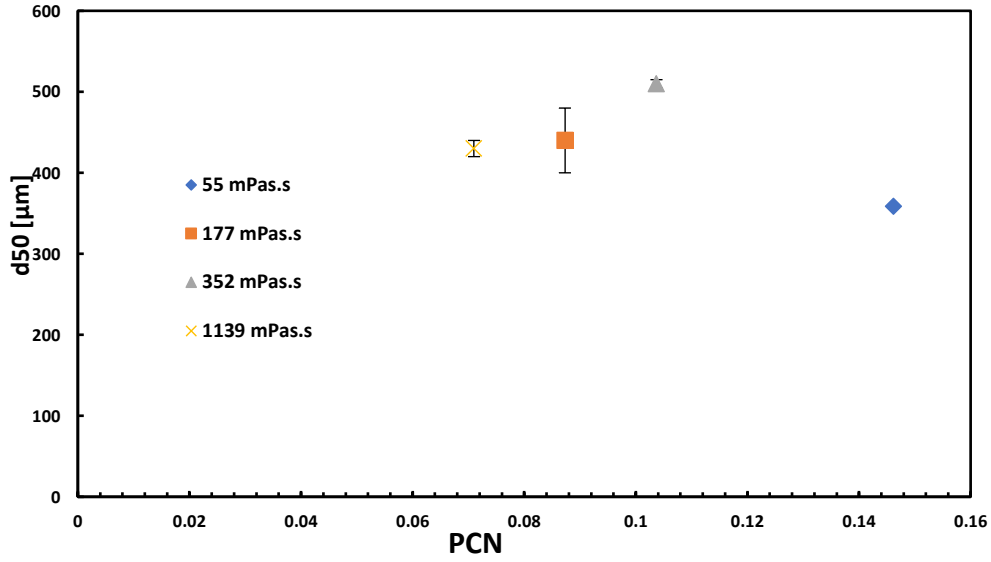

Figure 5.5: Nuclei size (d50) as a function of PCN calculated, the droplet sizes were 32.83, 39.33, 30.33 and 39.46 µm for 55, 177, 352 and 1139 mPa·s, respectively.

As viscosity increases, d_{50} increases and PCN decreases. The lowest viscosity HPMC 55 mPa·s produced the small (d_{50}) and had the highest PCN (0.146). The highest viscosity, HPMC 1139 mPa·s has the lowest PCN (0.071) and produced the highest yield with the second largest d_{50} size after HPMC 352 mPa·s.

Most parameters in this study were attempted to be similar to limit the change in the experimental data to the viscosity. Equal masses of different viscosity polymer solutions at the same concentrations were used to maintain similarity in liquid distribution, surface tension, and liquid densities. However, when the viscosity was increased, higher liquid pressure was applied to maintain same flow rate (Table 5.1 and Table 5.3). Also, other parameters were changed by changing viscosity such as droplet size, contact angle and droplet footprint.

By decreasing the viscosity, the global PCN was increased from 0.071 to 0.104. Local PCN also was increased from 1.15 to 2.38 (Table 5.3). It can capture the spray coverage area too (Section 4.6.3), but due to lack of measurement, it wasn't included in the calculation, as discussed in Section 3.3.2. Nevertheless, considering the same X_{LS} applied, this remarkable change in PCN reflects its capability to capture many of the viscosity related parameters.

Štěpánek et al. (2009) linked coalescence success to geometric factors expressed by the liquid coverage and thickness of the liquid layer during collision, besides physical factors expressed by critical Stokes number model by Ennis et al. (1991) which measures cohesive strength between wetted particles against breakup forces and it is valid for non-deformable glass beads (Rajniak et al., 2007, Litster and Ennis, 2004a). All systems used in the experiment resulted in nuclei formation. However, low viscous liquids dominate a faster initial growth shown in narrow size distribution for small nuclei sizes. In contrast, high viscous liquids dominate secondary growth demonstrated in large nuclei produced. (Figure 5.4). This suggests that physical success is dominant, i.e., the viscous liquid can absorb the energy generated by moving particles during an impact, preventing the particles from rebounding. The Stokes number calculated was dramatically decreased as the viscosity increased from 0.055 to 0.0026 (Table 5.3), indicating more coalescence as the number remains below a critical viscous Stokes number (Equation (2.37).

Nuclei are formed when the liquid binder is distributed over the moving particles. The coalescence of wetted particles requires enough fractional surface coverage to hold the particles together within the agglomerate. The geometric factors, related to liquid coverage and liquid thickness, include contact angle, which varied between 56° and 90°, clearly promoting nucleation and nuclei size (Figure 5.4). A larger contact angle gives a thicker layer and more volume for bond formation. The contact angle is explicitly considered because the model particle is non-porous, and no liquid penetration occurs. Low viscous liquids tend to spread more over the particle surface, subjecting the thinner liquid film to a faster drying rate. Studies have shown an increase in the droplet mean diameter with increasing viscosity under the same

liquid pressure (Mandato et al., 2012, Juslin et al., 1995). On the contrary, this study applied different liquid pressures to keep the same flow rates. There was an unclear correlation between droplet size measured by laser and the viscosity (Table 5.3), which might refer to the differences in the liquid pressures used or the complexity of viscous non-Newtonian polymer behaviour (Aliseda et al., 2008). This suggests further investigation. The highest viscosity (1139 mPa·s) produced the largest droplet size and the largest granulated fraction. However, the second highest viscosity, 352 mPa·s, produced the largest nuclei with a smaller droplet size.

The drying and solidification rates also seem to play important roles in defining the broadening of the nuclei size distribution. By referring to Figure 5.1 and Figure 5.3, the largest agglomerated fraction (32%) obtained by the highest viscosity of 1139 mPa·s was of a narrow distribution with d_{50} of 450 μm. The second high viscosity of 352 mPa·s had 26% agglomerated material of the broadest distribution with a d_{50} of 510 μm. This could be attributed to the accelerated solidifying rate, making the highest viscosity system less successful than the 352 mPa·s system towards forming large nuclei.

The lowest viscosity 55 mPa·s yield is 25% mainly of smaller size nuclei than that of the higher viscosity, HPMC177 mPa·s (20%) (Figure 5.1). This could be attributed to the slower drying rate of low viscosity aqueous solution. And the possibility of forming new liquid bridges after batch processing time (1 minute) (Figure 5.2).

5.3.2 The effect of initial particle size

This experiment was carried out in duplicate. The individual repeats are shown in the Appendix.5 A.6.2. Table 5.4 shows sub experiment conditions A and B, the X_{LS} used, and the corresponding measured droplet size and PCN and F. As seen in Table 5.6 A, the PCN and the fractional liquid coating increase as the primary particle size sustainably increases when the liquid mass to solid mass ratio is fixed (X_{LS} 0.014), the PCN values are 0.073, 0.110 and 0.168, for the sizes of 212, 425 and 511μm, respectively.

Table 5.4.B shows a slight change in PCN magnitude when the liquid mass to the particulate material surface area is kept constant (0.07, 0.08 and 0.09 for 212, 425 and 511μm), respectively. This is referred to the small differences in the bed masses used in the experiment because of their differences in bulk densities.

Table 5.4: Initial particle size experiments A & B, the X_{LS} used, the corresponding measured droplet size and calculated PCN and F%. Standard errors are shown in brackets.

Initial particle size experiment approach	A. Constant X_{LS}			B. Constant binder mass /bed surface area		
Glass beads size ranges (µm)	150-250	250-425	400-600	150-250	250-425	400-600
Particle Sauter mean($d_{3,2}$) (µm)	212	324	511	212	324	511
Liquid pressure (bar)	5			5	3.7	2.7
Liquid mass added (g)	13.5			13.5	9.07	5.66
X_{LS}	0.0147			0.0146	0.0098	0.0061
liquid mass/ total material surface area (kg/m^2)	0.0011	0.0016	0.0026	0.0011		
Stokes number **St_v**	0.00278	0.0065	0.0162	0.00278	0.0065	0.0162
Droplet Sauter mean (d3,2)(µm) Standard error	38.6 (±1.03)			38.6 (±1.03)	37.8 (±0.55)	35.83 (±0.41)
Average velocity of the droplets (m/s) Standard error	5.038 (±0.06)			5.038 (±0.06)	5.852 (±0.62)	5.648 (±0.29)
Global PCN	0.077	0.118	0.186	0.077	0.080	0.083
F%	0.074	0.111	0.170	0.074	0.077	0.080
Local PCN	1.192			1.192	0.810	0.533

The glass beads granulated with HPMC1139 mPa·s were examined under Olympus BX51 microscope. The Figure 5.6 shows examples of nuclei produced by the different initial particle sizes of 212, 324 and 511µm under the microscope.

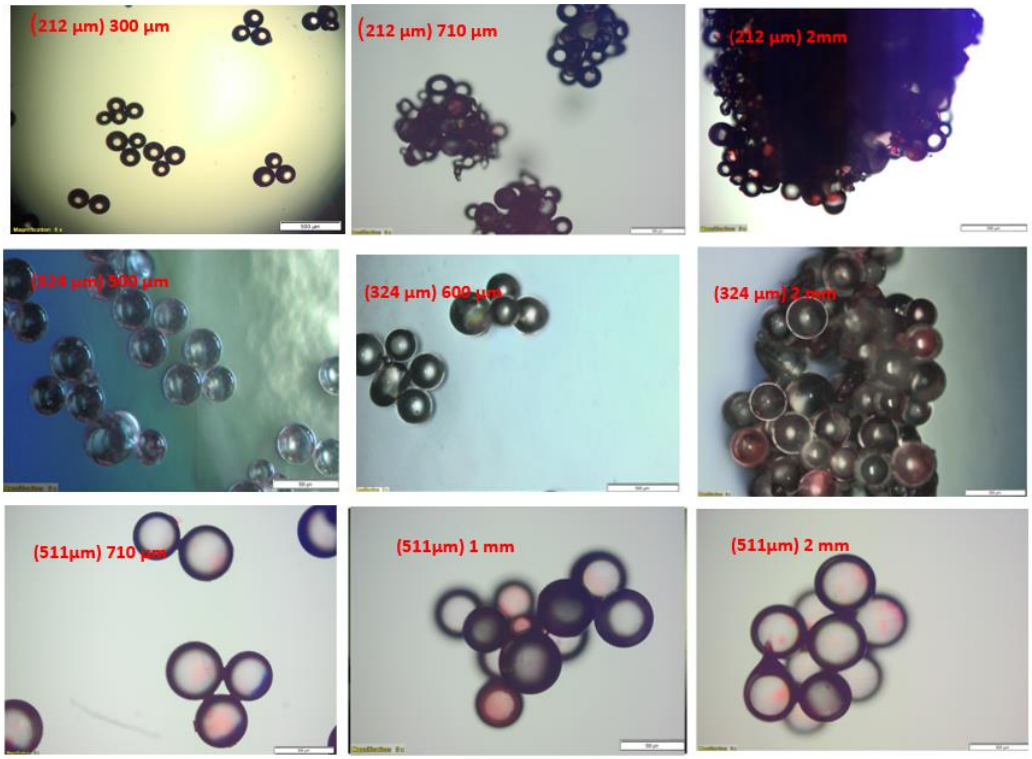

Figure 5.6: Glass beads-HPMC1139 mPa·s nuclei of different sizes under light microscope magnification 5x obtained by different initial particle sizes 150-250, 250-425 and 400-600 µm size ranges.

The photos show nuclei have an open structure, and no liquid trapped in the structure, which distinguishes the distribution nucleation from immersion nucleation.

The outcome of the two sub experiments, A and B were visually compared, starting with A, Figure 4.7 shows three sizes of glass beads that were granulated with the same X_{LS} = 0.014.

Figure 5.7: Three batches of granulated glass beads of three different primary particle sizes with X_{LS} = 0.0145. The colour intensity intensifies as the particle size increases.

The colour of the batches was intensified as the primary size increased, and the bed appeared less chunky. These batches had a liquid mass per powder surface area of 0.0011, 0.0016 and 0.0026 kg/m^2 for 212, 324 and 511 µm primary particle sizes (Table 5.4), which means less surface area of particle surface available for liquid distribution (Figure 5.7).

The second part of this study (Experiment B) shows what happens when liquid binder mass is evenly distributed across the same surface area of the particulate bed regardless of the initial size of the particle. Visual inspection for batches (Figure 5.8) shows a similarity in the colour intensity.

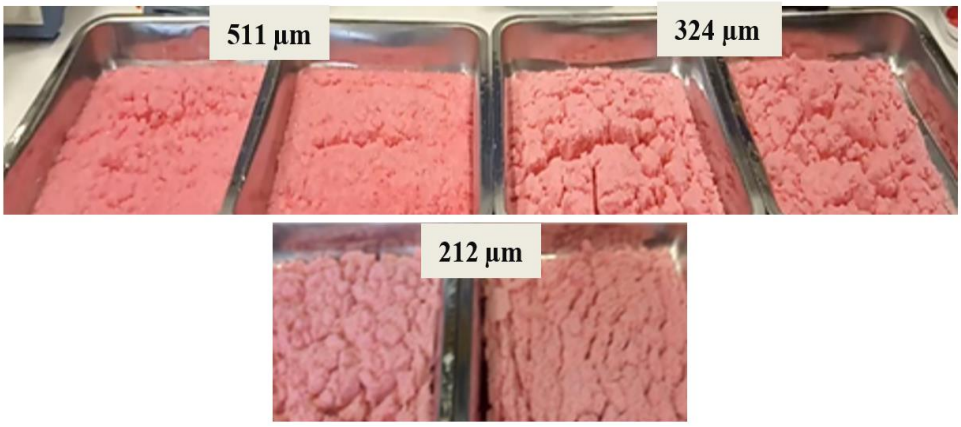

Figure 5.8: Two repeats of each size (212 µm, 324 µm and 511 µm).

This indicates similar coating and liquid dispersion among the particles when the liquid mass to the particulate material surface area is kept constant.

The graph in Figure 5.9 compares the % agglomerated fraction obtained by the three initial particle sizes in the two sub-experiments, A& B. The chart shows a reduction in % granulated fraction drops further when liquid mass is reduced to match the surface area (B) instead of powder mass (A).

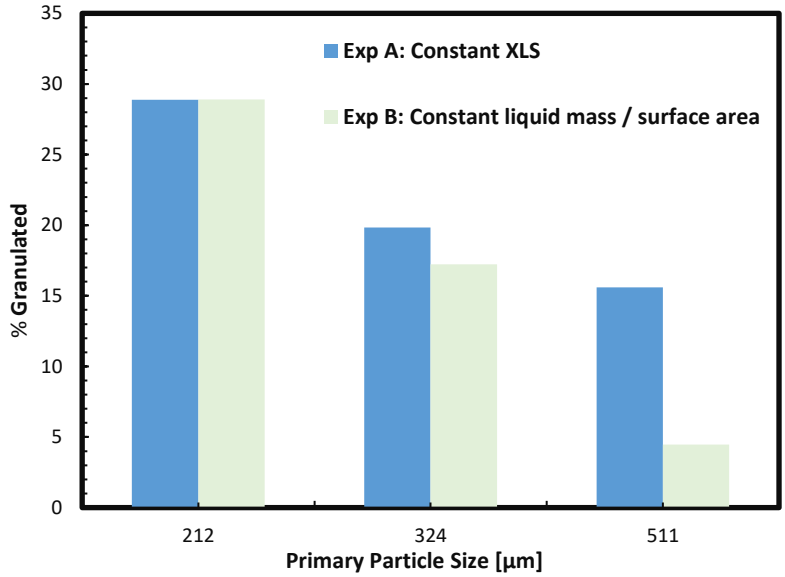

Figure 5.9: Averages of agglomerated fractions obtained by the HPMC 1138.5 mPa·s with three sizes (212, 324 and 511 µm) of glass beads with fixed X_{LS} & fixed liquid mass/surface area.

Figure 5.10 shows nuclei size distributions produced by both experiments A& B. Nuclei size/primary particle size ratios were plotted against frequency because of the differences in starting sizes on the x-axis.

The two graphs show similar behaviour. The smallest primary size shows the broadest distribution and less agglomeration success as the starting material primary particle size increased especially in experiment B when liquid mass was distributed over the same material surface area.

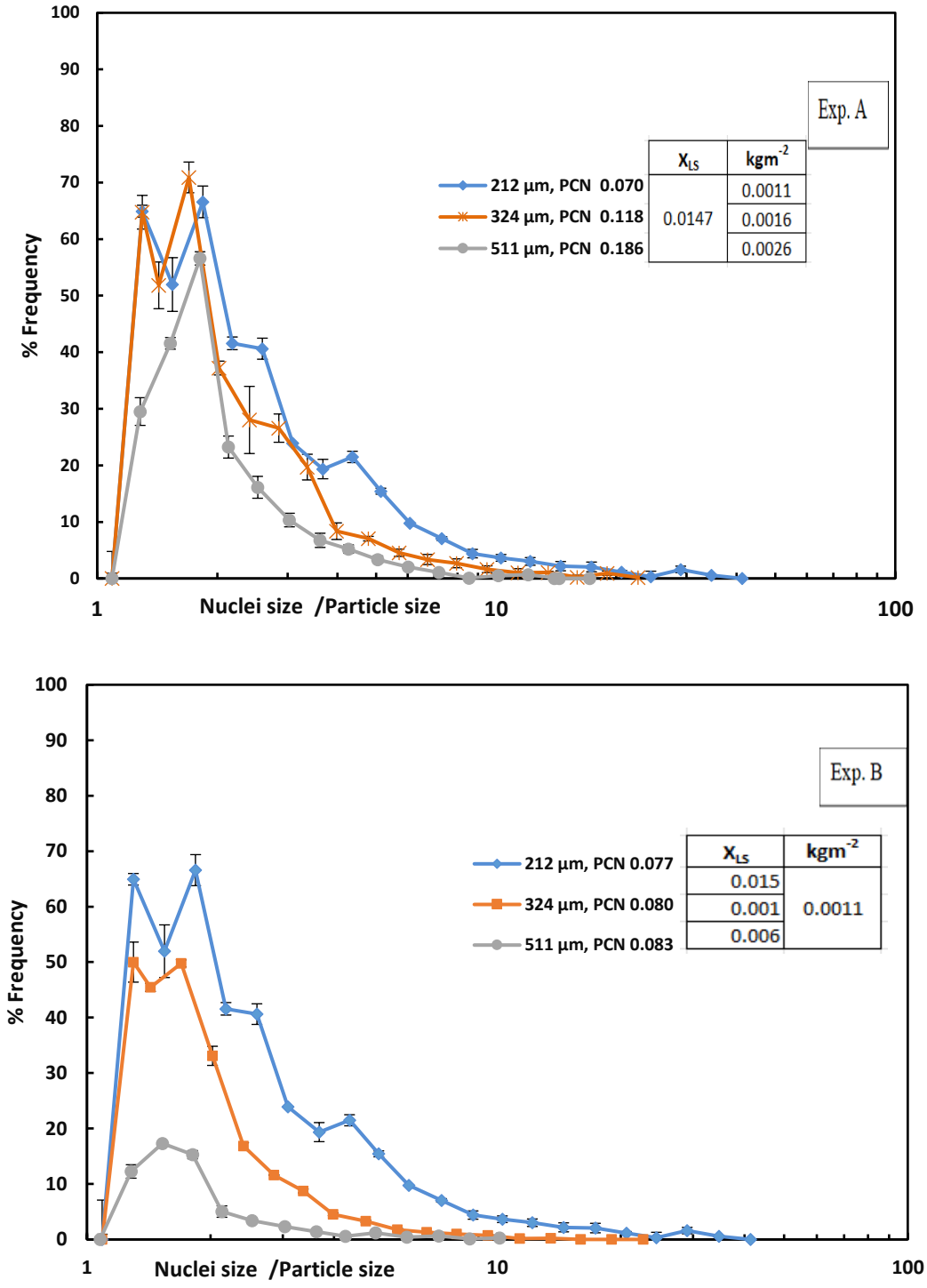

Figure 5.10: Average nuclei size distribution as a function of primary particle size: using constant X_{LS} = 0.0145 (Experiment. A) and using same liquid mass/surface area = 0.0012 kg/m^2 (Experiment B). The glass beads $d_{3,2}$ = 212, 324 and 511 µm were granulated with HPMC 1138.5 mPa·s fluidised for 60 s at 0.65, 0.70 and 0.81 m/s, respectively.

Nuclei size (d_{50}) produced by A & B sub experiments are plotted against PCN, in (Figure 5.11). A slight reduction in nuclei mean size produced by 511 µm primary size in Experiment B showed compared to Experiment A (925 µm and 850 µm). Nevertheless, it should be emphasised that the observed increase in d_{50} produced is not a realistic reflection of enhanced coalescence. It relates to the size of the primary particle.

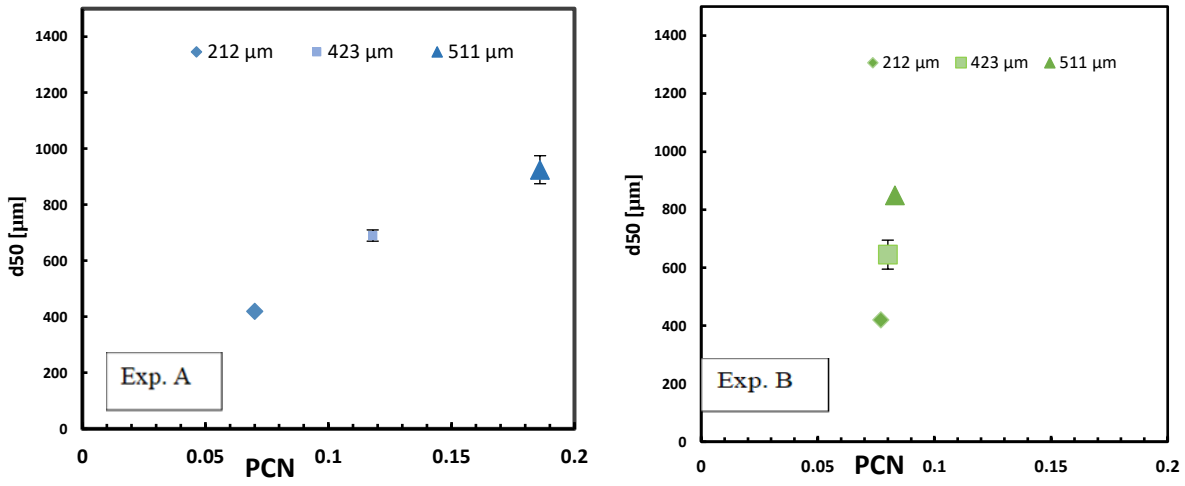

Figure 5.11: Nuclei size (d_{50}) versus PCN produced at fixed X_{LS} (A), and fixed liquid mass per material surface area (B) initial particle size subexperiments.

In order to investigate the impact of PCN on distribution nucleation, the experiment was conducted using two different approaches. In the first approach (A), the liquid mass was added to match the solid bed mass (same X_{LS} used for three sizes) while the liquid mass matched the surface area of the solid particle bed in the second approach (B). In experiment A as primary particle size increased, the PCN values increased to reflect the liquid volume distributed over a decreased solid bed surface, in experiment B where the liquid mass per solid surface area was fixed. The global PCN was almost the same PCN for all initial particle sizes (Table 5.4). The slight differences are attributed to the slight differences in the solid mass used due to minor differences in bulk densities.

Despite this similarity in PCN, the granulated fractions and nuclei size exhibited a remarkable reduction. This confirms that kinetic energy is the dominant factor when the liquid distribution is fixed. And to maintain the same behaviour when changing the particle size increasing PCN is required.

The glass beads are spherical, non-deformable and non-porous**.** Fluidisation velocities for the three initial sizes were attempted to be comparable. The excess air velocity was maintained with respect to initial particle size (U-Umf) as discussed in Chapter 4, Section 4.11, and the Method Section 5.2.2 (Smith and Nienow, 1983). The bubbling velocities were also similar (1.06 ms^{-1}). All velocities were able to keep the bed fluidised throughout the experiment. However, the largest size, 511µm, when granulated experienced a change in behaviour from group B to D on the Geldart chart, leading to slugging after some time.

The results showed a reduction in distribution nucleation and nuclei size as the primary particle size increased. This is in agreement with the literature, which indicates the smaller the mean particle size, the greater the particle growth rate (Smith and Nienow, 1983, Liu et al., 2013, Tan et al., 2006) and could be attributed to the decrease in nuclei adhesion strength due to the increased particle size (Hemati et al., 2003).

The increased particle mean size is believed to lead to larger dynamic forces, lower nucleation success and increased coating. This phenomenon may be attributed to the weakening of liquid bridges and an elevated rebound rate (Liu et al., 2013). The viscous Stokes number increased as the primary size increased. St_v were 0.00278, 0.0065, and 0.0162 for the primary particle sizes 212, 324 and 511 µm, respectively (Table 5.4) for both sub experiments. These values may be extended with caution to describe alternative collision scenarios, including granule impaction. Increased Stokes number to exceed critical viscous Stokes number $(St_v)^*$ slows down or stops the agglomeration process and moves the system into the layering mechanism.

When particle size changes, the Stokes forces opposing the kinetic energy of impact and the liquid distributed over the surface area of the particulate bed become key factors influencing distribution nucleation. Additionally, the PCN remains constant if the solid surface area does not change, indicating that an increase in PCN is necessary to maintain consistent behaviour.

5.4 Conclusion

This chapter explored the effect of the formulation related parameters, viscosity, and initial particle size on distribution nucleation using a small-scale fluidised bed. And how these parameters and the nucleation process outcome are linked to the predicted particle coating number.

In the viscosity study, physical and geometric factors dominated distribution nucleation outcomes. Viscous dissipation is described by Stokes number and liquid coverage is described

by PCN. Changes caused by viscosity were effectively captured by the PCN as contact angle, droplet size, and footprint area. A decrease in viscosity, for the same liquid-solid fraction, distinctly increased its magnitude. PCN is inversely proportional to viscosity, d_{50} and nucleation success. Despite the complexity of viscoelastic binder behaviour and discrepancies in droplet size measurements, PCN's ability to predict outcomes remains significant. Furthermore, within the experiment's time profile, the slow drying process of lower-viscosity aqueous solutions led to partial tray agglomeration, introducing bias in the results. In contrast, the rapid solidification rate of higher viscosity solutions interfered with d_{50} size and narrowed the product's size distribution.

Particle size as a material variable has inversely impacted the nucleation process. The larger particles led to larger kinetic energy and lowered nucleation success. When PCN is held constant, it was shown that the kinetic energy was dominating the process because PCN is related to the solid surface area and describes the actual liquid distribution. Therefore, to enhance the success of the distribution nucleation, the PCN has to be elevated by increasing the liquid content.

Chapter 6: Effect of Process Parameters on Distribution Nucleation in a Fluidised Bed

6.1 Introduction

In the previous chapter, the effects of material parameters on granulation via distribution nucleation were investigated in a lab-scale fluidised bed. This chapter examines the impact of operational parameters on granulation via distribution nucleation using the same lab-scale fluidised bed. The analysis is based on the nuclei size distribution of resultant granules. The aim is to relate the findings with the calculated particle coating number to determine if it is possible to predict the process outcome. Each parameter will be investigated, and the aim of each experiment will be briefly outlined in this section.

The effect of liquid flow rate:

This parameter will affect the liquid–solid mass fraction (X_{ls}) and, consequently, it will affect the particle coating number (PCN) value and fractional coverage (F) predicted. It will significantly affect the volumetric rate in the spray flux formula. If it is increased, it will cause overlapping in the droplet footprint, forming a thicker liquid layer, and the changes could be recognisable in terms of the granulated fraction.

The effect of mixing time:

In this study, the interest is in the nucleation phase and the timescale it takes. It is important to study the changes that might happen within the very early times of mixing and later during this type of granulation. Time of mixing in a fluidised bed in a turbulent phase promotes good liquid distribution on the bed but will subject the bed to air drying.

The effect of atomisation pressure:

Here, the influence of droplet size distribution on the nuclei size distribution via distribution nucleation will be explored. The main operational parameter to be investigated is the pneumatic pressure atomisation, which controls the droplet size while the liquid-solid fraction X_{LS} is constant; consequently, the PCN will be affected.

The effect of fluidisation velocity:

Investigating different fluidisation velocities or different excess velocities will show the effect of increased surface renewal rate on the coating fraction or on the spray flux, while both the area of spray zone and the volumetric spray rate are kept constant.

6.2 Materials & methods

The model particulate material used in this set of experiments was non-porous glass beads from Lumachel Abrasiv Limited. The liquid binders used were Hydroxypropyl methylcellulose (HPMC) of two molecular weights (Tylopur 606 has a molecular weight of 35,600 Da and Tylopur 615 has a molecular weight of 60,000). These were supplied by Shin-Etsu Chemical Co. Ltd.

The main characteristics of the glass beads size range (150-250 µm) used in this set of experiments are listed in Table 3.3, Table 3.6,

Table 3.7 and Table 4.2.

The main characteristics for liquid binders HPMC10% 606 and HPMC10% 615 are listed in Table 3.8, Table 3.9, Table 3.10 and Table 3.11.

In addition to the general method used to conduct all the experiments, as mentioned in Chapter 3, in all experiments, bed height was 10 cm, nozzle height was 25 cm and spray time was 10 s. The specific experimental conditions related to each study are given in Sections 6.2.1- 6.2.4. As described in Chapter 3, sieve analysis was used to determine the size distribution of the granulated material in all experiments.

6.2.1 Effect of flow rate

In this experiment, glass beads ($d_{3,2}$ = 212 µm) were granulated with HPMC 352 mPa·s. The operational conditions are given in Table 6.1. The spray time was 10 s, and the post spray operation time was 50 s. The only operational variable that was changed was the liquid pressure to give different liquid flow rates. As has been discussed in Chapter 4, Section 4.7.1, a calibration curve for liquid flow rate against liquid pressure was plotted (Figure 4.13). The graph shows a linear relationship between the liquid pressure and the liquid mass delivered by the spray nozzle.

Table 6.1: Flow rate experimental conditions

Size range (μm)	Glass beads (150-250)				
Powder mass (g)	930.33				
Type of liquid	HPMC606 10% w/w				
Liquid viscosity (mPa·s)	358.46				
Liquid pressure (bar)	1	2	3	4	5
Equivalent flow rate (g/s)	0.28	0.847	1.29	1.862	2.28
The volume of air (L/min)	200				
Fluidisation velocity (m/s)	0.524				
U/Umf	13.33				
U-Umf	0.48				
Atomisation pressure (bar)	4				
Mixing time (s)	60				

6.2.2 Effect of mixing time

In this experiment, glass beads of size range 150-250 μm, ($d_{3,2}$ = 212μm) were granulated with HPMC with a viscosity of 352 mPa·s. The spray time was 10 seconds. The experiment was performed at 4 bar atomisation pressure at a superficial velocity of 0.524 m/s. The liquid pressure was at 3 bar to give a binder flow rate of 1.29 g/s and a liquid-solid mass ratio, X_{LS}, of 0.01386. The time was set from the beginning; mixing times were 10 s, 20 s, 60 s, 120 s and 300 s. The experiment was carried out in batches, and each batch was repeated three times. The operating conditions for this study are listed in Table 6.2. mPa·s.

Table 6.2: Mixing time experimental conditions

Glass beads size range (μm)	150-250				
Powder mass (g)	930.33				
Type of liquid	HPMC606 10% w/w				
Viscosity of liquid (m Pa·s)	352.36				
Liquid pressure (bar)	3				
Liquid mass (g)	12.9				
The volume of air (L/min)	200				
Fluidisation velocity (m/s)	0.524				
U/U_{mf}	13.33				
$U-U_{mf}$	0.48				
Atomisation pressure (bar)	4				
Mixing time (s)	10	20	60	120	300

6.2.3 Effect of atomisation pressure

For this experiment, glass beads ($d_{3,2}$ = 212 μm) were granulated with HPMC 352m Pa·s. The spray time was 10 seconds. The experiment was performed at a superficial velocity of 0.524

m/s, the liquid pressure was set at 3 bar, and atomisation pressure was set at 3, 4, and 5 bar. The mixing time was 60 s (Table 6.3). The experiments were performed in duplicate.

Table 6.3:Atomisation pressure experimental conditions

Glass beads size range (μm)	150- 250		
Powder mass (g)	930.33		
Type of liquid	HPMC606 10% w/w		
Viscosity of liquid (m Pa·s)	358.46		
The volume of air (L/min)	200		
Fluidisation velocity (m/s)	0.524		
U/Umf	13.33		
U-Umf	0.48		
Mixing time (s)	60		
Liquid pressure (bar)	3		
Atomisation pressure (bar)	3	4	5
Liquid flow rate (g/s)	1.31	1.29	1.29

6.2.4 Effect of fluidisation velocity

In this experiment, glass beads ($d_{3,2}$ = 212 μm) were granulated using HPMC 615 (1139.5 mPa·s). The experimental conditions are shown in Table 6.4. Operational variables were set as has been specified in the general procedure in Chapter 3. Using the calibration curve shown in Chapter 4 Section 4.7.2, the liquid pressure was 5 bar to give 13.5 g of HPMC 1138.5 mPa·s for 10 seconds of spray time (Figure 4.14). The atomisation pressure was kept constant at 4 bar. The inlet air volume was varied to give three corresponding fluidisation velocities whilst the air was pressurised at 3 bar, and air inlet volumes were 175, 200, and 250 L/min. Therefore, the bed was fluidised at velocities of 0.458, 0.524 and 0.654 m/s, respectively (Table 6.4). These air volumes were specifically chosen to keep the bed fluidised and to show noticeable differences among the three velocities. The bed was fluidised for 60 s in total.

Table 6.4: Fluidisation velocity experimental conditions

Glass beads size range (μm)	150-250		
Powder mass (g)	930.33		
Type of liquid	HPMC615 10% w/w		
Viscosity of liquid (m Pa·s)	1139.5		
Liquid mass (g)	13.631		
Atomisation pressure(bar)	4		
Mixing time (s)	60		
Liquid pressure (bar)	5		
Liquid solid fraction X_{LS}	0.0146		
Fluidisation velocity (m/s)	0.45	0.52	0.65
Volume of air (L/min)	175	200	250

6.3 Results and discussion

6.3.1 Effect of flow rate

The effect of flow rate on nuclei size distribution experiment was carried out using glass beads of 212µm size and HPMC (352 mPa·s) as the liquid binder. The droplet size measurement data is outlined in Table 6.5. There was a slight increase in the droplet Sauter mean by increasing liquid pressure and liquid mass delivered by the spray nozzle. This increased the calculated particle coating number (PCN) and the predicted fractional surface coating (F) values. The experiments were conducted in triplicate, and the size distribution results for each flow rate are shown in Appendix 6.1. 1A – 6.1.5 A. The averages of the three repeats are individually shown in Appendix 6.1.1B - 6.1. 5B. The graphs that show the whole material size distribution profile (granulated and ungranulated) are shown in Appendix 6.1. 1C- 6.1. 5 C.

Table 6.5: Liquid pressures used, the equivalent measured droplet Sauter mean, velocity with standard errors shown in brackets and the **calculated PCN values.**

Liquid pressure (bar)	**1**	**2**	**3**	**4**	**5**
Liquid mass added (g)	2.86	8.47	12.98	17.87	22.8
X_{Ls}	0.00307	0.00910	0.01395	0.01921	0.02450
Liquid mass/ total material surface (kg/m2)	0.00026	0.000786	0.001204	0.00166	0.002115
Viscous Stokes number S_{tv}	0.00863				
Droplet Sauter mean $d_{3,2}$ (µm)	28.333 (±0.58)	30.966 (±1.34)	30.333 (± 0.26)	31.133 (± 0.57)	31.766 (± 0.36)
Average droplet velocity (m/s)	7.364 (± 0.19)	8.617 (± 0.28)	9.135 (± 0.26)	8.787 (± 0.63)	9.109 (± 0.099)
Global PCN Φp	0.024	0.066	0.104	0.140	0.175
Fractional surface coating F %	0.023	0.0645	0.099	0.130	0.160
Local PCN	0.40	1.085	1.697	2.282	2.853

Figure 6.1 shows the average granule size distribution of agglomerated material obtained at each liquid flow rate, and the equivalent PCN values. Figure 6.2 shows the percentage granulated fraction.

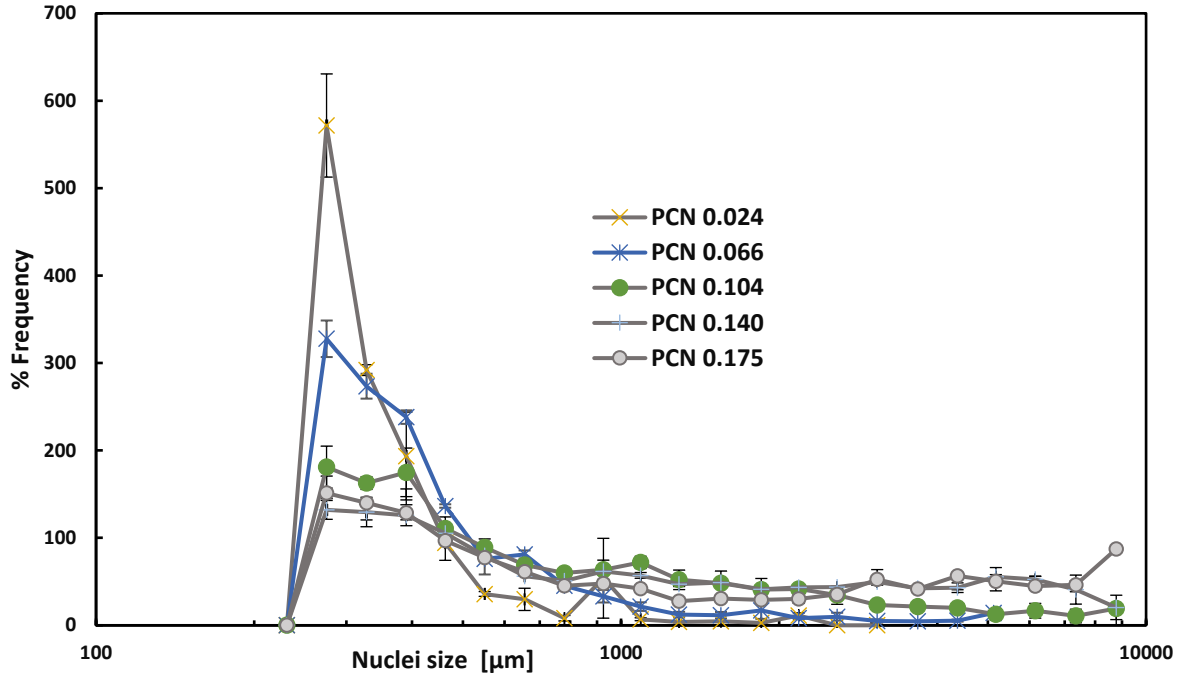

Figure 6.1: Effect of flow rate (0.28 - 2.28 g/s) and equivalent PCNs on nuclei size distribution (HPMC 352 mPa·s -212 µm glass beads). NSD of the agglomerated material is plotted against % frequency standard errors shown.

Figure 6.1 shows a large dependency of the nuclei distribution on the PCN. With the lowest PCN (0.024), equivalent to the flow rate of 0.28 g/s, the narrowest nuclei size distribution was obtained, and the nuclei sizes ranged from 0.23 mm to 1 mm. By increasing the liquid pressure to 2 bar, the PCN rose to 0.066; this resulted in an increased agglomeration, and the distribution was still relatively narrow and restricted to sizes smaller than 1 mm. Higher PCN values (0.140 and 0.175) show the largest nuclei sizes and the broadest distributions.

Figure 6.2 shows the % granulated fraction plotted against the liquid mass added as a function of PCN. The agglomerated fraction increased as the PCN increased. However, with the highest PCN (0.175) corresponding to a spray rate of 2.28 g/s, the granulated fraction doesn't exceed 27.6 %.

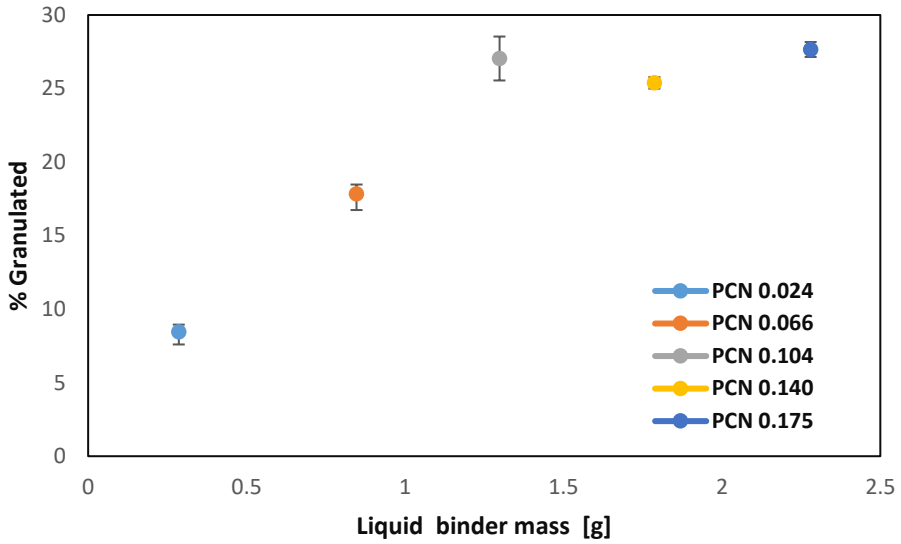

Figure 6.2: Percentage of granulated material (by mass) as a function of different PCN.

Figure 6.3 shows d_{50} of the produced granules plotted against PCN magnitude. Direct relationship between PCN and the median size of the resulting nuclei. The d_{50} of the nuclei produced with a PCN of 0.024 was 0.315 mm in size, slightly increased to 0.365 mm with a PCN of 0.066. Increasing the flow rate by approximately four times (1.29g/s) almost doubled the size from 0.31 mm to 0.54 mm.

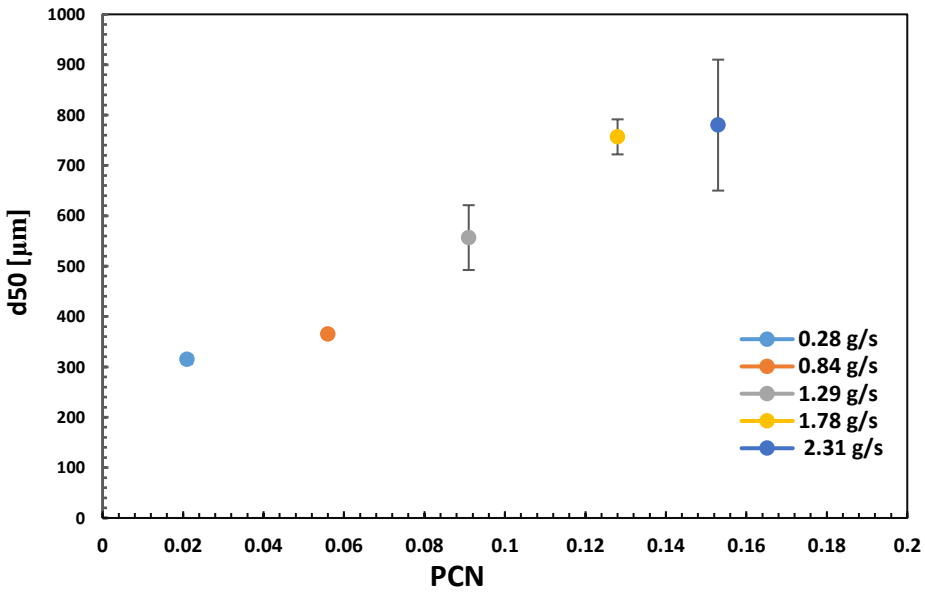

Figure 6.3: d_{50} of granules obtained plotted against PCN.

A further increase in the flow rate to 1.78 g/s (0.140 PCN) and 2.31 g/s (0.175 PCN) increased the d_{50} to 0.756 and 0.780 mm, respectively. Overall, there is a direct correlation between the PCN and the d_{50} of the nuclei size.

In the current system, where the liquid droplet is far smaller than the model particle size, the outcome of this experiment is mainly due to the changed flow rate and binder mass added (Table 6.5). According to the literature, the liquid flow rate and the droplet size play a significant role in fluidised bed granulation and control the final granule size distribution (Faure et al., 2001). The increased flow rate causes changes in the process. It influences the spray pattern and widens the spray cone's angle (Figure 4.10). The spray flux also increases as the volumetric flow increases, i.e., the density of the drops falling on the particle surface increases (Hapgood, 2000). Consequently, more liquid is available for bond formation.

The droplet size increases by increasing the flow rate (Juslin et al., 1995), however, the change in the droplet size caused by increasing the binder flow rate is smaller than that caused by the atomisation rate (Hemati et al., 2003). Drop footprint overlap will also be increased (Litster et al., 2001). This provides more liquid volume, enhances the Laplace suction and strengthens the liquid bridge.
Increased liquid mass being added per time increases the relative humidity inside the bed (Schaafsma et al., 1999) to a certain extent, leading to the liquid being adsorbed on the particle surface, enhancing the interparticle adhesion forces and eventually resulting in the wet bed quenching (Hemati et al., 2003, Walker et al., 2006).

The bed in this experiment is fluidised at turbulent velocity (0.524 m/s) and subjected to low liquid flow rates. The partially wetted particles collide at high velocities, resulting in some collisions rebounding due to the thin liquid layer available and high kinetic energy. This partial successful coalescence is evident in the low granulated fraction, characterised by small-sized nuclei and a narrow nuclei size distribution, as shown in Figure 6.1 and Figure 6.2.

At higher liquid flow rates, the particles are subjected to a higher liquid binder volumetric flow rate and increased spray flux (Equation (2.21) (Litster et al., 2001)**,** which increases the fractional surface coating, as seen in the rising F magnitude (Table 6.5). The increased amount of liquid binder helps wetted particles to form more nuclei (Tan et al., 2006) and enhances the liquid distribution due to the contact spreading (Yusof et al., 2019). However, the enlarged nuclei masses slow down and extend the residence time of the newly formed nuclei, subjecting them to new liquid droplets at the spray zone and promoting adjacent droplets to merge on the particle surface to form larger droplets.

A few large granules were formed at a flow rate of 1.29 g/s (PCN 0.104) and were poorly fluidised at the bottom of the fluidised bed because of their increased mass. The small nuclei size still dominates the distribution. This flow rate represents a start in broadening the nuclei size distribution, where smaller wet nuclei continue to impact, forming larger granules. This explains the broadening of the size distribution as the flow rate increases (Figure 6.1) despite no significant increase in the overall percentage of granulated fraction with more liquid added (Figure 6.2). This could be attributed to reaching high kinetic energy during the collision of elevated mass agglomerates, making them rebound without further growth or break (Ennis, 2005).

The drying time could be considered of limited effect as the whole experiment was conducted over a relatively short period (60 s) at room temperature (21°C). However, at low liquid flow rates (0.31 g/s and 0.81 g/s), the humidity is assumed to be less, which assists in drying the liquid droplets and minimises the opportunity for small size nuclei to undergo further growth.

In this experiment, liquid coverage, relative humidity, and increased kinetic energy were the key factors influencing the nuclei size distribution. The global PCN effectively predicted the liquid coverage and tracked changes in liquid mass, droplet size, and footprint area, and adjusted accordingly. In addition to contact angle, a parameter which wasn't changed during the experiment. The bubbling velocity was also accounted for by the local PCN and may have captured the spray coverage area, which is largely influenced by the liquid flow rate, as discussed in Chapter 3, Section 4.6.2. However, due to a lack of measurements, this was not included in the calculation, and the bed sectional area was used instead. Contributory factors such as relative humidity and drying rate need to be assessed separately.

6.3.2 Effect of mixing time

Mixing time is a process parameter that controls the exposure of the formed nuclei to mechanical agitation, drying thermodynamics, and kinetic impact energy for further growth or breakage. To design the time frame for the experiment, the interest was in the nucleation phase and the time scale it takes. Thus, it was essential to perform a study to recognise the changes that might happen in early time. With liquid mass added remaining constant, mixing time will influence the kinetics of the particulate material. As a result, the outcomes of the experiment, conducted under a specific PCN that characterizes liquid distribution, will contribute to the

impact of mixing time. Table 6.6 shows the different mixing times employed, measured droplet size, and the calculated PCN & F values.

Table 6.6: Different mixing times, the equivalent measured droplet size and corresponding PCN and F.

Mixing time (s)	10	20	60	120	300
X_{LS}	0.014				
liquid mass/ total material surface (kg/m^2)	0.0012				
Viscous Stokes number S_{tv}	0.00863				
Droplet Sauter mean $d_{3,2}$ (µm)	30.3 (± 0.26)				
Global PCN Φp	0.1056				
Fractional surface coating F	0.100				
Local PCN	1.717				

The nuclei size distribution of the three runs of each mixing time and the averages of every triplicate are shown in Appendix 6.2. A and 6.2. B respectively. The PSD graphs of the whole material obtained after the different mixing time intervals are shown in Appendix 6.2. C.

Visual inspection of the first time (10 s) mixing batch finished with stopping the spray time (10 s) showed dry spots in the bed. The binder colour wasn't distributed efficiently among the bed. Figure 6.4 below shows the averages of % granulated fraction within each time: 25.34 %, 25.02 %, 27.04 %, 26.39 % and 22.09 % at 10 s, 20 s, 60 s, 120 s and 300 s, respectively. Figure 6.5 shows the nuclei size distribution obtained after different mixing intervals.

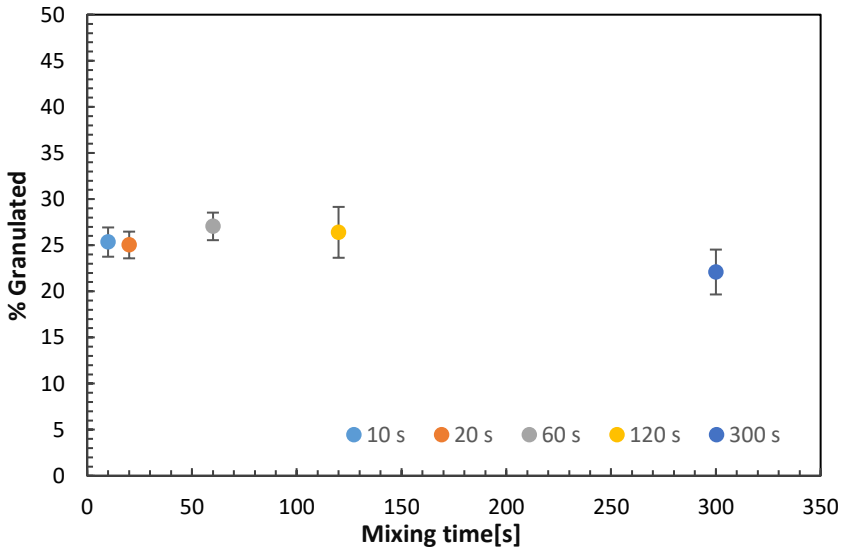

Figure 6.4: The % agglomerated material plotted against the five mixing times used (10, 20, 60, 120 and 300 seconds).

The percentages of granulated fractions after 10 and 20 seconds exhibit similarity. However, the nuclei distribution obtained at 10 s, i.e., when the spray time of 10 s finishes, has the second-

largest nuclei size (Figure 6.6). This is surpassed only by the distribution seen at 60 seconds. Subsequent to an additional 10 seconds of mixing (20 s), the distribution slightly narrows, accompanied by a minor reduction in nuclei size. Extended mixing for 60 seconds broadens the size distribution, yielding the largest granulation fraction of 27%, favouring large sized granules. After 120 s, there was a reduction in the granulated fraction. This was accompanied by the formation of smaller nuclei and a narrower size distribution. There was a further reduction in the granulated fraction from 26.3% at 120 seconds to 22% after an additional 3 minutes (300 s). Nevertheless, their size distribution profiles look almost identical (Figure 6.4).

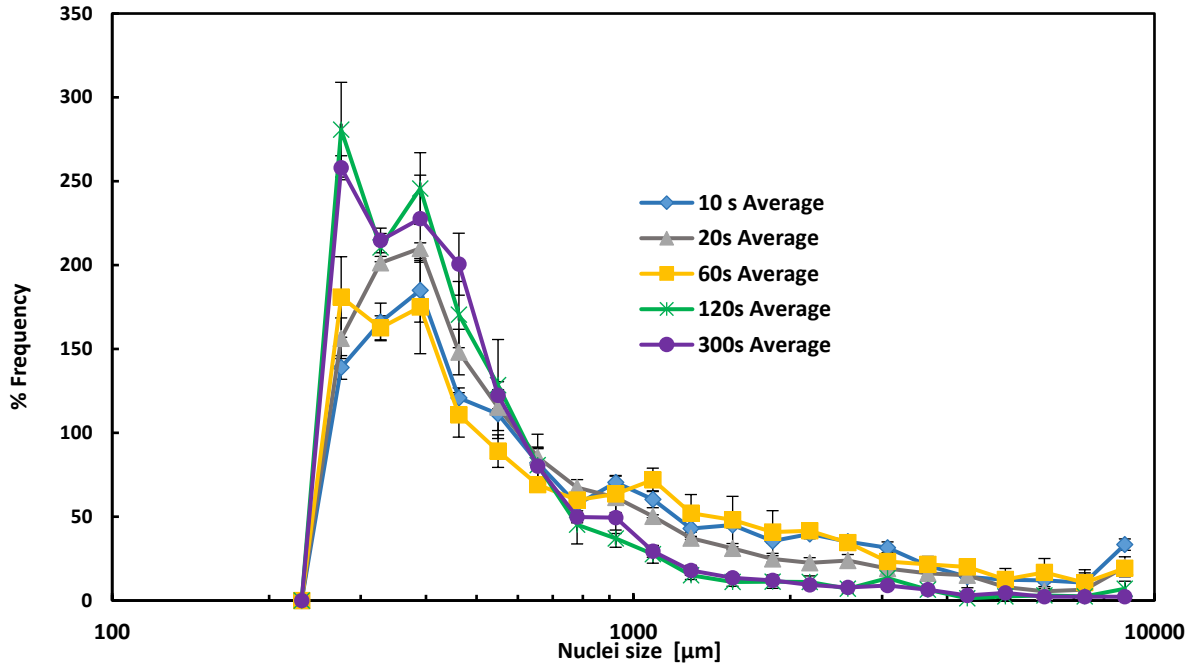

Figure 6.5: Nuclei size distribution of the granulated fraction plotted against % frequency for the five different mixing times (10, 20, 60, 120 and 300 seconds).

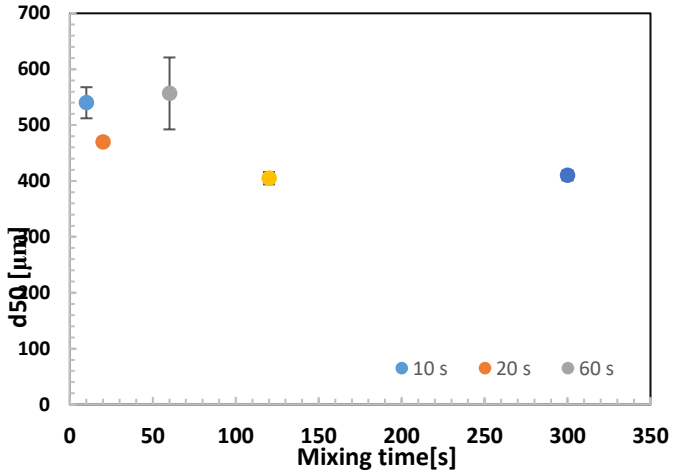

Figure 6.6: The d_{50} of the nuclei plotted against the five mixing times (10, 20, 60, 120 and 300 s).

As shown in Figure 6.6 10 s mixing time data point is associated with the largest median size (540 µm), which was mostly made on static bases after the experiment finished because the liquid binder was still able to wet inside the solid batch, and the median, in this case, isn't related to the fluidisation bed granulation. The d_{50} size of 470 µm obtained at 20 s was increased to the largest size of 520 µm at 60 s. This decreased in size to 405 µm after another 1 minute of mixing and remained unchanged after three additional minutes.

This experiment was conducted at a constant PCN of 0.105 and a fluidising velocity of 0.52 ms^1. Extending mixing time with the same liquid coating and consistent agitation increases the frequency of particle collisions, leading to increased contact spreading and potential liquid bridge formation, where the coating of particles, initial nuclei formation and drying process are taking place simultaneously. Thus, there is a general reduction in the liquid available for bond formation.

The nucleation seemed to be successful within the first two intervals (10 s, 20 s), shown in equal granulated fractions (Figure 6.4). The first 10 s produced a relatively large mean size, a d_{50} of 540 µm which dropped to 470 µm at 20 s. This suggested that it formed in a stationary bed because when the agitation stops, the powder flux stops leaving some spots extremely wet without being subjected to the fluidising air volume, and drying thermodynamics associated with fluidisation. This indicated substantial nuclei formation when the bed was static.

After 60 s time, significant change is observed, represented in the highest fraction, largest d_{50} and broadest distribution obtained (Figure 6.6). This successful coalescence suggested that the liquid coating was at the optimum, with enough liquid for bond formation. Drying might start by then. It contributes to minor evaporation of the aqueous binder, making it more viscous to assist the agglomeration process. The d_{50} is 520 µm, d_{90} is 2700 µm and 27% agglomerated fraction (Figure 6.4).

Extending mixing for two minutes increases the coating by the contact spreading with inadequate liquid for bridge formation. Weakening bridges with a drying rate becomes more effective in solidifying the liquid on the primary particles and/or nuclei surfaces. With this time, a narrow size distribution was obtained with a d_{50} of 405µm, d_{90} of 950 µm and 26% agglomerated fraction (Figure 6.4). The unchanged agglomerated fraction with a reduction of mean size means the coalescence has continued, however, breakage already started.

Continued nuclei impact for 5 minutes with high dynamic energy because of their enlarged masses will lead to their breakage (Zhai et al., 2009). This was reflected in the reduction of d_{90}

sizes from 2700 μm at 60 s to 940 μm at 300 s. The solidifying rate also becomes more effective, giving a drop in fraction from 26.39 to 22.09 %, shown in Figure 6.4, between 120 s to 300 s. Interestingly, the d_{50} remained unchanged between 2 and 5 minutes of mixing, which means new successful nucleation has stopped and only breakage occurs (Figure 6.6). One minute of mixing was chosen as the optimum time to perform other experiments.

With PCN fixed, higher kinetic energy from increased collisions and an accelerated drying process appear to be the dominant variables when mixing time is prolonged.

6.3.3 Effect of atomisation pressure

The operational parameter to be investigated is the pneumatic atomisation pressure, which directly controls the droplet size and the PCN. HPMC 352 mPa·s liquid binder was pressurised at 3, 4 and 5 bar pneumatic pressure. All other operational parameters were held constant (Table 6.3). The atomisation pressures used, the corresponding calculated PCN and viscous Stokes number are illustrated in Table 6.7. Appendix 6.3. A (3 -5 bar) shows the two runs of the same experiment.

Table 6.7: Atomisation pressures used, the equivalent measured droplet Sauter mean, velocity with standard errors shown in brackets **and the corresponding calculated PCN & F values.**

Atomisation pressure (bar)	3	4	5
Liquid mass (g)	13.1	12.90	12.97
Liquid mass/ total material surface (kg/m^2)	0.0012		
X_{Ls}	0.00140	0.00138	0.00138
Viscous Stokes number S_{tv}	0.00863		
Droplet Sauter mean $d_{3,2}$ (μm)	34.23 (±0.69)	30.96 (±1.34)	30.26 (0.45±)
Average droplet velocity (m/s)	8.071(±0.17)	9.135(±0.26)	8.48(±0.19)
Global Particle coating number PCN Φ_p	0.093	0.101	0.102
Fractional surface coating F%	0.089	0.0968	0.0969
Local PCN	1.65	1.65	1.52

Appendix 6.3. B (3–5 bar) shows the size distribution of the whole material. The binder droplet Sauter mean is in Table 6.7. was reduced as the atomisation pressure increased. However, this correlation between the 4 and 5 bars is unclear.

Figure 6.7 shows the average percentage of agglomerated material produced at atomisation pressures of 3, 4, and 5 bars. As atomisation pressure increased, the granulated mass increased;

22.9 %, 28.5 % and 30.8 % granulated fractions were obtained by 3, 4 and 5 air pressures, respectively.

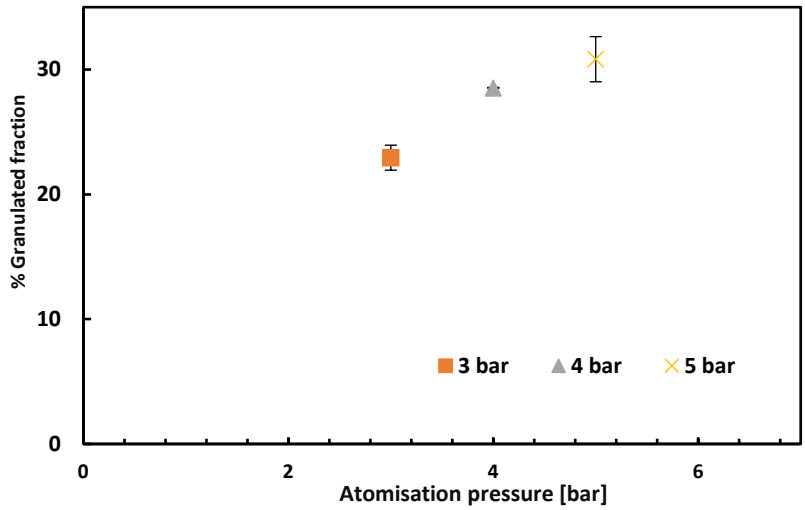

Figure 6.7: Average total percentage of granulated mass to the total bed mass plotted against 3, 4, and 5 bar atomisation pressures.

Figure 6.8 shows the d_{50} (a) and d_{90} (b) of nuclei obtained at atomisation air pressures of 3, 4 and 5 bar. There is an indirect relationship between atomising pressure and the nuclei size.

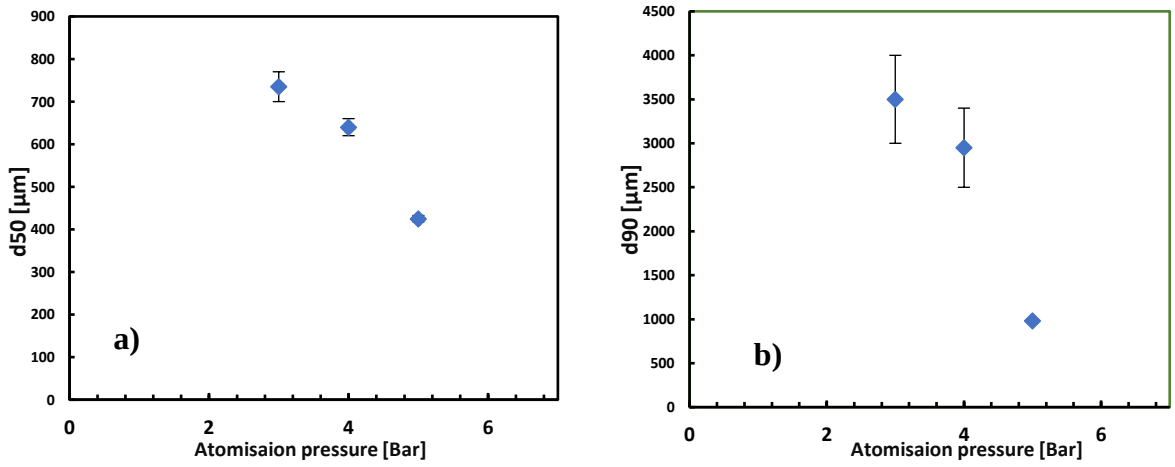

Figure 6.8: (a) d_{50} of produced nuclei size and (b): d_{90} plotted against the atomisation air pressure.

The highest pressure, 5 bar, produced the largest agglomerated fraction with the smallest mean size (d_{50} is 425 µm). In contrast, the lowest atomisation pressure 3 bar, produced the smallest agglomerated fraction with the largest mean size of 735µm. The d_{90} also shows the same trend: 980, 2950 and 3500 µm for 3, 4 and 5 bar atomisation pressure respectively. Figure 6.9 shows

the d_{50} of produced nuclei as a function calculated of PCN. The tight range of PCN (0.093-1.02) reflects the small differences in the droplet mean size when the X_{LS} is constant.

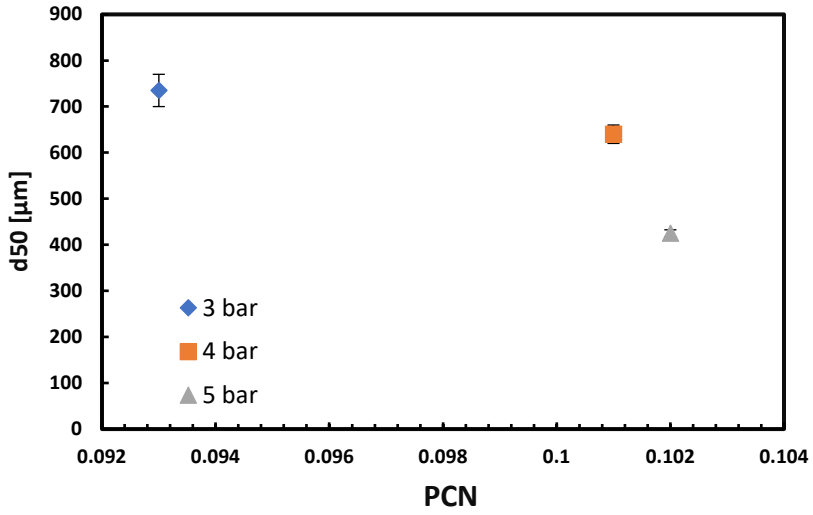

Figure 6.9: d_{50} of the produced nuclei versus PCN.

There is a direct relationship between PCN and the mean droplet size. However, the PCN at 4 bar was slightly higher than predicted, which could be attributed to a slightly high measured droplet mean size with a high standard error (Figure 6.9). Figure 6.10 shows the average nuclei size distributions of the granulated material.

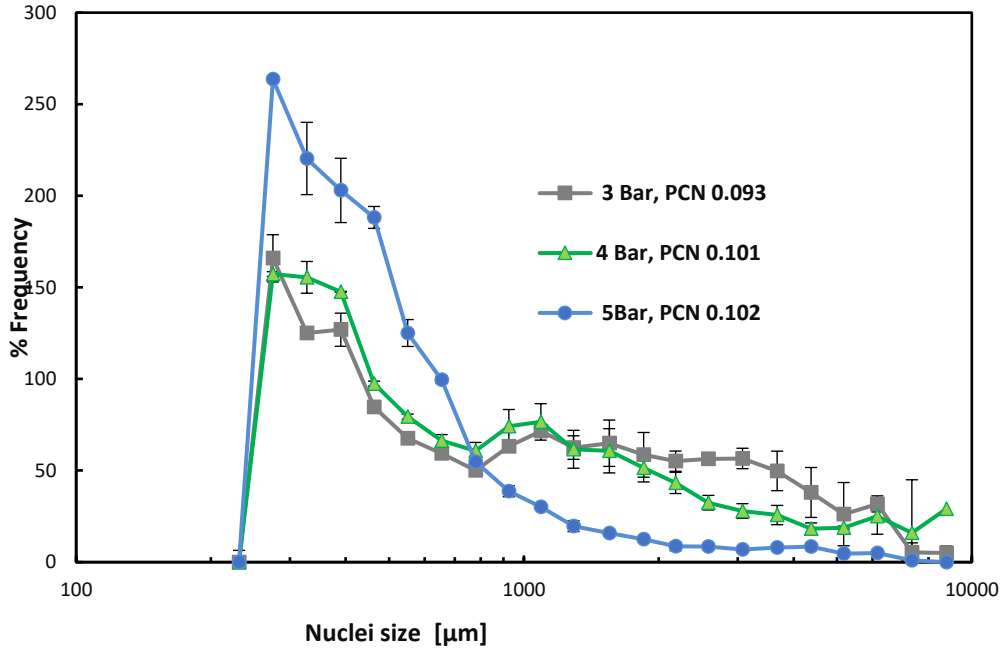

Figure 6.10: Nuclei size distribution of glass beads (d3,2 = 112 µm) granulated with 10% HPMC 352.36 mPa·s at 3, 4 and 5 bar atomisation pressure.

As shown in Figure 6.10, the narrowest nuclei size distribution is given by the highest atomisation pressure, 5 bar and vice versa.

Based on the literature, increasing the atomisation pressure typically reduces droplet size; however, increasing the pressure to the highest level does not reduce the size any further (Juslin et al., 1995). The results of this experiment are in agreement with the literature. Changing the air pressure inside the nozzle from 3 to 4 bar was accompanied by a change in droplet size, as shown in

Table 6.7, with almost no further reduction observed with 5 bar. However, the droplet mean size recorded with 4 bars showed a high error (

Table 6.7). Also, minimising the droplet size usually decreases the granule size (Burggraeve et al., 2013, Schœfer, 1978, Schaafsma et al., 2000, Tan et al., 2006). This experiment exhibited similar behaviour to that reported (Figure 6.8).

The high fraction with the narrower distribution obtained by increased atomising air pressure to 5 bar could also be explained by a faster drying rate (Dewettinck and Huyghebaert, 1998). Increased air volume decreases the droplet volume and weakens the bond strength to hold multiple particles, resulting in small nuclei sizes (Bouffard et al., 2005). Also, it accelerates the solidification of the liquid and terminates the coalescence process at small nuclei sizes without growing further to form larger nuclei.

On the other hand, due to raised airflow, the binder solution droplets become more susceptible to evaporation, and the viscosity of the system could be altered to be more effective due to the water loss and increased concentration.

Reduced droplet size means less liquid volume available on the surface to form new liquid bridges and less Laplace suction in the pendular state (Ennis, 2005, Rhodes, 2008, Seville et al., 2000), especially with the continuing increasing mass of the nuclei, and the bridge strength becomes weaker to hold the nuclei structure. Additionally, increased air velocity in the spray zone will increase the impact energy between the particles during the spray time. These factors control the success of liquid bridge formation, narrowing the size distribution (Figure 6.10). Applying lower atomisation pressure increases larger droplets' chance of merging over the particle surface, providing extra liquid to form a more effective liquid bridge to hold more particles within the nuclei matrix. Also, reduced atomising air in the spray zone keeps the drying rate low, the dynamic energy of particle collision low, and the liquid viscosity is not significantly altered.

The highest atomisation pressure resulted in the largest agglomerated fraction (Figure 6.7) the narrowest size distribution (Figure 6.10) and the smallest mean nuclei size (Figure 6.8 and Figure 6.9). Such successful nucleation, achieved by increasing atomisation pressure, can likely be attributed to the reduction in droplet size and footprint area, as well as the increased number of droplets, leading to improved liquid dispersion (Litster et al., 2001, Schaafsma et al., 2000). This conclusion is further supported by the rise in PCN magnitude. Although the X_{LS} was slightly higher at the lowest atomisation pressure of 3 bars, the PCN increased with rising atomisation pressure (Table 6.7).

The impact of small changes in PCN caused by atomisation pressure variations is critical, as even slight can lead to significant shifts in the nuclei size distribution. Increased kinetic energy and accelerated drying rate, resulting from higher air volume, contribute to the reduction in nuclei size.

Effect of fluidisation velocity

Exploring different superficial fluidisation velocities for the same particulate material, liquid binder, and PCN magnitude (Table 6.8) will show the effect of the changing kinetic energy during particle-particle impacts, increased drying rate and solidifying of the liquid because of the heat transfer. The effect of changing the surface renewal rate in the spray zone whilst the volumetric spray flux is kept constant also could be considered. The experiment was performed using the highest viscosity system, HPMC 1139 mPa·s, to promote successful granulation and clarify the effect of the air velocity as much as possible.

Table 6.8: Fluidisation velocities with calculated PCN & F. Droplet Sauter mean with standard error is shown in brackets.

Volume of air (L/min)	175	200	250
Fluidisation velocity (m/s)	0.45	0.52	0.65
Viscous Stokes number S_{tv}	0.0028	0.0028	0.0028
Liquid mass/ total material surface (kg/m^2)	0.0011		
Droplet Sauter mean (µm)	38.6 (±0.416)		
Global PCN Φ_p	0.077		
Fractional surface coating F%	0.074		
Local PCN Φp	1.192		

The three air volumes were explicitly chosen to keep the bed fluidised and to show noticeable differences among the three velocities. They were relatively high to maintain turbulent

fluidisation of the high-density particulate material without loss through the freeboard. They resulted in relatively similar granulation profiles, but differences were still observed. Also, the highest viscosity solution (HPMC 1138 mPa·s) was selected to obtain a considerable granulated fraction.

The fact that the binder was dyed allowed for the analysis of liquid dispersion. The intensity of the colour of the whole material granulated at a higher velocity of 0.65 ms^{-1} was more than that granulated with the same liquid at lower velocities.

Figure 6.11 shows the percentage agglomerated fraction obtained at the different fluidisation velocities. Even though there are no clear differences between the three air velocities in Figure 6.11 (a), a significant variation could be found when looking closely at specific nuclei sizes in Figure 6.11 (b). When the velocity increased from 0.49 ms^{-1} to 0.65 ms^{-1}, the fraction of nuclei

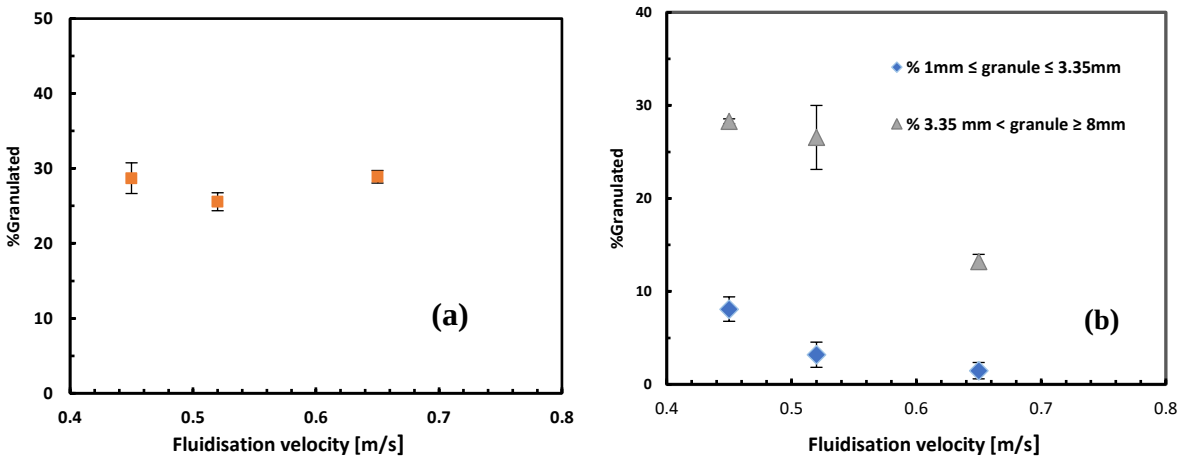

Figure 6.11: (a) The percentage agglomerated fraction obtained at the 0.45, 0.52 and 0.65 m/s (28.7, 25.5 and 28.9 %), respectively, (b) % fractions of specified size (1 mm ≤ granule size ≤ 3.35mm) and (3.35 mm < granule size ≥ 8mm).

size larger than 1mm and smaller than 3.35 mm was significantly reduced from 28 % to 13 % (Figure 6.11 b). Also, the fraction of nuclei size larger than 3.35 mm has declined from 8 to 1.4 %. This was calculated by the mass of nuclei larger than the sieve size of 335 mm, divided by the total nuclei mass. This means that most agglomerated fraction produced by the highest velocity was of nuclei size smaller than 1000 μm.

Figure 6.12 shows the nuclei size (d_{50}) produced at different fluidisation velocities. The mean nuclei size decreased as the fluidisation velocity increased. d_{90} of the nuclei produced also follows the same trend.

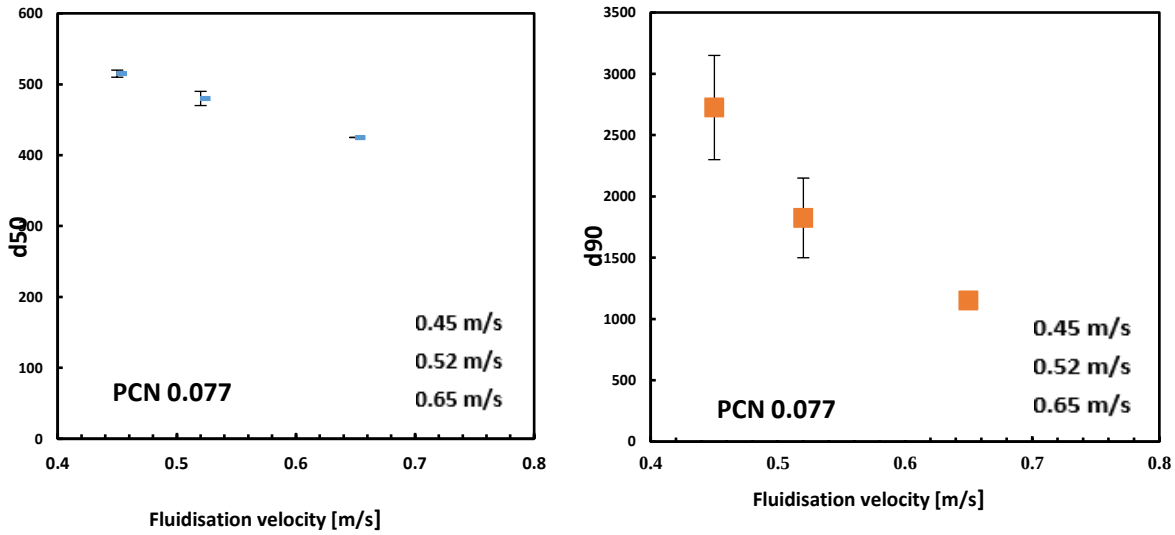

Figure 6.12: (d_{50}) and (d_{90}) of the nuclei produced as a function of fluidisation velocity.

Figure 6.13 shows the nuclei size distribution (NSD) of glass beads granulated at different fluidisation velocities of 0.45, 0.52 and 0.65 m/s. The two repeats are shown in Appendix 6.4 A. (0.45-0.65 m/s). The size distribution profile of both granulated and non-granulated material is shown in Appendix 6.4B.(0.45 –0.65 m/s).

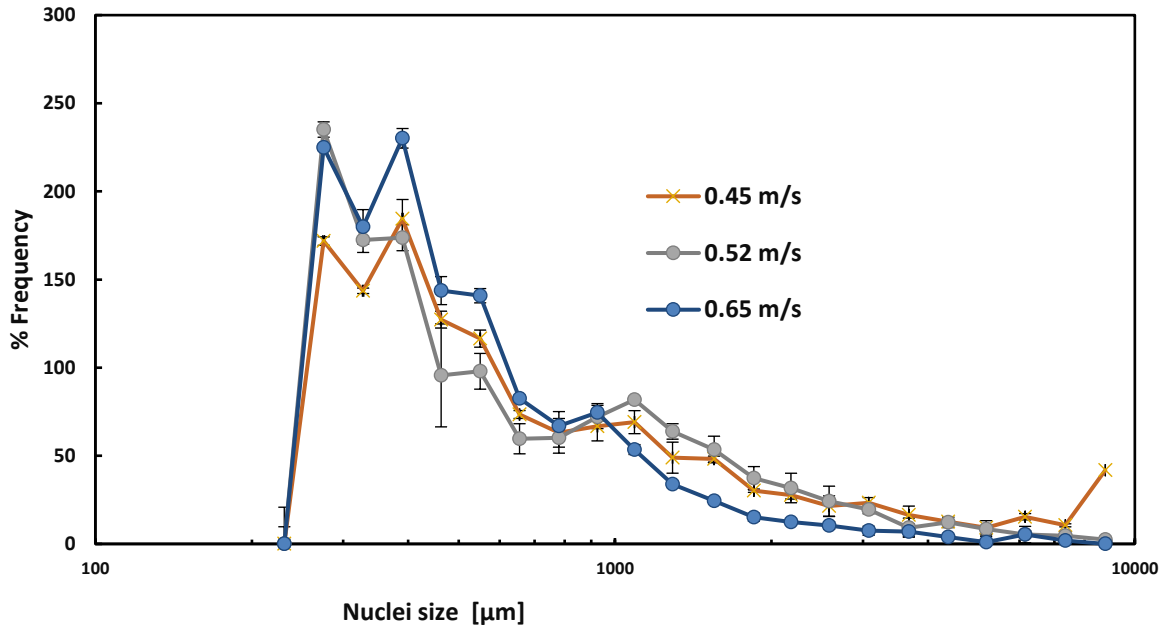

Figure 6.13: Effect of fluidisation velocity on the nuclei size distribution of glass beads $d_{3,2}$= 212 µm with 10% HPMC 1139 mPa·s.

The nuclei size distribution in Figure 6.13 shows the highest velocity of 0.654 m/s, resulting in the narrowest distribution size profile.

This experiment was conducted under three distinct air velocities and similar liquid distribution with constant PCN. Due to the high density of the model particles, high velocities were selected to be sufficient to fluidise the bed throughout the experiment.

Despite the equal liquid binder mass added, visual inspection showed that the bed operated at the highest velocity was of the highest colour intensity, suggesting that the liquid binder was subjected to more contact spreading due to the frequent collision, by time the volume of liquid reduced, and the coating fraction increased, and the growth becomes by the layering mechanism.

An increased impact rate between particles increases the probability of successful liquid bridge formation. Tan (2005) found that granules formed in an environment with increased turbulence may exhibit greater strength because such an environment takes more liquid to make successful particle coalescence effectively (Tan et al., 2006). This is evident in the highest granulated fraction with the narrowest size distribution. Also, raising the fluidisation velocity from 0.49 ms^{-1} to 0.65 ms^{-1}, the fraction of nuclei size between 1 and 3.35 mm has declined by almost a third (from 28 % to 13 %), and the fraction larger than 3.35mm has dropped from 8 to 1.4% (Figure 6.11 b).

There is an indirect relationship between the mean nuclei size produced and the velocity of the fluidising air (Figure 6.12). This suggests that the high kinetic energy of the primary particles or the small nuclei during the collision would reduce the capability of the system to dissipate this energy. Increased fluidisation velocity also increases powder flux in the spray zone (Iveson et al., 2001, Litster et al., 2001). Hence, more powder subjected to the spray nozzle droplets would prevent the rewetting by droplet merging or overlapping (Schaafsma et al., 1999). This ultimately reduces the available volume of liquid for forming new liquid bridges, resulting in nuclei of small size.

Moreover, the high velocity contributes to large nuclei breakage due to the enlarged impact energy (Smith and Nienow, 1983). Additionally, the highest velocity will accelerate the drying and solidification rate of the system. This will hinder or stop the coalescence process and yield a better contact spreading bed with a large agglomerated fraction of a narrow distribution (Figure 6.11).

In this study the highest viscosity (HPMC 1138 mPa·s) was selected to obtain a considerable granulated fraction with a narrow range of velocities to avoid material loss through the column freeboard. Higher fluidising velocities with lower viscosities would be recommended.

The increased fluidising velocity produced finer granulation and reduced the d_{50}. The viscous Stokes number for the three velocities remained constant (0.0028) because of the same excess air velocity ($U-U_{mf}$) used, and equal calculated bubbling velocity (Equation (2.8). This provides the system with similar viscous dissipation forces regardless of the applied fluidisation velocity. Liquid distribution described by PCN magnitude remained constant, and the outcome would be referred to factors as drying rate, surface renewal rate and frequency of particle collisions.

6.4 Conclusion:

In the liquid mass experiment, lower flow rates resulted in smaller droplets. The faster surface renewal rate prevents droplet coalescence and produces smaller, more narrowly distributed nuclei. In contrast, higher flow rates promoted droplet merging, leading to larger nuclei. Increased relative humidity within the bed strengthened liquid bridges and improved interparticle adhesion. Introducing more liquid into the system caused larger granules to become less fluidised.

Both global and local PCN values increased with rising flow rates, reflecting changes in X_{LS}, droplet size, and droplet footprint. This increase in PCN improved the success of nucleation distribution within the fluidised bed, resulting in larger mean nuclei sizes and a greater overall granulated fraction. Furthermore, the higher PCN broadened the nuclei size distribution until no clear correlation could be observed, suggesting that granules might be formed through a distribution–immersion mechanism. Local PCN may have captured the spray coverage area, which is primarily influenced by the liquid flow rate, as discussed in Chapter 3. However, due to the absence of relevant measurements, this was excluded from the calculation, and the bed sectional area was used instead. Based on the characteristics of the model particle and equipment used, the local PCN was approximately 15 times higher than the global PCN. This ratio may decrease with improvements in equipment features.

In mixing time experiment, extended mixing showed two phases: a growing phase followed by size reduction. Initially, the size distribution broadened with higher yield due to coalescence, but further mixing narrowed the distribution and reduced mean size because of breakage. Over time, the drying rate became more efficient, leading to a decrease in mean size and granulated fraction, likely due to binder solidification and subsequent breakage of large nuclei.

The broad size distribution recorded at zero time mainly resulted from granule formation by wet powder while static. With a constant PCN, extended mixing time led to a decrease in the

efficacy of liquid surface coverage due to continued drying, spreading, and the associated kinetic energy. These factors appear to be the dominant variables.

The alteration of atomisation pressure affected the droplet size and significantly impacted the distribution nucleation process. Increased atomisation pressure increased the agglomerated yield and narrowed the nuclei size distribution towards small nuclei sizes. Conversely, lowered atomisation pressure reduced the agglomerated yield and broadened the size distribution. The enhanced nucleation process is due to better liquid dispersion obtained by the high atomisation pressure via reduced droplet size and increased droplet number. Increased air volume and velocity in the spray zone may accelerate the drying rate and enhance the viscosity due to water evaporation. This narrows the size distribution towards small sizes. PCN captured the changes in droplet size and droplet footprint and changed accordingly. Local PCN is able to capture the surface coverage area too which is affected by atomisation pressure. Care should be taken when adjusting atomisation pressure, as changes in PCN can significantly affect the process.
The distribution nucleation improved with rising air velocity. The highest velocity yielded the largest fraction of nuclei with a narrower distribution toward smaller sizes, likely due to increased particle collisions. Additionally, accelerated binder solidification could minimise further liquid bridge formation. Furthermore, viscous dissipation becomes less effective at countering particle rebound, and more breakage occurs. With a constant PCN, higher velocity enhances powder flux throughout the spray zone, leading to better liquid distribution due to a reduced amount of binder picked up per unit of powder. It was concluded that higher velocity promotes finer granulation through distribution nucleation, while PCN lacks the capacity to predict the outcome. In addition, viscous dissipation becomes less effective in countering particle rebound, With constant PCN, higher velocity enhances the powder flux throughout the spray zone, which results in an evenly distributed liquid due to the reduced amount of binder picked up per unit of powder. It was concluded that the higher velocity promoted finer granulation via the distribution nucleation, and the PCN has no capacity to predict the outcome.

This chapter explored the effect of operational parameters on granulation via distribution nucleation using the small-scale fluidised bed. The agglomerated fraction obtained by distribution nucleation of the glass beads-HPMC solution system didn’t exceed 30%. The liquid binder mass added has the most dominant influence on the PCN value, the agglomerated fraction, and the agglomerated size distribution profile.

Chapter 7: PCN Case Study: Granulation of pharmaceutical lactose in the fluidised bed

7.1 Introduction

To explore what impact the material properties have on distribution nucleation whilst the liquid distribution is similar, a pharmaceutical excipient, Capsulac 60 (lactose), was chosen to replace the model material, the glass beads. Primarily, glass beads were employed as model particles to simplify the complexity associated with surface attributes like morphology, roughness, porosity for liquid penetration and rigidity. Subsequently, the use of Capsulac 60 aimed to provide insight into variations in powder characteristics and how they influence binder surface coverage and the resulting nucleation outcomes.

The results using glass beads presented in Chapter 6.1 showed that the PCN could predict the liquid surface coverage by changing the liquid mass introduced to the system and consequently the granulation outcome. Hence, the experiment was repeated using capsulac 60. To relate to both studies, the selected mean particle size of the powders was comparable, and the PCN applied was attempted to be equivalent. This was done by adjusting the liquid mass added to capsulac 60 to match the previously calculated PCN for glass beads using Equation(3.5).

7.2 Materials

Capsulac 60 is a coarse sieved crystalline material of alpha-lactose monohydrate from Meggle® Germany with good flow properties primarily used for capsule filling.

The main characteristics of the liquid binder solution used in the study, HPMC 352 mPa·s, are presented in Table, Table 3.9,Table 3.10 and Table 3.11.

Characterisation methods were mentioned in Chapter 3. The main Capsulac 60 and the model particle glass characteristics are illustrated in Table 7.1 for comparison.

Table 7.1: Particulate material properties used in the experiment.

Material used	Capsulac 60	Glass beads
Size range (μm)	150-250	150-250
Surface mean $d_{3,2}$ (μm)	190.9	212
The volume mean $d_{4,3}$ (μm)	207.5	219
d_{10} (μm)	134.6	170
d_{50} (μm)	201.4	216
d_{90} (μm)	294.5	271
True particle density (g/cm^3)	1.54	2.504
Bulk density (g/cm^3)	0.66	1.462
Bed porosity (%)	52.41	37.97
Minimum fluidisation velocity U_{mf} (m/s)	0.027	0.039
Malvern specific surface area (m^2/kg)	20.51	11.44

7.3 Methods

To relate this study to the flow rate study of the glass beads, capsulac 60 ($d_{3,2}$ =190.9 μm) was granulated with the same liquid binder HPMC 352 mPa·s. The size range of the two powders was the same, and the $d_{3,2}$ are similar. The operational conditions used for the two materials in the flow rate experiments are given in Table 7.2. Two of the operational variables were changed.

Firstly, the volume of the air used due to differences in U_{mf} to keep U-U_{mf} = 0.49 ms^{-1}. Secondly, the liquid pressure was changed to give different liquid flow rates equivalent to that applied for the glass beads in Chapter 6.1.

The corresponding X_{LS} and liquid pressure were found using the calibration curve presented in Figure 4.13. Chapter 4, Section 4.7.1.

When the experiment was designed, the PCN was previously calculated based on X_{LS}, specific surface area and droplet size. Accordingly, PCN for capsulac 60 was attempted to be comparable and the liquid mass was added to match the bed surface area of the two powders. This comparability in PCN couldn't be achieved because the contact angle incorporated into PCN created differences in PCN magnitude for both materials.

The droplet sizes also were estimated using the laser data used for the glass beads.

Table 7.2: Flow rate experimental conditions for glass beads and capsulac 60 (150-250 µm)

Size range (µm)	Capsulac 60 (150-250)					Glass beads (150-250)				
Liquid pressure (bar)	0.81	1.72	2.42	3.22	3.99	1	2	3	4	5
Liquid mass added (g)	2.22	6.72	10.23	14.12	18.1	2.8	8.47	12.9	18.62	22.8
X_{Ls}	0.0053	0.016	0.024	0.033	0.043	0.0030	0.009	0.014	0.019	0.0245
Powder mass (g)	420.08					930.33				
The volume of air (L/min)	193					200				
Fluidisation velocity (m/s)	0.507					0.524				
U-Umf	0.491									
Type of liquid	10% w/w HPMC606									
Liquid viscosity (mPa·s)	358.46									
Atomisation pressure (bar)	4									
Mixing time (s)	60									

Figure 7.1 shows a trend line derived from PIV laser droplet size measurements corresponding to the flow rates used in the glass beads experiment to be employed to estimate the droplet sizes for the capsulac 60 experiment.

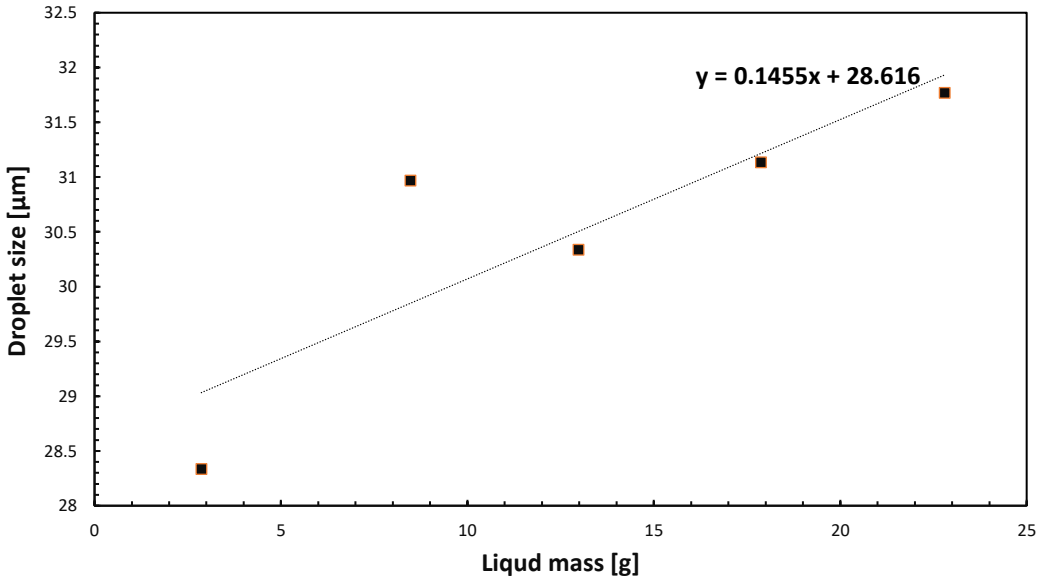

Figure 7.1: The Sauter mean of liquid binder droplet measured by PIV laser versus HPMC 352 mPa·s solution mass added in the glass beads experiment. A trend line equation was used to estimate the droplet size in capsulac 60 experiment.

The second data point in Figure 7.1. which shows the trend line correlating droplet Sauter means obtained by PIV laser by liquid mass added, appears anomalous. However, when considering the higher error value reported with this point in Table 6.5, this anomaly might be

attributed to instrumental error. However, that should be investigated further. This point could not be replicated due to equipment inaccessibility. Nevertheless, given the relatively narrow difference, it still doesn't significantly affect the estimated mean size.

7.4 Results and discussion

The comparison between the nucleation behaviour of the glass beads and the capsulac 60 permits understanding the differences in material characteristics. The liquid mass added was to match the bed surface area in both experiments. However, PCN is different because of the differences in the contact angle and affinity for the binder type. Solid mass fraction also was different because of the differences in the densities of the materials. Table 7.3 presents the calculated global PCN and other liquid distribution parameters for the two powders. Some experiment results presented in Chapter 6 Section 6.3.1 will be recalled where relevant for comparison with the capsulac 60 experiment outcome.

The experiments were conducted in duplicate, and the size distribution results for each flow rate are shown in Appendix 7.1. 1A – 7.1. 5A. The graphs that show the whole material size distribution profile (granulated and ungranulated) for each flow rate are shown in Appendix 7.1. 1B- 7.1. 5B.

Table 7.3: Liquid distribution parameters for capsulac 60 and glass beads. For capsulac 60, the droplet Sauter means are estimated.

Material	Contact angle (◦)	Liquid mass added (g)	Droplet Sauter mean (µm)	X_{Ls}	liquid mass/ material surface area (kg/m^2)	Global PCN Φp	Fractional surface coating F	Local PCN
Capsulac 60	58.95	2.22	28.93	0.00529	0.00026	**0.035**	0.0344	**0.336**
		6.72	29.59	0.01600	0.000786	**0.096**	0.0918	**0.914**
		10.23	30.10	0.02437	0.001197	**0.151**	0.140	**1.43**
		14.77	30.76	0.03517	0.001727	**0.316**	0.271	**3.00**
		18.09	31.24	0.04307	0.002115	**0.387**	0.321	**3.68**
Glass beads	82.37	2.86	28.33	0.003078	0.00026	**0.024**	0.023	**0.400**
		8.47	30.96	0.009108	0.000786	**0.066**	0.0645	**1.085**
		12.98	30.33	0.013954	0.001204	**0.104**	0.099	**1.697**
		17.87	31.13	0.019215	0.00166	**0.140**	0.13	**2.282**
		22.8	31.76	0.024507	0.002115	**0.175**	0.16	**2.853**

Visual inspection of the processed material showed a gradual increase in colour intensity for both capsulac 60 and glass beads, reflecting the increased liquid mass added. Figure 7.2 shows both materials with the highest PCN appeared chunky. However, in capsulac 60 batches, the chunks were less cohesive and easier to sieve.

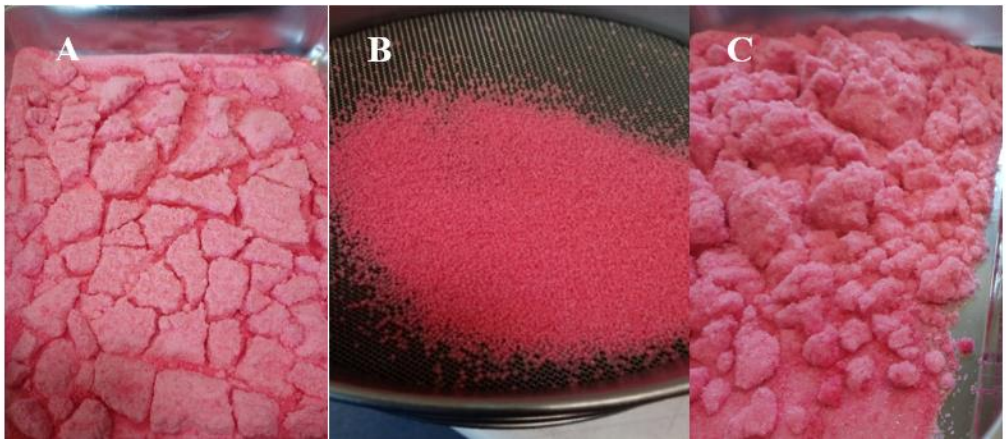

Figure 7.2: The processed batch of capsulac 60 of PCN 0.387 full of nuclei (A) appeared chunky, less cohesive (B) and easier to sieve. (C) The chunky glass beads batch of 0.175 PCN.

Figure 7.3 shows lactose nuclei examined under light microscope. They displayed an open structure without any consolidation or trapped liquid. Individual particles within the nuclei structure remained recognisable.

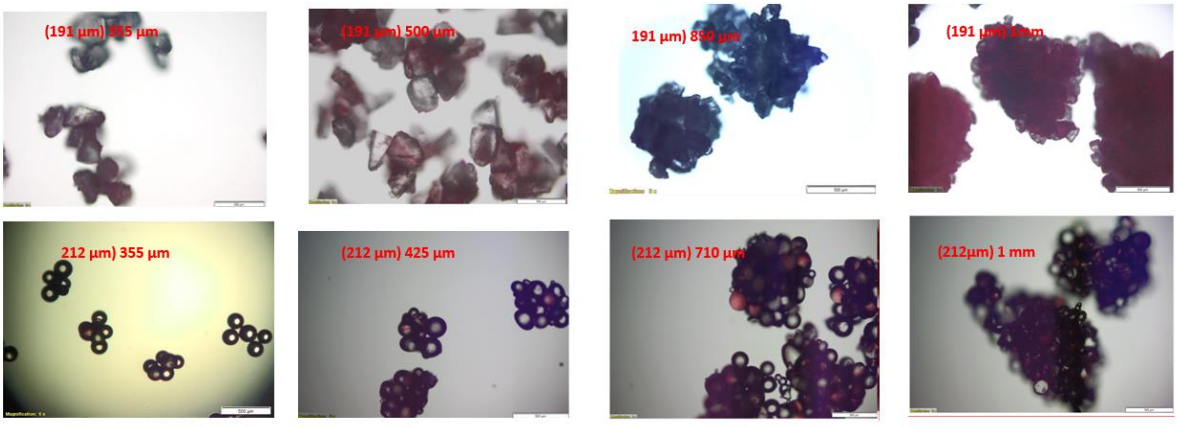

Figure 7.3: Capsulac 60 and glass beads nuclei of different sizes obtained by HPMC1139 mPa·s under optical microscope.

By comparing the agglomerated fraction obtained by the two systems in Figure 7.4, it is evident that capsulac 60 produced a substantially higher agglomerated percentage than glass beads, especially at high PCN in the given data. At the smallest PCN values, capsulac 60 had a slightly

higher agglomerated fraction (11.2 %) than 8.4 % for glass beads. As the PCN increases, the difference gradually duplicated to reach 65% of capsulac 60 agglomerated at 0.387 PCN against 27% at 0.175 PCN for glass beads.

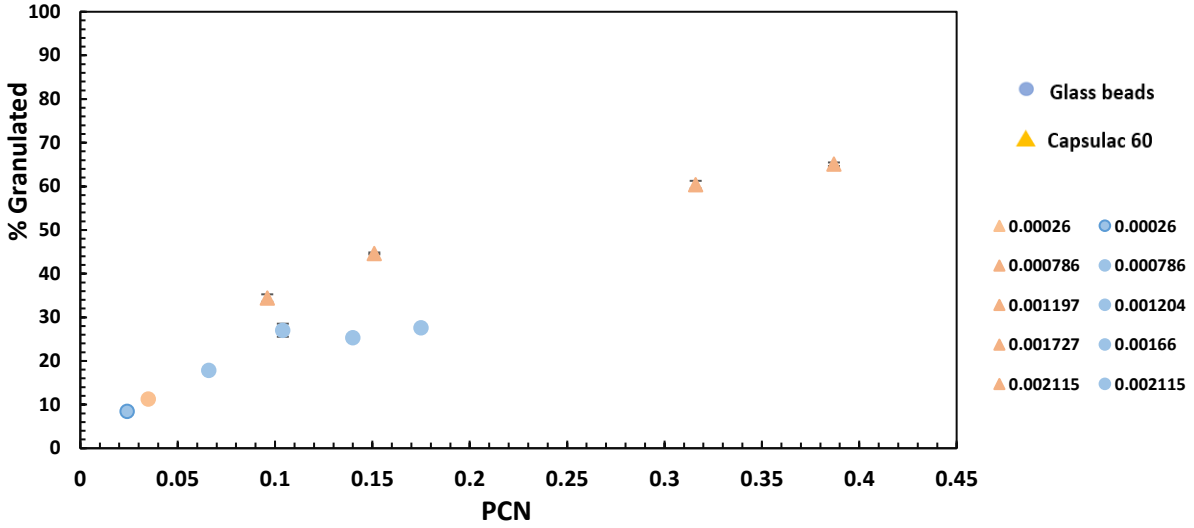

Figure 7.4: The % granulated by mass against the PCN magnitude as a function of HPMC 352 mPa·s mass added capsulac 60 and glass beads bed surface area.

The binder mass added is proportional to the SSA, although less liquid was added to capsulac 60 to match its smaller SSA, the PCN values enormously increased compared to those for glass beads. The d_{50} of granulated material for both systems as a function of PCN values is shown in Figure 7.5.

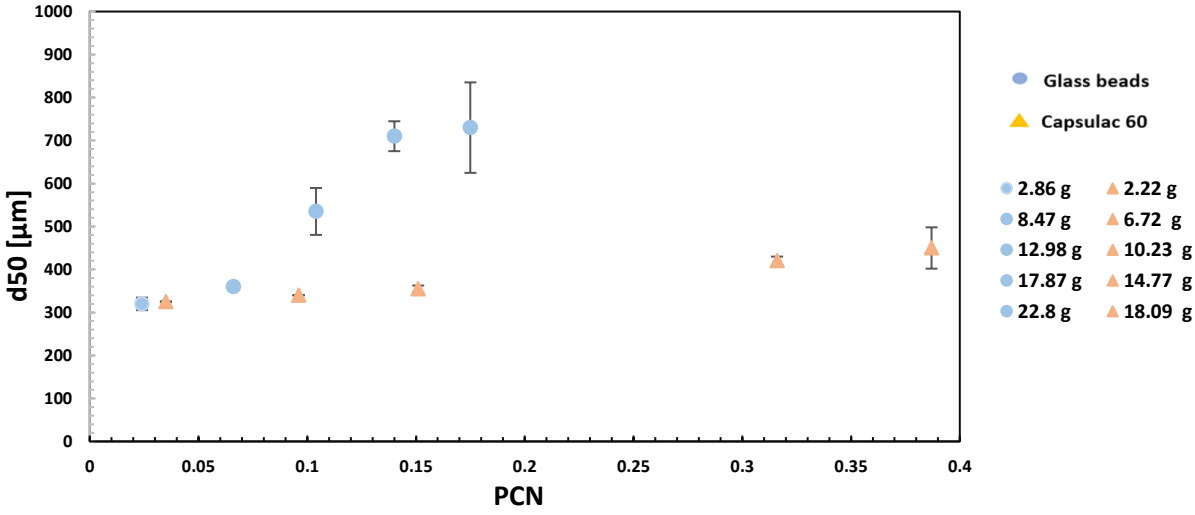

Figure 7.5: d_{50} of nuclei produced against PCN as a function of HPMC 352 mPa·s mass added for the capsulac 60 and glass beads systems.

The glass beads showed fast growth in d_{50} size, whereas the capsulac 60 system showed a slower correlation. The d_{50} of the glass beads reached 710 and 730 µm with 0.140 and 0.175 PCN values, respectively. While the capsulac 60 d_{50} were 420 and 450 µm at PCN values of 0.316 and 0.387, respectively.

The particle size distribution is plotted against frequency for the whole material in Figure 7.6. The two distributions appeared similar and followed the same trend. The peak was at the mean particle size of the two powders, where the first considered nuclei size is 275 µm. Generally, capsulac 60 seems to have a narrower distribution.

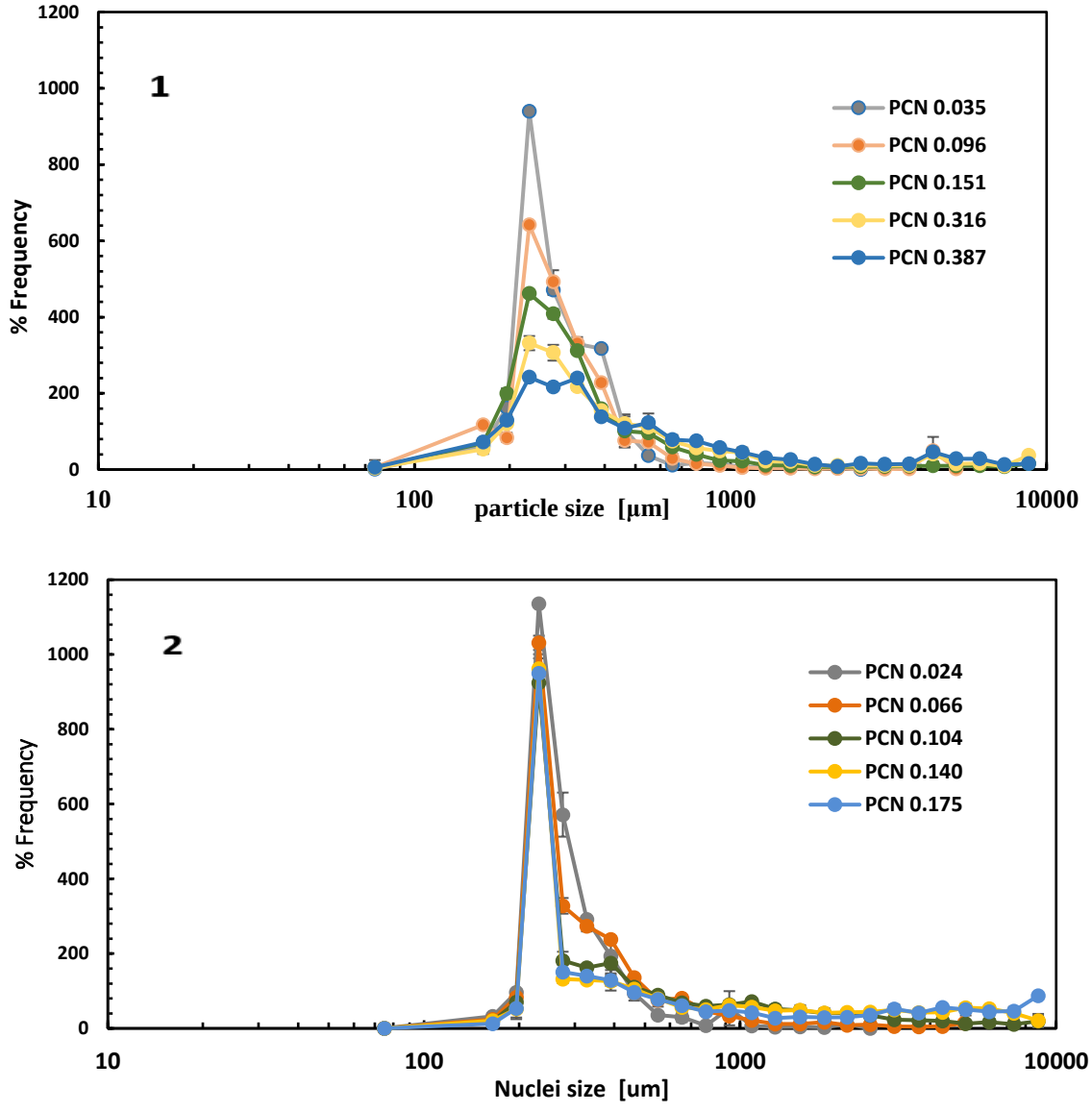

Figure 7.6 The particle size of the whole produced materials against frequency as a function of PCN for Capsulac 60 (1) and glass beads (2)

In **Error! Reference source not found.**, when excluding fines and focusing on nuclei sizes starting from 275 µm, it is evident that capsulac 60 exhibits a narrower distribution, indicating that most of the nuclei fall within a relatively small size range. However, both systems showed high yields in the size range of 275 to 500 µm, particularly with the two lowest PCN values, signifying that the liquid content was sufficient to produce small nuclei composed of only 2 to 3 particles.

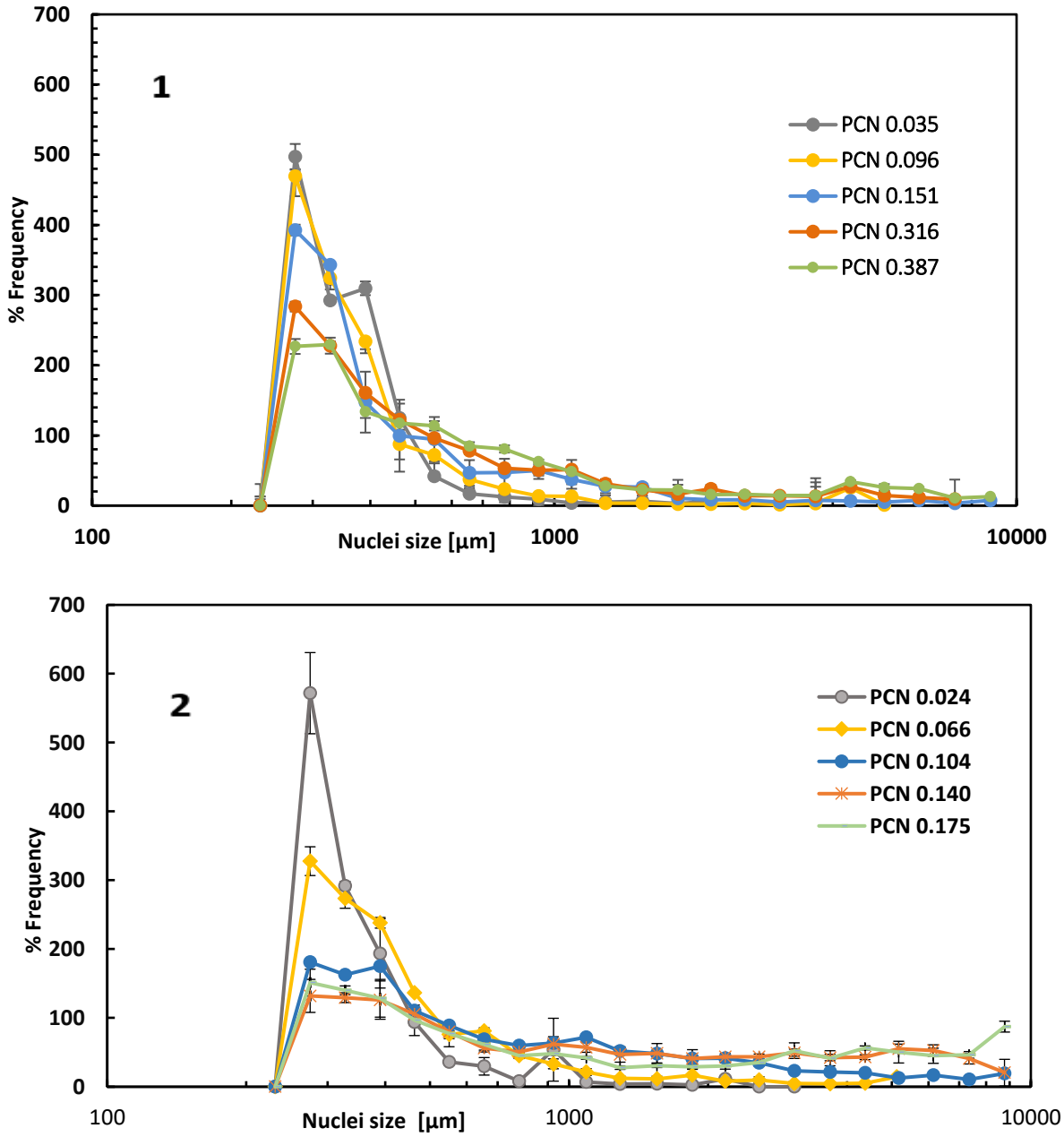

Figure 7.7: The nuclei size against frequency as a function of PCN for the capsulac 60 (1) and glass beads (2) HPMC 352 mPa·s systems.

Within the larger range of 500 to 1000 µm, nucleation of capsulac 60 was dominated by the PCN, whereas glass beads don't show the same impact. Beyond 1 mm, the nuclei size distribution of glass beads broadens toward larger sizes. The PCN appears to have a larger effect on the size distribution of capsulac 60 larger than 500 µm compared to glass beads. The d_{90} of the nuclei was plotted against the PCN for the two systems as a function of X_{LS} in Figure 7.8.

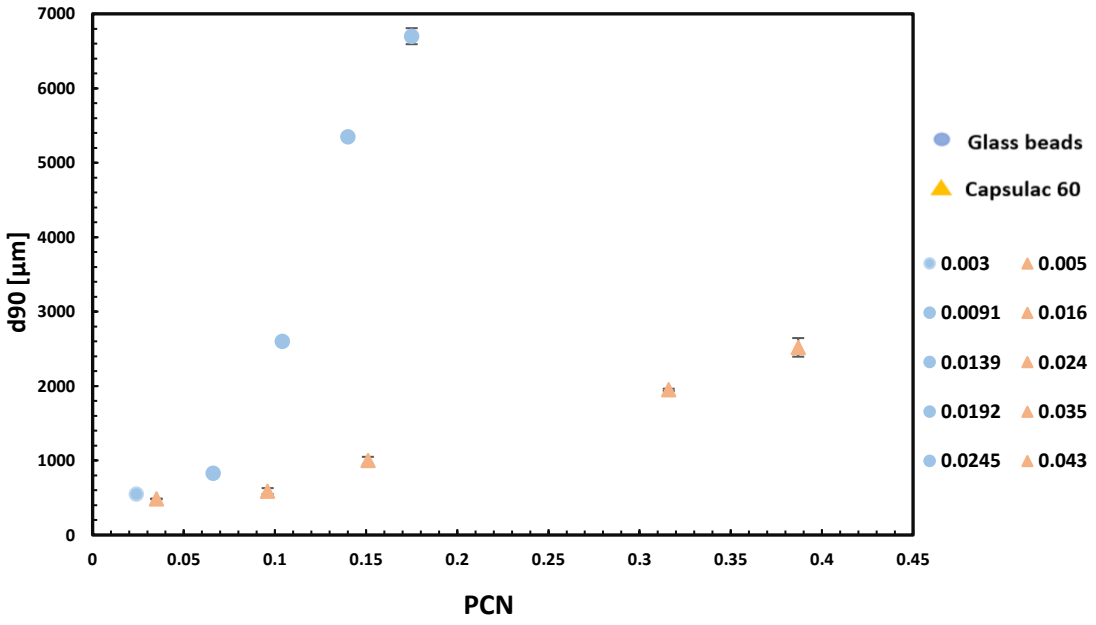

Figure 7.8: The d_{90} of nuclei produced by the capsulac 60 and glass beads HPMC 352 mPa·s systems at increased PCN values as a function of X_{LS}.

The glass bead graph indicates larger nuclei sizes were obtained than those of the capsulac 60 at the correspondent PCN values. The d_{90} is directly influenced by the PCN and the X_{LS} applied in both systems. Glass beads have shown more dependency as d_{90} reached 6700 µm at a PCN of 0.175, while it was just 2520 µm for capsulac 60 at 0.387 PCN.

The study was conducted using equivalent particle sizes and similar liquid distribution. Despite using the same ratio of liquid mass per material surface area in both experiments, the global and local PCN increased more rapidly in the capsulac 60 system. Capsulac 60 had significantly higher PCN values due to its smaller density and smaller contact angle resulting in a larger footprint on the particle surface. In both systems, the local PCN was approximately 15 times higher than the global PCN, reflecting higher spray density within the smaller spray zone.

The particles are in a motion state, subjecting to multiple droplets that partially wet the surface, with frequent collisions, contact spreading, and a drying process occurring simultaneously inside the bed.

The two materials exhibit differences in nucleation success and mean nuclei size. The differences could be attributed to material characteristics such as specific surface area, density, particle surface roughness, particle shape, porosity and the affinity to the binder solution expressed by the contact angle.

In addition to contact angle, liquid bridge formation mainly depends on the liquid viscosity and thickness of the liquid layer. The contact angle controls how the liquid binder will instantly spread over the surface and the thickness of the layer at equilibrium. The larger the contact angle and higher the thickness of the liquid layer, the more the energy dissipated during impact (Antonyuk et al., 2009). It is 58.95° for capsulac 60 HPMC 352 mPa·s system and 82.37° for glass beads HPMC 352 mPa·s system. It also significantly affects the restitution coefficient and the energy dissipation of the collisions.

The wet restitution coefficient, which quantifies how much kinetic energy is conserved during the particle impact, is also affected by the same parameters. The restitution coefficient decreases with the increase of layer thickness and liquid viscosity (Ma et al., 2016, Shao et al., 2022).

A larger yield was obtained by capsulac 60 at all coating numbers. The margin between the two materials in the granulated fraction by mass was negligible and widened as the PCN reached more than double at higher PCN values, 27.6% for glass beads and 65% for capsulac 60 at PCN 0.175 and 0.387 respectively (Figure 7.4). However, the degree to which the contact angle influences the restitution coefficient still depends on other factors, such as the size and shape of the particle and the velocity of impact.

The non porous spherical shape of the glass beads and the porous irregular shape of the capsulac 60 particle also can affect the wet restitution coefficient during the collision. Irregularly shaped capsulac 60 has more surface area and contact points with each other compared to spherical particles, making them exhibit behaviour dominated by viscosity. Spherical glass beads with smaller specific surface area and fewer contact points tend to conserve more kinetic energy during collisions. Štěpánek (2009) expressed the physical success of a collision based on the critical viscous Stokes number, $St^* \upsilon$, with two factors, the binder distribution or the layer thickness and the surface asperity (Štěpánek et al., 2009). The viscous Stokes number (Stv)

was calculated for both systems. It was larger for glass beads (0.0086) than capsulac 60 (0.00429). As the surface asperity increases, the critical Stokes number increases. Ma (2016) also found that smooth spheres have a higher tangential restitution coefficient during wet impacts than rough surface particle impacts due to additional energy loss caused by physical interactions between surface asperities.

Increased mass makes the coalescence between wet pairs collide depending on the entire dissipation of the kinetic energy of the impact by the viscous forces which dominate the situation. The glass beads have a higher density than the capsulac 60, making the impact energy much higher and harder to dissipate as the nuclei size grows. Liquid bridge tends to be ruptured for large agglomerates as the kinetic energy of the impact exceeds the viscous dissipation and rebound will occur.

The d_{50} s in both systems have increased with increasing the PCN, where glass beads show a proportional increase in mean size. In contrast, capsulac 60 showed a lower correlation (Figure 7.5), which could be attributed to the liquid penetrating the pores on capsulac60 particles. While it remains on the glass bead surface to form more liquid bridges. The morphology of the lactose particles might have contributed to the nuclei mean size. Angular shapes of the lactose particles make the nuclei more condensed and occupy smaller volumes for the same number of constituting particles.

7.5 **Conclusion:**

This study was conducted under comparable conditions that permit distinguishing the differences related to the material characteristics. The glass beads and the capsulac 60 powders were selected to have a similar mean particle size and granulated with a binder, assumed to distribute evenly among the particles by applying equal liquid mass distribution per the bed surface area. The calculated PCN increased with the incorporation of more liquid binder mass in both systems. However, differences in contact angle and droplet footprint led to variations in PCN values between capsulac 60 and glass beads. The PCN effectively predicted greater liquid coverage on the capsulac bed. Both global and local PCN values for capsulac 60 significantly increased with increasing liquid flow rate more than those for glass beads, owing to capsulac 60's smaller contact angle and larger droplet footprint. This predicted higher coverage is evident in better nuclei formation, with up to 60% of the bed mass agglomerated, compared to 30% for glass beads. Additionally, the higher density and rigidity of the glass

beads caused less energy loss and a higher restitution coefficient, leading to more rebound and less successful coalescence. In contrast, the deformability of lactose promoted greater granulation.

The d_{50} values in both systems increased as the PCN increased. Faster rise in the mean particle size for glass beads. capsulac 60 displayed a weaker correlation, likely because less liquid thickness was available for more liquid bridges due to the smaller contact angle and more liquid penetration. In contrast, higher contact angle with non porous glass beads, a thicker liquid layer for bond formation. The morphology may have also influenced the mean size of the nuclei. The angular shape of lactose particles makes the nuclei of same number of constituent particles more compact, allowing them to occupy smaller volumes.

7.6 Comparison of the findings with prior studies

There is an absolute lack in the literature regarding the distribution of nucleation. Only a few studies were found when the distribution mechanism was not the primary focus of their research though distribution mechanisms appeared to partially control the outcome. This study aims to address this gap by presenting a novel approach to understanding nucleation distribution and providing new insights that extend beyond the scope of previous research.

This work will also recall some findings from earlier studies, comparing them with the results of this research to gain any useful insights, even though those studies did not fully adhere to distribution nucleation conditions. More importantly, the novel PCN will be applied to a different mechanism, FHMG, where the solidification rate exclusively governs the process. Due to the limited information available on binder particle size, estimations will be used where necessary.

Tan et al. (2006) was identifying the agglomeration rate process in fluidised hot melt granulation (FHMG) using a small meltable particle size for a wide size range of solid material. Tan and co-workers could obtain a 28.5 µm droplet size at 1.5 bar atomisation pressure of PEG 1500 meltable binder for the 75-375µm solid material glass beads they used. The volume based mean $d_{3,4}$ was 175 µm. In the Tan (2006) study protocol, eight liquid spray rates ranging from (3.5- 10 g/min) were applied throughout eight different processing periods (3-16 minutes) to capture the change in the growth according to the time (Tan et al., 2006)).

Because in Figure 7.9, the mean droplet size didn't significantly change by changing the flow rate, the same droplet size measured at the atomisation pressure of 1.5 bar will be used to

approximate the PCN value. Moreover, the measurements account for the volume mean size, not the surface mean.

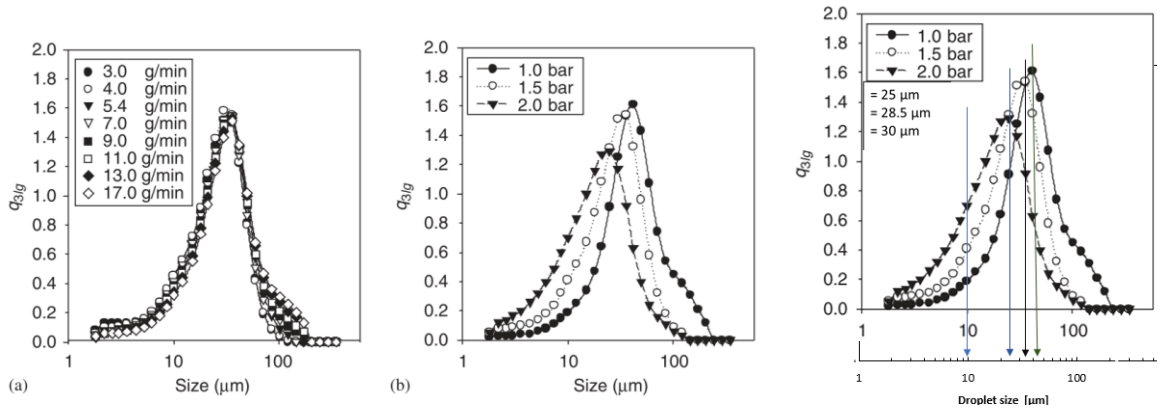

Figure 7.9: Droplet size distribution (volume based) at different (a) binder spray rates and (b) atomising pressure for PEG1500 (Tan et al., 2006).

In the flow rate Tan (2006) experiment, the authors used the same $X_{LS.}$ They varied the liquid spray rates to be applied over extended periods of processing time. The results show the mean granule size increased by increasing the flow rate of the liquid in all spray periods. Also, it shows the higher the spray rate, the faster growth and larger mean nuclei size obtained via distribution nucleation. The PCN shown is changing in magnitude over time. Tan's work agrees with this work that the higher the flow rate, the larger the nuclei size.

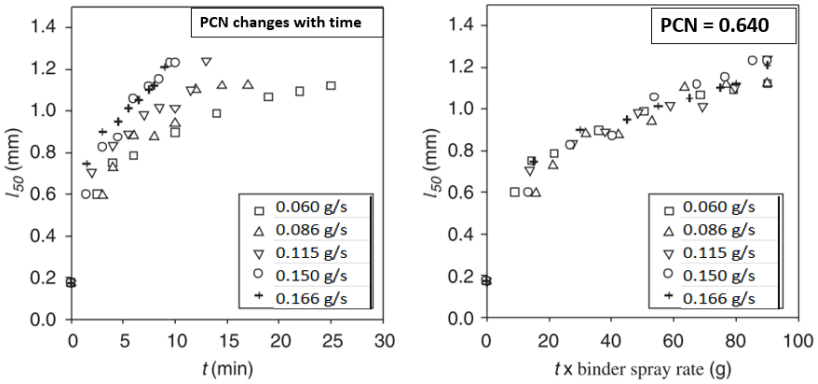

Figure 7.10: The change in volumetric median size with (a) time, (b) mass of binder at various binder spray rates. PEG1500, bed temperature 32 ◦C, atomising pressure 1.5 bar (droplet size 28.5µm), fluidising air velocity 0.97 m/s (Tan et al., 2006).

Tan (2006) also investigated the effect of atomisation pressure using different flow rates throughout different time periods. The PCN was calculated upon estimating the mean droplet size from the graph provided by the researchers.

The rate of growth in Figure 7.11 reveals changes over time and as the X_{LS} changes. The lowest atomisation pressure, 1.0 bar, caused a faster and consistent increase in the nuclei mean size, whilst this rate is the slowest for the highest atomisation pressure of 2 bar.

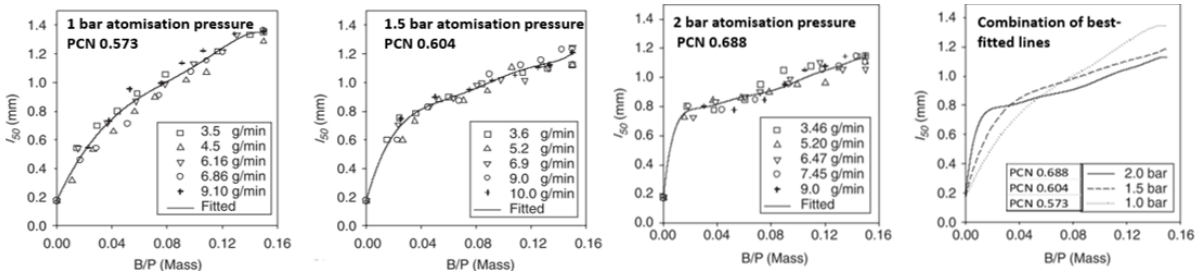

Figure 7.11: Granule growth (PEG1500) at different atomising pressures: (a) 1 bar, (b) 1.5 bar, (c) 2 bar, (d) combination of best-fitted lines. Bed temperature 32 ◦C, fluidising velocity 0.97 m/s (Tan et al., 2006).

In very early processing time and low liquid solid fractions incorporated (below 0.04), 2 bar atomisation pressure equivalent to approximately PCN 0.688 produced a larger nuclei size. This changed and showed the slowest coalescence success rate. Similarly, in this study, the lowest atomisation pressure produced the largest nuclei size and vice versa, which agrees with the later part of the results.

For the fluidisation velocity, Tan's study also showed similar results to this research, an inverse relationship with the mean nuclei size.

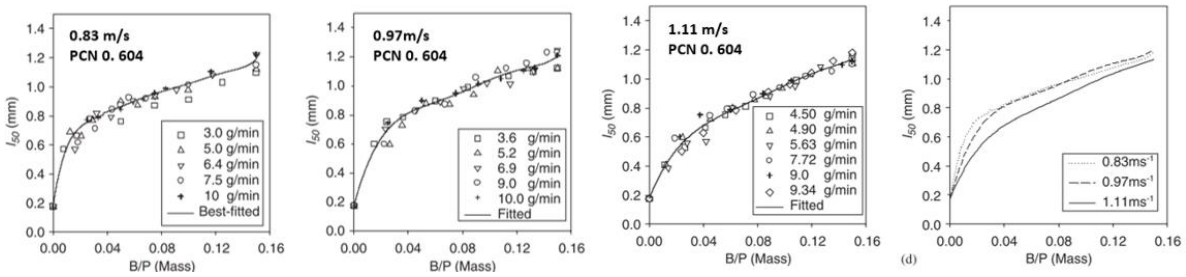

Figure 7.12: Granules growth (PEG1500) at different fluidising air velocities: (a) 0.83m s−1, (b) 0.97m s−1, (c) 1.11 m/s, (d) combination of fitted lines. Bed temperature 32 ◦C, atomising pressure 1.5 bar (droplet size 28.5 μm) (Tan et al., 2006).

A study was conducted by Zhai et al., 2010 to investigate the effect of viscosity and mixing time in FHMG. The hot bed containing glass beads 150–250 μm was mixed for 5 s, 15 s, 30 s, 45 s, 1 min, and 3 min separately. They applied many binder sizes, but the binder particle size extracted from the study, in this context, is 45–90 μm; using the arithmetic mean, 67.5 μm, the PCN calculated was 0. 604. The results shown in Figure 7.13 agree with this research findings (Zhai et al., 2010).

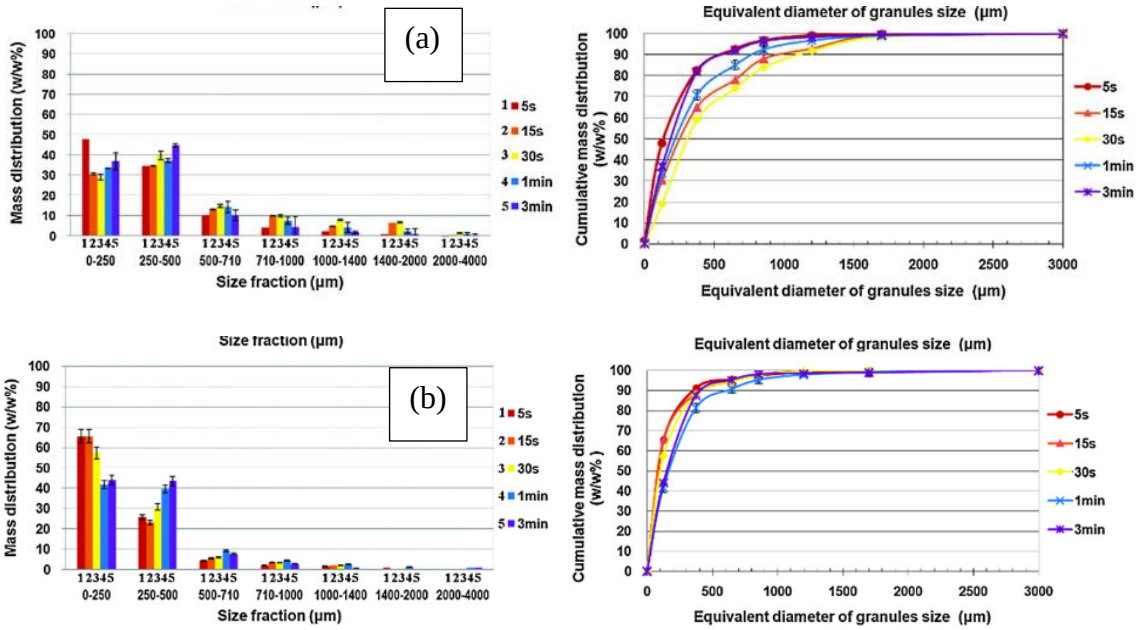

Figure 7.13:The size distributions of the granules produced by FHMG at 65 ◦C and the cumulative particle size distribution of the granules produced by FHMG for various granulation times. (a) (Poloxamer 188 binder 171 mPa.s 45–90 µm - glass beads 150–250 µm), (b) (Poloxamer 407 binder 720 mPa.s 45–90 µm - glass beads 150–250 µm) (Zhai et al., 2010).

As can be seen, the droplet size /particle size ratio doesn't confirm the distribution of nucleation was the only mechanism involved in the studies. Also, the PCN magnitude that could be barely estimated (*due to lack of precise data and some parameters, as contact angle*) is larger in both studies than the number calculated in this study. The differences between the two techniques, the FB and the FHMG should be considered, where the high temperature readily solidifies the binder, and no drying rate is involved during the used spray times. Yet, similarities in behaviour can still be seen.

Chapter 8: Conclusion and Future Work

This research aimed to provide a better understanding of the distribution nucleation mechanism and to investigate the role of the PCN in nucleation in fluidised bed granulation. A small droplet/particle size ratio leads to the distribution nucleation mechanism. The particle coating number (Φ) is a recently developed dimensionless number aimed at predicting the liquid distribution on a particulate solid material regardless of the thickness of the liquid layer to predict the behaviour of particle systems and the rate of granulation rate. This approach was designed to enhance real-time process control and help improve batch and continuous granulation control in the pharmaceutical industry. For instance, to predict if the liquid-solid fraction is adequate for consistent wetting and subsequent agglomeration. Or to help the coating industry minimise agglomeration issues and maintain stable coating conditions by adjusting drop size or particle size. This is critical for ensuring the quality and consistency of granulated products, particularly in pharmaceutical manufacturing. In order to understand the role of particle coating number in this process, the following parameters were experimentally investigated in this research.

The PCN was able to describe the liquid mass per particulate surface area. When the liquid rate changed, the PCN was better than $X_{LS,}$ for example, in predicting the influence of increasing liquid on nucleation success. Increasing PCN resulted in increased agglomerated fraction, and nuclei mean size and broadened the size distribution of the produced granules. Despite using the same liquid mass/material surface area ratio, the PCN increased more rapidly in the capsulac 60 system compared to the model glass beads due to its lower density, smaller contact angle and larger footprint area. capsulac 60 showed better nucleation success and the yield was largely increased because of the deformability of lactose whereas, higher density and rigidity of the glass beads caused less energy loss and led to less successful coalescence. Regarding d_{50} glass beads show more dependency on PCN due to fewer surface complexities interfered.

When the atomisation pressure increased, the distribution nucleation was considerably affected. The PCN has changed accordingly. It increases the agglomerated yield, reducing the nuclei mean size, narrowing and improving the quality of granulation. The PCN effectively tracked changes in droplet size and footprint and has the potential to incorporate spray coverage

(local PCN). This should be taken into consideration when adjusting atomisation pressure in fluidised bed granulation, as small variations in PCN can significantly influence the process.

The viscosity improved the nucleation success, increased the yield fraction and narrowed the size distribution. The PCN was inversely related to viscosity and demonstrated sensitivity to system variations resulting from changes in viscosity. The change in PCN was due to changes in contact angle, droplet size and footprint area, however, the complexity of non-Newtonian (visco-elastic) behaviour of highly viscous binder inside the pneumatic atomiser didn't help to capture a consistent change in droplet mean size.

Increasing the initial particle size has reduced the nucleation in every aspect, and the kinetic energy appeared to play a dominant role in the outcome. Interestingly, the study in terms of liquid content separately stabilised the PCN and the X_{LS} when the primary particle size was changed. The change in the outcome related to PCN was significant, which reflects a better relation between liquid coverage and the solid particle size and surface area.

Mixing time has shown two phases, fast growth followed by a slower reduction in the nuclei size due to breakage. Elevated fluidising velocity also showed a reduction in nuclei size, which may be attributed to kinetic energy and effective dry rate. These variables are not related to the PCN, the change is not anticipated when using this approach alone.

Unlike $X_{LS,}$ the global PCN model integrates both process and material-related parameters, including droplet size, contact angle, and liquid density. Additionally, the local PCN accounts for factors such as solid density, bubbling velocity, and spray coverage area, making it a valuable metric for equipment scaling up. In conclusion, the PCN model proposed by Kariuki was found to be a reliable approach for predicting solid coverage by liquid and the granulation behaviour in the fluidised bed system. And to play a significant role in the design and scale up of the fluidised bed granulation and coating industry as it provides a better tool for anticipating the distribution nucleation outcome than just $X_{LS.}$

Figure 8.1 shows a chart for the effect of the different variables investigated or discussed in this research and their relation to the PCN and distribution nucleation success.

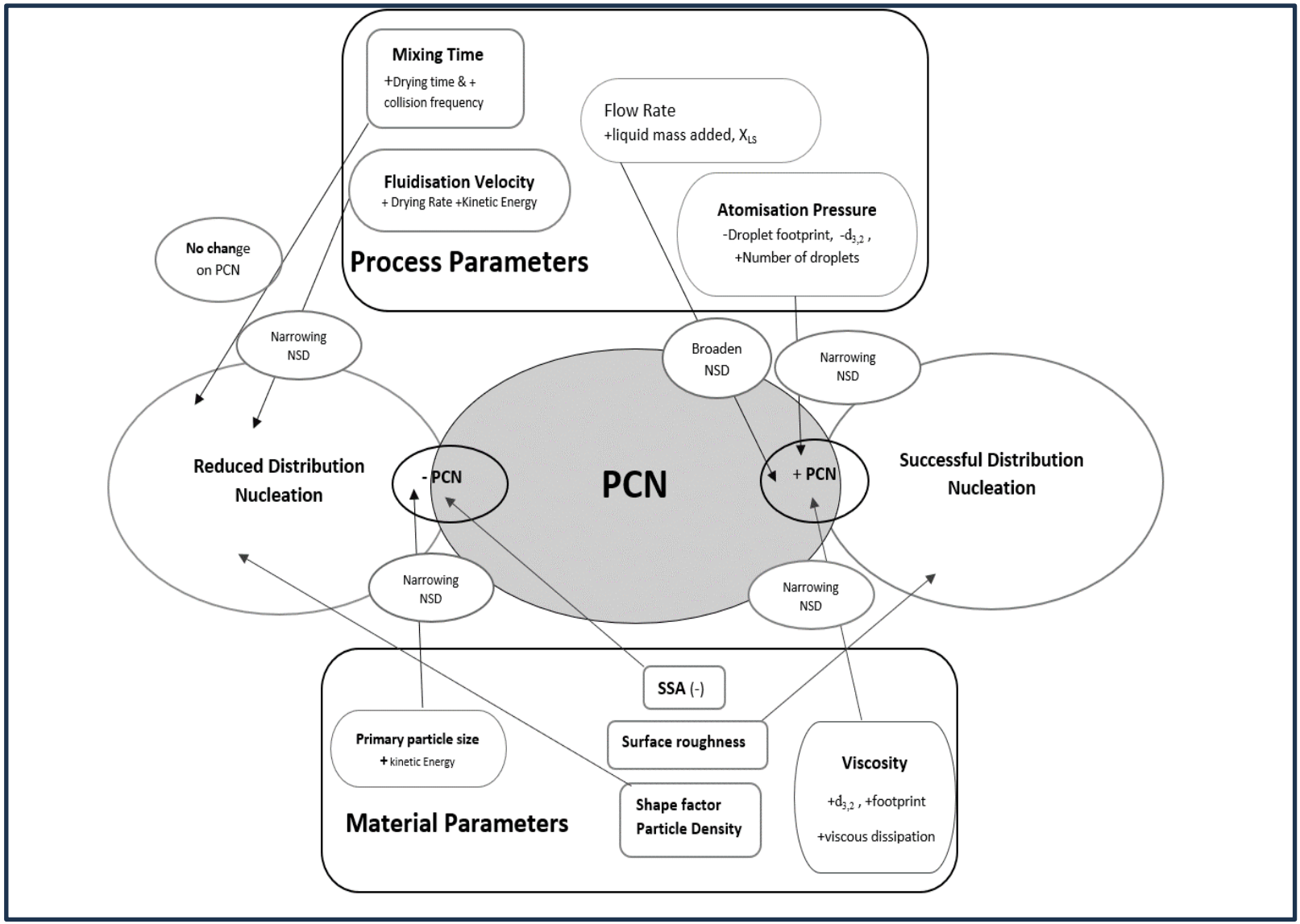

Figure 8.1: PCN and distribution nucleation chart

8.1 Future work

This work provides an overview of the distribution nucleation to understand the mechanism and how the various variables affect the outcome. It examines the capacity of the particle coating number to predict the outcome in a fluidised bed experiment.

This is a quantitative study carried out in a small fluidised bed. However, due to equipment limitations, it still lacks some rate process calculations due to the difficulty of sampling. Also the cylinder-shaped column doesn't allow the incorporation of more liquid because of defluidisation. In addition, the time limit didn't allow for performing this study in a conical Glatt design FB topped by a conical freeboard to investigate the effect of equipment type on the findings.

The recommended future work is:

- To build on this work using computational fluid dynamics (CFD) simulations to incorporate the fluidised bed dynamics and the behaviour of liquid bridges within the bed. This will allow a better understanding of the distribution nucleation mechanism and its behaviour under different conditions.
- To design another dimensionless parameter with the PCN and develop a regime map for distribution nucleation that illustrates the different conditions and parameters under which distribution nucleation occurs within the fluidised bed. This map can help identify optimal operating conditions and provide insights into the underlying mechanisms governing nucleation.
- To relate findings with a larger scale fluidised bed. Conducting experiments or simulations on larger equipment will allow industries to apply the research results to practical processes.

References

ABBERGER, T. 2001. Influence of binder properties, method of addition, powder type and operating conditions on fluid-bed melt granulation and resulting tablet properties. *Die Pharmazie,* 56**,** 949-952.

ABBERGER, T., SEO, A. & SCHAEFER, T. 2002. The effect of droplet size and powder particle size on the mechanisms of nucleation and growth in fluid bed melt agglomeration. *International Journal of Pharmaceutics,* 249**,** 185-197.

ALGHUNAIM, A., KIRDPONPATTARA, S. & NEWBY, B. M. Z. 2016. Techniques for determining contact angle and wettability of powders. *Powder Technology,* 287**,** 201-215.

ALISEDA, A., HOPFINGER, E. J., LASHERAS, J. C., KREMER, D. M., BERCHIELLI, A. & CONNOLLY, E. K. 2008. Atomization of viscous and non-newtonian liquids by a coaxial, high-speed gas jet. Experiments and droplet size modeling. *International Journal of Multiphase Flow,* 34**,** 161-175.

ALMAYA, A. 2008. Development of Low-Dose Solid Oral Formulations Using Wet Granulation. *In:* ZHENG, J. Y. (ed.) *Formulation and Analytical Development for Low-Dose Oral Drug Products.* John Wiley & Sons

AM ENDE, M. T., BLACKWOOD, D.O., GIERER, D.S. AND NEU, C.P. 2008. Challenges in development and scale-up of low-dose drug products by dry granulation: a case study. *In:* ZHENG, J. Y. (ed.) *Formulation and Analytical Development for Low-Dose Oral Drug Products.* John Wiley and Sons.

ANTONYUK, S., HEINRICH, S., DEEN, N. & KUIPERS, H. 2009. Influence of liquid layers on energy absorption during particle impact. *Particuology,* 7**,** 245-259.

BELLINGHAUSEN, S., GAVI, E., JERKE, L., GHOSH, P. K., SALMAN, A. D. & LITSTER, J. D. 2019. Nuclei size distribution modelling in wet granulation. *Chemical Engineering Science: X,* 4**,** 100038.

BÖRNER, M., HAGEMEIER, T., GANZER, G., PEGLOW, M. & TSOTSAS, E. 2014. Experimental spray zone characterization in top-spray fluidized bed granulation. *Chemical Engineering Science,* 116**,** 317-330.

BOUFFARD, J., KASTER, M. & DUMONT, H. 2005. Influence of process variable and physicochemical properties on the granulation mechanism of mannitol in a fluid bed top spray granulator. *Drug development and industrial pharmacy,* 31**,** 923-933.

BRIENS, L. & LOGAN, R. 2011. The Effect of the Chopper on Granules from Wet High-Shear Granulation Using a PMA-1 Granulator. *AAPS PharmSciTech,* 12**,** 1358-1365.

BURGGRAEVE, A., MONTEYNE, T., VERVAET, C., REMON, J. P. & DE BEER, T. 2013. Process analytical tools for monitoring, understanding, and control of pharmaceutical fluidized bed granulation: A review. *European Journal of Pharmaceutics and Biopharmaceutics,* 83**,** 2-15.

COCCO, R., KARRI, S. B. R. & KNOWLTON, T. 2014. Introduction to Fluidization. *Chemical Engineering Progress,* 110**,** 21-29.

COLLINS, R., DE MORAES, F., DAVIDSON, J. & HARRISON, D. 1978. The motion of a large gas bubble rising through liquid flowing in a tube. *Journal of Fluid Mechanics,* 89**,** 497-514.

DAVIDSON, J., HARRISON, D. & CARVALHO, J. 1977. On the liquidlike behavior of fluidized beds. *Annual Review of Fluid Mechanics,* 9**,** 55-86.

DE KOSTER, S. A., PITT, K., LITSTER, J. D. & SMITH, R. M. 2019. High-shear granulation: An investigation into the granule consolidation and layering mechanism. *Powder Technology,* 355**,** 514-525.

DEWETTINCK, K. & HUYGHEBAERT, A. 1998. Top-spray fluidized bed coating: Effect of process variables on coating efficiency. *Food Science and Technology-Lebensmittel-Wissenschaft & Technologie,* 31**,** 568-575.

DHENGE, R. M., CARTWRIGHT, J. J., HOUNSLOW, M. J. & SALMAN, A. D. 2012. Twin screw wet granulation: Effects of properties of granulation liquid. *Powder technology,* 229**,** 126-136.

EHLERS, H., LARJO, J., ANTIKAINEN, O., RAIKKONEN, H., HEINAMAKI, J. & YLIRUUSI, J. 2010. In situ droplet size and speed determination in a fluid-bed granulator. *International Journal of Pharmaceutics,* 391**,** 148-154.

ENGINEERINGTOOLBOX. 2009. *Air - Density, Specific Weight and Thermal Expansion Coefficient vs. Temperature and Pressure* [Online]. Available: https://www.engineeringtoolbox.com/air-density-specific-weight-d_600.html [Accessed 2022].

ENNIS, B. J. 2005. Theory of Granulation: An Engineering Perspective. *In:* PARIKH, D. M. (ed.) *Handbook of Pharmaceutical Granulation Technology.* 2nd Edition ed.: Taylor & Francis Group.

ENNIS, B. J. 2010. Agglomeration technology: equipment selection. *Chemical Engineering,* 117**,** 50-54.

FAURE, A., YORK, P. & ROWE, R. C. 2001. Process control and scale-up of pharmaceutical wet granulation processes: a review. *European Journal of Pharmaceutics and Biopharmaceutics,* 52**,** 269-277.

FOLK, R. L. & WARD, W. C. 1957. A study in the significance of grain size parameters. *Journal of sedimentary research,* 27**,** 3-26.

GAO, J. Z. H., JAIN, A., MOTHERAM, R., GRAY, D. B. & HUSSAIN, M. A. 2002. Fluid bed granulation of a poorly water soluble, low density, micronized drug: comparison with high shear granulation. *International Journal of Pharmaceutics,* 237**,** 1-14.

GELDART, D. & BAEYENS, J. 1985. The Design of Distributors for Gas-Fluidized Beds. *Powder Technology,* 42**,** 67-78.

HAPGOOD, K. 2000. *Nucleation and binder dispersion in wet granulation.* PhD book The University of Queensland.

HAPGOOD, K. P., AMELIA, R., ZAMAN, M. B., MERRETT, B. K. & LESLIE, P. 2010. Improving liquid distribution by reducing dimensionless spray flux in wet granulation—a pharmaceutical manufacturing case study. *Chemical Engineering Journal,* 164**,** 340-349.

HAPGOOD, K. P., LITSTER, J. D., BIGGS, S. R. & HOWES, T. 2002. Drop penetration into porous powder beds. *Journal of Colloid and Interface Science,* 253**,** 353-366.

HAPGOOD, K. P., LITSTER, J. D. & SMITH, R. 2003. Nucleation regime map for liquid bound granules. *AIChE Journal,* 49**,** 350-361.

HAPGOOD, K. P., TAN, M. X. L. & CHOW, D. W. Y. 2009. A method to predict nuclei size distributions for use in models of wet granulation. *Advanced Powder Technology,* 20**,** 293-297.

HEDE, P. D., BACH, P. & JENSEN, A. D. 2008. Two-fluid spray atomisation and pneumatic nozzles for fluid bed coating/agglomeration purposes: A review. *Chemical Engineering Science,* 63**,** 3821-3842.

HEMATI, A., CHERIF, R., SALEH, K. & PONT, V. 2003. Fluidized bed coating and granulation: influence of process-related variables and physicochemical properties on the growth kinetics. *Powder Technology,* 130**,** 18-34.

HOORNAERT, F., WAUTERS, P. A. L., MEESTERS, G. M. H., PRATSINIS, S. E. & SCARLETT, B. 1998. Agglomeration behaviour of powders in a Lodige mixer granulator. *Powder Technology,* 96**,** 116-128.

HOUNSLOW, M., OULLION, M. & REYNOLDS, G. 2009. Kinetic models for granule nucleation by the immersion mechanism. *Powder technology,* 189**,** 177-189.

IVESON, S. M., LITSTER, J. D., HAPGOOD, K. & ENNIS, B. J. 2001. Nucleation, growth and breakage phenomena in agitated wet granulation processes: a review. *Powder Technology,* 117**,** 3-39.

JUSLIN, L., ANTIKAINEN, O., MERKKU, P. & YLIRUUSI, J. 1995. Droplet Size Measurement .1. Effect of 3 Independent Variables on Droplet Size Distribution and Spray Angle from a Pneumatic Nozzle. *International Journal of Pharmaceutics,* 123**,** 247-256.

KARIUKI, W. I. J., FREIREICH, B., SMITH, R. M., RHODES, M. & HAPGOOD, K. P. 2013. Distribution nucleation: Quantifying liquid distribution on the particle surface using the dimensionless particle coating number. *Chemical Engineering Science,* 92**,** 134-145.

KAYRAK-TALAY, D. & LITSTER, J. D. 2011. A priori performance prediction in pharmaceutical wet granulation: Testing the applicability of the nucleation regime map to a formulation with a broad size distribution and dry binder addition. *International Journal of Pharmaceutics,* 418**,** 254-264.

KEARY, C. M. & SHESKEY, P. J. 2004. Preliminary report of the discovery of a new pharmaceutical granulation process using foamed aqueous binders. *Drug Development and Industrial Pharmacy,* 30**,** 831-845.

KRISTENSEN, H. G., HOLM, P. & SCHAEFER, T. 1985. Mechanical-Properties of Moist Agglomerates in Relation to Granulation Mechanisms .1. Deformability of Moist, Densified Agglomerates. *Powder Technology,* 44**,** 227-237.

KUNII, D. & LEVENSPIEL, O. 1991. *Fluidization engineering*, Butterworth-Heinemann.

KUNII, D., LEVENSPIEL, O. 1991. *Fluidization and mapping of regimes. Fluidization engineering*, Boston, Butterworth—Heinemann.

LI, W., CUNNINGHAM, J., RASMUSSEN, H. & WINSTEAD, D. 2007. A qualitative method for monitoring of nucleation and granule growth in fluid bed wet granulation by reflectance near-infrared spectroscopy. *Journal of pharmaceutical sciences,* 96**,** 3470-3477.

LITSTER, J. 2003. Scaleup of wet granulation processes: science not art. *Powder Technology,* 130**,** 35-40.

LITSTER, J. 2016a. *Design and processing of particulate products,* Cambridge, Cambridge University Press.

LITSTER, J. 2016b. Particle Characterization and Particle Property Distributions. *Design and Processing of Particulate Products.* Cambridge: Cambridge University Press.

LITSTER, J. & ENNIS, B. 2004a. *The Science and Engineering of Granulation Processes,* Dordrecht Springer-Science+Business Media, B.V.

LITSTER, J. & ENNIS, B. 2004b. Tumbling Granulation. *The Science and Engineering of Granulation Processes.* Dordrecht: Springer Netherlands.

LITSTER, J. D., HAPGOOD, K. P., MICHAELS, J. N., SIMS, A., ROBERTS, M., KAMENENI, S. K. & HSU, T. 2001. Liquid distribution in wet granulation: dimensionless spray flux. *Powder Technology,* 114**,** 32-39.

LIU, L., ZHOU, L., ROBINSON, D. & ADDAI-MENSAH, J. 2013. A nuclei size distribution model including nuclei breakage. *Chemical engineering science,* 86**,** 19-24.

LOH, Z. H., ER, D. Z. L., CHAN, L. W., LIEW, C. V. & HENG, P. W. S. 2011. Spray granulation for drug formulation. *Expert Opinion on Drug Delivery,* 8**,** 1645-1661.

MA, J., LIU, D. & CHEN, X. 2016. Normal and oblique impacts between smooth spheres and liquid layers: Liquid bridge and restitution coefficient. *Powder Technology,* 301**,** 747-759.

MALVERN. 2023a. *Laser Diffraction (LD) Particle size distributions from nanometers to millimeters* [Online]. Available: https://www.malvernpanalytical.com/en/products/technology/light-scattering/laser-diffraction [Accessed 19/09/2023].

MALVERN, M. 2023b. *Distribution; Uniformity; Specific Surface Area (Ssa) - Malvern Mastersizer 3000 User Manual* [Online]. Available: https://www.manualslib.com/manual/1524845/Malvern-Mastersizer-3000.html?page=123#manualMalvern [Accessed].

MANDATO, S., RONDET, E., DELAPLACE, G., BARKOUTI, A., GALET, L., ACCART, P., RUIZ, T. & CUQ, B. 2012. Liquids' atomization with two different nozzles: Modeling of the effects of some processing and formulation conditions by dimensional analysis. *Powder technology,* 224**,** 323-330.

MANGWANDI, C., ZAINAL, N. A., LIU, J. T., GLOCHEUX, Y. & ALBADARIN, A. B. 2015. Investigation of influence of process variables on mechanical strength, size and homogeneity of pharmaceutical granules produced by fluidised hot melt granulation. *Powder Technology,* 272**,** 173-180.

MARSTON, J., SPRITTLES, J. E., ZHU, Y., LI, E., VAKARELSKI, I. U. & THORODDSEN, S. T. 2013. Drop spreading and penetration into pre-wetted powders. *Powder technology,* 239**,** 128-136.

MCNAUGHT, A. D. & WILKINSON, A. 1997. *Compendium of chemical terminology,* Blackwell Science Oxford.

PARIKH, D. M. & MOGAVERO, M. 2005. Batch fluid bed granulation. *In:* PARIKH, D. M. (ed.) *Handbook of Pharmaceutical Granulation Technology.* 2nd Edition ed. Boca Raton: Taylor & Francis Group, LLC.

PAROLINE, G. 2016. Basics of applied rheology. *Anton Paar*.

PATNAIK, K. R., HARSHA, K. S., KUMAR, P. V. & SATYANARAYANA, B. Design studies on granulation processes in a fluidized bed. 2010 International Conference on Chemistry and Chemical Engineering, 2010. IEEE, 199-203.

PONT, V., SALEH, K., STEINMETZ, D. & HEMATI, M. 2001. Influence of the physicochemical properties on the growth of solid particles by granulation in fluidized bed. *Powder Technology,* 120**,** 97-104.

RAJNIAK, P., MANCINELLI, C., CHERN, R., STEPANEK, F., FARBER, L. & HILL, B. 2007. Experimental study of wet granulation in fluidized bed: Impact of the binder properties on the granule morphology. *International journal of pharmaceutics,* 334**,** 92-102.

RETSCH. 2015. Sieve Analysis: Taking a close look at quality. An expert guide to particle size analysis. Available: https://www.retsch.com/files/8785/expert-guide-sieving.pdf.

RHODES, M. J. 2008. *Introduction to Particle Technology,* Wiley.

SALEH, M. F., DHENGE, R. M., CARTWRIGHT, J. J., HOUNSLOW, M. J. & SALMAN, A. D. 2015. Twin screw wet granulation: Effect of process and formulation variables on powder caking during production. *International Journal of Pharmaceutics,* 496**,** 571-582.

SAXENA, S. C., CHATTERJEE, A. & PATEL, R. C. 1979. Effect of Distributors on Gas-Solid Fluidization. *Powder Technology,* 22**,** 191-198.

SCHAAFSMA, S. H., KOSSEN, N. W., MOS, M. T., BLAUW, L. & HOFFMANN, A. C. 1999. Effects and control of humidity and particle mixing in fluid-bed granulation. *AIChE journal,* 45**,** 1202-1210.

SCHAAFSMA, S. H., VONK, P. & KOSSEN, N. W. F. 2000. Fluid bed agglomeration with a narrow droplet size distribution. *International Journal of Pharmaceutics,* 193**,** 175-187.
SCHÆFER, T. & MATHIESEN, C. 1996. Melt pelletization in a high shear mixer. IX. Effects of binder particle size. *International journal of pharmaceutics,* 139**,** 139-148.
SCHAEFER, T. & WORTS, O. 1977. Control of Fluidised Bed Granulation: IV. Effects of Binder Solution and Atomization on Granule Size and Size Distribution. *Arch. Pharm. Chem. Sci,,* 5**,** 51-60.
SCHŒFER, T. 1978. CONTROL OF FLUIDIZED BED GRANULATION. IV. EFFECTS OF BINDER SOLUTION AND ATOMIZATION ON GRANULE SIZE AND SIZE DISTRIBUTION.
SCOTT, A. C., HOUNSLOW, M. J. & INSTONE, T. 2000. Direct evidence of heterogeneity during high-shear granulation. *Powder Technology,* 113**,** 205-213.
SEVILLE, J. P. K., WILLETT, C. D. & KNIGHT, P. C. 2000. Interparticle forces in fluidisation: a review. *Powder Technology,* 113**,** 261-268.
SHAO, L., LIU, D., MA, J. & CHEN, X. 2022. Normal collision between partially wetted particles by using direct numerical simulation. *Chemical Engineering Science,* 247**,** 117090.
SIMONS, S. & FAIRBROTHER, R. 2000. Direct observations of liquid binder–particle interactions: the role of wetting behaviour in agglomerate growth. *Powder Technology,* 110**,** 44-58.
SMIRANI-KHAYATI, N., FALK, V., BARDIN-MONNIER, N. & MARCHAL-HEUSSLER, L. 2009. Binder liquid distribution during granulation process and its relationship to granule size distribution. *Powder technology,* 195**,** 105-112.
SMITH, P. G. 2007. *Applications of fluidization to food processing,* John Wiley & Sons.
SMITH, P. G. & NIENOW, A. W. 1983. Particle Growth Mechanisms in Fluidized-Bed Granulation .2. Comparison of Experimental-Data with Growth-Models. *Chemical Engineering Science,* 38**,** 1233-1240.
STEFFENS, K. E., BRENNER, M. B., HARTIG, M. U., MONSCHKE, M. & WAGNER, K. G. 2020. Melt granulation: A comparison of granules produced via high-shear mixing and twin-screw granulation. *International Journal of Pharmaceutics,* 591.
ŠTĚPÁNEK, F. & RAJNIAK, P. 2006. Droplet morphologies on particles with macroscopic surface roughness. *Langmuir,* 22**,** 917-923.
ŠTĚPÁNEK, F., RAJNIAK, P., MANCINELLI, C., CHERN, R. & RAMACHANDRAN, R. 2009. Distribution and accessibility of binder in wet granules. *Powder Technology,* 189**,** 376-384.
TAFRESHI, Z., KIRPALANI, D., BENNETT, A. & MCCRACKEN, T. 2002. Improving the efficiency of fluid cokers by altering two-phase feed characteristics. *Powder Technology,* 125**,** 234-241.
TAN, H. S., SALMAN, A. D. & HOUNSLOW, M. J. 2006. Kinetics of fluidised bed melt granulation I: The effect of process variables. *Chemical Engineering Science,* 61**,** 1585-1601.
TAN, M. X. L. & HAPGOOD, K. P. 2012. Foam granulation: Effects of formulation and process conditions on granule size distributions. *Powder Technology,* 218**,** 149-156.
VU, T. 2021. Technical perspective: Liquid testing using built-in phone sensors. *Communications of the ACM,* 64**,** 74-74.
WADE, J. B., MARTIN, G. P. & LONG, D. F. 2015. An assessment of powder pycnometry as a means of determining granule porosity. *Pharmaceutical Development and Technology,* 20**,** 257-265.
WALDIE, B. 1991. Growth mechanism and the dependence of granule size on drop size in fluidized-bed granulation. *Chemical Engineering Science,* 46**,** 2781-2785.

WALKER, G., BELL, S., VANN, M., ZHAI, H., JONES, D. & ANDREWS, G. 2007. Pharmaceutically engineering powders using FHMG: The effects of process parameters and formulation variables. *Chemical Engineering Research and Design,* 85**,** 981-986.

WALKER, G. M., ANDREWS, G. & JONES, D. 2006. Effect of process parameters on the melt granulation of pharmaceutical powders. *Powder Technology,* 165**,** 161-166.

WAN, L. S. C., HENG, P. W. S. & LIEW, C. V. 1995. The Influence of Liquid Spray Rate and Atomizing Pressure on the Size of Spray Droplets and Spheroids. *International Journal of Pharmaceutics,* 118**,** 213-219.

WATANO, S., TAKASHIMA, H. & MIYANAMI, K. 1997. Scale-up of agitation fluidized bed granulation by neural network. *Chemical and pharmaceutical bulletin,* 45**,** 1193-1197.

WEBB, P. A. 2001. Volume and density determinations for particle technologists. *Micromeritics Instrument Corp,* 2**,** 01.

WILDEBOER, W., LITSTER, J. & CAMERON, I. 2005. Modelling nucleation in wet granulation. *Chemical Engineering Science,* 60**,** 3751-3761.

WONG, T. W., CHEONG, W.S. AND HENG, P.W.S. 2005. Melt granulation and pelletization. *Handbook of pharmaceutical granulation technology.* CRC Press.

ZHAI, H., LI, S., ANDREWS, G., JONES, D., BELL, S. & WALKER, G. 2009. Nucleation and growth in fluidised hot melt granulation. *Powder Technology,* 189**,** 230-237.

ZHAI, H., LI, S., JONES, D. S., WALKER, G. M. & ANDREWS, G. P. 2010. The effect of the binder size and viscosity on agglomerate growth in fluidised hot melt granulation. *Chemical Engineering Journal,* 164**,** 275-284.

ZHANG, D. 2002. F| oryJH, Panmai S, Batra U, Kaufman Ml. *Colloid Surface A,* 206**,** 547-54.

ZHOU, J. J. & LIPP, R. 2009. Development of Low-Dose Formulations Using Fluidized Bed Granulation. *In:* ZHENG, J. Y. (ed.) *Formulation and Analytical Development for Low-Dose Oral Drug Products.* Second ed.: John Wiley and Sons.

.

APPENDIX

Appendix 5A.1: Effect of liquid viscosity

The following graphs are in two groups. The top one, from (1A -4A), shows nuclei sizes plotted against frequency for four different viscosities and two runs for every viscosity. The bottom graphs (1B -5B) show the averages of the two runs for the whole material for every system.

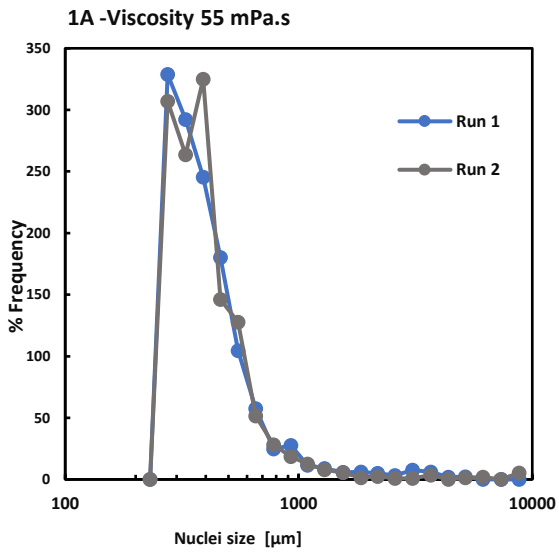

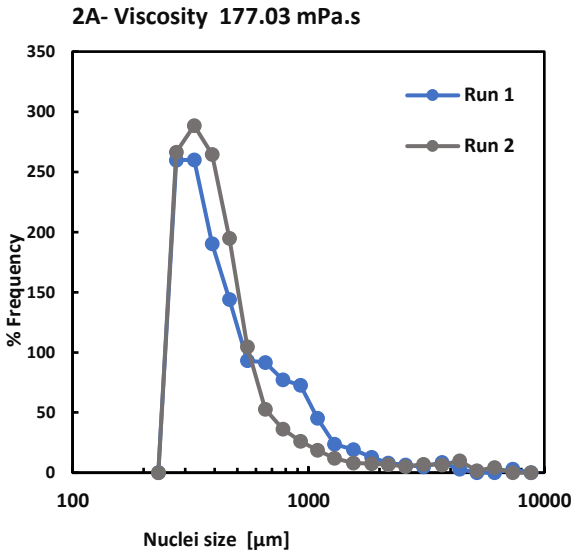

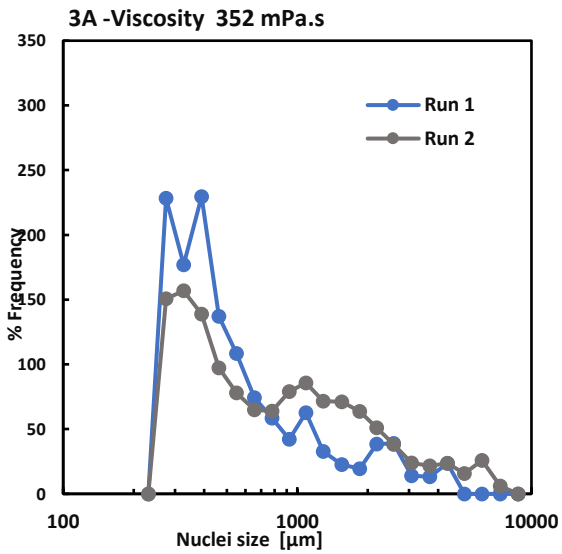

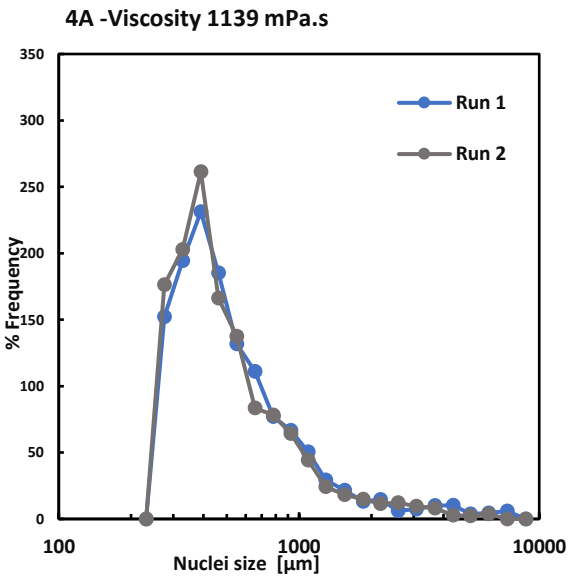

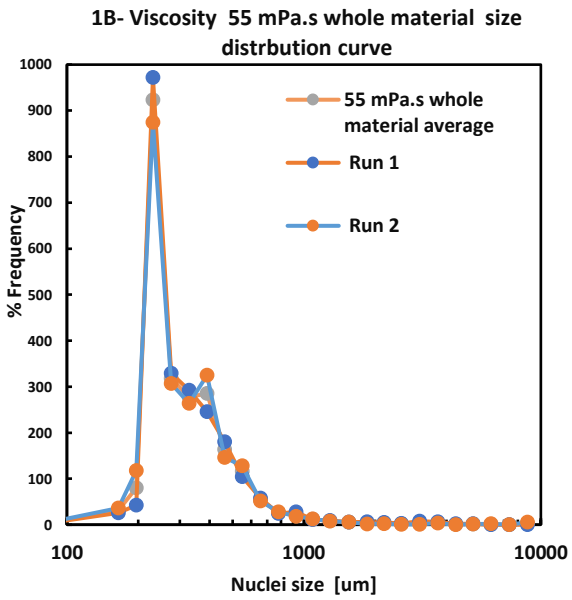
1B- Viscosity 55 mPa.s whole material size distrbution curve
55 mPa.s whole material average
Run 1
Run 2
% Frequency
Nuclei size [um]
100
1000
10000

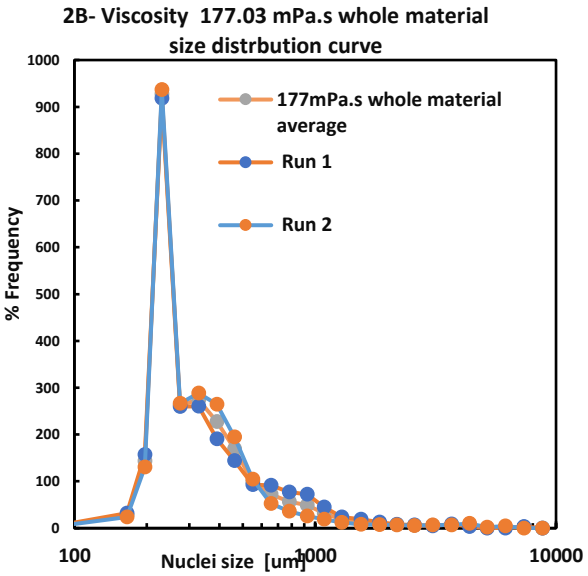
2B- Viscosity 177.03 mPa.s whole material size distrbution curve
177mPa.s whole material average
Run 1
Run 2
% Frequency
Nuclei size [um]
100
1000
10000

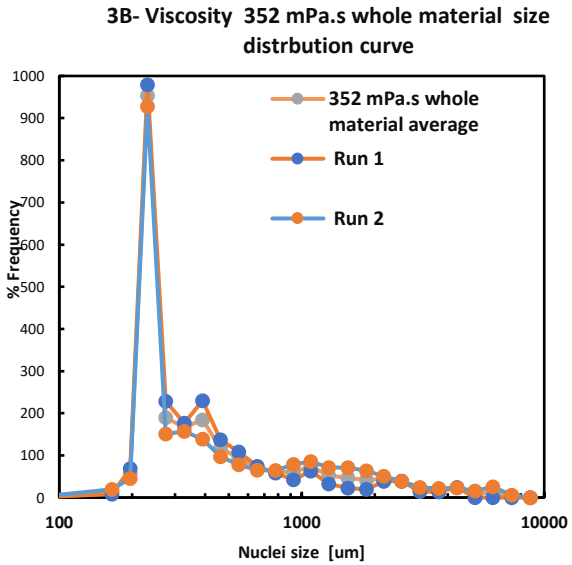
3B- Viscosity 352 mPa.s whole material size distrbution curve
352 mPa.s whole material average
Run 1
Run 2
% Frequency
Nuclei size [um]
100
1000
10000

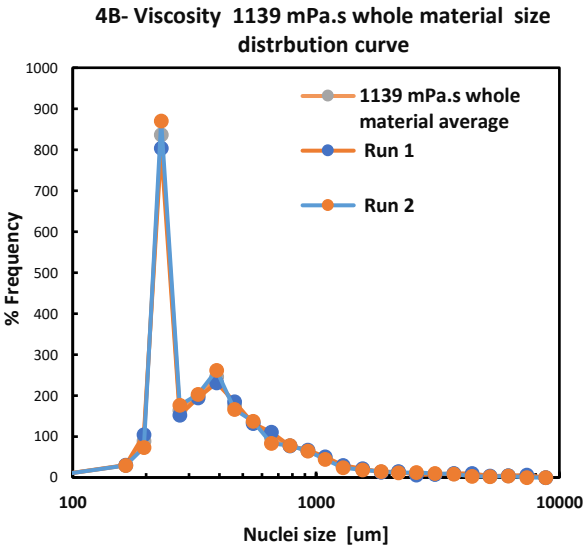
4B- Viscosity 1139 mPa.s whole material size distrbution curve
1139 mPa.s whole material average
Run 1
Run 2
% Frequency
Nuclei size [um]
100
1000
10000

Appendix 5A.2: Effect of primary particle size on nuclei size distribution (in duplicate)

5A.2A Effect of primary particle size using constant liquid /solid fraction X_{LS}

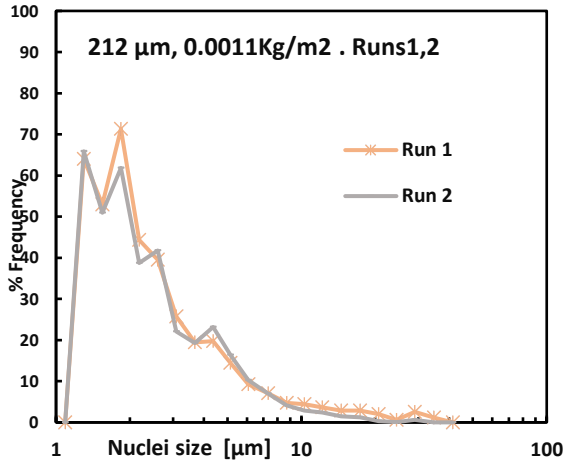

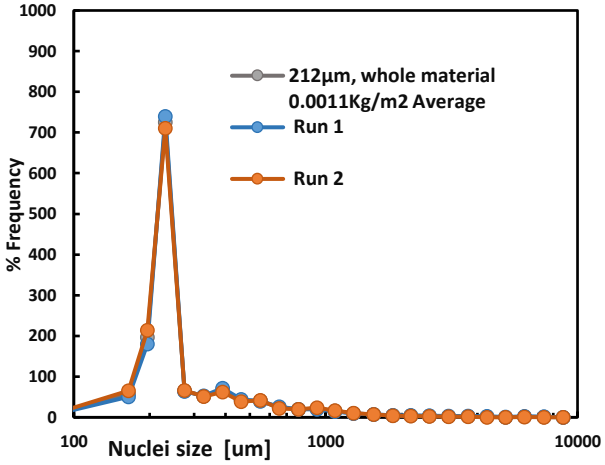

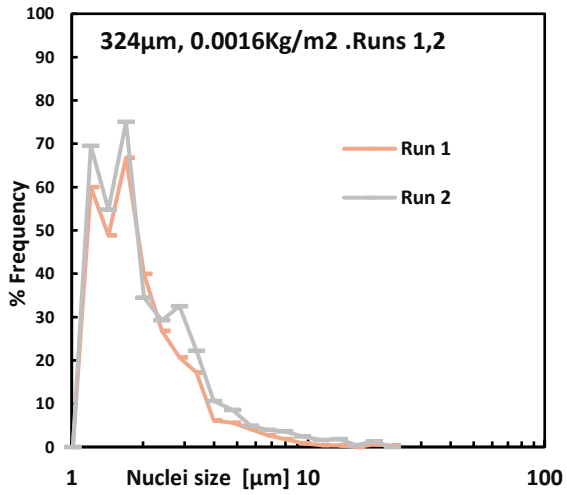

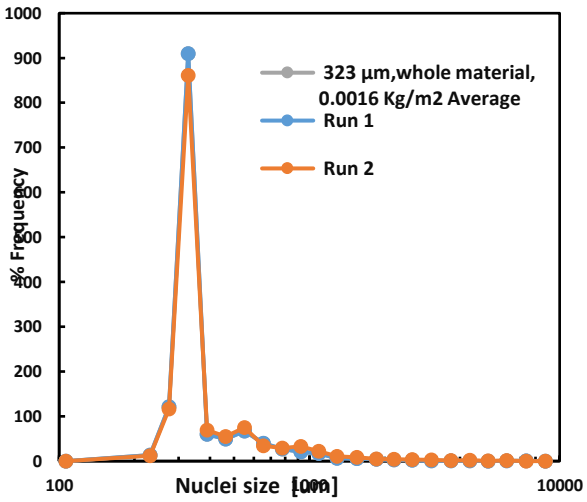

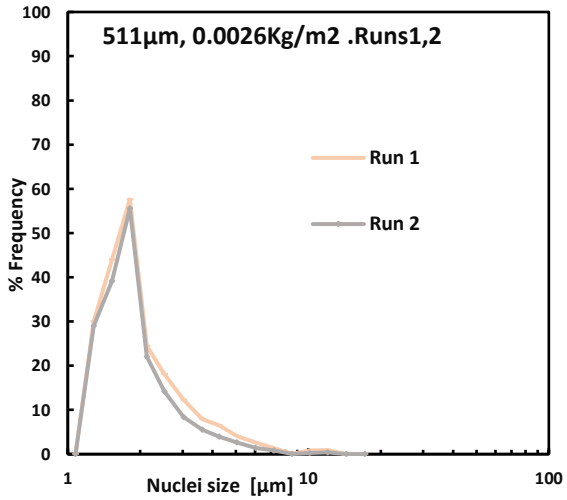

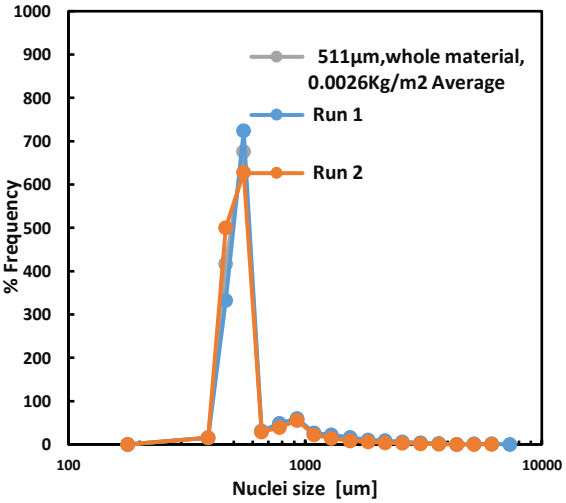

5A.2B. Effect of primary particle size using constant surface area

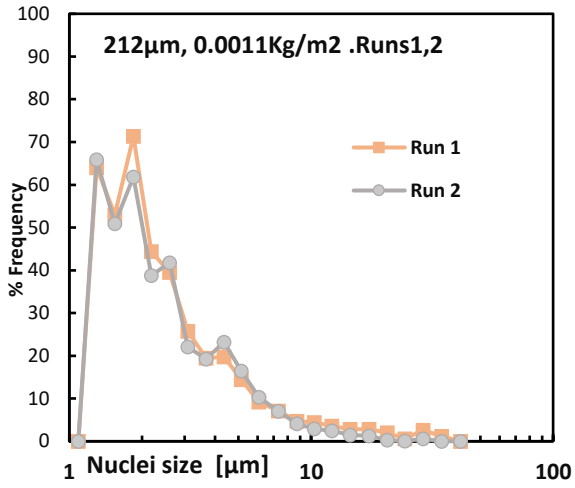

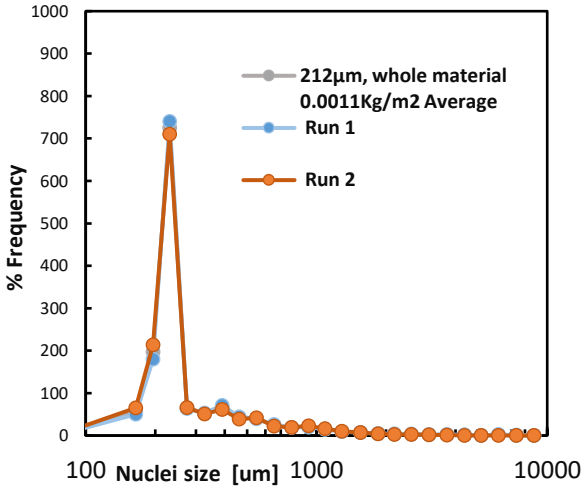

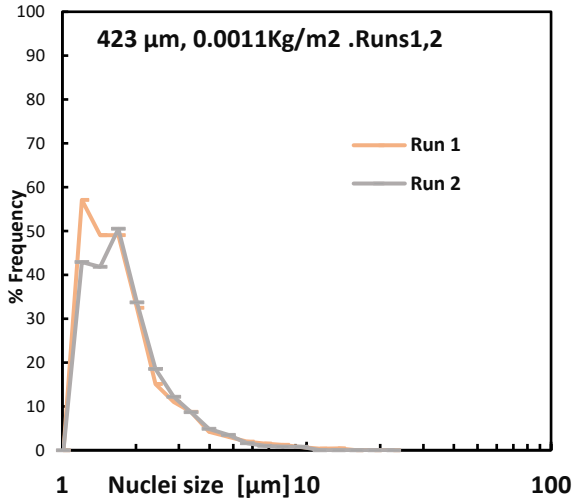

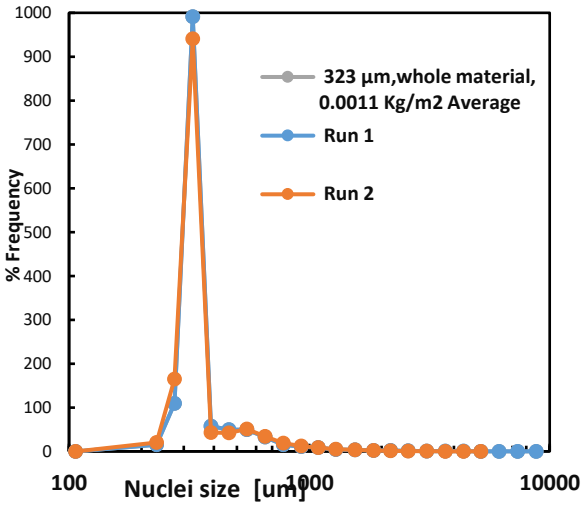

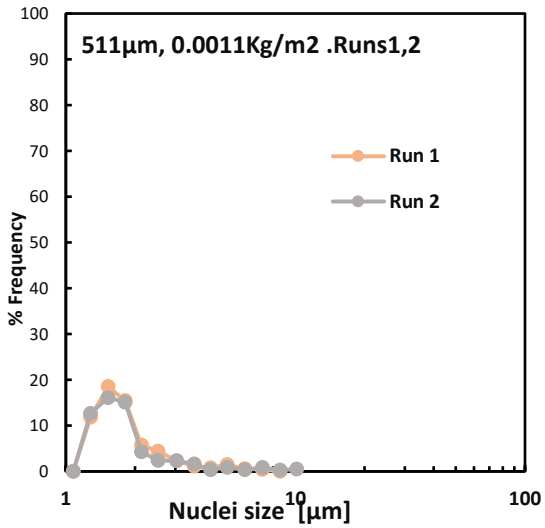

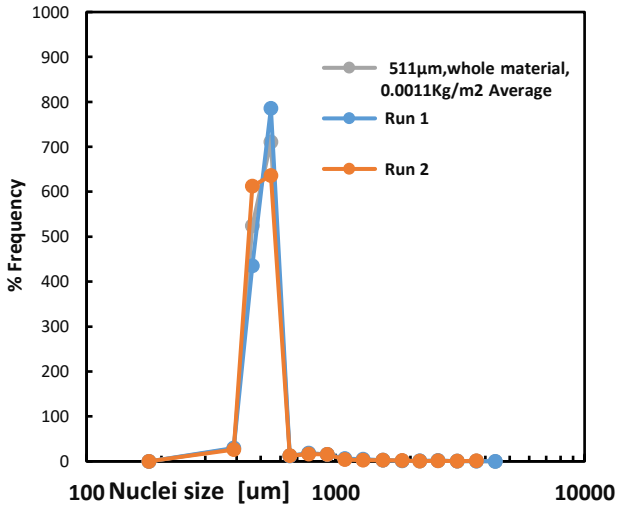

Appendix 6A.1: Effect of flow rate

The following graphs from 6.1. 1A – 6. 1.5 A shows nuclei sizes plotted against frequency at different flow rates obtained by applied liquid pressure from 1-5 bar. The graphs are in pairs, and the ones on the right (6.1.1B - 6.1. 5B) show the averages of the three runs at every liquid pressure.

The graphs (6.1. 1C- 6.1. 5 C) show the whole (granulated and ungranulated) material size distribution obtained by applying different 1-5 bar liquid pressure.

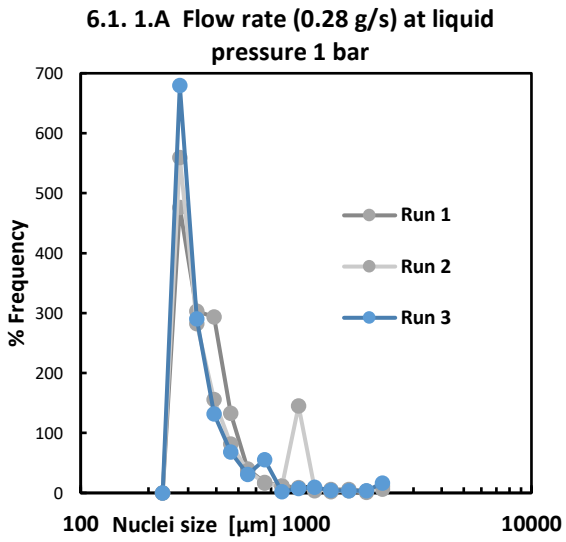

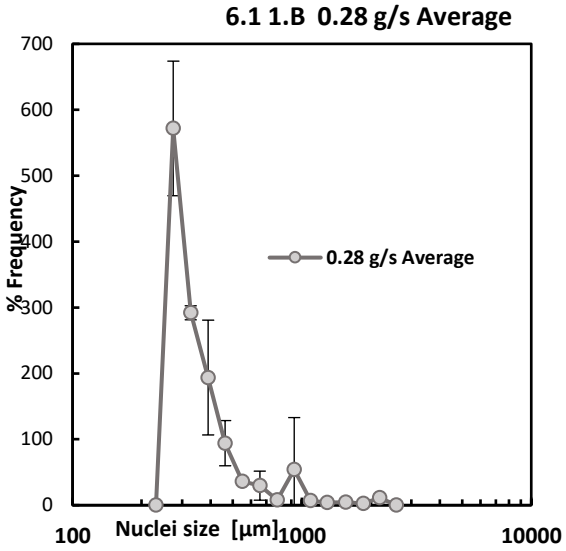

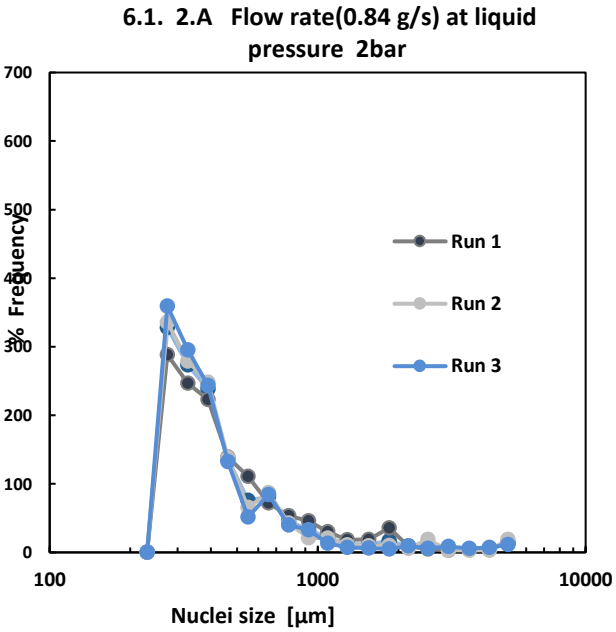

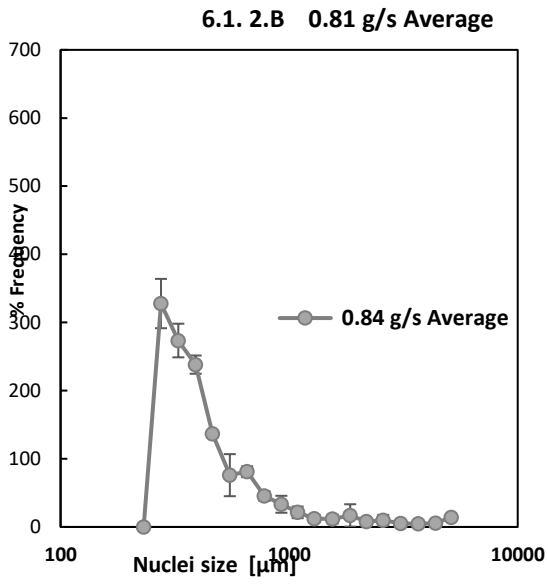

6.1. 3.A Flow Rate (1.29 g/s) at liquid pressure 3 bar

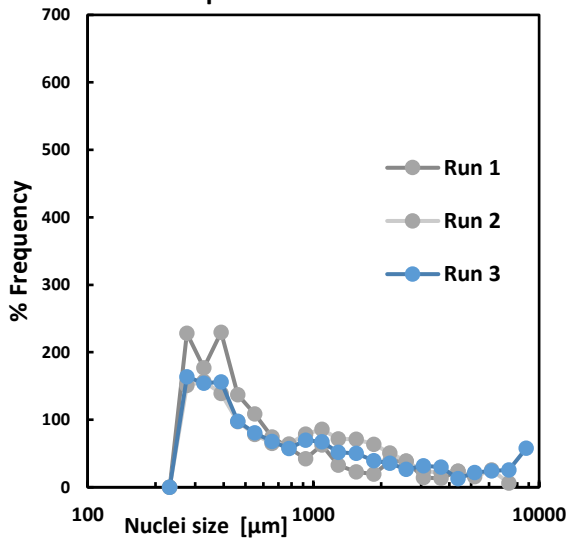

6.1. 3.B 1.29 g/s Average

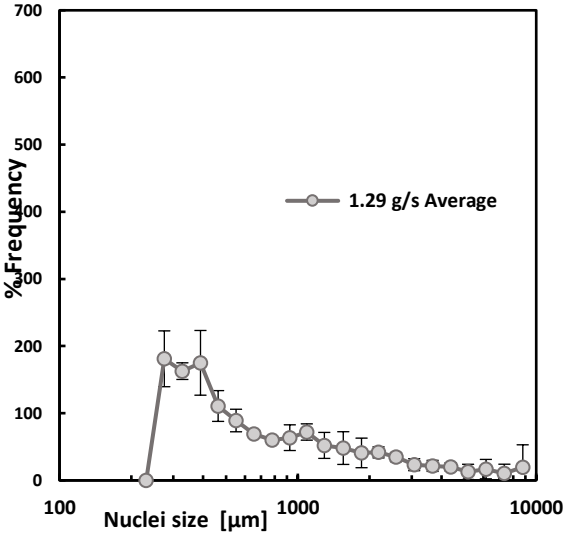

6.1. 4.B Flow Rate (1.78 g/s)at liquid pressure 4 bar

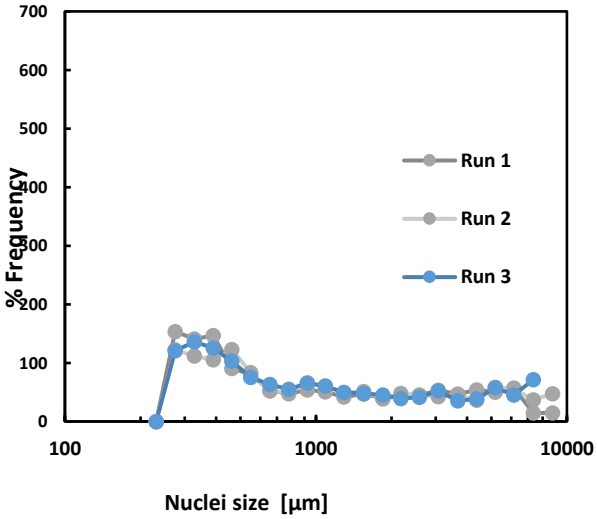

6.1. 4.B 1.78 g/s Average

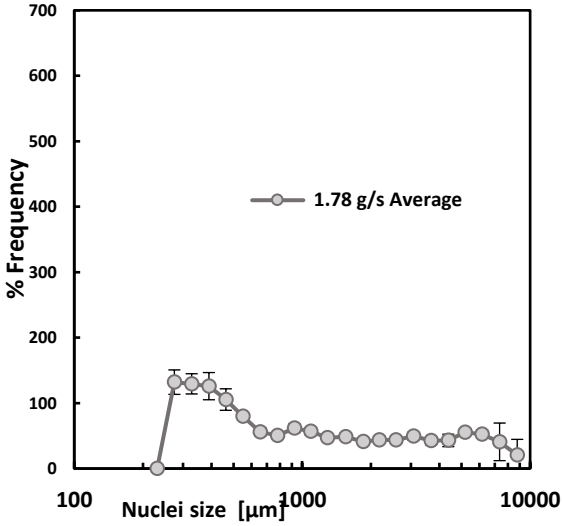

6.1. 5.A Flow rate(2.28 g/s) at liquid pressure 5bar

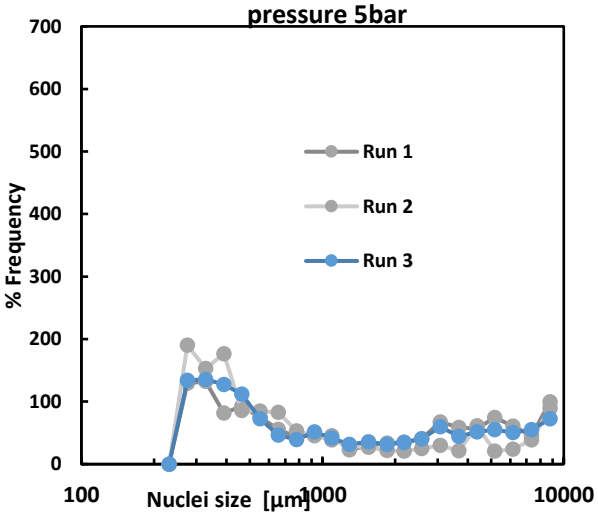

6.1. 4.B 2.28 g/s Average

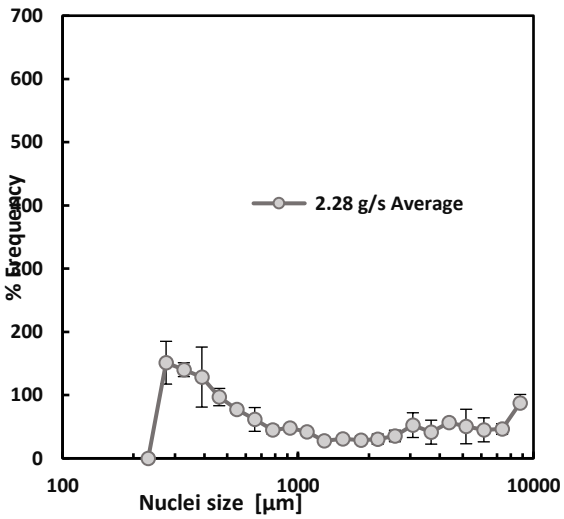

6.1. 1.C Whole material Flow rate (0.28 g/s)

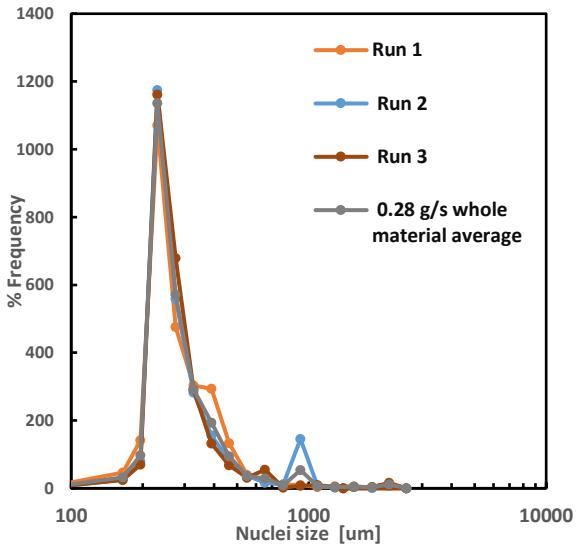

6.1. 2.C whole material 0.81 g/s Average

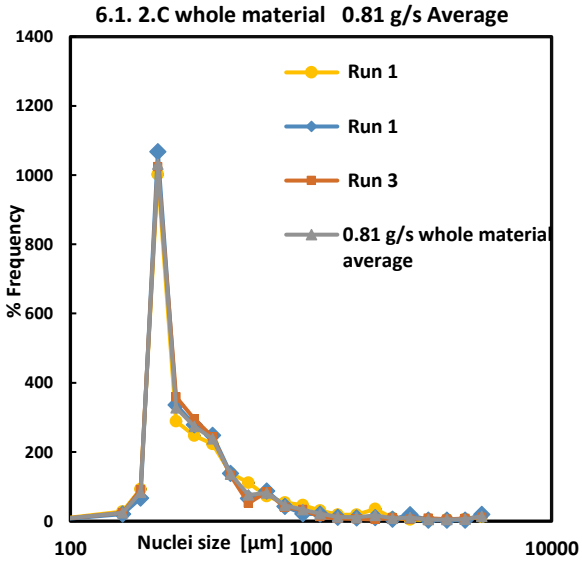

6.1. 3.C whole material 1.29 g/s Average

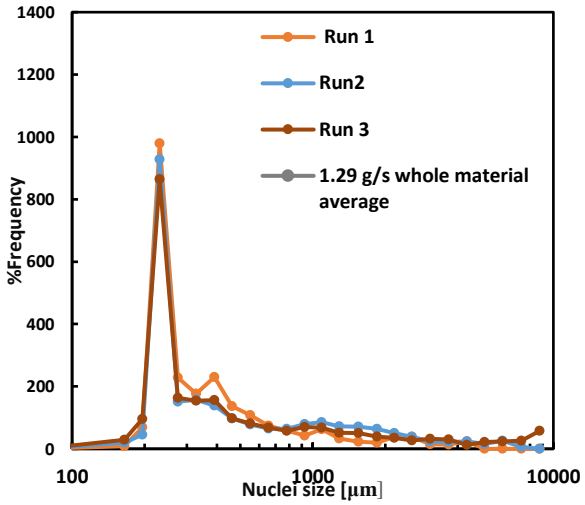

6.1. 4.C whole material 1.78 g/s Average

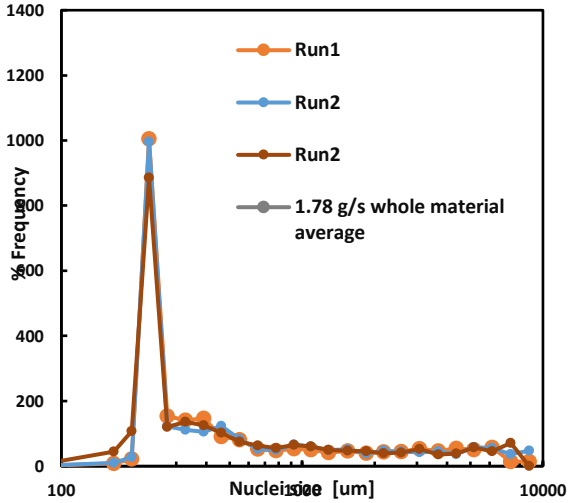

6.1. C.5 Whole material 2.28 g/sAverage

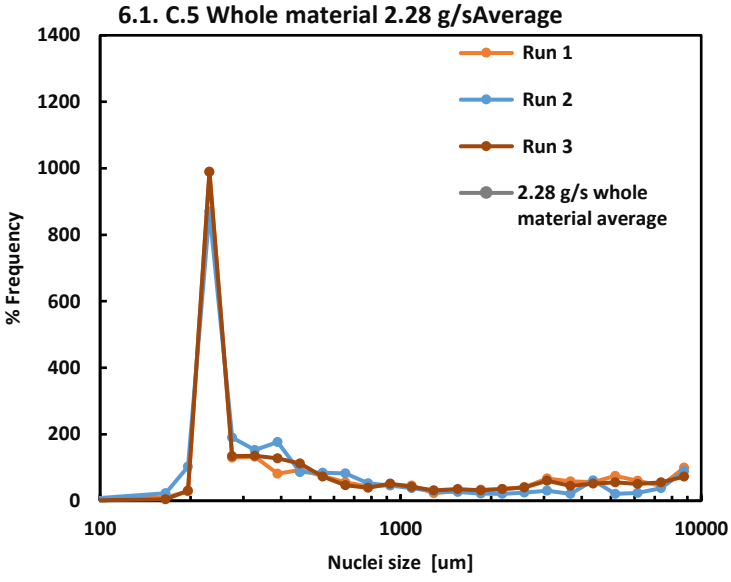

Appendix 6A.2: Effect of mixing time

The following graphs from (6.2. A.10 -300 s) show nuclei sizes plotted against frequency at different mixing times. The graphs are in pairs, and the ones on the right (6.2. B.10 -300 s) show the averages of the three runs at every time.

The graphs (6.2. C.10 -300 s) show the whole (granulated and ungranulated) material size distribution obtained after different mixing times (10 s-300 s).

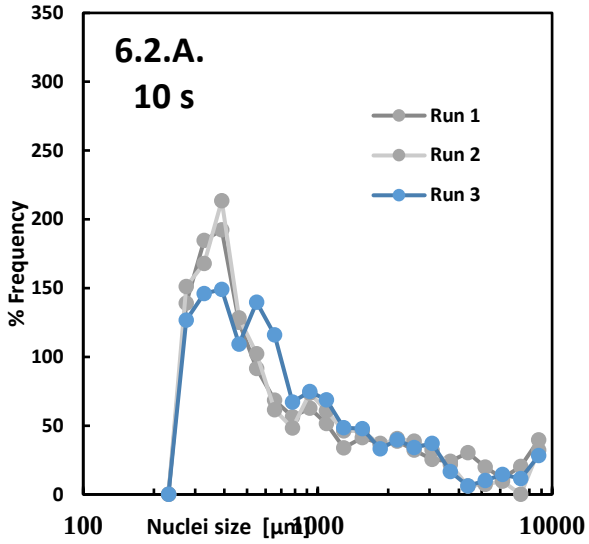

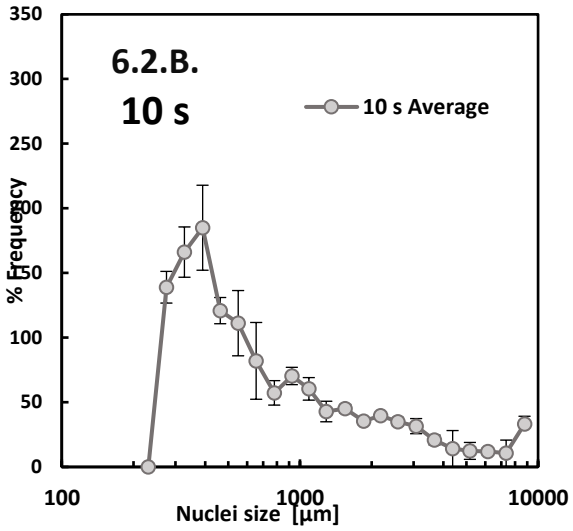

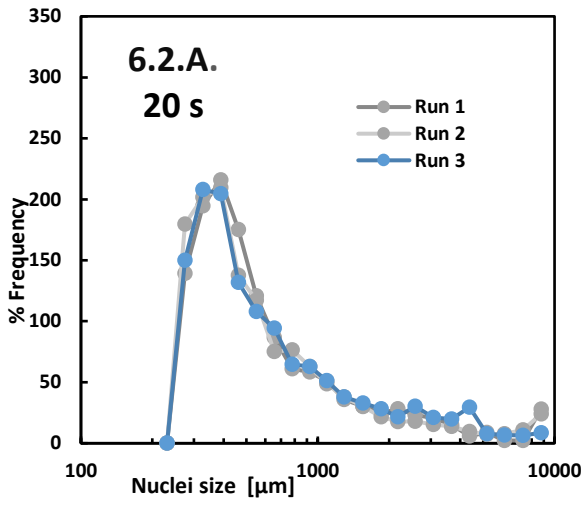

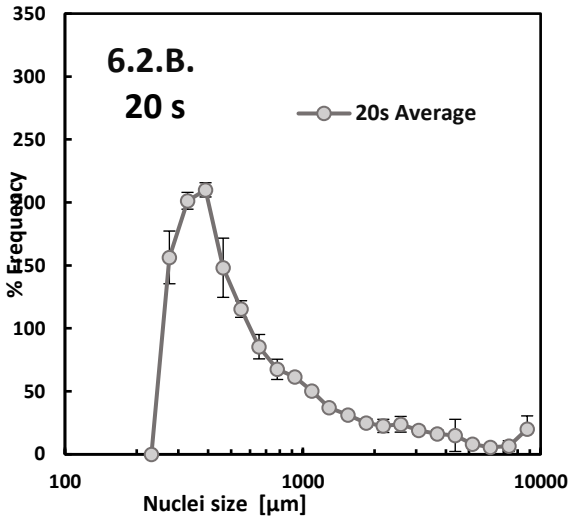

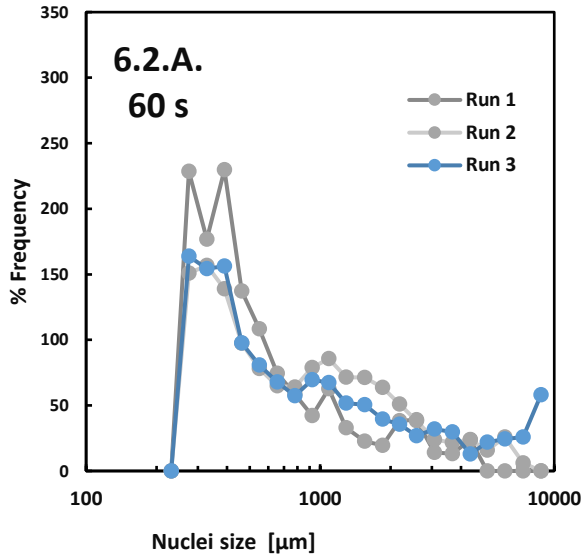
6.2.A.
60 s
Run 1
Run 2
Run 3
% Frequency
Nuclei size [µm]

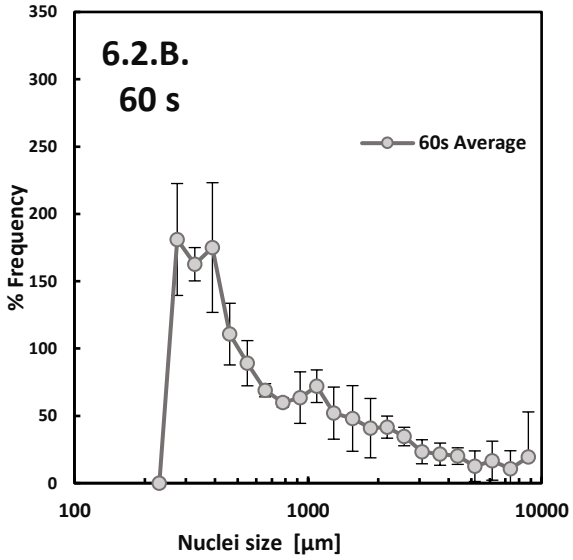
6.2.B.
60 s
60s Average
% Frequency
Nuclei size [µm]

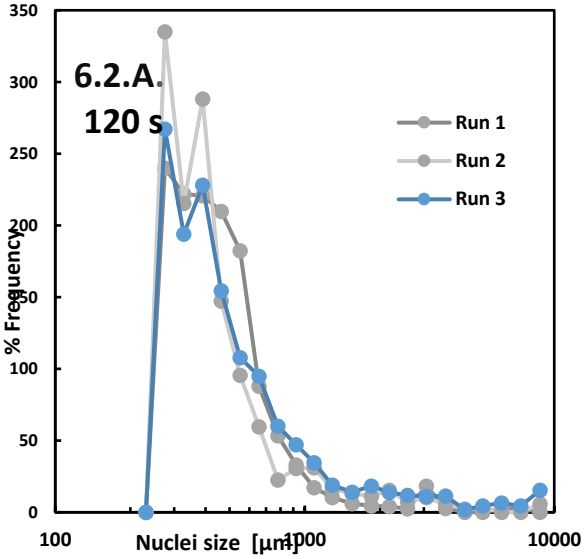
6.2.A.
120 s
Run 1
Run 2
Run 3
% Frequency
Nuclei size [µm]

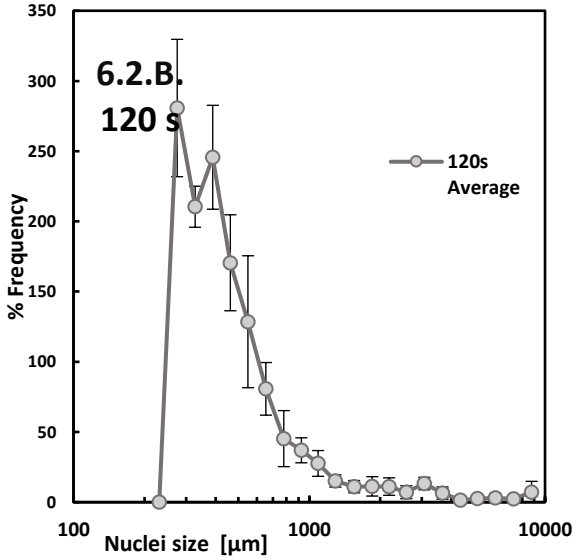
6.2.B.
120 s
120s
Average
% Frequency
Nuclei size [µm]

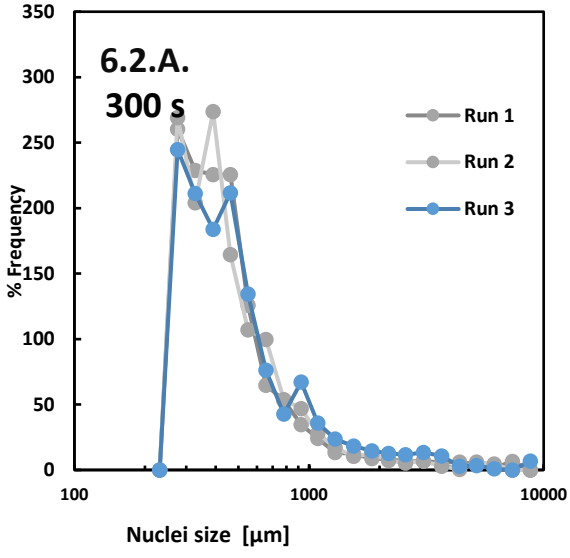
6.2.A.
300 s
Run 1
Run 2
Run 3
% Frequency
Nuclei size [µm]

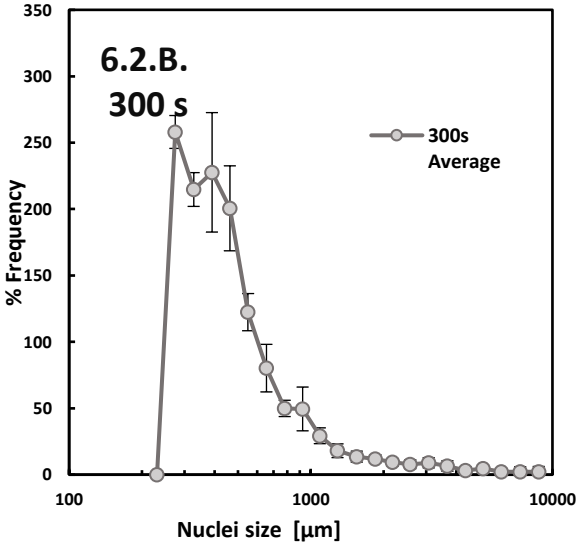
6.2.B.
300 s
300s
Average
% Frequency
Nuclei size [µm]

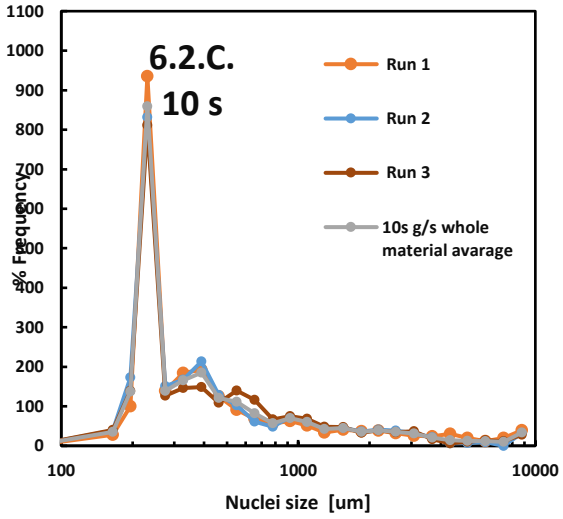
6.2.C.
10 s
Run 1
Run 2
Run 3
10s g/s whole material avarage
% Frequency
Nuclei size [um]

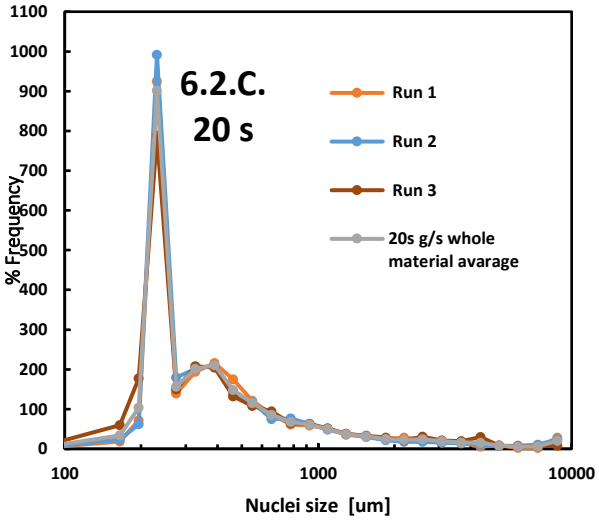
6.2.C.
20 s
Run 1
Run 2
Run 3
20s g/s whole material avarage
% Frequency
Nuclei size [um]

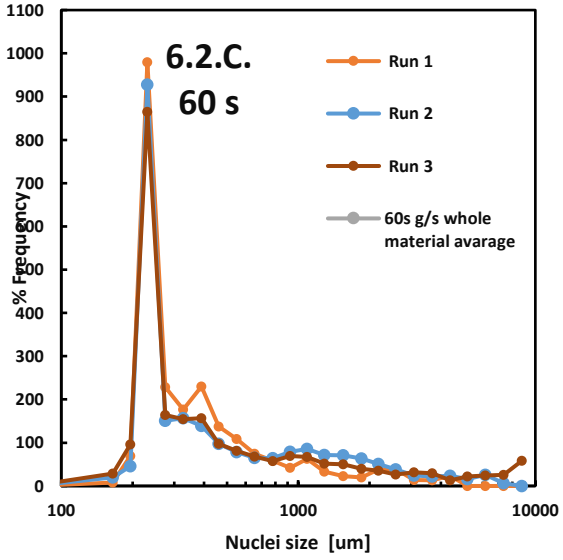
6.2.C.
60 s
Run 1
Run 2
Run 3
60s g/s whole material avarage
% Frequency
Nuclei size [um]

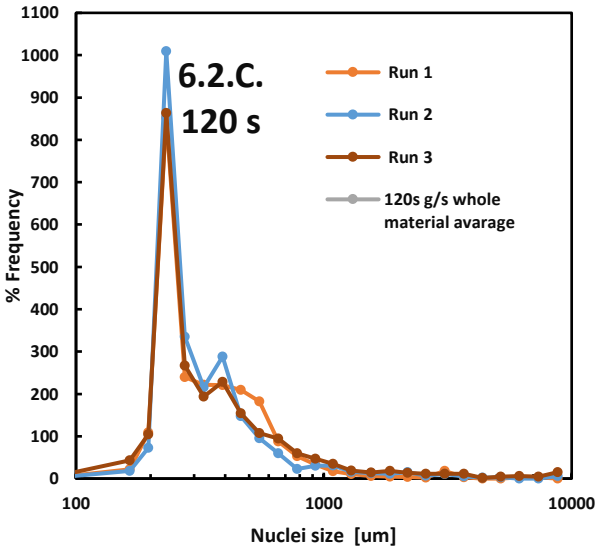
6.2.C.
120 s
Run 1
Run 2
Run 3
120s g/s whole material avarage
% Frequency
Nuclei size [um]

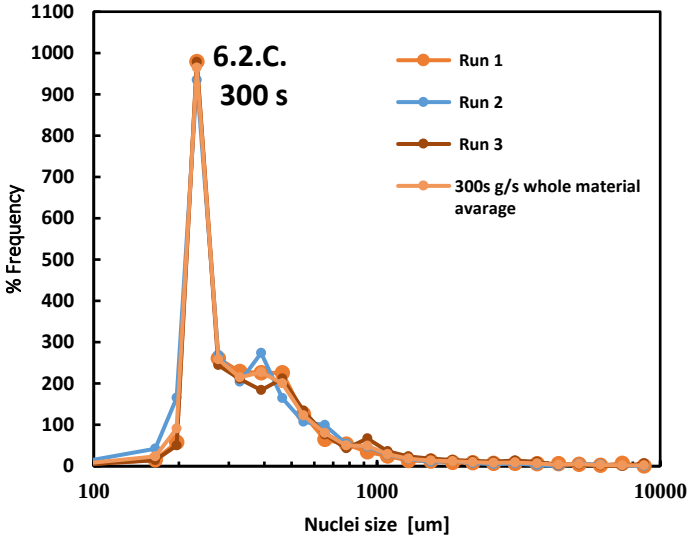
6.2.C.
300 s
Run 1
Run 2
Run 3
300s g/s whole material avarage
% Frequency
Nuclei size [um]

Appendix 6A.3: Effect of Atomisation Pressure

The following graphs are in pairs; the ones on the left from (6.3. A. 3 -5 bar) show the nuclei size plotted against % frequency at different atomisation pressures.

The graphs on the right (6.3.B. 3 -5 bar) show the size distribution of the whole material (granulated and ungranulated) obtained by applying atomisation pressure from 3 to 5 bars.

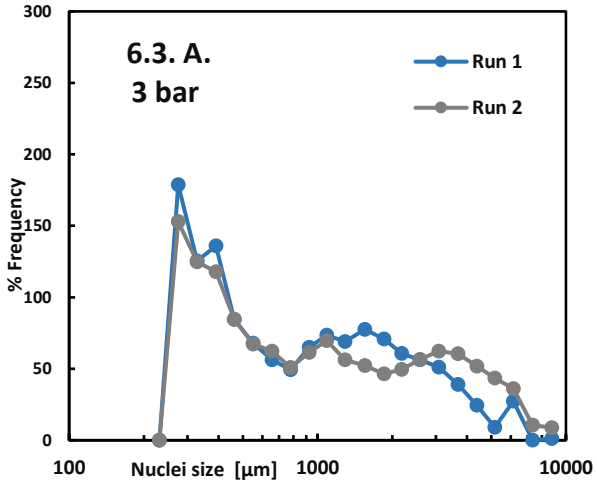

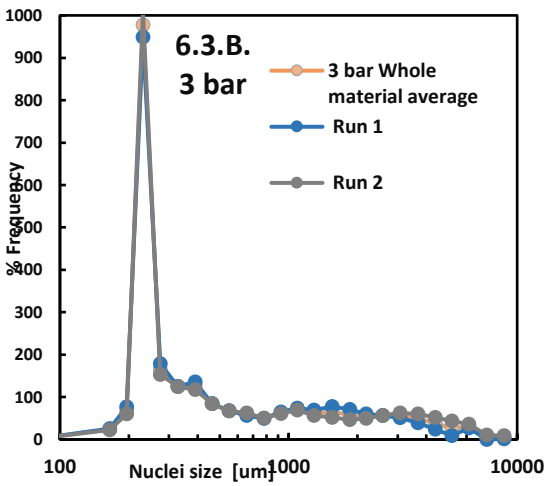

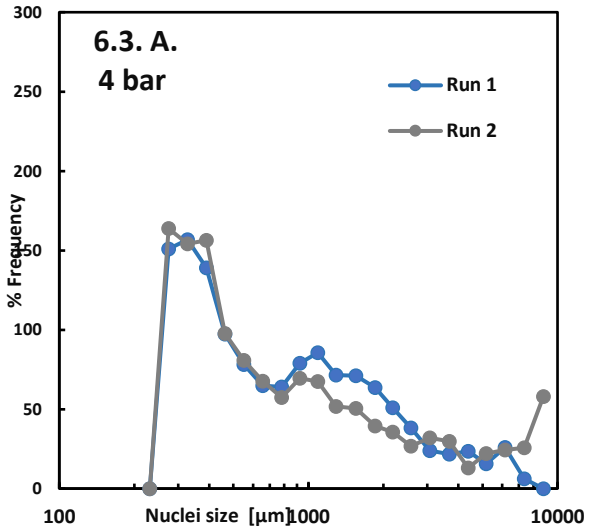

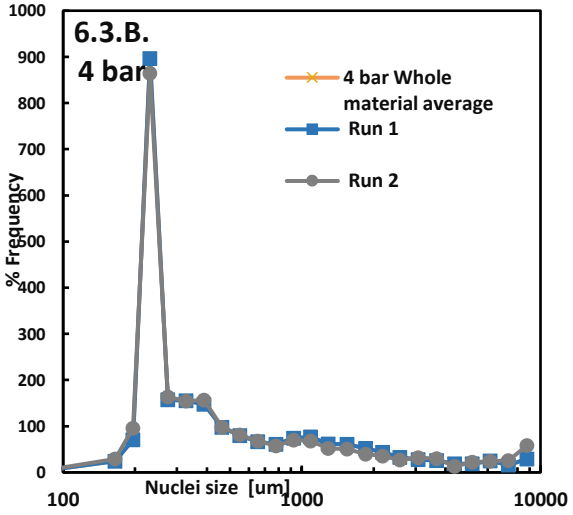

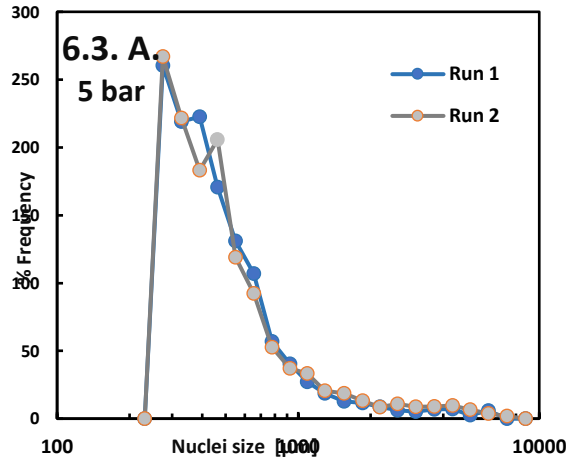

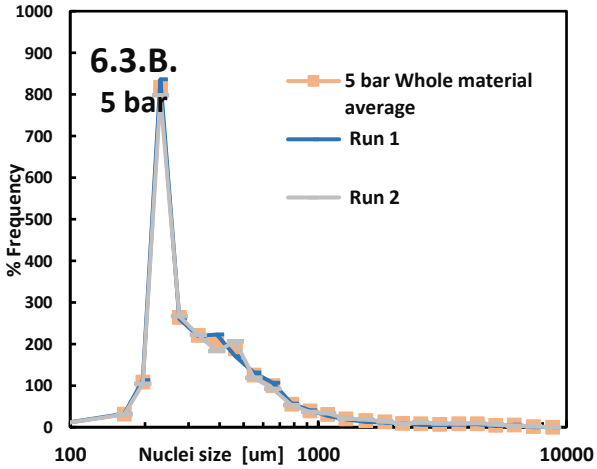

Appendix 6A.4: Effect of fluidisation velocity

The following graphs are in pairs; the ones on the left from (6.4. A. 0.45–0.65 m/s) show the nuclei size plotted against % frequency at different atomisation pressure.

The graphs on the right (6.4.B. 45– 0.65 m/s) show the size distribution of the whole material (granulated and ungranulated) obtained by applying fluidisation velocity from 0.45 to 0.65 m/s.

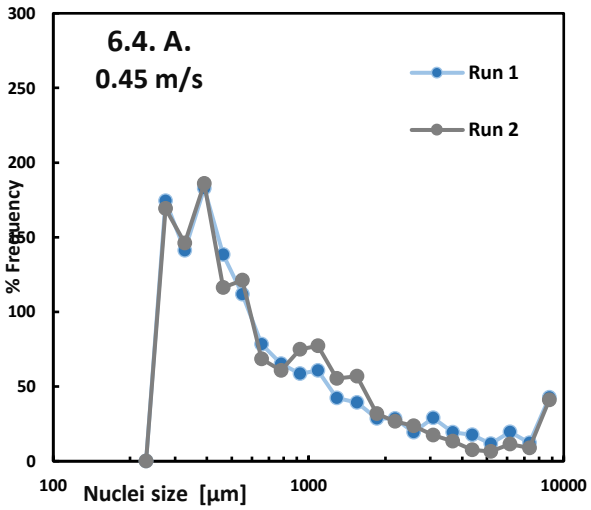

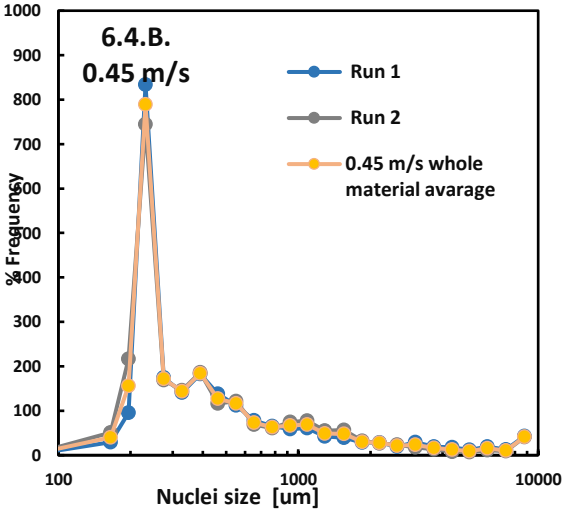

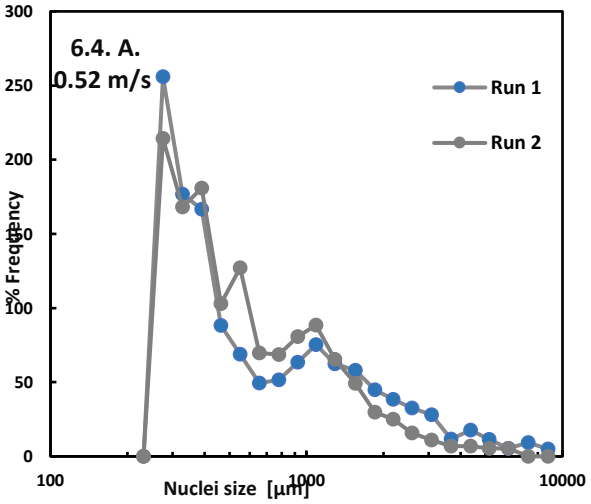

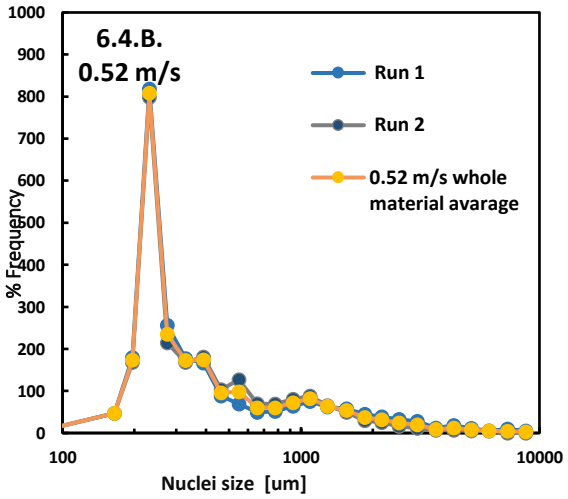

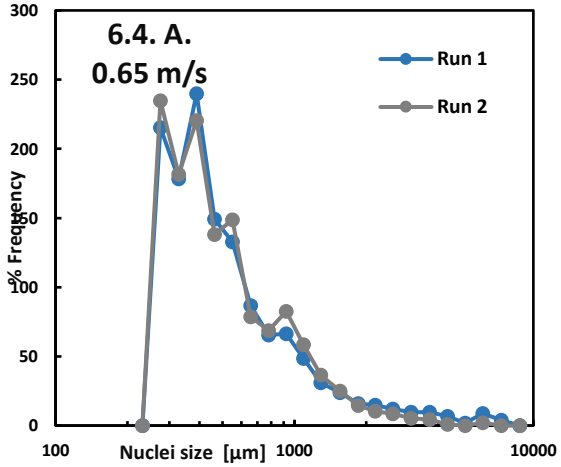

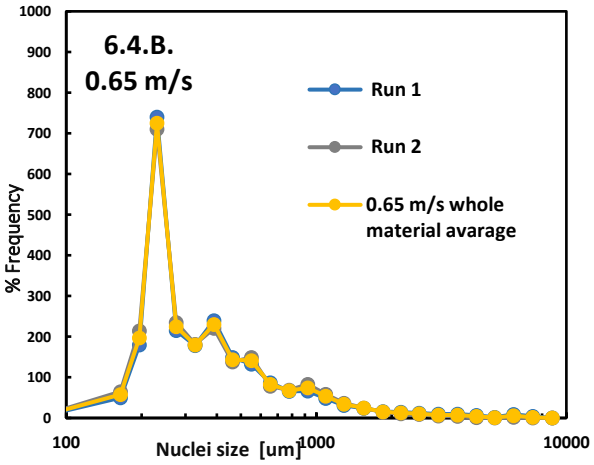

Appendix 7A.1: Effect of material

The following graphs from 7.1. 1 A – 7.1. 5 A show nuclei sizes plotted against frequency at different flow rates obtained by applied liquid pressure from 1-5 bar. The graphs are in pairs, and the ones on the right (7.1.1B – 7.1. 5B) show whole (granulated and ungranulated) material size distribution obtained by applying different 0.81- 4.0 bar liquid pressure.

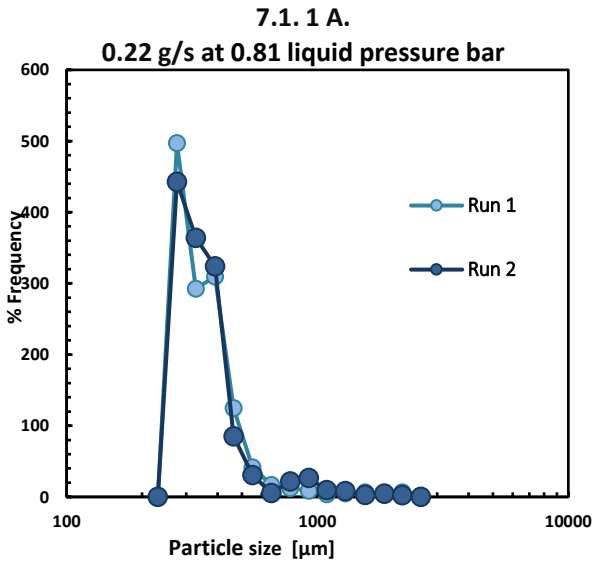

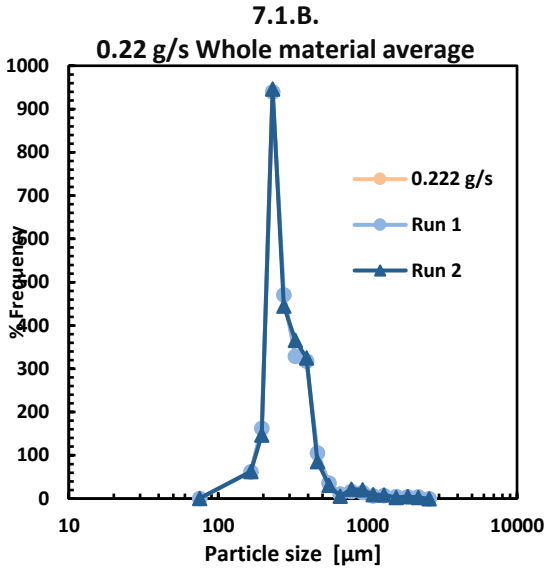

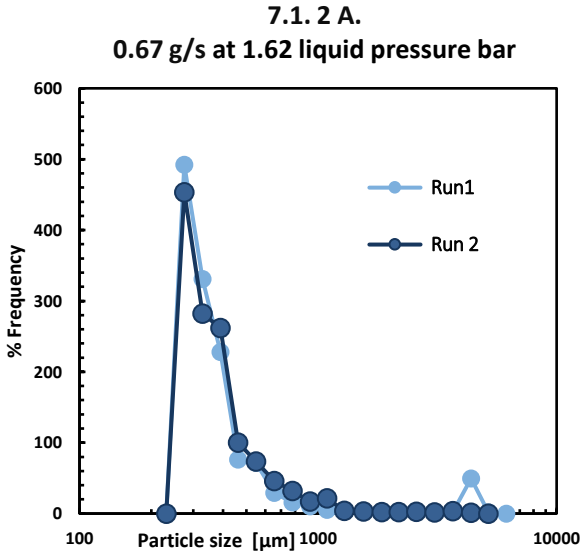

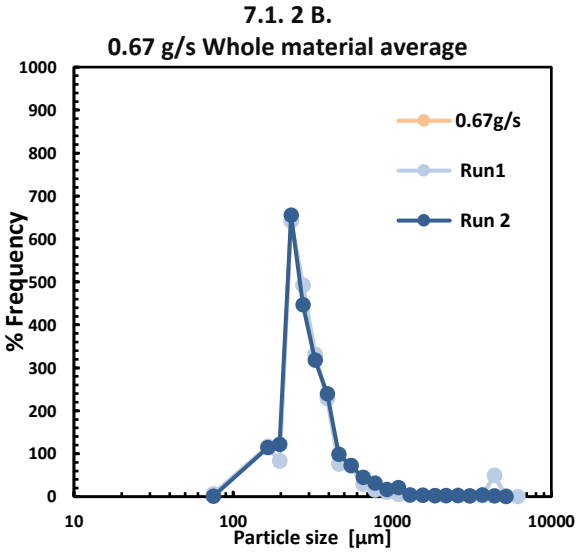

7.1. 3 A.
1.023 g/s at 2.43 liquid pressure bar

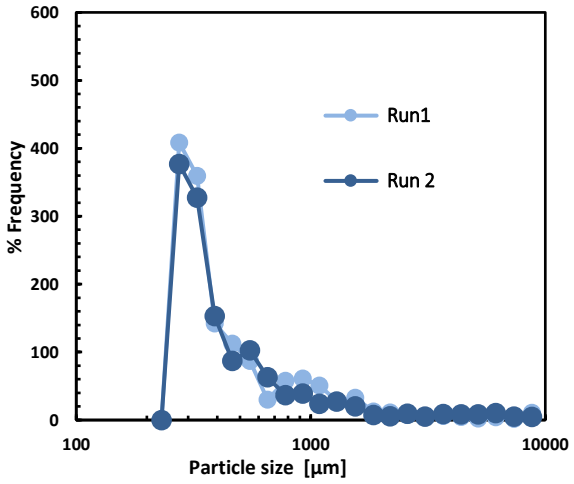

7.1. 3 B.
1.023 g/s Whole material average

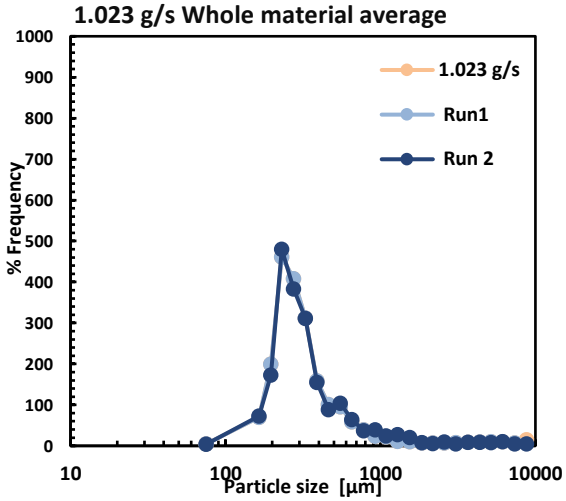

7.1. 4 A.
1.47 g/s at 3.60 liquid pressure bar

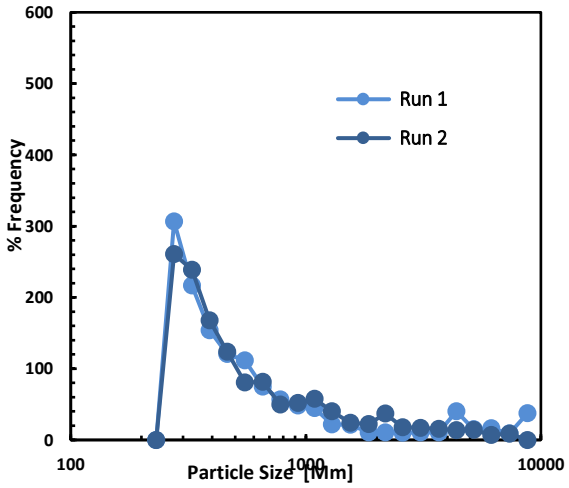

7.1. 4 B.
1.476 g/s Whole material average

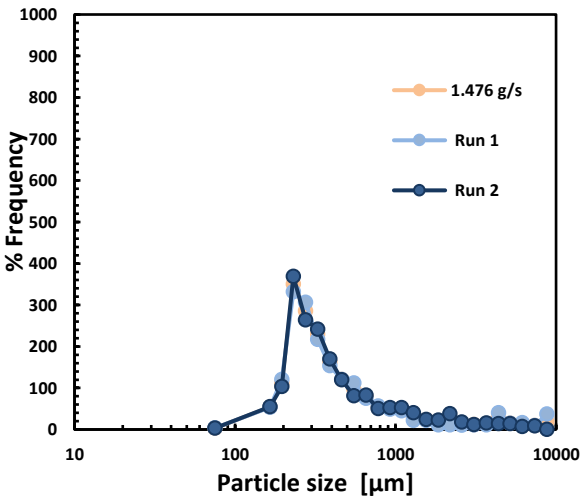

7.1. 5A.
1.81 g/s at 4.0 liquid pressure bar

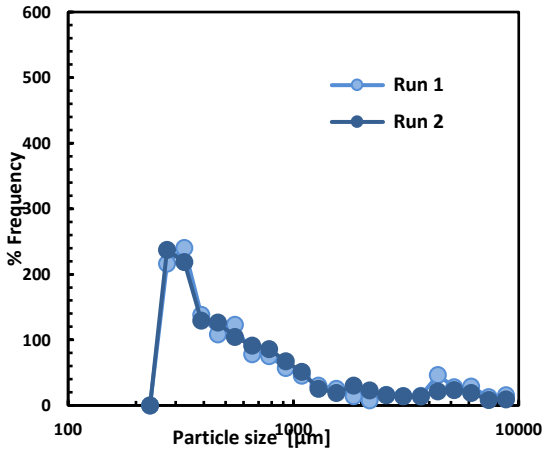

7.1. 5 B.
1.80 g/s Whole material average